UNIVERSITÀ DEGLI STUDI DI PARMA

Dipartimento di Chimica Organica ed Industriale
Ph.D. in Science and Technology of Innovative Material

XXII Cycle

Responsive Hybrid Materials *via* Molecular Recognition on Silicon and Single Molecule Magnets Assembly on Carbonanotubes

Elisa Biavardi

Coordinator: Prof. Anna Painelli

Supervisor: Prof. Enrico Dalcanale

Author: Elisa Biavardi

Contents

CHAPTER 1

Phosphorous-bridged Cavitands.

CHAPTER 2

Reversible guest exchange in tetraphosphonate cavitands.

CHAPTER 3

Molecular Recognition on Si(100) functionalized with tetraphosphonate cavitands.

CHAPTER 4

SWCNT functionalized with Cavitands for Biogenic Amines Sensing.

CHAPTER 5

Molecular Magnetism: Introduction.

CHAPTER 6

The first Carbon Nanotube functionalized with a Tiny Magnet.

CHAPTER 7

Tiny Magnet Functionalized with Charged Ligand.

Phosphorous-bridged Cavitands.

1

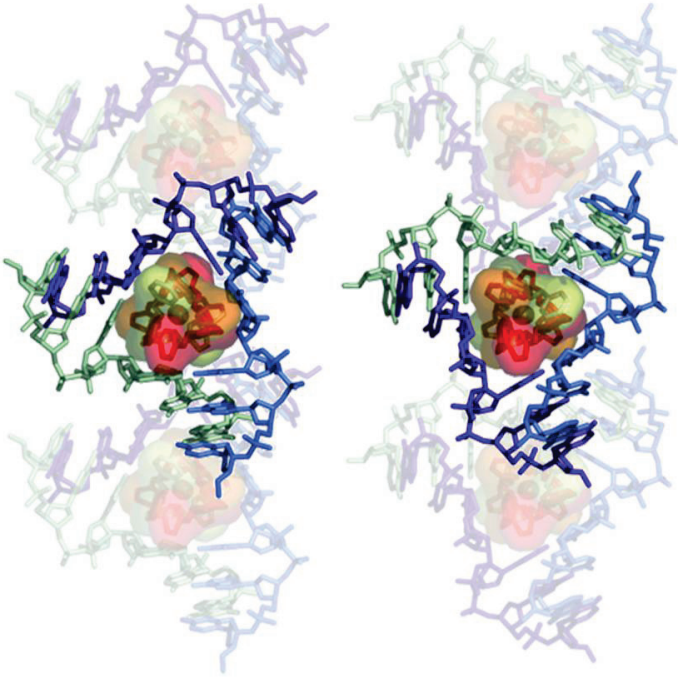

"Molecular Recognition"

Image refers to reference[7].

I.I Self-Assembly.

A peculiar trend in modern chemistry is its increasing ability to mimic form and structure in biology. This has largely been achieved using a principle which has been borrowed from biology: the spontaneous self-assembly of well-defined and complex molecular entities from constituent subunits in solution. There have been several attempts in literature to define the term "self-assembly": Whitesides defined it as "the spontaneous organization of molecules or objects into stable, well-defined structures by noncovalent forces".[1] Jean-Marie Lehn defined the supramolecular self-assembly as "the spontaneous association of either a few or many components resulting in the generation of either discrete oligomolecular supermolecules or of extended polymolecular assemblies such as molecular layers, films, membranes etc. The formation of the supramolecules results from the recognition-directed spontaneous association of a well-defined and limited number of molecular components under the intermolecular control of the noncovalent interactions that hold them together".[2] Nature offers the best examples, since self-assembly processes occur in everyday life and are optimised to a high degree by evolution.[3]

The virtues of self-assembly are:

Information: using few repeating subunits in building a large structure reduces the amount of information required, since the assembling parts contain all the needed information for the construction of well-defined assemblies.

Control: the assembly through non-covalent bonds of relatively low energy is a reversible process that leads to the thermodynamically most favourable structure. Switching between different states of organization can occur readily in response to environmental changes.

Error-checking: the constituent parts contain the directions for the assembly. Any malformed building block not leading to the most stable final structure will be excluded because of less favourable interactions. Self-assembly can be self-checking to overcome synthesis errors.

Efficiency: complex molecules can be constructed with great efficiency through the assembly of building blocks rather than by direct construction.

In all cases, three basic levels of operation are involved in the formation of a programmed supramolecular system: recognition of the assembling components, preorganization of these components to optimize the non-covalent interactions and termination into the thermodynamically most stable structure.

I.2 Multivalency and the Supramolecular Chemistry.

Within the field of supramolecular chemistry there is currently an increasing awareness of the potential of the multivalency concept:[4] the simultaneous interaction between multiple functionalities on one entity and complementary functionalities on another. This concept has been extensively studied in biochemistry for a long time.[1,5,6,7]

Multivalency constitutes a self-assembly pathway that combines all the attractive characteristics of self-assembly with the possibility to achieve thermodynamic and/or kinetic assembly stability at nano- or even picomolar concentrations.

Multivalency describes the binding of two (or more) entities that involves the simultaneous interaction between multiple, complementary functionalities on these entities. In the case of supramolecular multivalency these entities can be any supramolecular display, ranging from a molecule to a self-assembled monolayer (SAM). In this perspective, the complementary interacting functionalities are referred to as host and guest. The interaction between a host and a guest leads to the formation of a complex. The valency of an entity is the number of separate connections of the same kind that it can form through host-guest interactions with entities bearing the complementary functionality. The valency of the complex is defined by the number of shared interactions between the two interacting entities. All interactions involving more than one host-guest interaction are considered multivalent.

There is a tendency to use the term multivalency for any interaction that involves entities displaying multiple functionalities, even though many of these concern the interaction of a multivalent entity with multiple monovalent species or the formation of high stoichiometry or even polymeric systems in which the interaction between each two species in such an assembly is

monovalent.[8] On the whole, we can use the term multivalency for the self-assembly of well-defined complexes in which the separation of any entity or part from the complex requires the dissociation of at least two interactions.

I.3 Tetraphosphorous-bridged cavitands.

Self-assembly has been widely exploited by supramolecular chemists for the design and synthesis of molecular receptors which are useful to understand and mimic nature's specific interactions. Interesting and versatile molecular receptors are cavitands, originally defined by Cram as "*synthetic organic compounds with enforced cavities large enough to complex complementary organic molecules or ions*"[9], whose complexation properties have been extensively studied in the solid state[10], in solution[11] and in the gas phase.[12]

Historically, resorcin[4]arenes, which can be easily prepared in high yield by the acid-catalyzed condensation between resorcinol and either aliphatic or aromatic aldehydes, are the cavitands basic scaffold (Scheme I.1).[13]

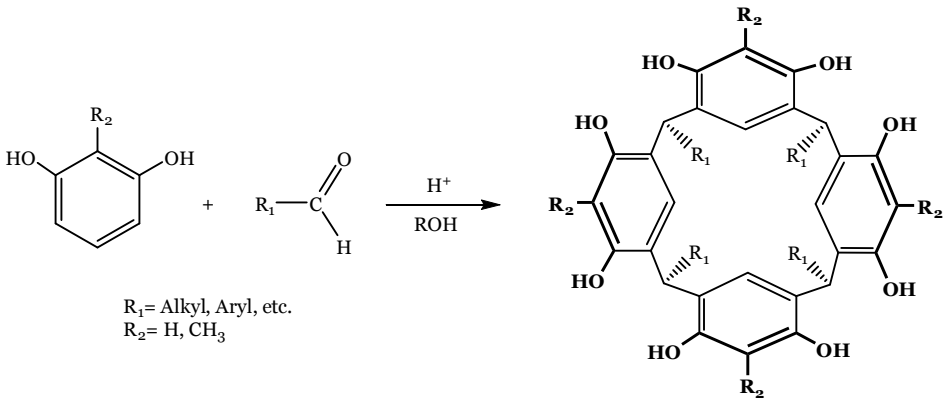

Scheme I.1. Synthesis of resorcin[4]arenes.

The flexible macrocycles obtained can be functionalized at the upper rim by reacting its four couples of adjacent phenolic oxygens with different bridging groups giving rigidified structures. In particular, in the design of

cavitands, the choice of the bridging groups is pivotal, since it determines shape, dimensions and complexation properties of the resulting cavity.

In our case, in order to enhance the complexation properties of cavitands, we introduced four phosphorous bridges which confer to the macrocycle particular complexation properties towards cationic species[14] and alcohols.[15]

In fact, as shown in past works,[15] increasing the number of $P{=}O_{in}$ groups on the cavitand corresponds to an enhancement of the molecular recognition properties.

Synthesis and stereochemical elucidation of tetraphosphonate cavitands have already been reported long ago.[16]

The first attempt to synthesize phosphorous-bridged cavitands was carried out in Cram's group in the 1980s by reacting a methyl-footed resorcin[4]arene with dichlorophenylphosphonate, obtaining a mixture of diastereomers difficult to isolate.[17]

In fact, the presence of four P^V stereogenic centers gives rise to six possible diastereomeric cavitands. The inward (i) and outward (o) configurations are defined relative to the different orientation of the P=O moieties (Scheme 1.2).[18]

The tetraphosphonate cavitands nomenclature, reported in Scheme 1.2, summarizes the number and relative positions of P^V bridges, their stereochemistry, and the type of substituents at the lower rim, at the apical positions, and on the phosphorus bridges, respectively, in a single term.

In particular, the capital letter, defines number and nature of bridges, the lower case letters define the in-out stereochemistry, and R_1, R_2 and R_3 in brackets define the substituents at the lower rim, in the apical positions and on the phosphorous stereocenters respectively.

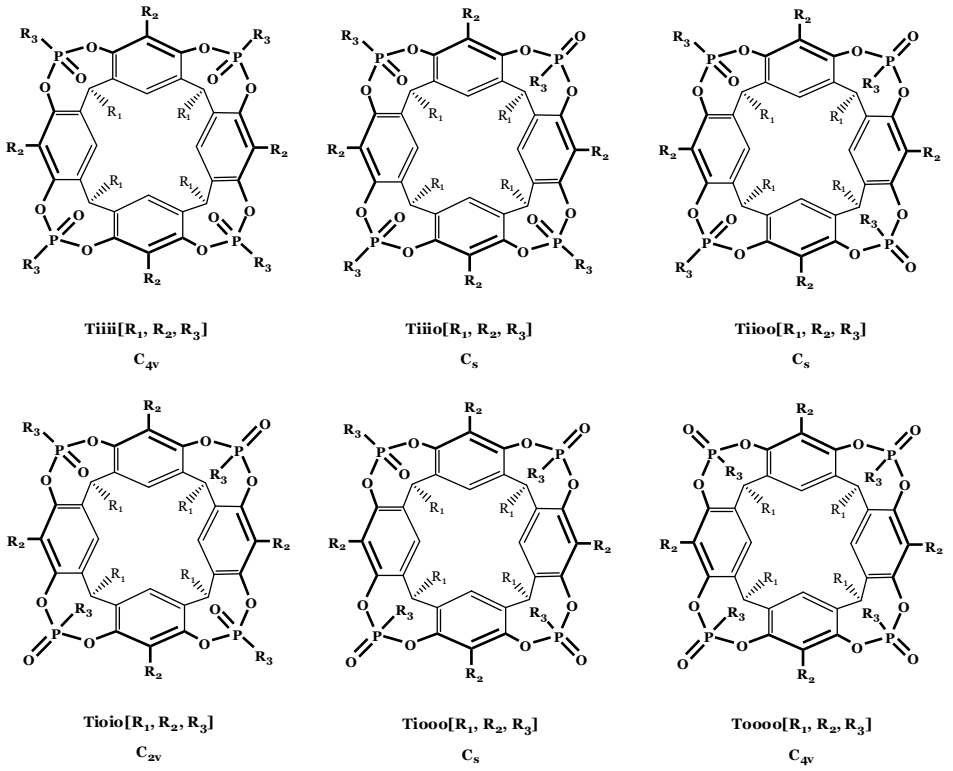

Scheme I.2. Isomers of tetraphosphonate bridged cavitands.

Later on, the topic was investigated by Puddephatt and co-workers, who prepared the T_{iiii}-P^{III} phosphonito cavitand and studied its transition metal complexation properties.[19] Treatment of a phenethyl-footed resorcin[4]arene with dichlorophenylphosphine results in the selective formation of the iiii isomer (lone pair directed inward), the favored one as indicated by molecular mechanics calculations.[17c]

At the same time, new cavitands with phosphonate bridging moieties have been obtained by J.-P. Dutasta and co-workers.[20] This new stereoselective sinthesis involved dichlorophenylphosphine oxide (P^{V}) instead P^{III} in the presence of an amine. This reaction was performed in refluxing toluene and N-methylpyrrolidine as amine, to provide the T_{iiii} with only a minor amount of T_{iiio} isomer present.

The origin of the reaction selectivity has been attributed to the template effect of the N-methylpyrrolidinium salt formed in situ. Therefore, in the first stage of the reaction, after the entrance of the first P=O bridge, the host-guest complex between resorcin[4]arene and ammonium cation, directed the incoming P=O groups inward via H-bonding and electrostatic interactions. Moreover, the formation of the T_{iiii} isomer is solvent dependent, since the ammonium ion interaction with the P=O groups is effective only in weakly solvating agents, such as toluene.

Recently, in our group has been developed a new method to achieve only pure T_{iiii} with high yields.[21] Reaction of resorcin[4]arene with dichlorophenylphosphine in the presence of pyridine affords exclusively the $4P^{III}_{iiii}$ cavitand. Its subsequent *in situ* oxidation with H_2O_2, proceeds with retention of configuration at the phosphorous centre and provides, in a single step, the T_{iiii} without need of purification. Unfortunately this method does not work well if the substituent on the phosphorous stereocentre (R_3) is a methyl instead phenyl group and for the tetrathiophosphonate cavitand (TS_{iiii}, the control receptor) synthesis.

TS_{iiii} cavitand is structurally identical to the T_{iiii} receptor except for the presence of four P=S instead of four P=O, and it has been synthesized via oxidation *in situ* of the tetraphosphonite cavitand with S_8.

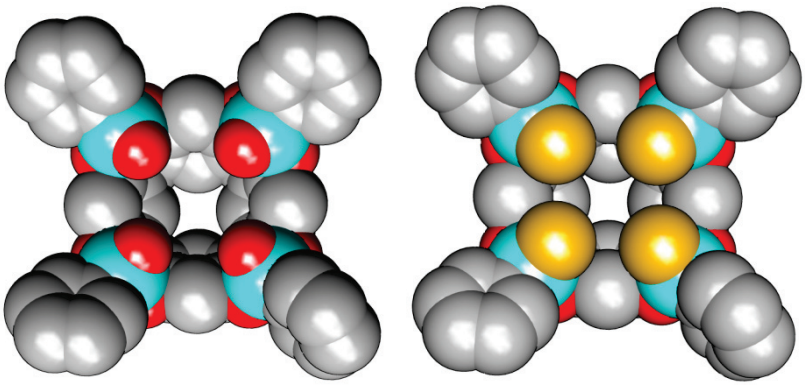

Figure I.1. Comparison between tetraphosphonate and tetrathiophosphonate cavitands (top view).

This substitution strongly reduces the molecular recognition properties, because sulphur has lower electronic density with respect to the oxygen and consequently less affinity for H-bonding interactions.[22] In addition the cavity of TS_{iiii} is much smaller and less prone to guest inclusion because sulphur is larger (atomic radius=1 Å) than oxygen (atomic radius=0.6 Å). (Figure 1.1)

1.4 Tetraphosphonate cavitands Multivalency.

Despite the excellent control over macromolecular architecture, all the supramolecular systems developed till now are far less advanced than natural macromolecular systems that can often spontaneously assemble and disassemble driven by the surrounding environmental needs. These natural responsive systems are based on a combination of macromolecules and non-covalent interactions including solvophobic and ionic interactions as well as hydrogen bonding and metal coordination.

The main advantage of supramolecular interactions is the reversible character of the supramolecular interactions adopted. In other words, the self-assembled systems can be switched between the assembled and the disassembled states by changing environmental parameters, such as temperature, pH, redox state or concentration.[23]

The possible secondary interaction involved in the self-association and the molecular recognition are reported in Table 1.1.

Interaction	Energy range [kJ/mol]	Type of interaction
Covalent bond	150-1100	Chemical reaction
Ion-Ion	100-400	Only between ions
Coordination, Complexation	8-200	Weak chemical interaction
Hydrogen-bond	5-180	Hydrogen bond A-H···B
Ion-dipole	40-600	Between ions and dipoles
Dipole-Dipole	5-25	Between polar molecules
London Forces \ Induced Dipole	0,05-40	Physical interaction

Table 1.1. Different types of interactions.

In particular, tetraphosphonate cavitand presents remarkable recognition properties toward N-methylammonium (K_{ass}~10^9, Figure 1.2a) and

N-methylpyridinium (K_{ass}~10^7, Figure 1.2b) salts, as we will see in Chapters 2 and 3, which can be attributed to three synergistic interaction modes:

(i) N^+•••O=P cation-dipole interactions;

(ii) CH_3-π interactions of the acidic ^+N-CH_3 group with the π basic cavity;

(iii) two simultaneous hydrogen bonds between two adjacent P=O bridges and the two nitrogen protons,[8] in the case of protonated secondary amines.

The simultaneous hydrogen bonds are the reason for the higher affinity of the N-methylammonium toward the cavity.

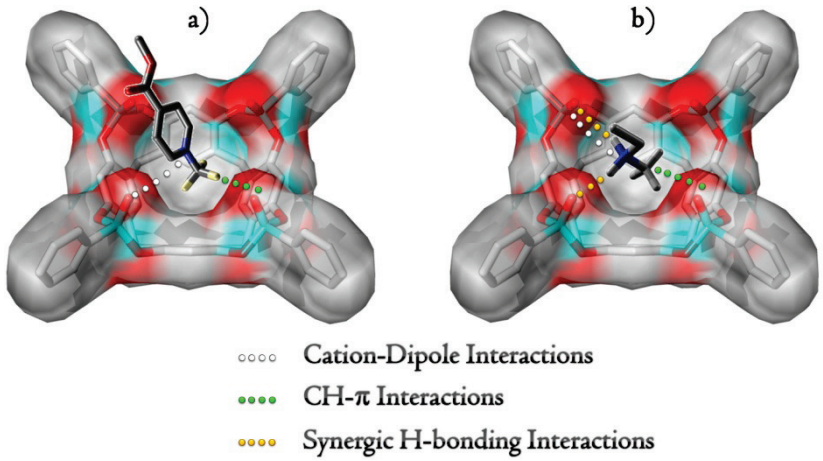

Figure 1.2. Interactions involved in the molecular recognition process.

Ion-Dipole Interactions.

An ion-dipole force is an attractive force that results from the electrostatic attraction between an ion and a neutral molecule that has a dipole (Figure 1.3):

- A positive ion (cation) attracts the partially negative end of a neutral polar molecule.
- A negative ion (anion) attracts the partially positive end of a neutral polar molecule.

Ion-dipole attractions become stronger as either the charge on the ion increases, or as the magnitude of the dipole of the polar molecule increases.

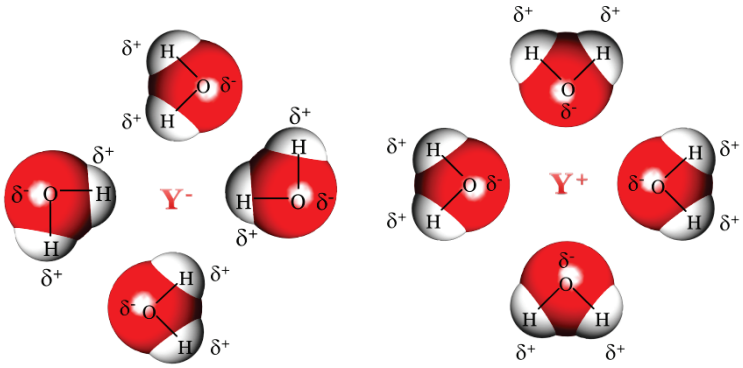

Figure I.3. Ion-Dipole Interactions.

CH-π interactions.

In the past few decades, evidence has gradually accumulated that forces weaker than the ordinary hydrogen-bonds, such as CH-O, CH-N, OH-π and NH-π interactions, are also important. Among these, the CH-π interaction (Figure I.4) has been found to play a central role in the fine tuning of organic-biochemical reactions and molecular recognition, influencing also biochemical processes.

In general, attractive interactions are present between C-H groups (soft acid) and π-electron systems (soft base).[24] The presence of CH-π interactions has been observed during the study of conformational problems of a series of compounds bearing an aliphatic group on one side of the molecule and a phenyl group at the other terminus.[25]

The CH-π interaction is characterized by a relatively large contribution from delocalization (charge transfer from π to σ*) and dispersive interaction as compared to the normal H-bonding, while the electrostatic contribution has been shown to be unimportant. A relevant observation is that the CH-π interaction plays a role either in polar or in non-polar media, unlike in the typical hydrogen bond between a hard acid and a hard base, where the presence (or absence) of water changes completely the final effect.

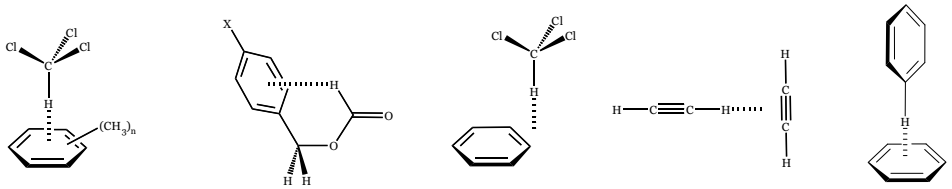

Figure I.4. Examples of CH-π interactions.

The extent of CH-π interactions becomes greater if the π-electron density of the aromatic ring involved increases, and at the same time the hydrogens of the guest molecule become more acidic (for example trimethyl ammonium chloride binds stronger than t-butyl alcohol).

Hydrogen-Bonding Interactions.

A hydrogen bond is the attractive interaction of a hydrogen atom with an electronegative atom, like nitrogen, oxygen or fluorine (thus the name *"hydrogen bond"*). The hydrogen must be covalently bonded to another electronegative atom to create the bond. These bonds can occur between molecules (intermolecularly), or within different parts of a single molecule (intramolecularly). The hydrogen bond is stronger than a van der Waals interaction, but weaker than covalent or ionic bonds. This type of bond occurs in both inorganic molecules such as water and organic molecules such as DNA.

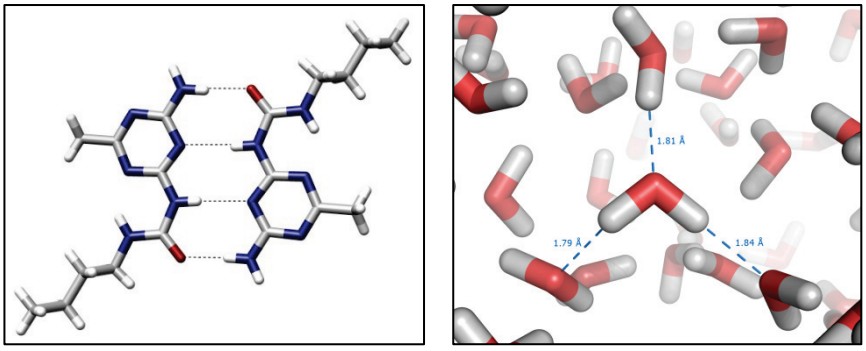

Figure I.5. Two molecules self-assembled into a dimer complex through four hydrogen bonds (left)[26] and hydrogen bonds in liquid water molecular dynamics simulation (right).

The formation of one or multiple hydrogen bonds (Figure I.5), especially in combination with other noncovalent forces, such as ionic or hydrophobic interactions, can lead to a wide change in the micro- and macroscopic properties of the resulting supramolecular assemblies.[1, 27]

In contrast to covalent bonds, which once formed are stable under normal conditions and can only be broken by providing sufficient energy, the formation of hydrogen bonds is reversible and their strength depends on the chemical environment, such as the solvent or temperature. Through a variation of the external parameters, this reversibility allows for the direct control of the physical properties of supramolecular assemblies[28] which are determined by the hydrogen bonds.

Hydrogen bonds present limited strength in polar solvent: the more polar is the solvent, the weaker are the hydrogen bonds. Polar solvents compete with the soluted in H-bonding making the interactions less effective. Therefore, it is possible to modulate the system stability by changing the solvent polarity. In particular, stable supramolecular assemblies can also be obtained in slightly polar solvents, such as chloroform or acetonitrile, by a combination of several such weak interactions in binding motifs with multiple hydrogen bonds.[29,30]

Hydrogen bonding is generally considered with a geometry, D (donor)-H···A (acceptor). Some of the commonly used functions involve the modified Lennard-Jones potentials with D-H···A angle dependent term like:[31]

$$\boldsymbol{E}_{\boldsymbol{H-Bond}}(\mathrm{R}) = \varepsilon\left[\boldsymbol{A}\left(\frac{\boldsymbol{R_0}}{\boldsymbol{R}}\right)^{\mathbf{12}} - \boldsymbol{B}\left(\frac{\boldsymbol{R_0}}{\boldsymbol{R}}\right)^{\mathbf{10}}\right](\boldsymbol{cos\theta}_{\boldsymbol{D-H\cdots A}})^{\mathbf{4}}$$

where R is the distance between the D and A, R_0 is the equilibrium distance, ε is the depth of the potential and A and B are the adjustable parameters. The angular term ensures that the strength of the H-bonding interaction maximizes for linear D-H···A bonds.[32]

It can be possible to classify hydrogen bond in "weak", "moderate" and "strong". *Moderate* [33] hydrogen bonds resemble those between water molecules or in carbohydrates and are associated with energies in the range 4-15 kcal/mol. Hydrogen bonds with energies above and below this range are

termed *strong* and *weak*, respectively. Some examples of these categories are reported in Table 1.2.

It must be stressed that there are no well defined borderlines between these categories.

	Strong	Moderate	Weak
Interaction type	strongly covalent	mostly electrostatic	electrostatic/dispersive
Length of H···A [Å]	1.2-1.5	1.5-2.2	>2.2
Length of X-H [Å]	0.08-0.25	0.02-0.08	<0.02
X-H versus H···A	X-H≈H···A	X-H<H···A	X-H<<H···A
X···A [Å]	2.2-2.5	2.5-3.2	>3.2
Directionality	Strong	Moderate	Weak
Bond angles [°]	170-180	>130	>90
Bond energy [kcal/mol]	15-40	4-15	<4

Table 1.2. Hydrogen bonding categories following the classification of Jeffrey.[33]

1.5 Grafting on surface.

Photochemical Hydrosylilation.

Over the past years several methods have been developed to prepare organic monolayers on various morphologies of hydrogen-terminated silicon.[34] Si-C bond attached monolayers have been prepared by making use of thermal conditions,[35] UV irradiation,[36] electrochemistry,[37] hydrosilylation catalysts,[38] and chemomechanical scribing.[39]

In particular, well-defined and highly stable organic monolayers on silicon surfaces can easily be prepared by irradiating a hydrogen-terminated silicon wafer, previously etched with an aqueous solution of HF in order to remove the SiO_2 film thermally grown on the surface, with light at room temperature in the presence of a 1-alkene or 1-alkyne.

The reaction is rather flexible with regard to the wavelength of irradiation and light source, and thus can avoid any light absorption by the agent that needs to be attached. These extremely mild conditions are compatible with a very large variety of active moieties that can be covalently linked to the reactive alkene or alkyne functionality. This method thus allows

the development of patterned, (bio)active monolayers,[40] via the combination of (bio)organic chemistry, surface science and (nano) techniques.

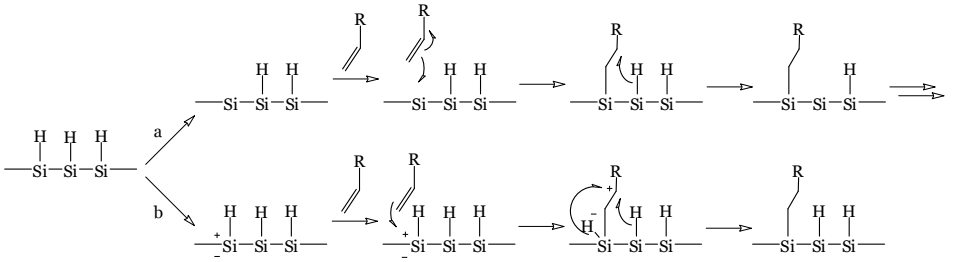

Scheme I.3. Representation of the Proposed (a) Radical Chain Mechanism[35b] under Thermal and UV Conditions and (b) Electron/Hole Pair Mechanism[41] for Visible-Light-Initiated Hydrosilylation on Porous Silicon

In the case of thermal and UV hydrosilylation is operative a radical chain mechanism[35b] (Scheme I.3, top), while in the case of visible light the mechanism involves the attack of an 1-alkene or 1-alkyne on a surface-localized positive charge (the hole) in a nucleophilic fashion, resulting in Si-C bond formation (Scheme I.3, bottom).[41]

In our case we functionalized a Si(100) surface with tetraphosphonate cavitands ended with double bond at the lower rim via UV irradiation (Chapter 3).

Carbon nanotubes and the π-π stacking interactions.

Carbon nanotubes (CNTs) are essentially a sheet of carbon atoms arranged in hexagons that curl into a tube. They come in two basic varieties: single wall carbon nanotubes (SWNTs), which are single coils of carbon hexagons, and multiwall carbon nanotubes (MWNTs), wherein single tubes are encased in wider tubes, which themselves are inside other tubes. Most of today's research concentrates on SWNTs, because they have been better characterized and possess characteristic fingerprints in several analytical and spectroscopic techniques.

Considerable efforts have been devoted to integrate the outstanding physicochemical properties of CNTs, either SWNTs or MWNTs, into

practical and useful devices. To name only a few of the remarkable features of these nanostructures, CNTs exhibit quasi-ballistic conductance, high tensile strength, and field-effect transistor properties.[42] They also have a high potential for photovoltaic applications, which, however, has received more limited attention.[43] This is due to the difficulties of processing these highly intractable carbon nanostructures and of obtaining batches with a homogeneous, narrow distribution of tubes diameters.

Several ways have been explored to integrate molecules with CNTs. In general, they fall into two categories: (i) covalently linked CNT nanoconjugates[44] and (ii) noncovalently associated CNT nanohybrids.[45] The latter method appears particularly promising since the covalent approach causes a partial loss of the electronic properties of the functionalized CNT.

In the present thesis we report about the grafting on SWCNTs of cavitands (Chapter 4) and a Single Molecule Magnet (Chapter 6), functionalized with pyrene moiety, via π-π interactions between the pyrene and the CNT.

The *π-π interactions* are non-covalent interactions caused by intermolecular overlapping of p-orbital in π conjugated systems, so they become stronger as the number of π-electrons increases.[46]

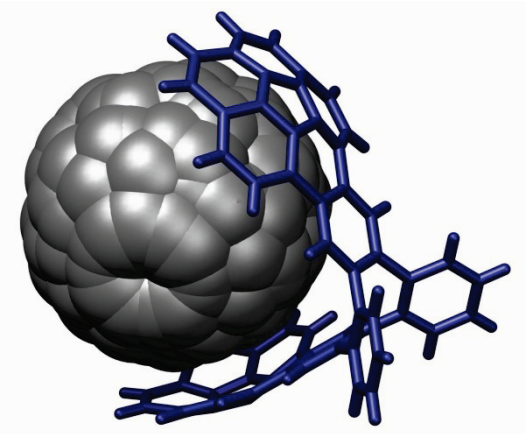

Figure I.6. Crystal structure of a fullerene bound in a buckycatcher through π-π stacking interactions.[47a]

Examples of π-π stacking interactions in allotropes of carbon are already reported in literature (Figure I.6).[47]

The aromatic groups implicated in these interactions, adopt one of the several geometries reported in Figure I.7, depending on the nature of the rings involved. Nevertheless, aromatic interactions are intriguing molecular recognition elements since they are expected to be strong in water (because the hydrophobic component of the interaction), and at the same time, should be selective if the electrostatic component is significant, thus providing the best features of both hydrophobic interactions and hydrogen bonding.

The electrostatic component has been proposed to arise from interactions of the quadrupole moments of the aromatic rings. Although benzene has no net dipole, it has an uneven distribution of charge, with greater electron-density on the face of the ring and reduced electron-density on the edge, which gives rise to the quadrupole moment.

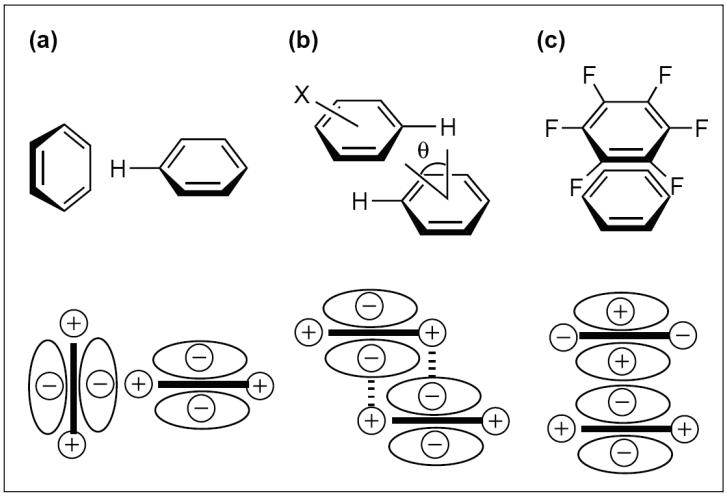

Figure I.7. Geometries of π-aromatic interactions.

The edge-to-face geometry (Figure I.7a), which can be considered a CH-π interaction, is found in benzene in the solid state, and is commonly observed between aromatic residues in proteins.[48] The offset stacked orientation (Figure I.7b) is also commonly found in porphyrin,[7] in proteins and is the geometry of base stacking in DNA. In this geometry, more surface

area is buried, and the van der Waals and hydrophobic interactions are increased. This orientation appears to be more common when the electron density on the face of one or both rings is reduced. A third possible geometry is the face-to-face stacked orientation (Figure 1.7c). This is commonly observed with donor-acceptor pairs and compounds that have opposite quadrupole moments, such that the interaction between the faces of the rings is attractive. The benzene-perfluorobenzene interaction is an excellent example of this type of aromatic interaction, and has been calculated to provide 15.5 kJ/mol in stability.[49]

I.6 References.

[1] G. M. Whiteside; J. P. Mathias; C. T. Seto, Molecular self-assembly and nanochemistry: a chemical strategy for the synthesis of nanostructures, *Science* **1991**, *254*, 1312-1319.

[2] a) J-M. Lehn, Perspectives in supramolecular chemistry: from molecular recognition to molecular information processing and self organization, *Angew Chem., Int. Ed. Engl.* **1990**, *29*, 1304-1319.
b) J-M. Lehn, *Supramolecular Chemistry: Concepts and Perspectives*, Wiley-VCH, Weinheim **1995**.

[3] L. Stryer, *Biochemestry 4th Ed.,* Freeman: New York **1995**.

[4] M. Mammen, S.-K. Choi, G. M. Whitesides, Polyvalent Interactions in Biological Systems: Implications for Design and Use of Multivalent Ligands and Inhibitors, *Angew. Chem., Int. Ed.* **1998**, *37*, 2754-2794.

[5] P. I. Kitov, J. M. Sadowska, G. Mulvey, G. D. Armstrong, H. Ling, N. S. Pannu, R. J. Read, D. R. Bundle, Shiga-like toxins are neutralized by tailored multivalent carbohydrate ligands, *Nature* **2000**, *403*, 669-672.

[6] J. Rao, J. Lahiri, L. Isaacs, R. M. Weis, G. M. Whitesides, A trivalent system from vancomycincntdot. D-Ala-D-Ala with higher affinity than avidin·biotin, *Science* **1998**, *280*, 708-711.

[7] A. Oleksi, A. G. Blanco, R. Boer, I. Usón, J. Aymamí, A. Rodger, M. J. Hannon, M. Coll, Molecular Recognition of a Three-Way DNA Junction by a Metallosupramolecular Helicate, *Angew. Chem., Int. Ed.* **2006**, *45*, 1227-1231.

[8] J. J. Lundquist and T. E. Toone, The Cluster Glycoside Effect, *Chem. Rev.* **2002**, *102*, 555-578.

[9] D. J. Cram, J. M. Cram, *In Container Molecules and Their Guests* (ED.: J. F. Stoddart), The Royal Society of Chemistry, Cambridge, **1994**, Chapter 5.

[10] D. J. Cram, S. Karbach, H.-E. Kim, C. B. Knobler, E. F. Maverick, J. L. Ericson, R. C. Helgeson, Host-guest complexation. 46. Cavitands as open molecular vessels form solvates, *J. Am. Chem. Soc.* **1988**, *110*, 2229-2237.

[11] a) J. A. Tucker, C. B. Knobler, K. N. Trueblood, D. J. Cram, Host-guest complexation. 49. Cavitands containing two binding cavities, *J. Am. Chem. Soc.* **1989**, *111*, 3688-3699.
b) P. Soncini, S. Bonsignore, E. Dalcanale, F. Ugozzoli, Cavitands as versatile molecular receptors, *J. Org. Chem.* **1992**, *57*, 4608-4612.
c) T. Haino, D. M. Rudkevich, A. Shivanyuk, K. Rissanen, J. Rebek, Jr., Induced-fit molecular recognition with water-soluble cavitands, *Chem. Eur. J.* **2000**, *6*, 3797-3805.
d) K. Paek, J. Cho, Versatile cavitands for small molecules: the entropically driven ethanol selectivity, *Tetrahedron Lett.* **2001**, *42*, 1927-1929.

[12] a) M. Vincenti, E. Dalcanale, P. Soncini, G. Guglielmetti, Host-guest complexation in the gas phase by desorption chemical ionization mass spectrometry, *J. Am. Chem. Soc.* **1990**, *112*, 445-447.
b) M. Vincenti, E. Pelizzetti, E. Dalcanale, P. Soncini, Molecular recognition in the gas phase, *Pure Appl. Chem.* **1993**, *65*, 1507-1512.

[13] L. M. Tunstad, J. A. Tucker, E. Dalcanale, J. Weiser, J. A. Bryant, J. C. Sherman, R. C. Helgeson, C. B. Knobler, D. J. Cram, Host-Guest Complexation. 48. Octol Building Blocks for Cavitands and Carcerands, *J. Org. Chem.* **1989**, *54*,1305-1312.

[14] a) E. Biavardi, G. Battistini, M. Montalti, R. M. Yebeutchou, L. Prodi, E. Dalcanale, Fully reversible guest exchange in tetraphosphonate cavitand complexes probed by fluorescence spectroscopy, *Chem. Commun.* **2008**, 1638-1640.
b) R. M. Yebeutchou, F. Tancini, N. Demitri, S. Geremia, R. Mendichi, E. Dalcanale, Host-guest driven self-assembly of linear and star supramolecular polymers, *Angew. Chem., Int. Ed.* **2008**, *47*, 4504-4508.

[15] a) R. Pinalli, F. F. Nachtigall, F. Ugozzoli, E. Dalcanale, Supramolecular sensors for the detection of alcohols, *Angew. Chem., Int. Ed.* **1999**, *38*, 2377-2380.
b) R. Pinalli, M. Suman, E. Dalcanale, Cavitands at work: from molecular recognition to supramolecular sensors, *Eur. J. Org. Chem.* **2004**, 451-462.
c) L. Pirondini, E. Dalcanale, Molecular recognition at the gas-solid interface: a powerful tool for chemical sensing, *Chem. Soc. Rev.* **2007**, *36*, 695-706.
d) M. Melegari, M. Suman, L. Pirondini, D. Moiani, C. Massera, F. Ugozzoli, E. Kalenius, P. Vainiotalo, J.-C. Mulatier, J.-P. Dutasta, E. Dalcanale, Supramolecular sensing with phosphonate cavitands, *Chem. Eur. J.* **2008**, *14*, 5772-5779.

[16] a) T. Lippmann, E. Dalcanale, G. Mann, Synthesis and configurational analysis of phosphorus bridged cavitands, *Tetrahedron Lett.* **1994**, *35*, 1685-1688.
b) T. Lippmann, H. Wilde, E. Dalcanale, L. Mavilla, G. Mann, U. Heyer, S. Spera, Synthesis and configurational analysis of a novel class of cavitands containing four dioxaphosphocin moieties, *J. Org. Chem.* **1995**, *60*, 235-242.

[17] K. D. Stewart, Ph.D. Dissertation, University of California, Los Angeles, **1984**.

[18] For a review on in-out isomerism see: R. W. Alder, S. P. East, In/Out Isomerism, *Chem. Rev.* **1996**, *96*, 2097-2111.

[19] a) W. Xu, J. P. Rourke, J. J. Vittal, R. J. Puddephatt, Anion inclusion by a calix[4]arene complex: a contrast between tetranuclear gold(I) and copper(I) complexes, *J. Chem.Soc., Chem. Commun.* **1993**, 145-147.
b) W. Xu, J. J. Vittal, R. J. Puddephatt, Selective anion inclusion in calix(4)arene complexes driven by face-bridging μ4-halide binding, *J. Am. Chem. Soc.* **1993**, *115*, 6456-6457.
c) W. Xu, J. P. Rourke, J. J. Vittal, R. J. Puddephatt, Transition metal rimmed-calixresorcinarene complexes, *Inorg. Chem.* **1995**, *34*, 323-329.
d) W. Xu, J. J. Vittal, R. J. Puddephatt, Inorganic Inclusion Chemistry: A Novel Anion Inclusion System, *J. Am. Chem. Soc.* **1995**, *117*, 8362-8371.
e) W. Xu, J. J. Vittal, R. J. Puddephatt, Anionic Calixarene Complexes of Copper(I) and Silver(I) as Cation Receptors, *Inorg. Chem.* **1997**, *36*, 86-94.

[20] a) P. Delangle, J.-P. Dutasta, Tetraphosphonate-calix[4]resorcinarene. A powerful host for alkali metal and ammonium cations encapsulation, *Tetrahedron Lett.* **1995**, *36*, 9325-9328.
b) P. Delangle, J.-C. Mulatier, B. Tinant, J.-P. Declercq, J.-P. Dutasta, Synthesis and binding properties of iiii (4i) stereoisomers of phosphonato cavitands - cooperative effects in cation complexation in organic solvents, *Eur. J. Org. Chem.* **2001**, 3695-3704.
c) B. Bibal, B. Tinant, J.-P. Declercq, J.-P. Dutasta, Preparation and Structure of [iiii] Tetraphosphonatocavitands Bearing Long Chain Functionality at the Lower Rim: Metal Picrates Extraction Studies, *Supramol. Chem.* **2003**, *15*, 25-32.

[21] R. M. Yebeutchou, Ph.D. Thesis, University of Parma, **2008**.

[22] D. Reyntjens-Van Damme, T. Zeegers-Huyskens, Infrared spectrometric study of hydrogen bonding of phenols with triethylthiophosphate, *J. Phys. Chem.* **1980**, *84*, 282-285.

[23] S. Rieth, C. Baddeley and J. D. Badjic, Prospects in controlling morphology, dynamics and responsiveness of supramolecular polymers, *Soft Matter* **2007**, *3*, 137-154.

[24] a) R. G. Pearson. Acids and bases, *Science* **1966**, *151*, 1721-1727.
b) R. G. Pearson, J. Songstad, Application of the principle of hard and soft acids and bases to organic chemistry, *J. Am. Chem. Soc.* **1967**,*89*, 1827-1836.

[25] a) M. Nishio, M. Hirota, Y. Umezawa, The CH-π Interactions, Wiley-VCH, New York, 1998.
b) M. Nishio, Y. Umezawa, M. Hirota, Y. Takeuchi, The CH/π interaction: Significance in molecular recognition, *Tetrahedron* 1995, *51*, 8665-8701.

[26] F. H. Beijer, H. Kooijman, A. L. Spek, R. P. Sijbesma, E. W. Meijer, Self-complementarity achieved through quadruple hydrogen bonding, *Angew. Chem., Int. Ed.* 1998, *37*, 75-78.

[27] a) N. B. Bowden, M. Weck, I. S. Choi, G. M. Whitesides, Molecule-mimetic chemistry and mesoscale self-assembly, *Acc. Chem. Res.* 2001, *34*, 231-238.
b) L. J. Prins, D. N. Reinhoudt, P. Timmerman, Noncovalent synthesis using hydrogen bonding. *Angew. Chem., Int. Ed.* 2001, *40*, 2382-2426.

[28] a) F. Vögtle, *Supramolecular Chemistry,* Wiley, Chichester, 1991.
b) J.-M. Lehn, *Supramolecular Chemistry; Concept and Perspectives,* VCH, Weinheim, 1995.
c) J. W. Steed, J. L. Atwood, *Supramolecular Chemistry,* Wiley, Chichester, 2000.

[29] a) W. L. Jorgensen, J. Pranata, Importance of Secondary Interactions in Triply Hydrogen Bonded Complexes: Guanine-Cytosine vs Uracil-2,6-Diaminopyridine, *J. Am. Chem. Soc.* 1990, *112*, 2008-2010.
b) J. Pranata, S. G. Wierschke, W. L. Jorgenseng, OPLS potential functions for nucleotide bases. Relative association constants of hydrogen-bonded base pairs in chloroform, *J. Am. Chem. Soc.* 1991, *113*, 2810-2819.

[30] J. Sartorius, H.-J. Schneider, A general scheme based on empirical increments for the prediction of hydrogen-bond associations of nucleobases and of synthetic host-guest complexes, *Chem. Eur. J.* 1996, *2*, 1446-1452.

[31] F. Jensen, *Introduction to Computational Chemistry*, Wiley, Chichester, 1999.

[32] T. Steiner, Reviews: The hydrogen bond in the solid state, *Angew. Chem., Int. Ed. Engl.* 2002, *41*, 48-76.

[33] G. A. Jeffrey, *An Introduction to Hydrogen Bonding*, Oxford University Press, Oxford, 1997.

[34] a) D. D. M. Wayner, R. A. Wolkow, Organic modification of hydrogen terminated silicon surfaces, *J. Chem. Soc., Perkin. Trans. 2* 2002, 23-34.
b) J. M. Buriak, Organometallic Chemistry on Silicon and Germanium Surfaces, *Chem. Rev.* 2002, *102*, 1271-1308.

c) A. B. Sieval, R. Linke, H. Zuilhof, E. J. R. Sudhölter, High-quality alkyl monolayers on silicon surfaces, *Adv. Mater.* **2000**, *12*, 1457-1460.

[35] a) M. R. Linford, C. E. D. Chidsey, Alkyl monolayers covalently bonded to silicon surfaces, *J. Am. Chem. Soc.* **1993**, *115*, 12631-12632.
b) M. R. Linford, P. Fenter, P. M. Eisenberger, C. E. D. Chidsey, Alkyl Monolayers on Silicon Prepared from 1-Alkenes and Hydrogen-Terminated Silicon, *J. Am. Chem. Soc.* **1995**, *117*, 3145-3155.
c) A. B. Sieval, A. L. Demirel, J. W. M. Nissink, M. R. Linford, J. H. van der Maas, W. H. de Jeu, H. Zuilhof, E. J. R. Sudhölter, Highly Stable Si-C Linked Functionalized Monolayers on the Silicon (100) Surface, *Langmuir* **1998**, *14*, 1759-1768.
d) A. B. Sieval, R. Opitz, H. P. A. Maas, M. G. Schoeman, G. Meijer, F. J. Vergeldt, H. Zuilhof, E. J. R. Sudhölter, Monolayers of 1-Alkynes on the H-Terminated Si(100) Surface, *Langmuir* **2000**, *16*, 10359-10368.
e) A. B. Sieval, B. van den Hout, H. Zuilhof, E. J. R. Sudhölter, Molecular Modeling of Covalently Attached Alkyl Monolayers on the Hydrogen-Terminated Si(111) Surface, *Langmuir* **2001**, *17*, 2172-2181.

[36] a) R. L. Cicero, M. R. Linford, C. E. D. Chidsey, Photoreactivity of Unsaturated Compounds with Hydrogen-Terminated Silicon(111), *Langmuir* **2000**, *16*, 5688-5695.
b) F. Effenberger, G. Gotz, B. Bidlingmaier, M. Wezstein, Photoactivated preparation and patterning of self-assembled monolayers with 1-alkenes and aldehydes on silicon hydride surfaces, *Angew. Chem., Int. Ed.* **1998**, *37*, 2462-2464.
c) T. Strother, R. J. Hamers, L. M. Smith, Covalent attachment of oligodeoxyribonucleotides to amine-modified Si (001) surfaces, *Nucleic Acid Res.* **2000**, *28*, 3535-3541.
d) T. Strother, W. Cai, X. Zhao, R. J. Hamers, L. M. Smith, Synthesis and Characterization of DNA-Modified Silicon (111) Surfaces, *J. Am. Chem. Soc.* **2000**, *122*, 1205-1209.

[37] a) C. H. de Villeneuve, J. Pinson, M. C. Bernard, P. Allongue, Electrochemical Formation of Close-Packed Phenyl Layers on Si(111), *J. Phys. Chem. B* **1997**, *101*, 2415-2420.
b) C. Gurtner, A. W. Wun, M. J. Sailor, Surface modification of porous silicon by electrochemical reduction of organo halides, *Angew. Chem., Int. Ed.* **1999**, *38*, 1966-1968.
c) E. G. Robins, M. P. Stewart, J. M. Buriak, Anodic and cathodic electrografting of alkynes on porous silicon, *Chem. Commun.* **1999**, 2479-2480.

[38] a) R. Boukherroub, S. Morin, F. Bensebaa, D. D. M. Wayner, New Synthetic Routes to Alkyl Monolayers on the Si(111) Surface, *Langmuir* **1999**, *15*, 3831-3835.

b) J. M. Buriak, M. J. Allen, Lewis Acid Mediated Functionalization of Porous Silicon with Substituted Alkenes and Alkynes, *J. Am. Chem. Soc.* **1998**, *120*, 1339-1340.
c) J. M. Buriak, M. P. Stewart, T. W. Geders, M. J. Allen, H. C. Choi, J. Smith, D. Raftery, L. T. Canham, Lewis Acid Mediated Hydrosilylation on Porous Silicon Surfaces, *J. Am. Chem. Soc.* **1999**, *121*, 11491-11502.
d) J. M. Holland, M. P. Stewart, M. J. Allen, J. M. Buriak, Metal Mediated Reactions on Porous Silicon Surfaces, *J. Solid State Chem.* **1999**, *147*, 251-258.

[39] a) T. L. Niederhauser, G. Jiang, Y.-Y. Lua, M. J. Dorff, A. T. Woolley, M. C. Asplund, D. A. Berges, M. R. Linford, A New Method of Preparing Monolayers on Silicon and Patterning Silicon Surfaces by Scribing in the Presence of Reactive Species, *Langmuir* **2001**, *17*, 5889-5900.
b) T. L. Niederhauser, Y.-Y. Lua, Y. Sun, G. Jiang, G. S. Strossman, P. Pianetta, M. R. Linford, Formation of (Functionalized) Monolayers and Simultaneous Surface Patterning by Scribing Silicon in the Presence of Alkyl Halides, *Chem. Mater.* **2002**, *14*, 27-29.
c) T. L. Niederhauser, Y.-Y. Lua, G. Jiang, S. D. Davis, R. Matheson, D. A. Hess, I. A. Mowat, M. R. Linford, Arrays of chemomechanically patterned patches of homogeneous and mixed monolayers of 1-alkenes and alcohols on single silicon surfaces, *Angew. Chem., Int. Ed.* **2002**, *41*, 2353-2356.

[40] L. C. P .M de Smet, G. A. Stork, G. H. F. Hurenkamp, Q.-Y. Sun, H. Topal, P. J. E. Vronen, A. B. Sieval, A. Wright, G. M. Visser, H. Zuilhof, E. J. R. Sudhölter, Covalently Attached Saccharides on Silicon Surfaces, *J. Am. Chem. Soc.* **2003**, *125*, 13916-13917.

[41] M. P. Stewart, J. M. Buriak, Exciton-Mediated Hydrosilylation on Photoluminescent Nanocrystalline Silicon, *J. Am. Chem. Soc.* **2001**, *123*, 7821-7830.

[42] a) R. C. Haddon, Carbon Nanotubes, Special issue *Acc. Chem. Res.* **2002**, *35*, 997.
b) S. Reich, C. Thomsen, J. Maultzsch, *Carbon Nanotubes: Basic concepts and Physical Properties*, Wiley-VCH: Weinheim, Germany, **2004**.
c) M. S. Dresselhaus, G. Dresselhaus, P. Avouris, *Carbon Nanotubes: Synthesis, Structure, Properties and Applications*, Springer: Berlin, **2001**.
d) P. J. F. Harris, *Carbon Nanotubes and Related Structures: New Materials for the Twenty-First Century*, Cambridge University Press: Cambridge, U.K., **2001**.
e) M. F. Yu, B. S. Files, S. Arepalli, R. S. Ruoff, Tensile loading of ropes of single wall carbon nanotubes and their mechanical properties, *Phys. Rev. Lett.* **2000**, *84*, 5552-5555.
f) S. Ijima, C. Brabec, A. Maiti, J. Bernholc, Structural flexibility of carbon nanotubes, *J. Chem. Phys.* **1996**, *104*, 2089-2092.
g) M. M. J. Treacy, T. W. Ebbesen, T. M. Gibson, Exceptionally high Young's modulus observed for individual carbon nanotubes, *Nature* **1996**, *381*, 678-680.

h) M. R. Falvo, G. J. Clary, R. M. Taylor, V. Chi, F. P. Brooks, S. Washburn, R. Superfine, Bending and buckling of carbon nanotubes under large strain, *Nature* **1997**, *389*, 582-584.
i) S. T. Huxtable, D. G. Cahill, S. Shenogin, L. Xue, R. Ozisik, P. Barone, M. Usrey, M. S. Strano, G. Siddons, M. Shim, P. Keblinski, Interfacial heat flow in carbon nanotube suspensions, *Nat. Mater.* **2003**, *2*, 731-734.
j) H. L. Zhang, J. F. Li, K. F. Yao, L. D. Chen, Spark plasma sintering and thermal conductivity of carbon nanotube bulk materials, *J. Appl. Phys.* **2005**, *97*, 114310.
k) P. Kim, L. Shi, A. Majumdar, P. L. McEuen, Thermal transport measurements of individual multiwalled nanotubes, *Phys. Rev. Lett.* **2001**, *87*, 215502.
l) J. Hone, B. Batlogg, Z. Benes, A. T. Johnson, J. E. Fischer, Quantized phonon spectrum of single-wall carbon nanotubes, *Science* **2000**, *289*, 1730-1734.
m) J. A. Misewich, P. Avouris, R. Martel, J.C. Tsang, S. Heinz, J. Tersoff, Electrically induced optical emission from a carbon nanotube FET, *Science* **2003**, *300*, 783-786.
n) N. De Jonge, M. Allioux, M. Doytcheva, M. Kaiser, K. B. K. Teo, R. G. Lacerda, W. I. Milne, Characterization of the field emission properties of individual thin carbon nanotubes, *Appl. Phys. Lett.* **2004**, *85*, 1607-1609.
o) S. H. Jo, D. Z. Wang, J. Y. Huang, W. Z. Li, K. Kempa, Z. F. Ren, Field emission of carbon nanotubes grown on carbon cloth, *Appl. Phys. Lett.* **2004**, *85*, 810-812.
p) S. M. Yoon, J. Chae, J. S. Suh, Comparison of the field emissions between highly ordered carbon nanotubes with closed and open tips, *Appl. Phys. Lett.* **2004**, *84*, 825-827.
q) A. Buldum, J. P. Lu, Electron field emission properties of closed carbon nanotubes, *Phys. Rev. Lett.* **2003**, *91*, 236801.
r) A. Hirsch, Functionalization of single-walled carbon nanotubes, *Angew. Chem., Int. Ed.* **2002**, *41*, 1853-1859.

[43] a) H. Imahori, Y. Sakata, Donor-linked fullerenes. Photoinduced electron transfer and its potential application, *Adv. Mater.* **1997**, *9*, 537-546.
b) M. Prato, [60]Fullerene chemistry for materials science applications, *J. Mater. Chem.* **1997**, *7*, 1097-1109.
c) N. Martín, L. Sánchez, B. Illescas, I. Pérez, C60-Based Electroactive Organofullerenes, *Chem. Rev.* **1998**, *98*, 2527-2547.
d) F. Diederich, M. Gomez-Lopez, Supramolecular fullerene chemistry, *Chem. Soc. Rev.* **1999**, *28*, 263-277.
e) D. M. Guldi, M. Prato, Excited-State Properties of C60 fullerene derivatives, *Acc. Chem. Res.* **2000**, *33*, 695-703.
f) D. Gust, T. A. Moore, A. L. Moore, Mimicking photosynthetic solar energy transduction, *Acc. Chem. Res.* **2001**, *34*, 40-48.
g) D. M. Guldi, M. Prato, Electrostatic interactions by design. Versatile methodology towards multifunctional assemblies/nanostructured electrodes, *Chem. Commun.* **2004**, 2517-2525.

h) D. M. Guldi, Fullerene-porphyrin architectures; photosynthetic antenna and reaction center models, *Chem. Soc. Rev.* **2002**, *31*, 22-36.
i) D. M. Guldi, G. M. A. Rahman, V. Sgobba, N. A. Kotov, D. Bonifazi, M. Prato, CNT-CdTe versatile donor-acceptor nanohybrids *J. Am. Chem. Soc.* **2006**, *128*, 2315-2323.
j) B. Mihaela, G. R. Pedro, Nanocomposites based on conducting polymers and carbon nanotubes: from fancy materials to functional applications, *J. Nanosci. Nanotechnol.* **2006**, *6*, 289-302.
k) W. Wu, S. Zhang, Y. Li, J. Li, L. Liu, Y. Qin, Z.-X. Guo, L. Dai, C. Ye, D. Zhu, PVK-Modified Single-Walled Carbon Nanotubes with Effective Photoinduced Electron Transfer, *Macromolecules* **2003**, *36*, 6286-6288.
l) J. U. Lee, Photovoltaic effect in ideal carbon nanotube diodes, *Appl. Phys. Lett.* **2005**, *87*, 073101/1.
m) M. H.-C. Jin, L. Dai, Vertically aligned carbon nanotubes for organic photovoltaic devices, *Opt. Sci. Eng.* **2005**, *99*, 579-597.

[44] a) H. Li, R. B. Martin, B. A. Harruff, R. A. Carino, L. F. Allard, Y.-P. Sun, Single-walled carbon nanotubes tethered with porphyrins: Synthesis and photophysical properties, *Adv. Mater.* **2004**, *16*, 896-900.
b) D. Baskaran, J. W. Ways, X. P. Zhang, M. S. Bratcher, Carbon nanotubes with covalently linked porphyrin antennae: photoinduced electron transfer , *J. Am. Chem. Soc.* **2005**, *127*, 6916-6917.

[45] a) H. Murakami, T. Nomura, N. Nakashima, Noncovalent porphyrin-functionalized single-walled carbon nanotubes in solution and the formation of porphyrin-nanotube nanocomposites, *Chem. Phys. Lett.* **2003**, *378*, 481-485.
b) J. Chen, C. P. Collier, Noncovalent functionalization of single-walled carbon nanotubes with water-soluble porphyrins, *J. Phys. Chem. B.* **2005**, *109*, 7605-7609.
c) H. Li, B. Zhou, Y. Lin, L. Gu, W. Wang, K. A. S. Fernando, S. Kumar, L. F. Allard, Y.-P. Sun, Selective interactions of porphyrins with semiconducting single-walled carbon nanotubes, *J. Am. Chem. Soc.* **2004**, *126*, 1014-1015.
d) T. Hasobe, S. Fukuzumi, P. V. Kamat, Ordered assembly of protonated porphyrin driven by single-wall carbon nanotubes. J- and H-aggregates to nanorods, *J. Am. Chem. Soc.* **2005**, *127*, 11884-11885.
e) N. Nakashima, Y. Tomonari, H. Murakami, Water-soluble single-walled carbon nanotubes via noncovalent sidewall-functionalization with a pyrene-carrying ammonium ion, *Chem. Lett.* **2002**, 638-639.
f) R. J. Chen, Y. Zhang, D. Wang, H. Dai, Noncovalent sidewall functionalization of single-walled carbon nanotubes for protein immobilization, *J. Am. Chem. Soc.* **2001**, *123*, 3838-3839.

[46] C. A. Hunter, K. R. Lawson, J. Perkins, C. J. Urch, Aromatic interactions, *J. Chem. Soc., Perkin Trans. 2* **2001**, 651-669.

[47] a) A. Sygula, F. R. Fronczek, R. Sygula, P. W. Rabideau, M. M. Olmstead, A Double Concave Hydrocarbon Buckycatcher, *J. Am. Chem. Soc.* **2007**, *129*, 3842-3843.
b) Y.-L. Zhao, L. Hu, J. F. Stoddart, G. Grüner, Pyrenecyclodestrin-decorated Single-Walled Carbon Nanotube Field-Effect Transistor as Chemical Sensors, *Adv. Mater.* **2008**, *20*, 1910-1915.

[48] E. A. Meyer, R. K. Castellano, F. Diedrich, Interactions with aromatic rings in chemical and biological recognition, *Angew. Chem., Int. Ed. Engl.* **2003**, *42*, 1210-1250.

[49] J. West, S. Mecozzi, D. A. Dougherty, Theoretical studies of the supramolecular synthon benzene···hexafluorobenzene, *J. Phys. Org. Chem.* **1997**, *10*, 347-350.

Reversible guest exchange in tetraphosphonate cavitands.†

2

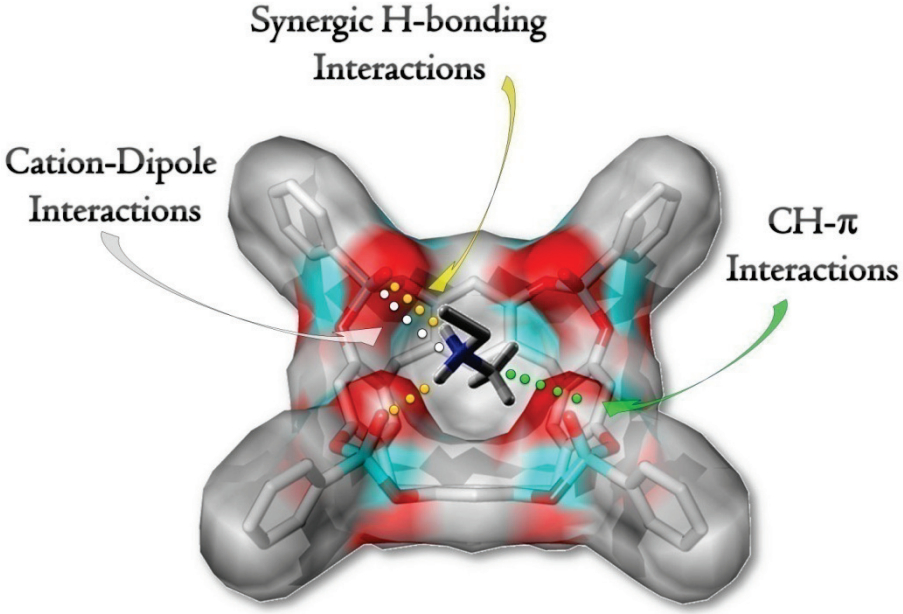

"Molecular Complementarity"

† Part of this work has been published: E. Biavardi, G. Battistini, M. Montalti, R. M. Yebeutchou, L. Prodi, E. Dalcanale, Fully reversible guest exchange in tetraphosphonate cavitand complexes probed by fluorescence spectroscopy, *Chem. Commun.* **2008**, 1638-1640.

2.1 Introduction: photoluminescence to probe self-assembly.

In this chapter we report the monitoring of reversible guest inclusion in phosphonate cavitands through a large increase in luminescence intensity caused by the modulation of the exoergonicity of an electron-transfer reaction. Photoluminescence is one of the most versatile and sensitive techniques for the detection of chemical species in solution, and for this reason standard UV-VIS-NIR spectrofluorimeters, easy to use and low-cost instruments, are largely employed in research and analytical laboratories. In particular, luminescence spectroscopy has been finding applications in fields of great impact from a social and economic point of view, such as medical diagnostics and imaging, environmental sciences, and molecular electronics. In this context, luminescence spectroscopy has proved to be a very powerful technique when it is necessary to monitor molecular recognition events in cells or on surfaces, because of its submicron visualisation and submillisecond temporal resolution. Furthermore, one can take advantage of the variety of possible ways of modulating the photophysical properties of a chromophore. Typical examples are the introduction of proton-, energy- and electron-transfer processes, the presence of heavy-atom effects, changes of electronic density, and the destabilisation of a nonemissive $n\pi^*$ excited state. Knowledge of the rules governing these processes is of great importance in obtaining an efficient signal transduction mechanism.[1,2]

Self-assembly is the most promising approach to build organic nanostructures on surfaces, leading to hybrid organic-inorganic materials.[3] Among the different kinds of surfaces, most of the activity in the past has been concentrated on gold, due to the easy access to SAMs (self-assembled monolayers), but the attention is now shifting towards silicon, because most electronic devices are Si-based. One of the obstacles hindering the development of Si-based hybrid materials is related to their characterization, and it was only very recently that we proposed the use in this context of luminescence spectroscopy, which helped to demonstrate the formation and distribution of coordination cages on Si(100), using a pyrene moiety as a fluorescent label.[4] The same approach could be used to monitor molecular

recognition phenomena on silicon surfaces, another important feature to be implemented in Si-based hybrid materials.

As a first step forward this direction, we report a suitable protocol for the reversible complexation of methylammonium and methylpyridinium salts by $T_{iiii}[C_{11}H_{23}, H, Ph]$[5] cavitand and its monitoring via fluorescence spectroscopy.

As already reported in the previous chapter, tetraphosphonate cavitands present remarkable molecular recognition properties toward charged N-methyl derivatives in the solid state,[6] in solution[7] and in the gas phase.[8]

2.2 Results and Discussion.

2.2.1 Receptors design and synthesis.

Our receptors are resorcin[4]arene functionalized at the upper rim with four phosphonate bridges and at the lower rim with different alkyl chain. As already explained in the previous chapter, the recognition properties toward N-methylammonium (K_{ass}~10^9) and N-methylpyridinium (K_{ass}~10^7) salts can be attributed to three synergistic interaction modes:

(i) N^+•••O=P cation-dipole interactions;

(ii) CH_3-π interactions of the acidic ^+N-CH_3 group with the π basic cavity;

(iii) two simultaneous hydrogen bonds between two adjacent P=O bridges and the two nitrogen protons,[8] in the case of protonated secondary amines like compound **10**.

These cavitands were synthesized and purified following a known procedure (see Experimental Section and Scheme 2.1).

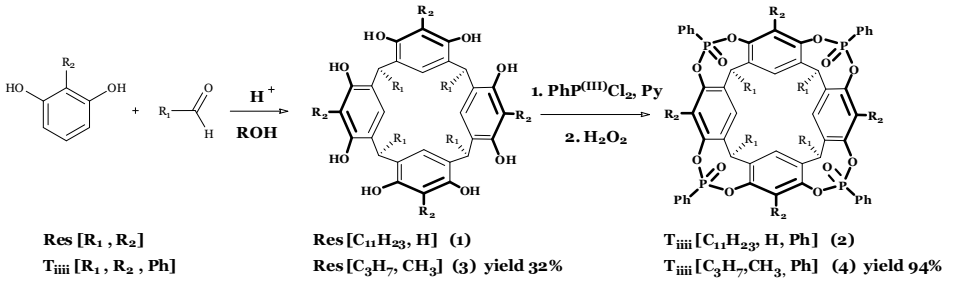

Scheme 2.1. Synthesis of $T_{iiii}[C_3H_7, CH_3, Ph]$ and $T_{iiii}[C_{11}H_{23}, H, Ph]$.

$T_{iiii}[C_3H_7, CH_3, Ph]$ cavitand (**4**), used for ITC measures, was prepared via an acid-catalyzed condensation between 2-methylresorcinol and the butyraldehyde leading to $Res[C_3H_7, CH_3]$ (**3**) in good yield. Subsequently, on the flexible macrocycles was performed the bridging reaction with P,P-dichlorophenylphosphine in anhydrous pyridine at 80°C to obtain the tetraphosphonite intermediate, then oxidized *in situ* with hydrogen peroxide.

Thanks to the stereospecificity of this reaction only the isomer featuring four inward-facing phosphonate bridges were formed.

The same reactions were accomplished to prepare $T_{iiii}[C_{11}H_{23}, H, Ph]$ cavitand (**2**), used for fluorescent titration, but using resorcinol and dodecylaldehyde to get $Res[C_{11}H_{23}, H]$ (**1**), subsequently bridged in a quantitatively yield.

2.2.2 Guests design and synthesis.

Guests for Photophysical experiments.

As a *fluorescent guest*, we synthesized compound **8**, which has a methylpyridinium unit as recognition moiety connected to a pyrene probe via a diester tether. In particular, pyrene was chosen as a fluorescent unit for several reasons:

(i) its high emission efficiency;
(ii) its ability to signal the presence of other pyrenes in the vicinity;
(iii) the possibility of observing its fluorescence close to a silicon surface;

(iv) the possibility of giving rise to electron-transfer processes with pyridinium units;

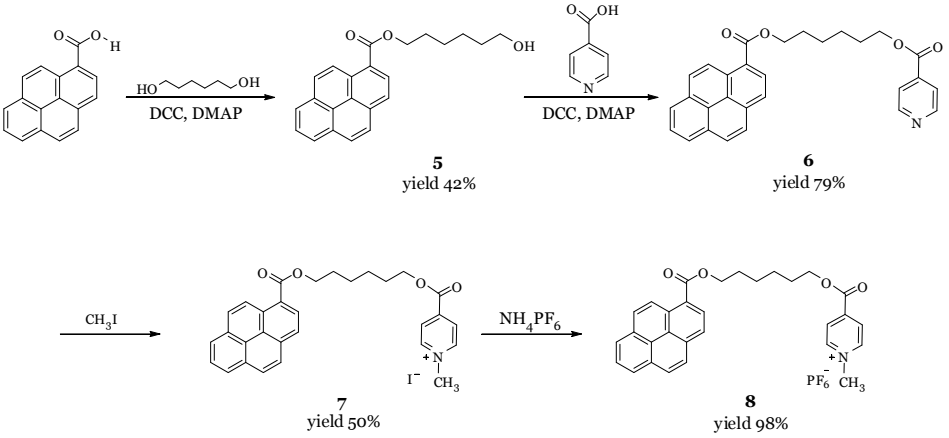

Scheme 2.2. Synthesis of fluorescent N-methylpyridinium salt **8**.

The synthesis of fluorescent guest **8**, shown in Scheme 2.2, started with two consecutive esterification reactions carried out exploiting the acid activation by N,N'-Dicyclohexylcarbodiimide (DCC) and catalyzed by 4-(dimethylamino)pyridine (DMAP). In the first esterification 1-pyrenecarboxylic acid was reacted with hexane-1,6-diol to give compound **5** which, after purification, underwent the second esterification with isonicotinic acid.

Finally, compound **6** was methylated with iodomethane in order to obtain **7**, subsequently subjected to an ion-exchange reaction with ammonium hexafluorophosphate to give the fluorescent guest **8**.

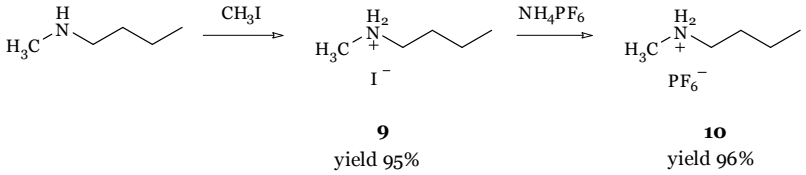

Scheme 2.3. Synthesis of the competitive guest N-methylbutylammonium salt **10**.

As a *competitive guest* (see Chapter 1, Paragraph 1.4) N-methylbutylammonium hexafluorophosphate(V) (**10**) was synthesized, prepared via methylation of the N-butylmethylamine with iodomethane followed by a counterion exchange performed with ammonium hexafluorophosphate (Scheme 2.3).

Guests for microcalorimetric and electrochemical test.

Methylpyridinium hexafluorophosphate **12** was prepared in order to determine the reduction potentials of the methylpyridinium moiety via cyclic voltammetric (CV) experiments while, the similar guest **14** was prepared in order to evaluate the association constant of methylpyridinium guest@tetraphosphonate cavitand complexes via Isothermal Titration Calorimetry (ITC).

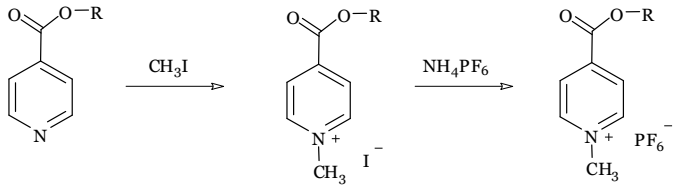

11 R= CH_3 - yield 87% **12** R= CH_3 - yield 97%
13 R= C_4H_9 - yield 80% **14** R= C_4H_9 - yield 95%

Scheme 2.4. Synthesis of the competitive guests N-methylpyridinium salts **12** and **14**.

Guests **12** and **14** were synthesised by methylation of methyl isonicotinate and butyl isonicotinate respectively with iodometane to give the corresponding isonicotinium iodide salts **11** and **13**. The final guests were obtained by ion-exchange reaction with ammonium hexafluorophosphate(V) (Scheme 2.4).

2.2.3 The electron-transfer and the modulation of the luminescence.

A K_{ass} of 7.8 x 10^6 M^{-1} has been determined for the $T_{iiii}[C_3H_7, CH_3, Ph]$@**14** complex in dichloromethane by ITC titrations

(Table 2.1 and Figure 2.6). Interestingly, the complexation is not only enthalpy but also entropy driven, indicating that solvation plays a pivotal role in the process. The corresponding K_{ass} for the $T_{iiii}[C_3H_7, CH_3, Ph]$@**10** complex could not be evaluated by ITC since its value in dichloromethane is above the ITC reliable measurement range ($10^2 < K_{ass} < 10^7$ M^{-1}).[9]

Host	Guest	n[a]	ΔH^b	$T\Delta S^b$	ΔG^b	$K_{ass\text{-}ITC}{}^c$	$K_{ass\text{-}Fluorescence}{}^c$
T_{iiii} **4**	**14**	0.95±0.01	-24.1±0.4	15.1±1	-39.2±0.2	(7.8±0.5)x10^6	-
T_{iiii} **2**	**8**	-	-	-	-39.3±0.2	-	(8.0±0.6)x10^6

[a] n: Molar ratio of both components in the complex. The theoretical value for all binding sites occupied is 1/1. [b] kJ mol^{-1}. [c] M^{-1}.

Table 2.1. Results of ITC titration of $T_{iiii}[C_3H_7, CH_3, Ph]$ (**4**) with **14** and fluorescence titration of $T_{iiii}[C_{11}H_{23}, H, Ph]$ (**2**) with **8** in dichloromethane at 298 K. The ITC value is the average of three independent measurements.

The absorption spectrum of **8** (Figure 2.1) is largely dominated by the transitions centred on the pyrene units, with a small additive contribution from the methylpyridinium moiety at around 300 nm.

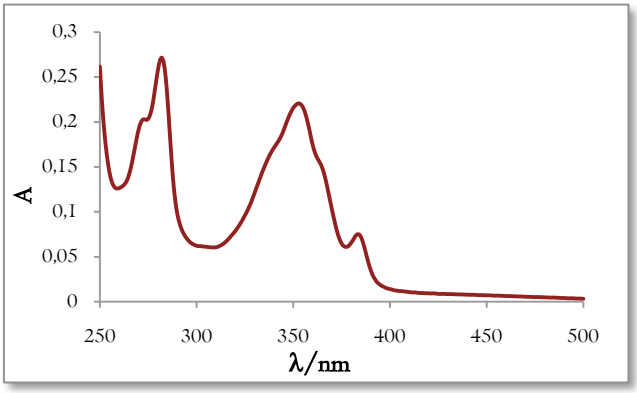

Figure 2.1. Absorption spectrum of a 4.2 x 10^{-6} M dichloromethane solution of **8**.

The fluorescence spectrum of **8** in dichloromethane solution (Figure 2.2) showed the typical monomeric band of pyrene, but with a thirty-fold lower intensity compared to that of the reference compound **5**; the excited state lifetime of **8** was correspondingly shorter (5.8 and 0.2 ns for **5** and **8**, respectively).

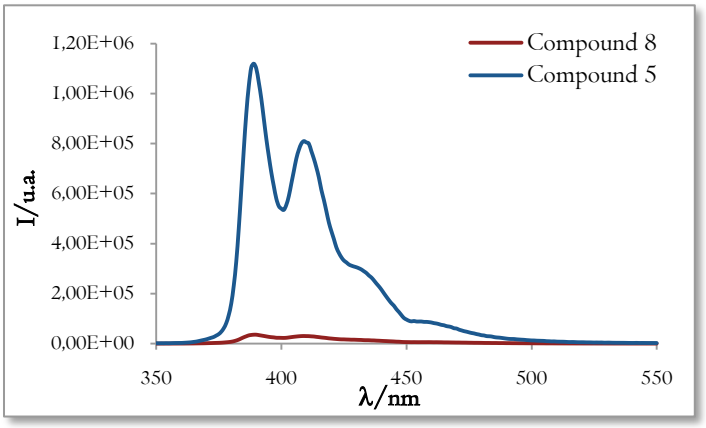

Figure 2.2. Fluorescent spectra of compound **8** and of the reference compound **5** in dichloromethane.

Apart from the lack of any other thermodynamically accessible quenching mechanism, the occurrence of an electron-transfer process was in this case also supported by electrochemical data. In fact the energy of the singlet excited state centred on the pyrene unit ($E^{\circ\circ}$ = 3.17 eV) is more than sufficient to transfer an electron from the pyrene ($E^{\circ}(\mathbf{5}^{+}/\mathbf{5})$ = +1.53V, irreversible process) to the pyridinium moiety ($E^{\circ}(\mathbf{12}/\mathbf{12}^{\bullet-})$ = - 0.68V, irreversible process). The addition of $T_{iiii}[C_{11}H_{23}, H, Ph]$ (**2**) to a dichloromethane solution of **8** did not cause appreciable changes in the absorption spectrum (Figure 2.3a) in the 320-450 nm region, while the absorbance at lower wavelengths increased as expected because of the contribution of the added species. On the contrary, the addition of $T_{iiii}[C_{11}H_{23}, H, Ph]$ (**2**) caused very evident changes in the fluorescence spectrum, since the intensity of the pyrene band underwent a six-fold increase (Figure 2.3 b and c). It is also noteworthy that the fluorescence revival is accompanied by a proportional increase of the excited state lifetime to 1.2 ns.

No changes either in absorption or in the fluorescence spectrum were instead observed upon addition to a solution of $T_{iiii}[C_{11}H_{23}, H, Ph]$ of the reference pyrene compound **5**.

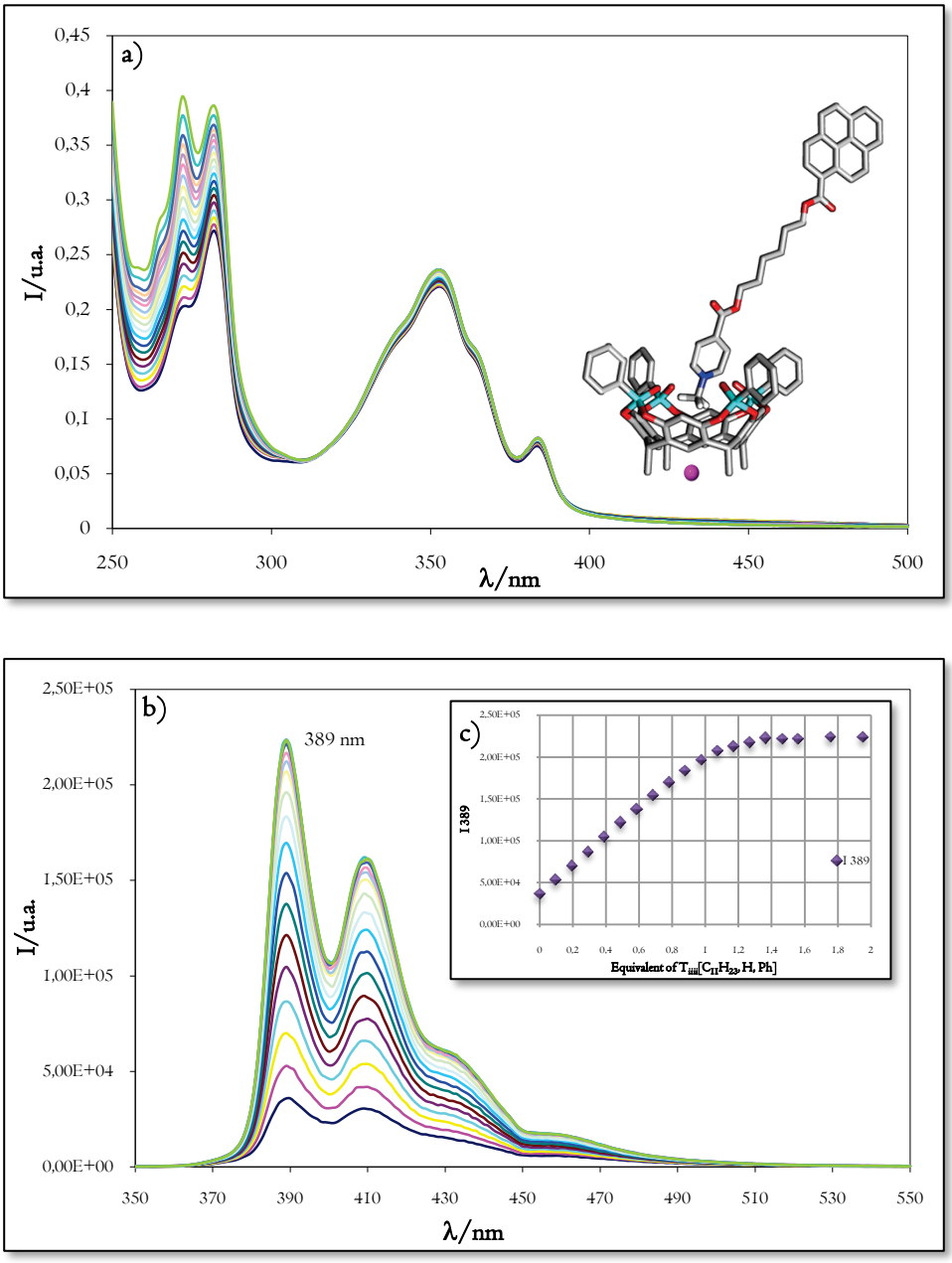

Figure 2.3. a) Absorbance spectra and b) Fluorescence spectra (λ_{exc}=345 nm) of a CH_2Cl_2 solution of **8** (1 x 10^{-5} M) upon addition of an increasing (0 - 1.2 equiv.) amount of the cavitand **2**; c) Trend of the emission at 389nm of **8** as a function of the equivalent of cavitand **2** added.

These results cannot be explained in terms of a direct interaction between $T_{iiii}[C_{11}H_{23}, H, Ph]$ and the pyrene moiety, since the lack of any change in the absorption spectrum in the transitions typical of pyrene leads to the conclusion that there is no electronic interaction between this latter unit and $T_{iiii}[C_{11}H_{23}, H, Ph]$ (**2**), also after the formation of the complex depicted in Figure 2.3a.

Rather, the observed increase of the luminescence can be ascribed to the decrease of the exoergonicity of the electron-transfer process that, in turn, leads to the decrease of the rate constant of the process. In fact, the inclusion inside the electron-rich cavity of the electron-poor methylpyridinium moiety is expected to make its reduction process more energy demanding.

Although it is very difficult to make a quantitative analysis from chemically irreversible processes, this is supported by a *ca.* 40 mV shift towards more negative values of the reduction potential of the methylpyridinium unit in **8** upon addition of two equivalents of $T_{iiii}[C_{11}H_{23}, H, Ph]$ cavitand (**2**).

From the changes observed in the fluorescence intensity during the association process between $T_{iiii}[C_{11}H_{23}, H, Ph]$ and **8**, it has been possible to measure a $K_{ass} = 8.0 \times 10^6\ M^{-1}$, in perfect agreement with the value obtained by ITC titration with reference compounds (Table 2.1).

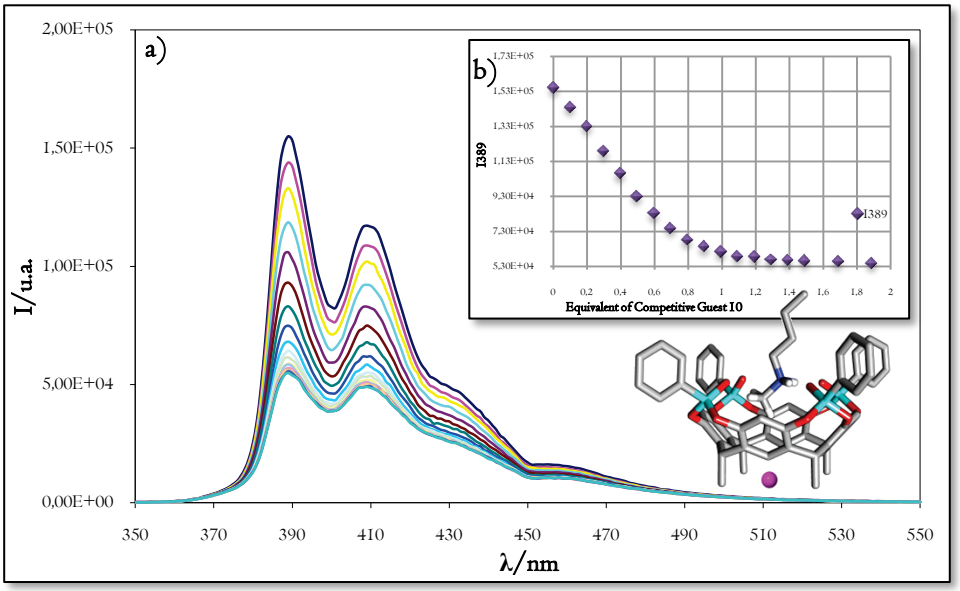

Figure 2.4. a) Fluorescence spectra (λ_{exc}=345 nm) of an equimolar CH_2Cl_2 solution of T_{iii}[$C_{11}H_{23}$, H, Ph] and **8** (1 x 10^{-5} M), upon addition of an increasing (0 - 1.3 equiv.) amount of the competitive guest **10**; b) Trend of the emission at 389nm of T_{iii}[$C_{11}H_{23}$, H, Ph]@**8** as a function of the equivalent of guest **10** added.

To prove the reversibility of the association process, we added an increasing amount of the methylammonium salt **10** to a solution containing the T_{iii}[$C_{11}H_{23}$, H, Ph]@**8** complex. As inferred by ITC, **10** has a much higher affinity than **14** towards T_{iii} cavitands. As can be observed from Figure 2.4 and 2.5, such addition is accompanied by a gradual decrease of the fluorescence until the intensity reaches the value typical of **8** alone when one equivalent is added, clearly demonstrating that **8** is ejected away from the cavity by the more competitive **10**. The dissociation of the T_{iii}[$C_{11}H_{23}$, H, Ph]@**10** complex was obtained by the addition of an hindered base (such as 1,8-diazabicyclo[5.4.0]undec-7-ene, DBU), that, by deprotonating the ammonium ion **10**, makes it unfit for interacting with the cavity, while the addition of triflic acid shifted the system towards the T_{iii}[$C_{11}H_{23}$, H, Ph]@**10** complex again. As can be seen from Fig. 2.5, all these processes, which are completely reversible, were clearly monitored by looking at the fluorescence of the pyrene unit.

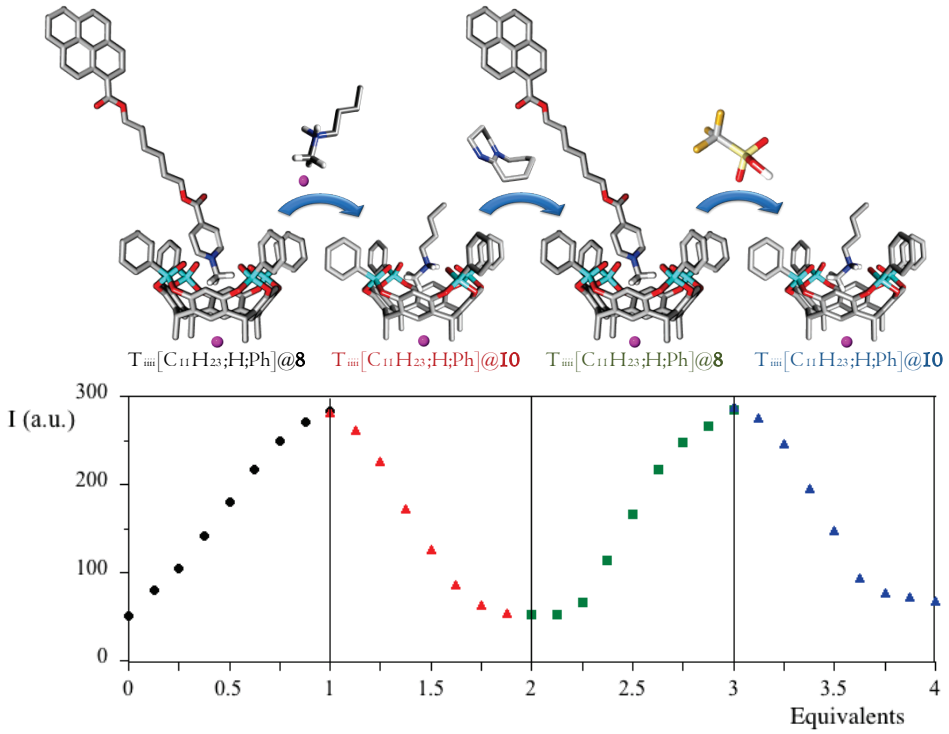

Figure 2.5. Fluorescence intensity (λ_{exc}=345 nm, λ_{em}=390 nm) of a 1 x 10^{-5}M CH_2Cl_2 solution of **8** upon a subsequent addition of one equivalent of cavitand $T_{iii}[C_{11}H_{23}, H, Ph]$ (from 0-1 in the figure), one equivalent of ammonium ion **10** (from 1 to 2), one equivalent of DBU (from 2 to 3), and one equivalent of triflic acid (from 3 to 4). In the structures of the complexes the alkyl feet are omitted for clarity.

It is important to note at this point that, as desired because of the intrinsic higher offered sensitivity, the $T_{iii}[C_{11}H_{23}, H, Ph]$@**8** complex formation is accompanied by a large increase in the luminescence signal, the final value of the fluorescence quantum yield being remarkably high (Φ=0.08). This is not a trivial result, since quenching between a pyrene chromophore and a resorcinarene receptor was previously observed.[10]

Furthermore, while photoinduced electron transfer (PET) processes have been often used with success to modulate the fluorescence intensity of a dye in a variety of sensors through the involvement of a nitrogen atom as electron donor,[2,11] this is in our opinion a rather elegant signal transduction mechanism since it makes the process orthogonal to the presence of protons

or metal ions. A different design of the molecular thread would not have led easily to similar results. For example, a hypothetical linear molecule with a pyrene and an amine group covalently linked to it could have the luminescence of the dye quenched if the two groups were not too far apart, and the protonation of the amine would lead to both insertion in the cavity, if present, and to an increase of the fluorescence signal. However this latter effect would be observed independently of the presence of the cavitand and, as a consequence, of the association process.

2.3 Conclusions.

Exploiting the remarkable molecular recognition properties of tetraphosphonate cavitands, a suitable protocol for the reversible complexation of the methylammonium and methylpyridinium salts by the $T_{iiii}[C_{11}H_{23}, H, Ph]$ cavitand was developed and monitored via fluorescence spectroscopy. The peculiarity of this system is the presence in compound **8** of electron-transfer between the pyrene and the methylpyridinium moiety quenching its fluorescence, which increases after complexation with the tetraphosphonate cavitand. The inclusion of the electron-poor methylpyridinium moiety inside the electron-rich cavity, makes its reduction process more energy demanding.

The next step will be to extend these protocol on surface in order to study the molecular recognition properties of the tetraphosphonate cavitands on silicon surfaces.

2.4 Acknowledgements.

Special thanks to Prof. Luca Prodi, Dr. Marco Montalti and Dr. Gionata Battistini of the University of Bologna for the Photophysical experiments, and Dr. Roger M. Yebeutchou of the University of Parma for the ITC analyses.

2.5 Experimental Section.

2.5.1 Reagent, Chemicals and Instruments used.

All commercial reagent were ACS reagent grade and used as received. For the synthesis all solvents were dried and distilled using standard procedures.

- Chromatography was performed using 70-230 mesh silica purchased from Merck and 40-120 μ Sephadex G-10 purchased from Pharmacia Fine Chemicals. Thin layer chromatography was performed on Kieselgel 60 F_{254} and Uniplate^{tm} Silica Gel GF silica-coated glass plates and visualized by UV.

- ^{1}H NMR and spectra were recorded on Bruker 300 (300 MHz) and Bruker Avance 300 (300 MHz) spectrometers and all chemical shifts (δ) were reported in parts per million (ppm) relative to proton resonances resulting from incomplete deuteration of NMR solvents. ^{31}P NMR spectra were recorded on AMX-400 (162 MHz) and all chemical shifts were reported to external 85% H_3PO_3 at 0 ppm.

- ESI-MS characterization experiments were performed on a Waters ACQUILITY SQD Detector equipped with a ESCi® multi mode ionization (APCI/ESI).

2.5.2 Photophysical Experiments.

The solvent used for photophysical measurements was dichloromethane from Merck (UVASOL) without further purification. Absorption spectra in solution were recorded on a Perkin–Elmer Lambda 40 spectrophotometer. The fluorescence spectra were recorded with an Edinburgh FLS920 equipped with a Hamamatsu R928P photomultiplier. The same instrument equipped with a PCS900 PC card was used for the Time Correlated Single Photon Counting experiments. All the photophysical measurements were performed in aerated solutions.

2.5.3 Spectrofluorimetric Titration.

Stability constants were determined by fitting the fluorescence spectra recorded during the titration of the hosts with the tetrabutyl ammonium salts; a solution of the host species of known concentration typically 4-12 μM was used. The data were fitted with the global analysis program SPECFIT.

2.5.4 Electrochemical Experiments.

Cyclic voltammetric (CV) experiments were carried out at room temperature, in argon-purged CH_2Cl_2 (Romil Hi-Dry) solutions containing 0.1 M Bu_4NPF_6 as supporting electrolyte, with an Autolab 30 multipurpose instrument interfaced to a personal computer. The working electrode was a glassy carbon electrode (0.08 cm^2, Amel); its surface was routinely polished with 0.3 micron alumina-water slurry on a felt surface, immediately prior to use. In all cases, the counter electrode was a Pt spiral, separated from the bulk solution with a fine glass frit, and an Ag wire was used as a quasi-reference electrode. Ferrocene ($E_{1/2}$ = +0.51 V vs SCE in CH_2Cl_2) was present as an internal standard.

2.5.5 ITC Titration.

ITC titrations were performed using an isothermal titration microcalorimeter Microcal VP-ITC. All measurements were performed at (298±0,02) K. The host solution was filled into the cell of the ITC instrument and guest solutions were added with the syringe. In each case control experiments with dilution of guest in the solvent were performed and were found to be negligible. Concentration of cavitand T_{iiii} [C_3H_7, CH_3, Ph] 0.25 mM in dichloromethane; concentration of the guest **14** 2.5 mM in dichloromethane. The volume of injection was 10 μL and the stirring speed was 300 rpm. Samples were weight with a microbalance Mettler Toledo MX5. The solvent was previously degassed by sonication during 15 min. Titrations were made 3 times in order to be reproducible. Analysis and curve fitting were done using the software MCS Origin-ITC 7.0 program. The experimental titration is reported in Figure 2.6.

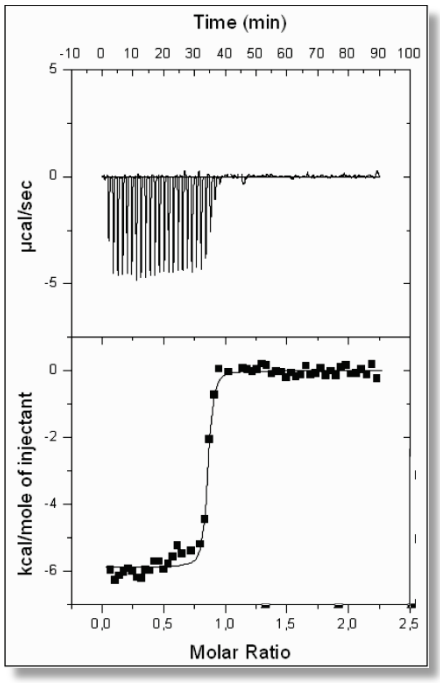

Figure 2.6. ITC trace of the titration of cavitand T_{iiii} [C_3H_7, CH_3, Ph] with **14** in CH_2Cl_2. Titration mode: guest (**14**) into host (T_{iiii} [C_3H_7, CH_3, Ph]) solution; one-site model.

2.5.6 Synthetic Protocol.

Resorcinarene Res[$C_{11}H_{23}$, H]. (1)

Resorcinarene **1** was prepared following a published procedure.[12]

Cavitand T_{iiii}[$C_{11}H_{23}$, H, Ph]. (2)

Cavitand T_{iiii}[$C_{11}H_{23}$, H, Ph] was prepared following a published procedure.[13]

Resorcinarene Res[C_3H_7, CH_3]. (3)

Resorcinarene Res[C_3H_7, CH_3] was prepared following a published procedure.[14]

Cavitand T$_{iiii}$[C_3H_7, CH_3, Ph]. (4)

To a solution of resorcinarene (0.60 g, 0.80 mmol) in freshly distilled pyridine (20 mL) dichlorophenylphosphine (0.447 mL, 3.39 mmol) was added slowly, at room temperature. After 3 hours of stirring at 80 °C, the solution was allowed to cool at room temperature and 8 mL of a mixture of 35% H_2O_2 and $CHCl_3$ (1:1) was added. The resulting mixture was stirred for 30 minutes at room temperature, then the solvent was removed under reduced pressure and water added. The precipitate obtained in this way was collected by vacuum filtration, and purified by re-crystallization (H_2O:CH_3CN 8:2). The product is a fine white powder (0.91 g, 0.76 mmol, 94%).

^{1}H NMR ($CDCl_3$, 300 MHz) δ (ppm): 8.09 (m, 8H, POArH_o); 7.61 (m, 4H, POArH_p); 7.52 (m, 8H, POArH_m); 7.13 (s, 4H, ArH_{down}); 4.81 (t, 4H, J = 7.4 Hz, ArCH); 2.34-2.20 (m, 8H + 12H, C$H_2$$CH_2CH_3$ + ArCH_3); 1.41 (m, 8H, CH_2C$H_2$$CH_3$); 1.04 (t, 12H, J = 7.4 Hz, CH_2CH_2CH_3). **^{31}P NMR** ($CDCl_3$, 162 MHz) δ (ppm): 4.02 (s, 4P, *P* OPh). **ESI-MS:** m/z 1201.6 $[M+H]^+$.

6-hydroxyhexyl pyrene-1-carboxylate. (5)

To a solution of 1-pyrene carboxylic acid (200 mg, 0.812 mmol) dissolved in 15 mL of CH_2Cl_2 and 1 mL of DMA, DCC (168 mg, 0.812 mmol) and DMAP (33 mg, 0.268 mmol) were added. The solution was stirred at room temperature for 4 hours, then hexane-1,6-diol (115 mg, 0.974 mmol) was added and the resulting mixture was stirred at room temperature for three days. The crude was purified by column chromatography on silica gel by using CH_2Cl_2 as eluant to give the desired compound as brown powder in 42% yield (117 mg, 0.338 mmol).

^{1}H NMR ($CDCl_3$, 300 MHz) δ (ppm): 9.25 (d, 1H, J=9.3 Hz, Pyrene$H$), 8.61 (d, 1H, J=8.1 Hz, Pyrene$H$), 8.27-8.02 (m, 7H, Pyrene$H$), 4.50 (t, 2H, J=6.6 Hz, PyreneCOOCH_2R), 3.67 (t, 2H, J=6.3 Hz, RCH_2CH_2OH), 1.91 (m, 2H, PyreneCOOCH_2CH_2R), 1.68-1.48 (m, 6H, RCH_2(CH_2)$_3$$CH_2$OH). **ESI-MS:** m/z 381.1 $[M+Cl]^-$.

6-(pyrene-1-carbonyloxy)hexyl isonicotinate. (6)

To a solution of 5 (117 mg, 0.338 mmol) dissolved in 10 mL of CH_2Cl_2 and 1 mL of DMA, DCC (139 mg, 0.676 mmol) and DMAP (50 mg, 0.446 mmol) were added. The solution was stirred at room temperature for 4 hours, then isonicotinic acid (83 mg, 0.676 mmol) was added and the resulting mixture was stirred at room temperature for three days. The crude was purified by column chromatography on silica gel by using CH_2Cl_2/ethyl acetate (90/10 υ/υ) as eluant to give the desired compound as brown powder in 79% yield (121 mg, 0.268 mmol).

^{1}H NMR ($CDCl_3$, 300 MHz) δ (ppm): 9.21 (d, 1H, J=9.6 Hz, Pyrene*H*), 8.71 (d, 2H, J=5.6 Hz, PyH_o), 8.53 (d, 1H, J=8.1 Hz, Pyrene*H*), 8.13-7.88 (m, 7H, Pyrene*H*), 7.76 (d, 2H, J=5.6 Hz, PyH_m), 4.47 (t, 2H, J=6.6 Hz, PyreneCOOCH_2R), 4.29 (t, 2H, J=6.3 Hz, RCH_2OCOPy), 1.86 (m, 2H, PyreneCOOCH$_2$CH_2R), 1.74 (m, 2H, CH_2CH$_2$OCOPy), 1.51 (m, 4H, PyreneCOO(CH$_2$)$_2$(CH_2)$_2$R). **ESI-MS:** m/z 452.4 $[M+H]^+$.

1-methyl-4-((6-(pyrene-1-carbonyloxy)hexyloxy)carbonyl)pyridinium Iodide. (7)

Iodomethane (83 μl, 1.34 mmol) was added to a solution of compound **6** (121 mg, 0.268 mmol) dissolved in 10 mL of CH_3CN. The solution was refluxed for two days and the precipitate formed was filtered to give the desired salt as yellow powder in 50% yield (80 mg, 0.135 mmol).

^{1}H NMR ($CDCl_3$, 300 MHz) δ (ppm): 9.20 (d, 1H, J=9.3 Hz, Pyrene*H*), 8.96 (d, 2H, J=6.3 Hz, PyH_o), 8.59 (d, 1H, J=8.1 Hz, PyreneH), 8.30-8.07 (m, 9H, Pyrene*H* e PyH_m), 4.55 (t, 2H, J=6.3 Hz, PyreneCOOCH_2R), 4.47 (t, 2H, J=6.3 Hz, RCH_2OCOPy), 4.41 (s, PyCH_3), 1.99 (m, 2H, PyreneCOOCH$_2$CH_2R), 1.89 (m, 2H, RCH_2CH$_2$OCOPy), 1.64 (m, 4H, PyreneCOO(CH$_2$)$_2$(CH_2)$_2$R). **ESI-MS:** m/z 466.4 $[M-I]^+$.

1-methyl-4-((6-(pyrene-1-carbonyloxy)hexyloxy)carbonyl)pyridinium hexafluorophosphate. (8)

To a solution of compound **7** (50 mg, 0.084 mmol) dissolved in 2 mL of CH_3CN and 1 mL of water, NH_4PF_6 (27 mg, 0.168 mmol) was added. The solution was stirred at room temperature for three hours, then the solvent was removed and the crude was extracted with water and CH_2Cl_2. The organic phase was dried over sodium sulphate and evaporated to give the desired compound as white powder in quantitative yield (51.4 mg, 0.080 mmol).

^{1}H NMR (CD_3CN, 300 MHz) δ (ppm): 9.04 (d, 1H, J=9.3 Hz, Pyrene*H*), 8.50 (d, 2H, J=5.7 Hz, Py*H*$_o$), 8.25-8.05 (m, 10H, Pyrene*H* e Py*H*$_m$), 4.45 (t, 2H, J=6.3 Hz, PyreneCOOC*H*$_2$R), 4.33 (t, 2H, J=6.6 Hz, RC*H*$_2$OCOPy), 4.16 (s, 3H, PyC*H*$_3$), 1.87 (m, 2H, PyreneCOOCH$_2$C*H*$_2$R), 1.78 (m, 2H, RC*H*$_2$CH$_2$OCOPy), 1.55 (m, 4H, PyreneCOO(CH$_2$)$_2$(C*H*$_2$)$_2$R. **^{31}P NMR** ($CDCl_3$, 162 MHz) δ (ppm): -141.1 (m, $J_{P\text{-}F}$=706 Hz, *P*F_6). **ESI-MS:** m/z 466.4 $[M\text{-}PF_6]^+$.

N-methylbutyl-1-ammonium iodide. (9)

An excess of a solution 57% of HI in water was added to a solution of N-methylbutylamine (2 mL, 16.9 mmol) dissolved in 20 mL of in diethyl ether. The resulting solution was stirred for 30 min at room temperature. The yellow suspension was filtered and re-crystallised in a mixture 1:99 of acetonitrile and diethyl ether (3.45 g, 1.6 mmol, 95%).

^{1}H NMR (CD_3CN, 300 MHz) δ (ppm): 0.91 (t, 3H, J=7.3 Hz, CH_2*CH*$_3$), 1.4 (m, 2H, *CH*$_2$$CH_3$), 1.7 (m, 2H, C*H*$_2$$CH_2NH_2CH_3$), 2.6 (s, 3H, NH_2C*H*$_3$), 2.9 (t, 2H, J=7.5 Hz, C*H*$_2$$NH_2CH_3$), 7.5 (broad, 2H, N*H*$_2$). **ESI-MS:** m/z 88.1 $[M\text{-}I]^+$.

N-methylbutyl-1-ammonium hexafluorophosphate. (10)

To a solution of compound **9** (200 mg, 0.930 mmol) dissolved in 0.5 mL of CH_2Cl_2, NH_4PF_6 (182 mg, 1.116 mmol) dissolved in 0.5 mL of acetone was added. The solution was stirred at room temperature for three hours, then the white precipitated formed was filtered to give the desired compound in quantitative yield (200 mg, 0.858 mmol).

^{1}H NMR ($CDCl_3$, 300 MHz) δ (ppm): 0.97 (t, 3H, J=7.5 Hz, CH_2CH_3), 1.46 (m, 2H, CH_2CH_3), 1.90 (m, 2H, $CH_2CH_2NH_2CH_3$), 2.68 (t, 3H, J=6 Hz, NH_2CH_3), 3.0 (m, 2H, $CH_2NH_2CH_3$), 8.4 (broad, 2H, NH_2); **^{31}P NMR** ($CDCl_3$, 162 MHz) δ (ppm): -141.08 (m, J_{P-F}=707 Hz, PF_6). **ESI-MS:** m/z 88.3 $[M-PF_6]^+$.

4-methoxycarbonyl-1-methylpyridinium iodide. (11)

Iodomethane (136 μl, 2.19 mmol) was added to a solution of isonicotinoyl methyl ester (200 mg, 1.46 mmol) dissolved in 15 mL of CH_2Cl_2 . The solution was stirred at 30°C overnight. After an addition of hexane (10 mL) the orange precipitate was sonicated and filtered off obtaining the desired product in 87% yield (354 mg, 1.27 mmol).

^{1}H NMR ($CDCl_3$, 300 MHz) δ (ppm): 9.06 (d, 2H, J=6.3 Hz, PyH_o), 8.43 (d, 2H, J=6.3 Hz, PyH_m), 4.56 (s, 3H, CH_3), 4.04 (s, 3H, CH_3). **ESI-MS:** m/z 152.5 $[M-I]^+$.

4-methoxycarbonyl-1-methylpyridinium hexafluorophosphate. (12)

To a solution of compound **11** (150 mg, 0.538 mmol) dissolved in 0.5 mL of CH_2Cl_2, NH_4PF_6 (132 mg, 0.807 mmol) dissolved in 0.5 mL of acetone was added. The solution was stirred at room temperature overnight, then the white precipitated formed was filtered and recrystallized from a mixture 1:1 of acetonitrile and diethyl ether to give the desired compound in 95% yield (152 mg, 0.511 mmol).

^{1}H NMR (DMSO-d_6, 300 MHz) δ(ppm): 3.98 (s, 3H, OCH_3), 4.41 (s, 3H, NCH_3), 8.48 (d, 2H, J=6.3 Hz, PyH_m), 9.14 (d, 2H, J=6.3 Hz, PyH_o). **^{31}P NMR** (DMSO-d_6, 162 MHz) δ(ppm): -141.3 (m, J_{P-F}=715 Hz, PF_6). **ESI-MS:** m/z 152.5 $[M-PF_6]^+$.

4-butoxycarbonyl-1-methylpyridinium iodide. (13)

To a solution of butyl isonicotinate (2.17 g, 11.2 mmol) dissolved in 50 mL of acetonitrile, iodomethane (12 mL, 22.4 mmol) was added. The reaction was stirred at reflux for 16h. The solvent was removed and the product was recrystallized from a mixture 1:1 of acetonitrile and ethyl acetate affording the desired product (2.86 g, 8.91 mmol, 80%).

^{1}H NMR: ($CDCl_3$, 300 MHz) δ (ppm): 0.96 (t, 3H, J=6.87 Hz, C*H*$_3$), 1.43 (m, 2H, $OCH_2CH_2CH_2CH_3$), 1.76 (m, 2H, $OCH_2CH_2CH_2CH_3$), 4.43 (t, 2H, J=6.7 Hz, $OCH_2CH_2CH_2CH_3$), 5.24 (s, 3H, N-C*H*$_3$), 8.45 (d, 2H, J=6.6 Hz, Py*H*$_m$), 9.5 (d, 2H, J=6.6 Hz, Py*H*$_o$). **ESI-MS:** m/z 195.1 $[M\text{-}I]^+$.

4-butoxycarbonyl-1-methylpyridinium hexafluorophosphate. (14)

To a solution of ammonium hexafluorophosphate (3.65 g, 22.4 mmol) dissolved in a hot mixture 7:3 of acetonitrile and water, compound **13** (3.6 g, 11.2 mmol) was added. The resulting yellow suspension was stirred at room temperature until the precipitate became white. Filtration and recrystallization from a mixture 9:1 of H_2O and CH_3CN afforded the product in a good yield (3.6 g, 10.2 mmol, 95%).

^{1}H NMR: ($CDCl_3$, 300 MHz) δ(ppm): 0.96 (t, 3H, J=7.3 Hz, C*H*$_3$), 1.43 (m, 2H, $OCH_2CH_2CH_2CH_3$), 1.76 (m, 2H, $OCH_2CH_2CH_2CH_3$), 4.41 (t, 2H, J=6.7 Hz, $OCH_2CH_2CH_2CH_3$), 4.47 (s, 3H, NC*H*$_3$), 8.40 (d, 2H, J=5.6 Hz, Py*H*$_m$), 8.84 (d, 2H, J=5.6 Hz, Py*H*$_o$). **^{31}P NMR** ($CDCl_3$, 162 MHz) δ(ppm): -146.5 (m, $J_{P\text{-}F}$=713 Hz, *P*F_6). **ESI-MS:** m/z 195.0 $[M\text{-}PF_6]^+$.

2.6 References.

[1] M. Montalti, A. Credi, L. Prodi and M. T. Gandolfi, *Handbook of Photochemistry*, CRC Taylor & Francis, Boca Raton, 3rd Edn, **2006**.

[2] L. Prodi, Luminescent chemosensors: from molecules to nanoparticles, *New J. Chem.* **2005**, *29*, 20-31.

[3] A. B. Descalzo, R. Martinez-Manez, F. Sancenon, K. Hoffmann and K. Rurack, The supramolecular chemistry of organic-inorganic hybrid materials, *Angew. Chem., Int. Ed.* **2006**, *45*, 5924-5948.

[4] M. Busi, M. Laurenti, G. G. Condorelli, A. Motta, M. Favazza, I. L. Fragalà , M. Montalti, L. Prodi and E. Dalcanale, Self-assembly of nanosize coordination cages on Si(100) surfaces, *Chem.-Eur. J.* **2007**, *13*, 6891-6898.

[5] For the nomenclature used to define tetraphosphonate cavitands see: R. Pinalli, M. Suman and E. Dalcanale, Cavitands at work: From molecular recognition to supramolecular sensors, *Eur. J. Org. Chem.* **2004**, 451-462.

[6] R. De Zorzi, B. Dubessy, J.-C. Mulatier, S. Geremia, L. Randaccio and J.-P. Dutasta, Structure of a 4p1:4 Supramolecular Assembly of Neutral T_{iiii}PO Cavitands and Tetrakis(N-methylpyridinium)porphyrin Iodide, *J. Org. Chem.* **2007**, *72*, 4528-4531.

[7] J.-P. Dutasta, New phosphorylated hosts for the design of new supramolecular assemblies, *Top. Curr. Chem.* **2004**, *232*, 55-91.

[8] E. Kalenius, D. Moiani, E. Dalcanale and P. Vainiotalo, Measuring H-bonding in supramolecular complexes by gas phase ion-molecule reactions, *Chem. Commun.* **2007**, *37*, 3865-3867.

[9] J. L. Sessler, D. E. Gross, W.-S. Cho, V. M. Lynch, F. P. Schmidtchen, G. W. Bates, M. E. Light and P. A. Gale, Calix[4]pyrrole as a Chloride Anion Receptor: Solvent and Countercation Effects, *J. Am. Chem. Soc.* **2006**, *128*, 12281-12288.

[10] M. Inhouye, K. Hashimoto and K. Isagawa, Nondestructive Detection of Acetylcholine in Protic Media: Artificial-Signaling Acetylcholine Receptors, *J. Am. Chem. Soc.* **1994**, *116*, 5517-5518.

[11] L. Prodi, F. Bolletta, M. Montalti and N. Zaccheroni, Luminescent Chemosensors for Transition Metal Ions, *Coord. Chem. Rev.* **2000**, *205*, 59-83.

[12] L. M. Tunstad, J. A. Tucker, E. Dalcanale, J. Weiser, J. A. Bryant, J. C. Sherman, R. C. Helgeson, C. B. Knobler, and D. J. Cram, Host-Guest Complexation. 48. Octol Building Blocks for Cavitands and Carcerands, *J. Org. Chem.* **1989**, *54*, 1305-1312.

[13] M. Melegari, M. Suman, L. Pirondini, D. Moiani, C. Massera, F. Ugozzoli, E. Kalenius, P. Vainiotalo, J.-C. Mulatier, J.-P. Dutasta, E. Dalcanale, Supramolecular Sensing with Phosphonate Cavitands, *Chem.-A Eur. J.* **2008**, *14*, 5772-5779.

[14] R. M. Yebeutchou, F. Tancini, N. Demitri, S. Geremia, R. Mendichi, E. Dalcanale, Host-guest driven self-assembly of linear and star supramolecular polymers, *Angew. Chem., Int. Ed.* **2008**, *47*, 4504-4508.

Molecular Recognition on Si(100) functionalized with tetraphosphonate cavitands.†

3

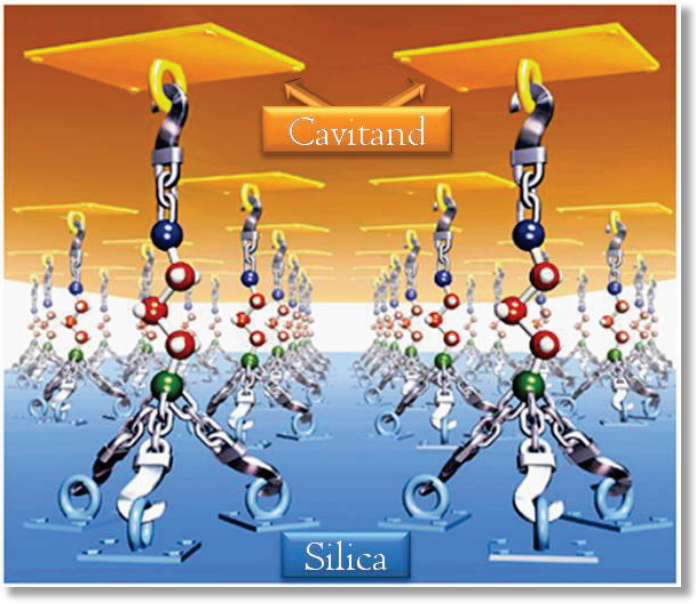

"Supramolecular Structure on Surface"

† This chapter is based on: E. Biavardi, M. Favazza, A. Motta, I. L. Fragala, C. Massera, L. Prodi, M. Montalti, M. Melegari, G. G. Condorelli, E. Dalcanale, Molecular Recognition on a Cavitand-Functionalized Silicon Surface, *J. Am. Chem. Soc.* **2009**, *131*, 7447-7455.

3.1 Introduction.

The introduction of specific functions onto surfaces represents one of the major themes in contemporary chemistry. Notable examples of functional surfaces include: self-cleaning surfaces mimicking the lotus leaf,[1] gecko-foot mimetic adhesive surfaces featuring carbon nanotubes-decorated silicon wafers,[2] monolayers with control of surface wettability via electrically triggered conformational transitions,[3] high density molecular electronic memory using bistable rotaxanes as storage elements.[4] Among the several surface functions identified to be worth pursuing, molecular recognition is particularly noteworthy for its profound impact on biology and materials science. In living organisms, multiple recognition events trigger the immune system response through antibodies, and they promote the adhesion of viruses on cell surfaces.[5] In nanotechnology, the controlled positioning of molecules and assemblies on surfaces can be driven by multiple binding events.[6] Another significant field impacted by molecular recognition on surfaces is chemical sensing, in which the recognition process is translated into an analytical signal.[7]

Organic monolayers hosted on inorganic surfaces[8] represent the best approach for harnessing the full potential of molecular recognition on surfaces.[9] Compared to both thin films and bulk materials containing molecular receptors, such hybrid organic-inorganic materials have the advantage of reducing or even eliminating nonspecific interactions which often mask the recognition events.[10]

Silicon is a particularly attractive inorganic platform, as it offers the possibility to make robust and durable devices by forming stable Si-C covalent bonds. Moreover, the grafting of molecular receptors on silicon wafers represents an important step toward the generation of silicon-integrated devices.

Phosphorus-bridged cavitands[11] are a promising class of synthetic molecular receptors. The introduction of four $P^{(V)}$ stereogenic centers as bridging units creates a family of six diastereomeric cavitands, each with a different orientation of the P=O groups, i.e. inward (i) or outward (o) with respect to the cavity.[12]

Among these molecules, tetraphosphonate cavitands with an all-inward configuration[13] (Figure 3.1) are particularly versatile in their ability to complex positively charged species, such as inorganic cations,[14] ammonium and pyridinium salts (see Chapter 2),[15] as well as neutral molecules such as alcohols.[16] This diverse complexation ability is the result of three interaction modes, which can be activated either individually or in combination by the host according to the guest requirements. These include (i) multiple ion-dipole interactions between the inward facing P=O groups and the positively charged guests,[14] (ii) single or multiple H-bonding involving the P=O groups,[14,17] and (iii) CH_3-π interactions between an acidic methyl group present on the guest and the π -basic cavity of the host.[16] Depending on the type and number of interactions activated, the measured K_{ass} in nonpolar solvents can vary between 10^2 M^{-1} for shortchain alcohols to 10^9-10^{10} M^{-1} for *N,N*-methylalkylammonium salts.[18]

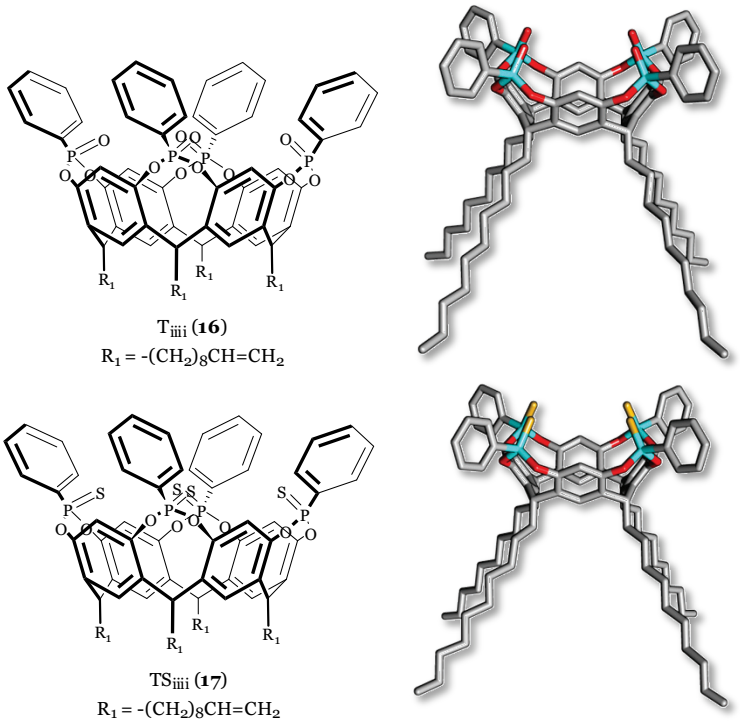

Figure 3.1. Tetraphosphonate cavitands *T_{iiii}[$C_{10}H_{19}$, H, Ph]* and *TS_{iiii}[$C_{10}H_{19}$, H, Ph]*.

Our group has recently published a protocol for the covalently assembly of cavitands on silicon surface,[19] along with various aspects of the coordination chemistry of the resulting cavitand-decorated assemblies.[20]

In the current study we report a comprehensive investigation of the molecular recognition properties of a silicon surface decorated with phosphonate cavitands toward methylpyridinium and methylammonium guests. The entire process, consisting of methylpyridinium complexation, guest exchange with methylammonium salts, base-driven decomplexation of the latter accompanied by restoration of the initial complex, is fully reversible. Each step of the process was monitored using two independent techniques, namely X-ray photoelectron spectroscopy (XPS) and fluorescence spectroscopy. Control experiments with a silicon surface covered with a structurally similar, yet complexation inactive, thiophosphonate cavitand[18] further validated the entire complexation cycle.

The active monolayer is constituted by a tetraphosphonate cavitand $T_{iiii}[C_{10}H_{19}, H, Ph]$[21] (**16**) with decyl feet (thereafter T_{iiii}, Figure 3.1) anchored on H-terminated Si(100) surfaces via photochemical hydrosilylation of the double bonds.[22] This same procedure was likewise used to graft the control monolayer containing tetrathiophosphonate cavitand $TS_{iiii}[C_{10}H_{19}, H, Ph]$ (**17**) (thereafter TS_{iiii}, Figure 3.1), unable to complex N-methyl derivarives.

Trifluoro-, trichloro-, and bromo-marked guests **22**, **24**, **25**, **26** were specifically designed and prepared for XPS detection, while the methylpyridinium guest **8** contains pyrene as fluorescent probe.

3.2 Results and Discussion.

3.2.1 Receptors design and synthesis.

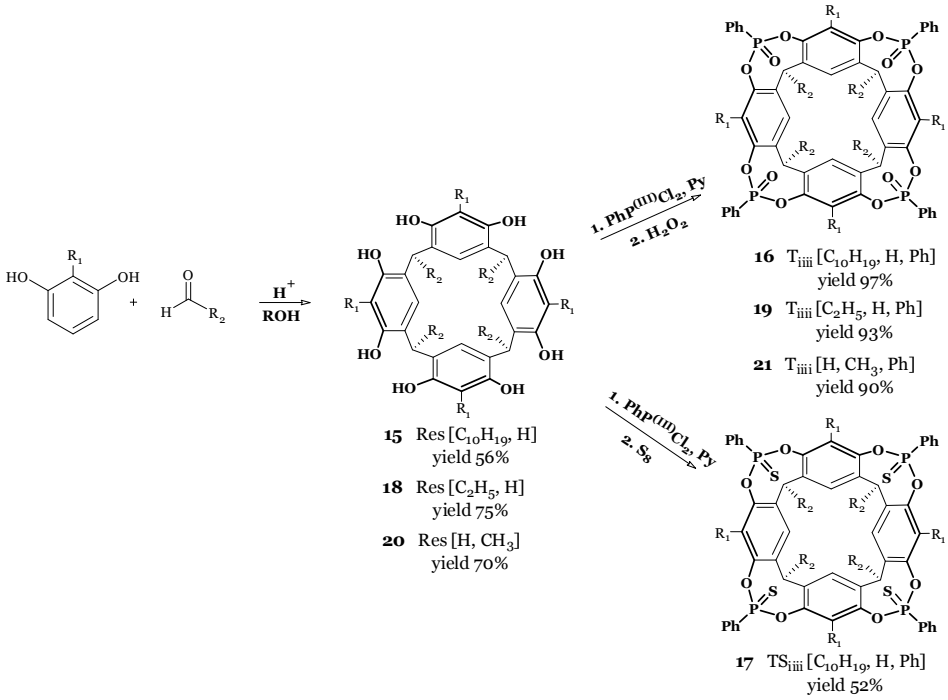

15 Res [$C_{10}H_{19}$, H]
yield 56%

18 Res [C_2H_5, H]
yield 75%

20 Res [H, CH_3]
yield 70%

16 T_{iiii} [$C_{10}H_{19}$, H, Ph]
yield 97%

19 T_{iiii} [C_2H_5, H, Ph]
yield 93%

21 T_{iiii} [H, CH_3, Ph]
yield 90%

17 TS_{iiii} [$C_{10}H_{19}$, H, Ph]
yield 52%

Scheme 3.1. Synthetic protocol of cavitands **16**, **17**, **19** and **21**.

Cavitands were obtained following the synthetic protocol reported in Scheme 3.1.

The tetraphosphonate cavitand T_{iiii}[$C_{10}H_{19}$, H, Ph] (**16**) with decyl feet was prepared via an acid-catalyzed condensation between resorcinol and 10-undecenal leading to Res[$C_{10}H_{19}$, H] (**15**). Subsequently, on the flexible macrocycles was performed the bridging reaction with *P,P*-dichlorophenylphosphine in anhydrous pyridine at 80°C to obtain the tetraphosphonite intermediate, then oxidized *in situ* with hydrogen peroxide.

The same reactions were accomplished to prepare TS_{iiii}[$C_{10}H_{19}$, H, Ph] cavitand (**17**), but performing the oxidation *in situ* with octathiocane.

$T_{iii}[C_2H_5, H, Ph]$ (**19**) and $T_{iii}[H, CH_3, Ph]$ (**21**) cavitands were obtained following the same protocol but using propionaldehyde and 2-methylresorcinol respectively.

3.2.2 Guests design and synthesis.

Synthesis of methylpyridinium guest **8** and methylamonium guest **9** was already reported in Chapter 2 (Experimental Section, Subparagraph 2.6.6).

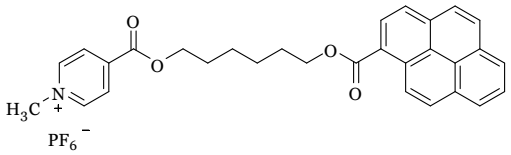

8

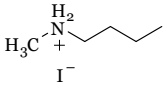

9

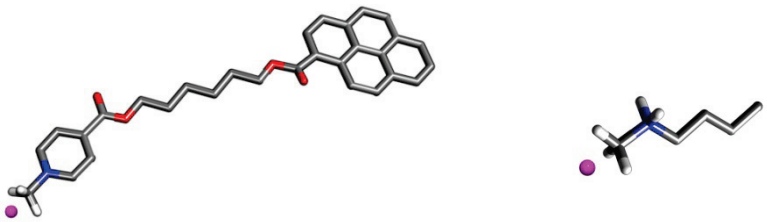

Scheme 3.2. Structure of guests **8** and **9**.

Guest **22** was prepared, following a published procedures[43], via methylation of 4-(trifluoromethyl)pyridine with iodomethane.

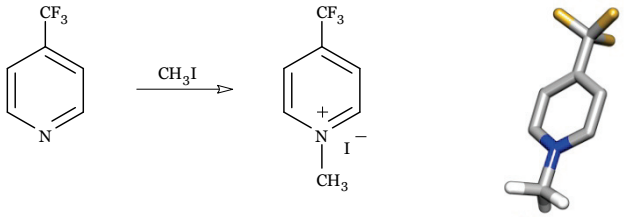

22
yield 85%

Scheme 3.3. Synthesis of guest **22**.

To prepare guest **24** was exploited the nucleophilic acylic substitution reaction between the isonicotinoyl chloride and 2,2,2-trichloroethanol obtaining the intermediate **23**, which was subsequently methylated with iodomethane affording the desired product **24** in a good yield.

Compound **24** was subjected to an ion-exchange reaction with ammonium hexafluorophosphate to give guest **25** in quantitative yield.

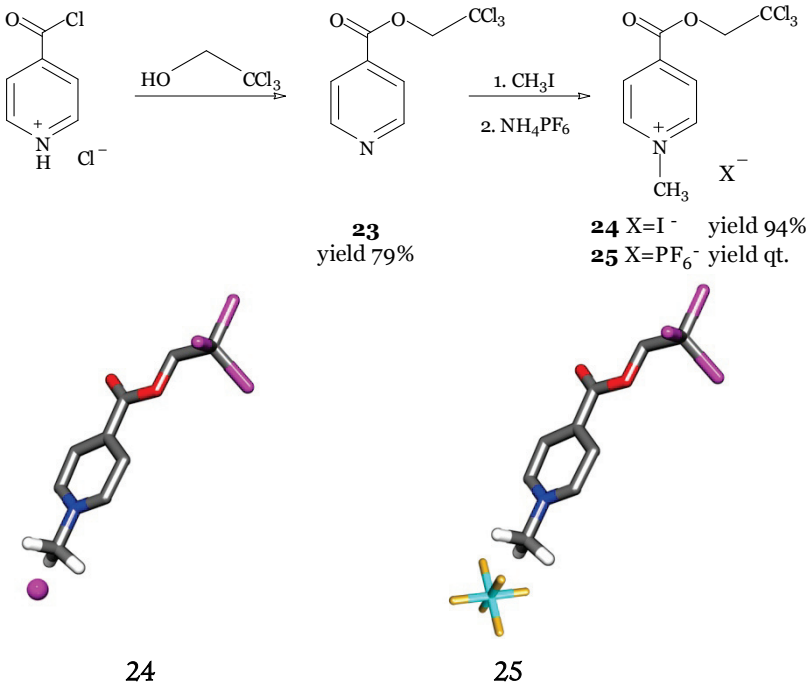

Scheme 3.4. Synthesis of guests **24** and **25**.

Finally, guest **26** was obtained via bromuration with thionyl bromide (Scheme 3.5). In this reaction, we observed not only the direct bromination of the primary alcohol but also the protonation of the methylamine moiety due to HBr, formed *in situ* during the bromination reaction.

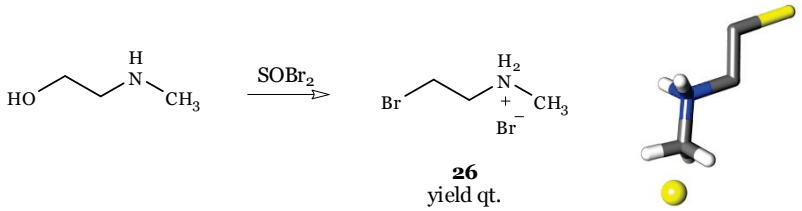

Scheme 3.5. Synthesis of guest **26**.

3.2.3 Silicon Surface Functionalization with Cavitands.

Photochemical hydrosilylation is a method of grafting molecules on silicon surfaces that exploit the rapid formation of monolayers through Si-C covalent bonds by the reaction of ω-functionalized 1-alkene precursors with hydrogen-passivated silicon.

Pure and mixed monolayers of cavitands with 1-octene (Oct) as spectator spacer were prepared. The use of the Oct spectator spacer in the mixed monolayers improves the passivation of the Si surface, thus minimizing substrate oxidation due to aging.[19] Mixed Si-T$_{iiii}$/Oct and Si-TS$_{iiii}$/Oct surfaces were obtained by Si grafting a cavitand/Oct mixtures of 1:4 (cavitand mole fraction χ=0.2).

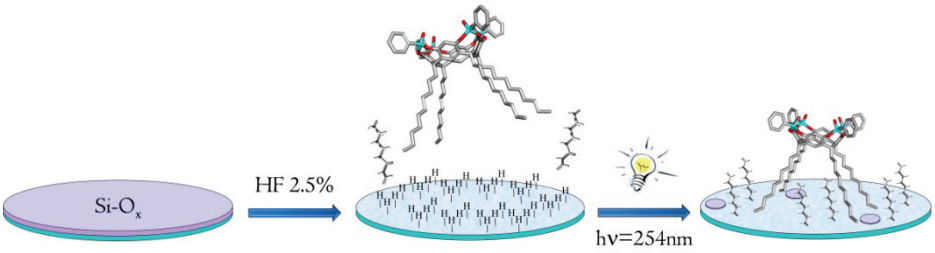

Figure 3.2. Surfaces functionalization protocol.

The surfaces functionalization was carried out in two subsequent steps: at first the H-terminated surfaces were prepared by etching the oxidized wafers with a 2.5% of an HF solution, followed by the functionalization with the cavitand via photochemical hydrosilylation (Figure 3.2).

The elemental surface distribution and the bonding states of the Si-T$_{iiii}$/Oct and Si-TS$_{iiii}$/Oct monolayers were characterized by XPS

analyses. Table 3.I compares the elemental compositions obtained at 10° takeoff angle of (a) a HF etched surface, (b) pure Si-T$_{iiii}$ monolayers, (c) mixed (χ=0.2) Si-T$_{iiii}$/Oct monolayers (d) pure Si-TS$_{iiii}$ monolayers, and (e) mixed (χ=0.2) Si-TS$_{iiii}$/Oct monolayers.

Surface	Si 2p	O Is	C Is	P 2p	S 2s
HF etched	77.0	7.8	15.2	-	-
Pure Si-T$_{iiii}$	15.0	17.3	65.0	2.7	-
Si-T$_{iiii}$/Oct χ = 0.2	15.9	16.0	61.2	2.0	-
Pure Si-TS$_{iiii}$	15.0	14.2	66.0	2.7	2.1
Si-TS$_{iiii}$/Oct χ = 0.2	12.5	9.4	74.3	2.1	**1.6**

Table 3.I. XPS atomic composition analysis of a) HF freshly etched surface, b) Pure Si-T$_{iiii}$ monolayers, c) Mixed (χ = 0.2) Si-T$_{iiii}$/Oct monolayers d) Pure Si-TS$_{iiii}$ monolayers, e) Mixed (χ = 0.2) Si-TS$_{iiii}$/Oct monolayers. Data are obtained at a 10° electron takeoff angle with respect to the sample surface.

These data reveal an enhancement of the C Is and O Is signals as compared to the freshly etched silicon surface. This enhancement, together with the observation of P 2p signal, and, for the Si-TS$_{iiii}$/Oct monolayers, an S 2s signal, indicates the presence of cavitand molecules on the silicon surface.

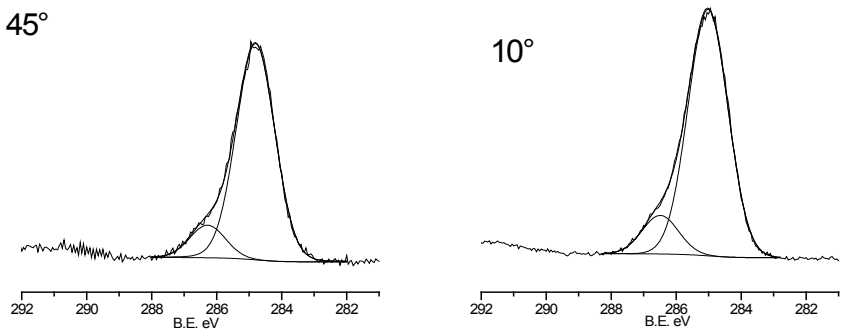

Figure 3.3. Typical high-resolution C 1s spectra from grafted cavitands at 45° take-off electron angle (left) and 10° takeoff electron angle (right).

The high resolution C 1s region (Figure 3.3) of Si-T$_{iiii}$ and Si-TS$_{iiii}$ grafted monolayers (pure and mixed) always included two main components:

(i) a C^0 component at 285.0 eV, due to the aliphatic and aromatic hydrocarbon backbone;[23,24,25]

(ii) a C^{1+} component at 286.4 eV, due to the aromatic carbons bearing the bridging oxygens of the resorcinarene skeleton.

No significant dependence of the intensity ratio of these components ($I_{C^{+1}}/I_{C^0}$) upon the electron takeoff angle has been observed in angular resolved XPS experiments. This is compatible with the position of the oxidized carbons between the aryl and alkyl moieties (both responsible of the C^0 signals) on the upper rim and the bottom feet of the cavitands, respectively (Scheme 3.1 and Figure 3.1). Moreover, one should note that additional contributions to these two components are always present due to adventitious hydrocarbons and the Si-O-C framework.[19]

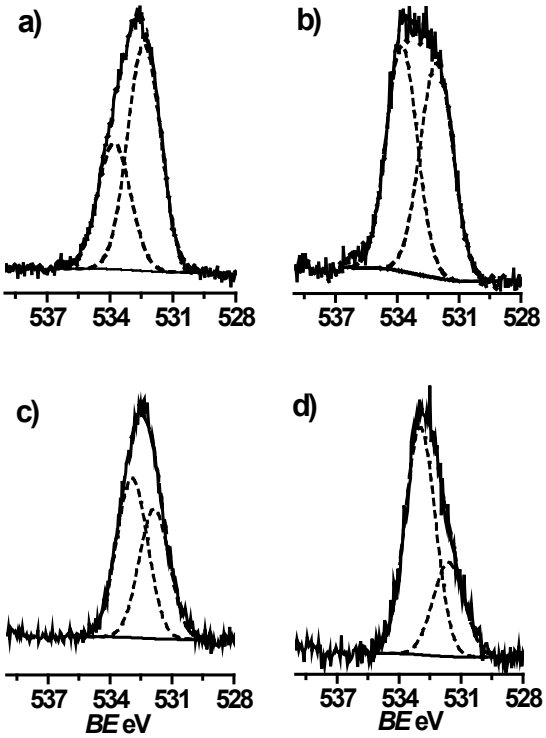

Figure 3.4. High-resolution O 1s spectra from pure Si-T$_{iiii}$. a) 45° electron takeoff angle, b) 10° electron takeoff angle, and from pure Si-TS$_{iiii}$. c) 45° electron takeoff angle d) 10° electron takeoff angle.

The O 1s band (Figure 3.4) of a pure silicon surface with covalently assembled Si-T_{iiii} monolayer consists of two main components centered at 533.5 eV (O_{cav}) and at 532.5 eV (O_{SiOx}). They are due to, respectively, phosphorus-bonded oxygen atoms of the cavitand and the SiO_x formed from partial oxidation of the substrate. As expected for a carbonaceous overlayer on the silicon substrate, the O_{SiOx} component decreases at low takeoff angles, while the O_{cav} component increases at low takeoff angles. This behaviour is consistent with the expected grafting of the cavitand feet on the silicon surface, leaving the P=O bridges at the upper rim significantly distant from the surface oxide. Similar trends are observed for the mixed Si-T_{iiii}/Oct monolayers and for the Si-TS_{iiii} analogues (Figure 3.4).

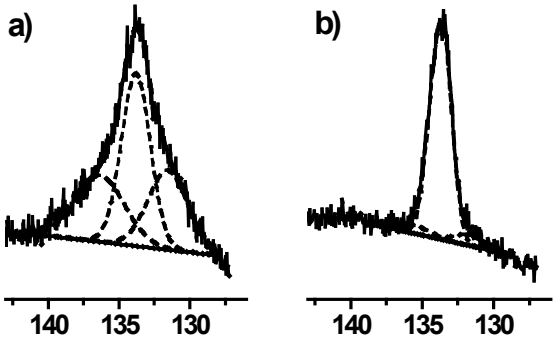

Figure 3.5. Typical angular dependence of high-resolution P 2p spectra from Si-T_{iiii} monolayer. a) 45° electron takeoff angle b) 10° electron takeoff angle. The tentative deconvolution reported in a) shows band overlapping.

The presence of the P 2p band is indicative of the presence of T_{iiii} and TS_{iiii} cavitands on the surface. In this context, a clear distinction of phosphorus on silicon signals is not trivial, as the 2p and 2s bands of the phosphorus nearly overlap with plasmon loss bands of the silicon. To obtain a clear spectrum and a rigorous quantification of the P concentration, it is necessary to acquire XPS measurements at low takeoff angles. In fact, the substrate plasmon loss contribution decreases at low takeoff electron angles and becomes negligible at 10° (Figure 3.5b).

In the XPS spectrum of Si-TS_{iiii}, along with the presence of the P 2p band (Figure 3.6a), the presence of S 2p and S 2s signals clearly demonstrates

the grafting of TS_{iiii}. Overall, the S 2s XPS region (Figure 3.6b) provides clearer information compared to the S 2p band, which partially overlaps with a plasmon loss band of the Si substrate.

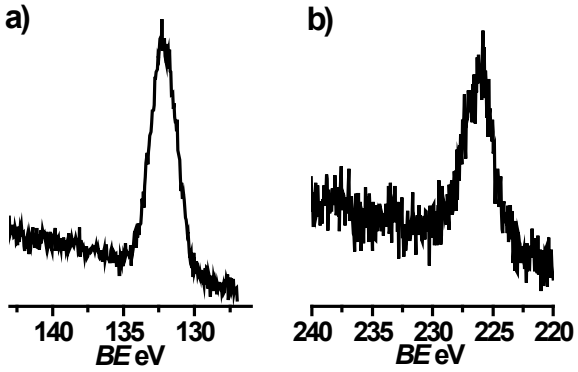

Figure 3.6. a) P 2p region and b) S 2s region from Si-TS_{iiii} monolayer at 10° electron takeoff angle.

The atomic ratio (P/O/C) of pure Si-T_{iiii} was inferred from the intensity of the P 2p signal obtained at a 10° takeoff angles, along with the O_{cav} component of the O 1s band and the C 1s signal (Table 3.1). The measured 1/3.1/24.1 ratio is very close to the theoretical value of 1/3/23 expected from the molecular structure. The analogous P/O/C ratio observed for mixed Si-T_{iiii} is more carbon-rich (1/3.2/30.7), as expected when grafting from a mixed T_{iiii} /Oct (χ=0.2) solution (solution atomic ratio: 1/3/31).

Similarly, the P/S/O/C ratios estimated by XPS for pure and mixed Si-TS_{iiii} (1/0.8/2.4/24.3 and 1/0.8/2.5/35.5, respectively) are consistent with the expected values calculated from pure TS_{iiii} (1/1/2/23) and from the mixed T_{iiii}/Oct (χ=0.2) grafting solution (1/1/2/31).

*3.2.4 Crystal Structure of the T_{iiii}[C_2H_5, H, Ph]@**22** Complex.*

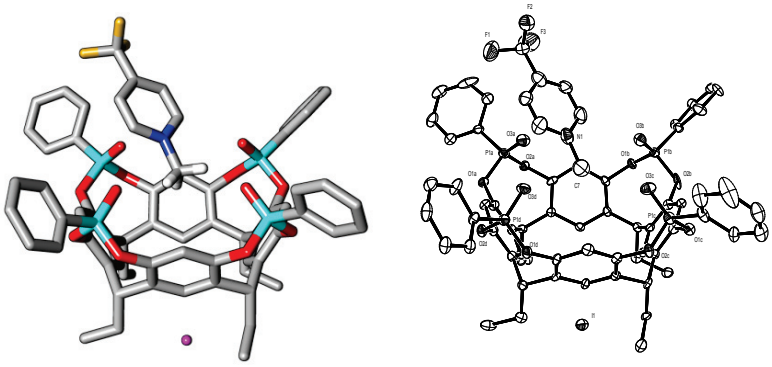

Figure 3.7. X-Ray structure of T_{iiii}[C_2H_5, H, Ph]@**22**. Ortep view (20% probability). Hydrogen atoms are omitted for clarity.

The reported crystal structure (Figure 3.7) reveals in the solid state the interaction modes between guest **22** and T_{iiii}[C_2H_5, H, Ph] (the short feet version of the grafted cavitand).

The inclusion of **22** into the cavity is driven by strong dipolar interactions between the positively charged nitrogen atom and the P=O groups of T_{iiii} (the shortest distance for P=O•••N^+ is 2.845(5) Å). Further stabilization is provided by a C-H•••π interaction between a methyl hydrogen of the cation and an aromatic ring of the cavity (the C-H•••centroid distance is of 3.575(2) Å, with an angle of 158.46(1)°).

The iodide counterion is located below the cavity at 1.904(1) Å from the least-squares plane defined by the four CH_2 carbons, roughly in the middle of the four alkyl chains at the lower rim. This position is stabilized by C-H•••I^- interactions with the CH_2 groups of the chains, which range in length from 3.077(1) to 3.246(1) Å. The distance between I^- and the positive nitrogen of the guest is of 8.743(6) Å. All the above values are in good agreement with previously reported findings in the literature.[26] This represents the optimal arrangement for the counterion in order both to stabilize the ion-pair and to experience aliphatic CH-anion interactions.

The localization of the iodide counterion is important not only for the stabilization of the complex in solution, but also for the surface complexation mode (as it will be discussed later in Subparagraph 3.2.6).

*3.2.5 Crystal Structure of the T_{iiii}[H, CH_3, Ph]@**9** Complex.*

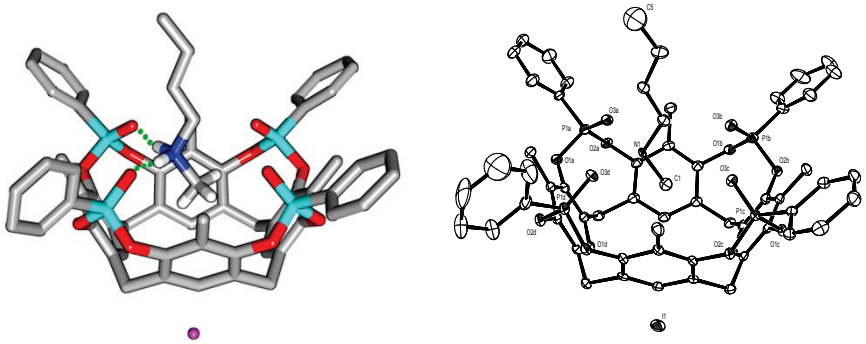

Figure 3.8. X-Ray structure of T_{iiii}[H, CH_3, Ph]@**9**. H-bonding is represented by green dots. Only the H atoms involved in interactions are shown. The solvent molecules and the second orientation of guest **9** are not shown. Ortep view (20% probability).

A second crystal structure was pursued to demonstrate the presence of H-bonding interactions between the tetraphosphonate cavitands and the secondary ammonium ions in the solid state. Solution (see Chapter 2) and gas phase[17] data already indicate that H-bonding interactions strongly enhance complexation in the case of protonated ammonium salts. However, structural evidence of the number and geometry of these H-bonding interactions is currently lacking. The crystal structure of T_{iiii}[H, CH_3, Ph]@**9** complex reported here fills this gap (Figure 3.8).

The cavitand receptor employed here does not bear alkyl chains at the lower rim. In the complex, two hydrogen bonds are present between adjacent P=O and the NH_2 protons (dotted green lines in Figure 3.8). The NH_2 moiety of the guest is disordered over two positions, each showing an occupancy factor of 0.5. This allows the formation of two sets of energetically and geometrically equivalent hydrogen bonds, which increase the entropic stabilization of the complex (see Experimental Section for details).

Further stabilization is provided by several C-H•••π interactions among the N-CH_3 hydrogens and the aromatic rings of the cavity (the C-H•••centroids distances span from 2.923(9) to 2.992(9) Å and the angles span from 136.6(3) to 147.4(4)°). Due to the disorder of the nitrogen, also the methyl hydrogens adopt two different orientations.

The iodide counterion is located below the cavity at 3.188(3) Å from the least-squares plane defined by the four CH_2 carbon atoms of the lower rim, roughly aligned with the cation in the cavity (in the T_{iiii}[C_2H_5, H, Ph]@**22** complex this value is 3.449(2) Å). This is the optimal position of the iodide counterion in the solid state, independent from the presence of alkyl chains at the lower rim. The distance between I^- and the disordered nitrogen atom of the guest is of 7.199(6) Å (N1) and of 7.269(9) Å (N1′). These values indicate that the guest in the T_{iiii}[H, CH_3, Ph]@**9** complex is located deeper within the cavity, with respect to the T_{iiii}[C_2H_5, H, Ph]]@**22** case, drawn in by the formation of the two H-bonds.

Therefore, the reported crystal structures validate the higher affinity of T_{iiii} cavitands for *N,N*-methylalkyl ammonium salts over methylpyridinium salts due to the presence, in the first case, of two H-bonding interactions that increase the stability of the complex.

3.2.6 Complexation on Si-surface: XPS Detection.

The affinity of the Si-T_{iiii} toward guests **22-25** was evaluated by XPS. The guests were specifically functionalized with three halogen atoms to allow XPS quantification. The Cl 2p and F 1s peaks were monitored as the main indicators of guest complexation; they have a significant advantage with respect to the other pyridinium bands (namely N 1s at 402 eV, and C 1s component at 289.6 eV) in that they are located in a less crowded spectral region and possess a higher intensity.

Complexation was performed by treating both mixed (χ = 0.2) Si-T_{iiii}/Oct (active sensing) and mixed (χ = 0.2) Si-TS_{iiii}/Oct (control experiment) substrates with guests **22-25** (10^{-3} M solution in CH_2Cl_2 for **22** and in CH_3CN for **24** and **25**).

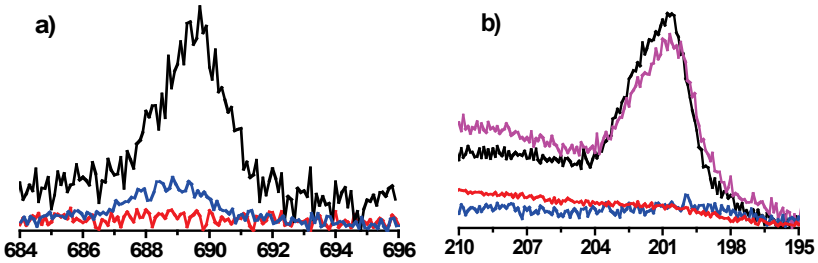

Figure 3.9. a) F 1s XPS region of Si-TS$_{iiii}$/Oct after complexation with guests **22** (red curve), Si-T$_{iiii}$/Oct before complexation (blue curve) and Si-T$_{iiii}$/Oct complexed with guest **22** (black curve); b) Cl 2p XPS regions of Si-TS$_{iiii}$/Oct after complexation with guests **24** and **25** (red curve), Si-T$_{iiii}$/Oct before complexation tests (blue curve); Si-T$_{iiii}$/Oct complexed with guest **24** (pink curve) and Si-T$_{iiii}$/Oct complexed with guest **25** (black curve).

Figure 3.9 compares the F 1s and the Cl 2p regions of mixed ($\chi = 0.2$) Si-T$_{iiii}$/Oct and Si-TS$_{iiii}$/Oct after the complexation reaction with either (a) guest **22** or (b) guests **24** and **25**. Precomplexation spectra are also reported for reference.

The presence of halogen bands in the Si-T$_{iiii}$/Oct grafted samples following exposure to the guests demonstrates surface complexation. At the same time, the absence of halogen signals for inert Si-TS$_{iiii}$/Oct precludes the possibility of physisorption, due to nonspecific interactions between the charged guest and the surface.

An interesting observation regards the role played by the counterions: in all cases, no significant signals were observed for the I^- and PF_6^- counterions. The kinetics of iodide disappearance on the surface was monitored via XPS for guest **24**. Immediately following exposure of the surface to the guest, the I 3d$_{5/2}$ signal was observed. After several minutes, however, the intensity of the signal began to decrease, disappearing entirely in about one hour (Figure 3.10 and 3.11).

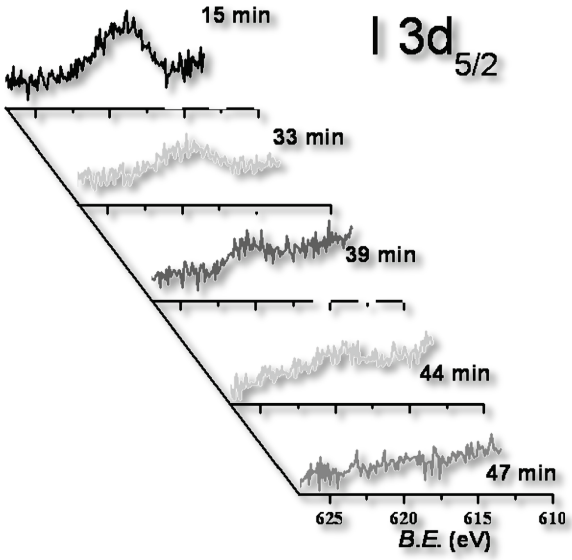

Figure 3.10. Evolution of the high-resolution I $3d_{5/2}$ spectra of Si-T$_{iiii}$@**24** samples as function of the permanence time in CH_3CN.

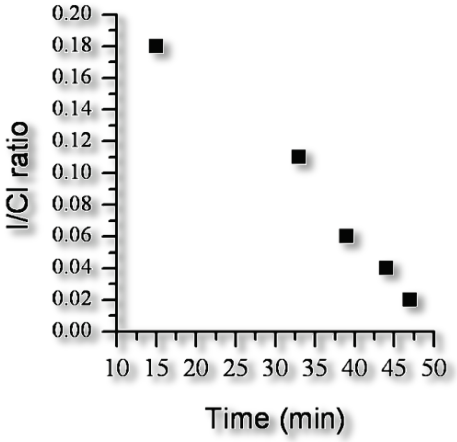

Figure 3.11. Dependence of the XPS I/Cl atomic ratio upon the permanence time of the Si-T$_{iiii}$@**24** samples in CH_3CN.

The counterions, positioned between the alkyl chains as indicated by the crystal structures, are sufficiently close to the surface to react with the residual Si-OH surface terminations. The reaction leads to the formation of HF plus PF_5 in the case of guest **25**, and HI in the case of guests **22** and **24**. These molecules are sufficiently volatile to escape from the surface. The Si-O^- terminations on the surface become the new counterions of the Si-T_{iiii} complexes, sufficiently close to the guest to stabilize the ion-pair (Figure 3.12). This anion replacement by a charged surface is unexpected and unprecedented.

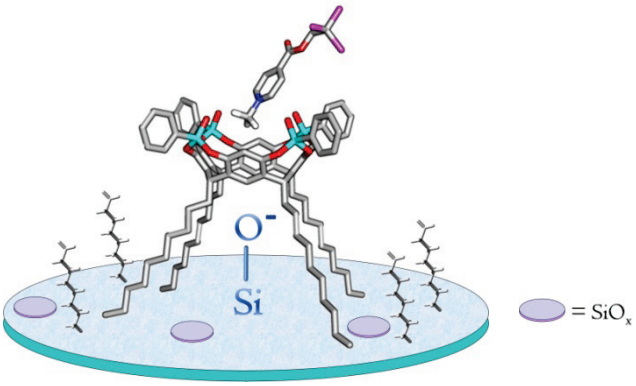

Figure 3.12. Proposed ion-pair formation for Si-T_{iii} complexes on the silicon surface.

XPS analyses allowed to estimate the efficiency of host-guest complexation. In this context, the chlorine-marked guests **24** and **25** are better probes than guest **22**, both to monitor the success of the complexation and to evaluate quantitatively its efficiency. This is due to the fact that the presence of chlorine, unlike fluorine, cannot be confused with contaminants resulting from the HF etching process. Given the 1:1 stoichiometry of all the complexes reported, the theoretical atomic ratio between P and Cl for the complexed species is 3/4. Hence, the efficiency of complexation (i.e., yield of the complex formed) on the surface can be calculated as follows:

$$Yield\ of\ complexation\ \% = \frac{\frac{\%Cl}{\%P}}{\frac{3}{4}} x100$$

The complexation yield was estimated in the range 60-70% for both guests **24** and **25**. Similar results were obtained for guest **26** (see next paragraph). No remarkable differences were observed by changing the solvent. The independence of surface complexation from both the guest and solvent nature, together the lower efficiency compared to solution data, suggests that the binding is related to the percentage of surface bonded cavitands whose cavity is available for complexation.

3.2.7 Complexation on Si-surface: Fluorescence Detection.

To confirm the complexation properties of Si-T$_{iiii}$/Oct silicon surface, we used a pyridinium salt connected to a pyrene probe via a diester tether. As already reported in Chapter 2, guest **8** has the peculiar property of activating the fluorescence emission of this pyrene probe upon complexation. This because the inclusion of the electron-poor methylpyridinium moiety within the electron-rich cavity of T$_{iiii}$ decreases the exoergonicity of the electron-transfer process from pyrene to the methylpyridinium unit, leading to a thirty-fold increase in fluorescence emission.

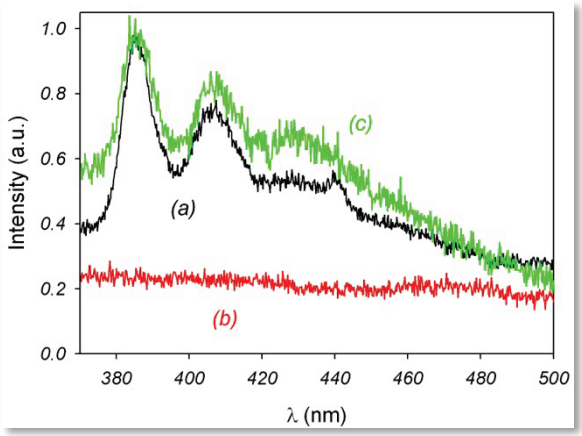

Figure 3.13. Fluorescence spectra of: a) Si-T$_{iiii}$/Oct surface after complexation test with guest **8**, b) after addition of the ammonium ion **9**, and c) after treatment with DBU and subsequent treatment with a solution of **8**. The spectrum resulting from a pristine Si-T$_{iiii}$/Oct surface is superimposable to curve b.

Figure 3.13 (curve a) shows the typical structure of the fluorescence band of the pyrene moiety with λ_{max} = 384 nm for the Si-T$_{iiii}$/Oct complexed with guest **8**. No signal is evident for Si-TS$_{iiii}$/Oct under the same conditions (curve b).

These data validate the XPS results, i.e. pyridinium salts are captured on the surface only in the presence of the T$_{iiii}$ cavities. Moreover, the absence of the excimeric band in spectra a) and c) indicates that the complexes on the surface are isolated and not clustered.

3.2.8 Molecular Recognition on Si-surface: Reversible Guest Exchange.

Considering the potential application of tetraphosphonate cavitand-decorated silicon surfaces as sensor elements in integrated devices, a fundamental issue to be addressed regards the capability of these systems to perform reversible guest exchange processes. The reversibility of the association process was tested by performing cyclic guest exchange between methylpyridinium and *N,N*-methylalkyl ammonium salts. The proposed complexation cycle replicates the one previously studied in solution, monitored via fluorescence spectroscopy (see Chapter 2).

XPS measurements were used to monitor the steps of this cycle, specifically by tracking the presence of the chlorine-marked guest **24** and the bromine marked guest **26**.

The Si-T$_{iiii}$/Oct@**24** surface (henceforth referred to as Si-T$_{iiii}$@**24**), was taken as the starting point of the cycle; it shows a prominent signal in the Cl 2p region (as described above) and, obviously, no signal in the Br 3d region (Figure 3.14a). After treatment of Si-T$_{iiii}$@**24** with a solution of guest **26** (10^{-3} M in CH_3CN), a negligible signal is present in the Cl 2p region, while the Br 3d region presents an evident Br 3d signal (Figure 3.14b).

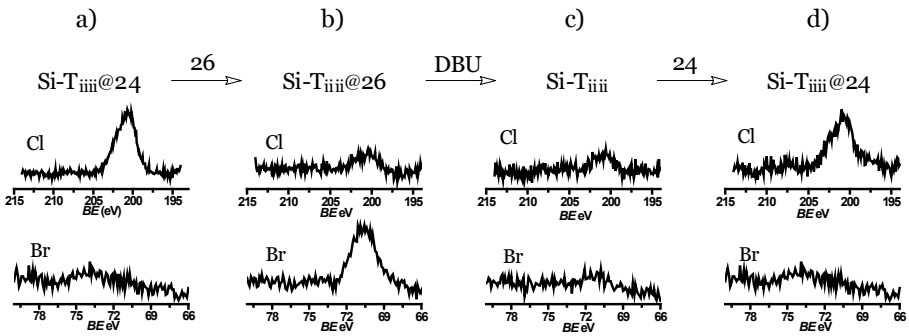

Figure 3.14. Cl 2p and Br 3d XPS region after treatment of the T_{iiii}-grafted silicon surface with a) a solution of guest **24**, b) a solution of guest **26**, c) a solution of DBU, and d) a solution of guest **24**, again.

These results are diagnostic of the exchange of the guest **24** with the guest **26** in the cavity of the tetraphosphonate cavitand, forming the Si-T_{iiii}@**26** system. On silicon, as in solution, the higher affinity of the guest **26** for tetraphosphonate cavitands[18] drives the exchange process. The obtained complexation yield expressed as:

$$Yield\ \% = \frac{\frac{\%Br}{\%P}}{\frac{1}{4}} x100$$

was similar (70%) to that calculated for guests **24** and **25**.

Treatment of the Si-T_{iiii}@**26** surface with a hindered Brønsted base (such as 1,8-diazabicyclo[5.4.0]undec-7-ene, DBU; 10^{-3} M in CH_3CN), led to complete removal of guest **26** from the surface, as demonstrated by the absence of both halogen signatures in Cl 2p and Br 3d regions (Figure 3.14c).

DBU, by extracting a proton from guest **26**, induces the dissociation of the Si-T_{iiii}@**26** complex, restoring the pristine Si-T_{iiii} surface. Exposure of the resulting Si-T_{iiii} surface to a solution of guest **24** led to the original Si-T_{iiii}@**24** complex (Figure 3.14d). Figure 3.15 illustrates the fully reversible cycle consisting of (i) the complexation of the guest **24**, (ii) the exchange of **24** with the protonated guest **26**, and (iii) the regeneration of the original surface by removal of guest **26** with DBU.

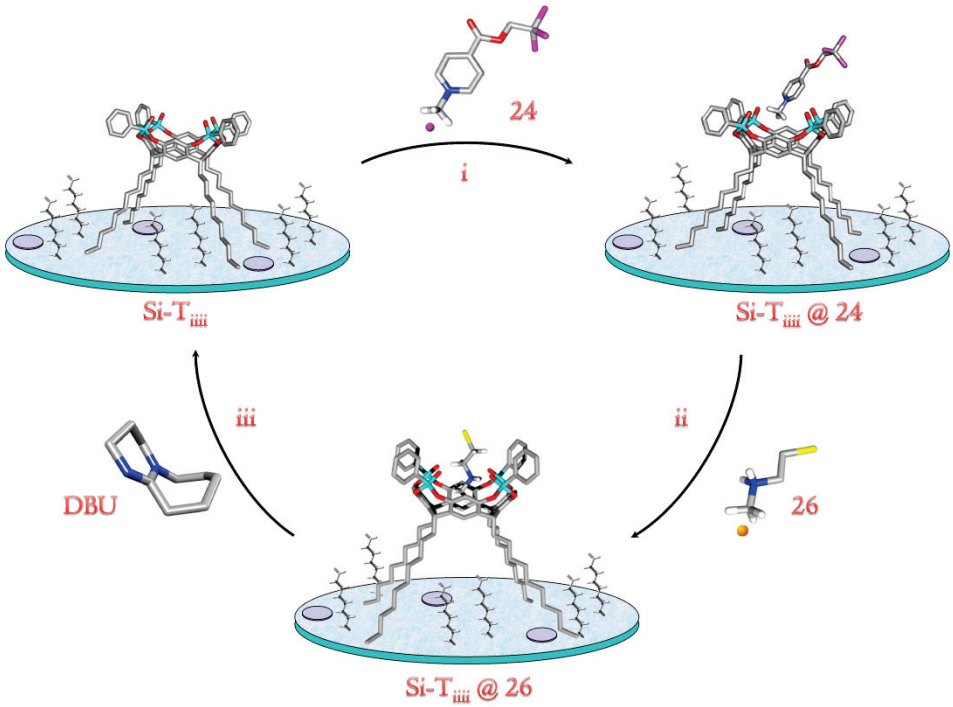

Figure 3.15. Complexation cycle of Si-T$_{iiii}$, as monitored by XPS. The Si-O$^-$ counterions are omitted for clarity.

The same complexation cycle was monitored by fluorescence spectroscopy using guests **8** and **9**, respectively (Figure 3.16). In this case, the addition of the guest **9** to the Si-T$_{iiii}$@**8** system (Figure 3.13, curve a) led to the complete disappearance of the fluorescence signal on the surface, due to the formation of fluorescence silent complex Si-T$_{iiii}$@**9** (Figure 3.13, curve b).

Addition of DBU, followed by the treatment of the silicon surface with a solution of **8**, restored the initial fluorescent Si-T$_{iiii}$@**8** complex (Figure 3.13, curve c).

The combination of XPS and fluorescence spectroscopy provides a consistent and reliable picture of the three consecutive recognition steps (complexation, guest exchange, and decomplexation) occurring on the surface of a Si-T$_{iiii}$ wafer.

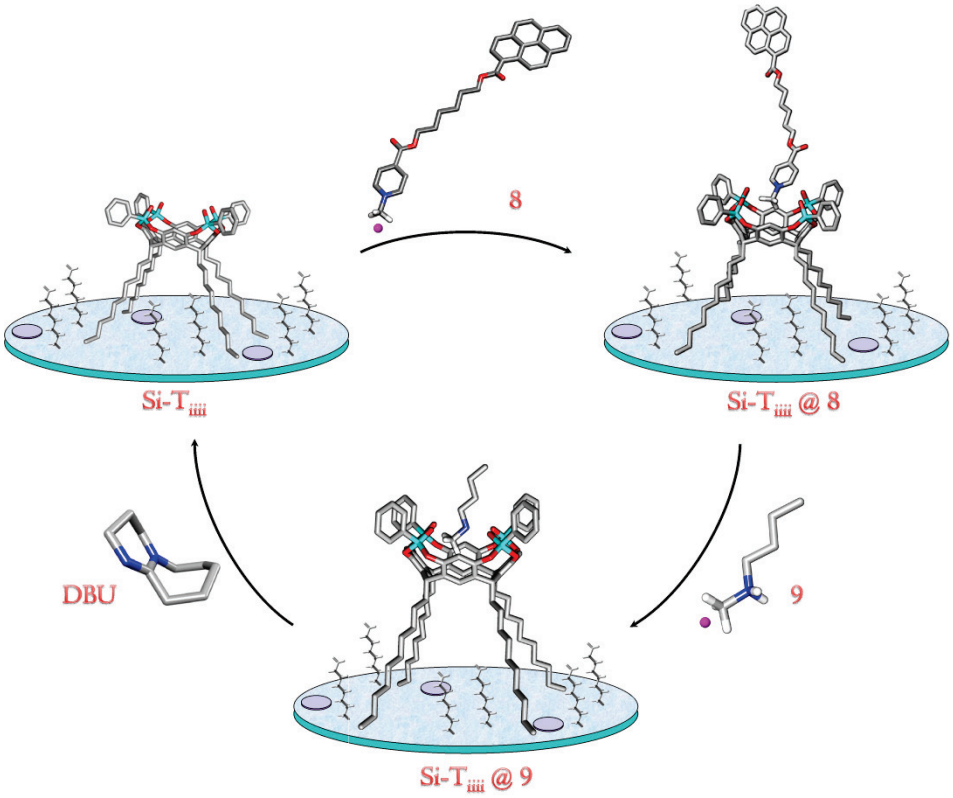

Figure 3.16. Complexation cycle of Si-T$_{iiii}$, as monitored by fluorescence. The Si-O$^-$ counterions are omitted for clarity.

3.3 Conclusions.

In this chapter, we have described the preparation, characterization, and molecular recognition properties of a functional surface featuring phosphonate cavitands as receptors. The relevant findings can be summarized as follows: (i) The photochemical hydrosilylation protocol is compatible with the presence of P=O/P=S bridging units on the cavitands, allowing the formation of both pure and mixed monolayers on the silicon surface. The mixed monolayers improve the coverage of the surface, minimizing substrate oxidation. (ii) The noteworthy molecular recognition properties of this class of synthetic receptors were successfully transferred to a technologically relevant silicon platform. (iii) The preferential positioning of the counterions between the alkyl chains at the lower rim allows for their replacement by the $Si\text{-}O^-$ groups generated on the surface.

A unique feature of this study has been the possibility to record independent sets of measurements by monitoring the surface complexation experiments with two different techniques, namely XPS and fluorescence spectroscopy. The resulting cross validation provides a highly reliable, comprehensive picture of the complexation cycle on the Si-T_{iiii} surface. Moreover, control experiments with the structurally similar, but complexation inactive, Si-TS_{iiii} surface excluded the possibility of nonspecific interactions between the substrate and the guests.

The sequence complexation-guest exchange-decomplexation demonstrated that all three interaction modes of the host available for complexation are operative on the silicon surface without interference. In particular, the two additional H-bonds experienced by guests **26** and **9** upon complexation, inferred from the crystal structure, are sufficient to induce the complete guest exchange on the Si-T_{iiii} surface. Removal of these guests by deprotonation resets the original surface cleanly and efficiently.

Besides sensing[16] and synthetic applications,[27] the functional surface described in this work represents a useful addition to the available pool of molecular printboards for the self-assembly of complex supramolecular architectures on surfaces.[6]

3.4 Acknowledgements.

Special thanks to Prof. Guido Condorelli and Dr. Maria Favazza of the University of Catania for the experiments and XPS analyses on surfaces, and Prof. Luca Prodi, Dr. Marco Montalti and Dr. Gionata Battistini of the University of Bologna for the Fluorescence experiments.

3.5 Experimental Section.

3.5.1 Reagent, Chemicals and Instruments used.

All commercial reagent were ACS reagent grade and used as received. For the synthesis all solvents were dried and distilled using standard procedures.

♣ Chromatography was performed using 70-230 mesh silica purchased from Merck and 40-120 μ Sephadex G-10 purchased from Pharmacia Fine Chemicals. Thin layer chromatography was performed on Kieselgel 60 F_{254} and Uniplate^{tm} Silica Gel GF silica-coated glass plates and visualized by UV.

♣ ^{1}H NMR and spectra were recorded on Bruker 300 (300 MHz), Bruker Avance 300 (300 MHz) and Varian INOVA 600 (600 MHz).spectrometers and all chemical shifts (δ) were reported in parts per million (ppm) relative to proton resonances resulting from incomplete deuteration of NMR solvents. ^{31}P NMR spectra were recorded on AMX-400 (162 MHz) and all chemical shifts were reported to external 85% H_3PO_3 at 0 ppm.

♣ ESI-MS characterization experiments were performed on a Waters ACQUILITY SQD Detector equipped with a ESCi® multi mode ionization (APCI/ESI).

3.5.2 Crystal Structures.

The crystal structure of the complexes $T^{iii}[C_2H_5, H, Ph]$@**22** and $T^{iii}[H, CH_3, Ph]$@**9** were determined by single crystal X-ray diffraction methods. Crystallographic and experimental details for the structures are summarized in Table 3.2.

Intensity data and cell parameters were recorded at room temperature for $T^{iii}[C_2H_5, H, Ph]$@**22** and at 173 K for $T^{iii}[H, CH_3, Ph]$@**9** on a Bruker AXS Smart 1000 single-crystal diffractometer, equipped with a CCD area detector using graphite monochromated Mo K_α radiation.

The structures were solved by direct methods using the SIR97 program[28] and refined on F_o^2 by full-matrix leastsquares procedures, using the SHELXL-97 program.[29] Both programs were used in the WinGX suite.[30]

The data reduction was performed using the SAINT[31] and SADABS[32] programs.

The PLATON SQUEEZE procedure[33] was used to treat regions of diffuse solvent which could not be sensibly modeled in terms of atomic sites. Their contribution to the diffraction pattern was removed and modified F_o^2 written to a new HKL file. The number of electrons thus located, 191 per unit cell, are included in the formula, formula weight, calculated density, μ and $F(000)$. This residual electron density was assigned to six molecules of acetone solvent per unit cell (six molecules of acetone would give 192 e).

All the non-hydrogen atoms were refined with anisotropic atomic displacements, with the exclusion of one of the fluorine atoms of the guest **22**, of two carbon atoms of the guest **9** and of one carbon atom of the phenyl group in the T_{iiii}[H, CH_3, Ph] host. The hydrogen atoms were included in the refinement at idealized geometries (C-H 0.95 Å) and refined "riding" on the corresponding parent atoms.

In the guest **9**, the nitrogen atom was found disordered over two positions, each showing an occupancy factor of 0.5. The weighting scheme used in the last cycle of refinement was:

$$w = \frac{1}{[\sigma^2 F_o^2 + (0.0865P)^2 + 0.7176P]}$$

and

$$w = \frac{1}{[\sigma^2 F_o^2 + (0.0927P)^2]}$$

where

$$P = \frac{(F_o^2 + 2F_c^2)}{3}$$

for T_{iiii}[C_2H_5, H, Ph]@**22** and T_{iiii}[H, CH_3, Ph]@**9**, respectively.

CCDC-731069 and -731070 contain the supplementary crystallographic data. These data can be obtained free of charge at www.ccdc.cam.ac.uk/conts/retrieving.html [or from the Cambridge Crystallographic Data Centre, 12 Union Road, Cambridge CB2 1EZ, UK; Fax: +44-1223/336-033]. Geometric calculations were performed with the PARST97 program.[34]

	T$_{iii}$[C$_2$H$_5$, H, Ph]@22	**T$_{iii}$[H, CH$_3$, Ph]@9**
Formula	$C_{67}H_{59}F_3INO_{12}P_4$	$C_{73}H_{82}INO_{16}P_4$
Formula weight	1378.0	1480.2
Crystal system	Triclinic	Triclinic
Space group	*P*-1	*P*-1
a/Å	13.653(4)	15.313(3)
b/Å	14.230(4)	16.539(4)
c/Å	17.518(5)	16.677(4)
α/°	77.440(4)	67.754(4)
β/°	86.604(4)	68.076(4)
γ/°	89.381(4)	85.881(4)
V/ Å^3	3316(1)	3615(1)
Z	2	2
D_c/g cm^{-3}	1.380	1.360
F(000)	1408	1536
μ/mm^{-1}	0.648	0.598
$\theta_{min, max}$/°	2.89, 26.61	1.33, 27.59
Reflections collected	29032	44133
Independent reflections	12291 [R(int)=0.0182]	16510 [R(int)=0.0753]
Observed reflections	8821	8571
Data/restr./param.	12291 / 0 / 797	16510 / 0 / 734
R [F_o>4σ(F_o)][a], $wR2$[a]	0.0468, 0.1403	0.0751, 0.1825
$\Delta\rho_{min, max}$/e Å^{-3}	1.606, -0.575	2.852, -0.845
S[b]	1.029	1.011

[a] $R_1 = \sum||Fo|-|Fc||/\sum|Fo|$, $wR_2 = [\sum w(Fo^2-Fc^2)^2/]\sum wFo^4]^{1/2}$. [b] Goodness-of-fit $S = [\sum w(Fo^2-Fc^2)^2/(n-p)]^{1/2}$, where n is the number of reflections and p the number of parameters.

Table 3.2. Crystallographic data and refinement details for T$_{iii}$[C$_2$H$_5$, H, Ph]@**22** and for T$_{iii}$[H, CH$_3$, Ph]@**9**.

List of the hydrogen bonds activated by guest **9** interacting with the host.

- Orientation I (see Figure 3.8):
  P=O3A•••N1 2.795(8) Å, O3A•••H1E-N1 169.5(5)°; P=O3D•••N1 2.916(9) Å, O3D•••H1F-N1 169.7(5)°.
- Orientation 2 (not shown):
  P=O3A•••N1' 2.785(9) Å, O3A•••H1H-N1' 170.1(8)°, P=O3B•••N1' 2.980(9) Å, O3B•••H1G-N1' 173.1(8)°.

3.5.3 Cavitand Grafting on Si.

For grafting monolayers, pure cavitand (χ_{cav} = 1.0) and cavitand/1-octene mixtures (χ_{cav}=0.2) were dissolved in mesitylene (solution concentration = 0.05 M). Cavitand solutions (2.0 mL) were placed in a quartz cell and deoxygenated by stirring in a drybox for at least 1 h. A Si(100) substrate was dipped in H_2SO_4/H_2O_2 (3:1) solution for 12 min to remove organic contaminants, then it was etched in a hydrofluoric acid solution (1% v/v) for 90 s and quickly rinsed with water. The resulting hydrogenated silicon substrate was immediately placed in the mesitylene solution. The cell remained under UV irradiation (254 nm) for two hours. The sample was then removed from the solution and sonicated in dichloromethane for 10 min to remove residual physisorbed material.

3.5.4 Cavitand Complexation Tests.

To test the complexation properties of Si-T_{iiii} and Si-TS_{iiii}, samples were dipped in a solution 10^{-3} M of guests **22**-**9** in CH_3CN for 30 min and then sonicated in CH_3CN for 10 min. The same treatment was followed for the DBU decomplexation.

3.5.5 XPS Characterizations.

The XPS spectra were run with a PHI ESCA/SAM 5600 Multy technique spectrometer equipped with a monochromated Al K_α X-ray source,

a standard dual-anode Mg/Al source and a spherical capacitor analyzer (SCA) with a mean diameter of 279.4 mm. The analyses were carried out at various photoelectron angles (relative to the sample surface) in the 10°-80° range with an acceptance angle of ±7° (the acceptance angle was fixed high to avoid photoelectron diffraction effects).

Atomic concentrations have been evaluated from the intensity of both standard Mg and monochromatic Al spectra after removing of a Shirley background and correction for the Wagner sensitivity factors.[35] All high-resolution XPS spectra were recorded adopting only monochromatic Al radiation. Experimental uncertainties in binding energies lie within ±0.28 eV.[36] Some spectra were deconvoluted by fitting the spectral profiles with a series of symmetrical Gaussian envelopes after subtraction of the background.

The agreement factor R, reported below, after minimization of the function $\Sigma(F_o - F_c)^2$ converged to R values ≤0.04. XPS B.E. scale was calibrated by centering the C 1s peak of the adventitious carbon at 285.0 eV.[37,38]

$$R = \left[\frac{\sum(F_0 - F_c)^2}{\sum - F_0^2}\right]^{1/2}$$

3.5.6 Fluorescence Measurements.

Fluorescence spectra on Si-T$_{iiii}$ and Si-TS$_{iiii}$ surfaces were obtained using a spectrofluorimeter ISA FLUOROLOG 3 in a front-face geometry, with a He-Cd continuum laser at 325 nm, 50 mW power, as excitation source.

3.5.7 Synthetic Protocol.

1-methyl-4-((6-(pyrene-1-carbonyloxy)hexyloxy)carbonyl)pyridinium hexafluorophosphate. (8)

The synthesis of guest **8** was already reported in Chapter 2 (Subparagraph 2.7.6).

N-methylbutyl-1-ammonium iodide (9)

The synthesis of guest **9** was already reported in Chapter 2 (Subparagraph 2.7.6).

Resorcinarene Res[$C_{10}H_{19}$, H]. (15)

Resorcinarene **15** was prepared following a published procedure.[39]

Cavitand T_{iiii}[$C_{10}H_{19}$, H, Ph]. (16)

Cavitand T_{iiii}[$C_{10}H_{19}$, H, Ph] was prepared following a published procedure.[40]

Cavitand TS_{iiii}[$C_{10}H_{19}$, H, Ph]. (17)

To a solution of Res[$C_{10}H_{19}$, H]. (**15**) (3 g, 2.88 mmol) in 80 mL of freshly distilled pyridine, dichlorophenylphosphine (1.56 mL, 11.5 mmol) was added slowly, at room temperature. After stirring for 3 hours at 80 °C, S_8 (0.59 g, 2.30 mmol) was added and the mixture was stirred again for 2 hours. The solvent was removed under vacuum and the crude was purified by column chromatography on silica gel by using CH_2Cl_2/hexane (9/1) as eluant to give the product in 52% yield.

^{1}H NMR: ($CDCl_3$, 300 MHz) δ (ppm): 8.15 (dd, 8H, POArH_o), 7.52 (m, 4H+8H, POArH_p + POArH_m), 7.28 (s, 4H, ArH_{down}), 6.66 (s, 4H, ArH_{up}), 5.90-5.78 (m, 4H, CH_2=CH_2), 5.02-4.91 (m, 8H, CH_2=CH_2), 4.74 (t, 4H, J=7.2 Hz, CH_{bridge}), 2.36-2.30 (m, 8H, CH_2(CH_2)$_7$CH=CH_2), 2.07-2.01 (m, 8H, C$H_2$$CH_2$=$CH_2$), 1.43-1.33 (m, 48H, CH_2(CH_2)$_7$CH=CH_2). **^{31}P NMR:** ($CDCl_3$, 162 MHz) δ (ppm): 79.87 (s, 4P, *P*SPh). **ESI-MS:** m/z 1629.55 $[M+K]^+$.

Resorcinarene Res[C_2H_5, H]. (18)

Resorcinarene **18** was prepared following a published procedure.[41]

Cavitand T_{iiii}[C_2H_5, H, Ph]. (19)

To a solution of Res[C_2H_5, H] (**18**) (1.5 g, 2.50 mmol) in 50 mL of freshly distilled pyridine, dichlorophenylphosphine (1.45 mL, 10.63 mmol) was added slowly, at room temperature. After 3 hours of stirring at 80 °C,

the solution was allowed to cool at room temperature and 10 mL of a mixture of 35% H_2O_2 and $CHCl_3$ (1:1) was added. The resulting mixture was stirred for 30 minutes at room temperature, then the solvent was removed under reduced pressure and water added. The precipitate obtained in this way was collected by vacuum filtration, and purified by re-crystallization (H_2O: diethyl ether 8:2) to give the desired product in 93% yield.

^{1}H NMR: ($CDCl_3$, 300 MHz): δ (ppm): 8.17 (m, 8H, POArH_o), 7.56 (m, 4H, POArH_p), 7.51 (m, 8H, POArH_m), 7.30 (s, 4H, ArH_{down}), 6.67 (s, 4H, ArH_{up}), 4.64 (t, 4H, J=7.9 Hz, ArCH), 2.39 (m, 8H, CH_2CH$_3$), 1.06 (t, 12H, J=6.8, CH$_2$CH_3). **^{31}P NMR** ($CDCl_3$, 162 MHz) δ (ppm): 4.45 (s, 4P, *P*OPh). **ESI-MS:** m/z 1089.34 $[M+H]^+$.

Resorcinarene Res[H, CH_3]. (20)

Resorcinarene **20** was prepared following a published procedure.[42]

Cavitand T$_{iiii}$[H, CH_3, Ph]. (21)

Cavitand T$_{iiii}$[H, CH_3, Ph] was prepared following a published procedure.[10]

1-methyl-4-(trifluoromethyl)pyridinium iodide. (22)

Guest **22** was prepared following a published procedure.[43]

2,2,2-trichloroethyl isonicotinate. (23)

To a solution of isonicotinoyl chloride (200 mg, 1.123 mmol) dissolved in 10 mL of pyridine, 2,2,2-trichloroethanol (216 µl, 2.247 mmol) was added. The solution was stirred at 100°C for 3 hours. The crude was extracted with water and CH_2Cl_2, the organic phase was dried under vacuum to give compound (**23**) in 79% yield.

^{1}H NMR: ($CDCl_3$, 300 MHz) δ (ppm): 8.78 (d, 2H, J=5.7 Hz, PyH_o), 7.87 (d, 2H, J=5.7 Hz, PyH_m), 4.93 (s, 2H, OCH_2CCl$_3$). **ESI-MS:** m/z 254.95 $[M+H]^+$.

1-methyl-4-((2,2,2-trichloroethoxy)carbonyl)pyridinium iodide. (24)

Iodomethane (274 μl, 4.4 mmol) was added to a solution of compound **23** (224 mg, 0.88 mmol) dissolved in 5 mL of CH_3CN. The solution was refluxed overnight, then the solvent was removed to give the desired salt in 94% yield.

^{1}H NMR: (CD_3CN, 300 MHz) δ (ppm): 8.91 (d, 2H, J=6.3 Hz, PyH_o), 8.48 (d, 2H, J=6.3 Hz, PyH_m), 5.12 (s, 2H, OCH_2CCl$_3$), 4.40 (s, 3H, PyCH_3). **ESI-MS:** m/z 268.9 $[M\text{-}I]^+$.

1-methyl-4-((2,2,2-trichloroethoxy)carbonyl)pyridinium hexafluorophosphate. (25)

To a solution of guest **24** (150 mg, 0.378 mmol) dissolved in 2 mL of CH_3OH and 1 mL of water, NH_4PF_6 (123 mg, 0.756 mmol) was added. The solution was stirred at room temperature overnight, then the solvent was removed and the product was precipitate in CH_3OH/H_2O to give compound **25** in quantitative yield.

^{1}H NMR: (CD_3OD, 300 MHz) δ (ppm): 9.04 (d, 2H, J=6.3 Hz, PyH_o), 8.48 (d, 2H, J=6.3 Hz, PyH_m), 4.46 (s, 3H, PyCH_3), 4.05 (s, 2H, OCH_2CCl$_3$). **^{31}P NMR**: (CD_3OD, 162 MHz) δ (ppm): -144.06 (m, $J_{P\text{-}F}$=707 Hz, PF_6). **ESI-MS:** m/z 268.9 $[M\text{-}PF_6]^+$.

N,N-methyl(2-bromo-ethyl)ammonium bromide. (26)

To a solution of 2-(methylamino)ethanol (2.13 ml, 0.027 mol) in 10 mL of toluene and a catalytic amount of DMF, thionyl bromide (6.19 ml, 0.080 mol) was added drop by drop. The solution was stirred at 50°C for 8 hours and then dried to give the desired product in quantitative yield.

^{1}H NMR: (DMSO-d_6, 300 MHz) δ (ppm): 8.81 (m, 2H, NH_2), 3.72 (t, 2H, J=6.5 Hz, RCH_2Br), 3.36 (m, 2H, $NH_2C\mathit{H}_2CH_2Br$), 2.57 (t, 3H, J=5.5 Hz, $NH_2C\mathit{H}_3$). **ESI-MS:** m/z 137.8 $[M\text{-}Br]^+$.

3.6 References.

[1] (a) H. Y. Erbil, A. L. Demirel, Y. Avci, O. Mert, Transformation of a Simple Plastic into a Superhydrophobic Surface, *Science* **2003**, *299*, 1377-1380.
(b) X.-M. Li, D. N. Reinhoudt, M. Crego-Calamata, What do we need for a superhydrophobic surface? A review on the recent progress in the preparation of superhydrophobic surfaces, *Chem. Soc. Rev.* **2007**, *36*, 1350-1368.

[2] L. Qu, L. Dai, M. Stone, Z. Xia, Z. L. Wang, Carbon Nanotube Arrays with Strong Shear Binding-On and Easy Normal Lifting-Off, *Science* **2008**, *322*, 238-242.

[3] J. Lahann, S. Mitragotri, T.N. Tran, H. Kaido, J. Sundaram, I. S. Choi, S. Hoffer, G. A. Somorjai, R. Langer, A reversibly switching surface, *Science* **2003**, *299*, 371-374.

[4] J. E. Green, J. W. Choi, A. Boukai, Y. Bunimovich, E. Johnston- Halperin, E. DeIonno, Y. Luo, B. A. Sheriff, K. Xu, Y. S. Shin, H.-R. Tseng, J. F. Stoddart, J. R. Heath, A 160-kilobit molecular electronic memory patterned at 1011 bits per square centimeter, *Nature* **2007**, *445*, 414-417.

[5] M. Mammen, S.-K. Choi, G. M. Whitesides, Polyvalent interactions in biological systems: implications for design and use of multivalent ligands and inhibitors, *Angew Chem., Int. Ed.* **1998**, *37*, 2755-2794.

[6] (a) M. J. W. Ludden, D. N. Reinhoudt, J. Huskens, Molecular printboards: versatile platforms for the creation and positioning of supramolecular assemblies and materials, *Chem. Soc. Rev.* **2006**, *35*, 1122-1134.
(b) M. J. W. Ludden, A. Mulder, R. Tampe, D. N. Reinhoudt, J. Huskens, Molecular printboards as a general platform for protein immobilization: a supramolecular solution to nonspecific adsorption, *Angew. Chem., Int. Ed.* **2007**, *46*, 4104-4107.

[7] a) J. J. Lavigne, E. V. Anslyn, Sensing a paradigm shift in the field of molecular recognition: from selective to differential receptors, *Angew. Chem., Int. Ed.* **2001**, *40*, 3118-3130.
b) L. Pirondini, E. Dalcanale, Molecular recognition at the gas-solid interface: a powerful tool for chemical sensing, *Chem. Soc. Rev.* **2007**, *36*, 695-706.

[8] a) M. Dubey, S. L. Bernasek, J. J. Schwartz, Highly Sensitive Nitric Oxide Detection Using X-ray Photoelectron Spectroscopy, *J. Am. Chem. Soc.* **2007**, *129*, 6980-6981.
b) S. Zhang, C. M. Cardona, L. Echegoyen, Ion recognition properties of self-assembled monolayers (SAMs), *Chem. Commun.* **2006**, 4461-4473.

c) A. Facchetti, E. Annoni, L. Beverina, M. Morone, P. Zhu, T. J. Marks, G. A. Pagani, Very large electro-optic responses in H-bonded heteroaromatic films grown by physical vapour deposition, *Nat. Mater.* **2004**, *3*, 910-917.
d) Z. Liu, A. A. Yasseri, J. S. Lindsey, D. F. Bocian, Molecular Memories That Survive Silicon Device Processing and Real-World Operation, *Science* **2003**, *302*, 1543-1545.
e) M. Altman, A. D. Shukla, T. Zubkov, G. Evmenenko, P. Dutta, M. E. van der Boom, Controlling structure from the bottom-up: structural and optical properties of layer-by-Layer assembled palladium coordination-based multilayers, *J. Am. Chem. Soc.* **2006**, *128*, 7374-7382.
f) T. Gupta, M. E. van der Boom, Optical sensing of parts per million levels of water in organic solvents using redox-active osmium chromophore-based monolayers, *J. Am. Chem. Soc.* **2006**, *128*, 8400-8401.

[9] a) A. B. Descalzo, R. Martìnez-Màòez, F. Sancenòn, K. Hoffmann, K. Rurack, The supramolecular chemistry of organic-inorganic hybrid materials, *Angew. Chem., Int. Ed.* **2006**, *45*, 5924-5948.
b) C. Lagrost, G. Alcaraz, J.-F. Bergamini, B. Fabre, I. Serbanescu, Functionalization of silicon surfaces with Si-C linked β-cyclodextrin monolayers, *Chem. Commun.* **2007**, 1050-1052.

[10] For a clearly defined example of the influence of non specific interactions on the sensing performances of cavitand layers see: M. Tonezzer, M. Melegari, G. Maggioni, R. Milan, G. Della Mea, E. Dalcanale, Vacuum-evaporated cavitand sensors: Dissecting specific from nonspecific interactions in ethanol detection, *Chem. Mater.* **2008**, *20*, 6535-6542.

[11] a) J.-P. Dutasta, New phosphorylated hosts for the design of new supramolecular assemblies, *Top. Curr. Chem.* **2004**, *232*, 55-91.
b) R. Pinalli, M. Suman, E. Dalcanale, Cavitands at work: From molecular recognition to supramolecular sensors, *Eur. J. Org. Chem.* **2004**, 451-462.
c) E. E. Nifantyev, V. I. Maslennikova, R. V. Merkulov, Design and Study of Phosphocavitands-A New Family of Cavity Systems, *Acc. Chem. Res.* **2005**, *38*, 108-116.
d) R. J. Puddephatt, Montreal Medal Award Lecture - Coordination chemistry of molecular bowls: Ligands and their complexes derived from resorcinarenes, *Can. J. Chem.* **2006**, *84*, 1505-1514.

[12] a) T. Lippmann, G. Mann, E. Dalcanale, Synthesis and configurational analysis of phosphorus bridged cavitands, *Tetrahedron Lett.* **1994**, *35*, 1685-1688.
b) T. Lippmann, H. Wilde, E. Dalcanale, L. Mavilla, G. Mann; U. Heyer, S. Spera, Synthesis and Configurational Analysis of a Novel Class of Cavitands Containing Four Dioxaphosphocin Moieties, *J. Org. Chem.* **1995**, *60*, 235-242.

[13] P. Delangle, J.-P. Dutasta, Tetraphosphonate-calix[4]resorcinarene. A powerful host for alkali metal and ammonium cations encapsulation, *Tetrahedron Lett.* **1995**, *36*, 9325-9328.

[14] P. Delangle, J.-C. Mulatier, B. Tinant, J.-P. Declercq, J.-P. Dutasta, Synthesis and binding properties of iiii (4i) stereoisomers of phosphonato cavitands - cooperative effects in cation complexation in organic solvents, *Eur. J. Org. Chem.* **2001**, 3695-3704.

[15] R. De Zorzi, B. Dubessy, J.-C. Mulatier, S. Geremia, L. Randaccio, J.-P. Dutasta, Structure of a 4:1:4 Supramolecular Assembly of Neutral TiiiiPO Cavitands and Tetrakis(N-methylpyridinium)porphyrin Iodide, *J. Org. Chem.* **2007**, *72*, 4528-4531.

[16] M. Melegari, M. Suman, L. Pirondini, D. Moiani, C. Massera, F. Ugozzoli, E. Kalenius, P. Vainiotalo, J.-C. Mulatier, J.-P. Dutasta, E. Dalcanale, Supramolecular sensing with phosphonate cavitands, *Chem.-Eur. J.* **2008**, *14*, 5772-5779.

[17] E. Kalenius, D. Moiani, E. Dalcanale, P. Vainiotalo, Measuring H-bonding in supramolecular complexes by gas phase ion-molecule reactions, *Chem. Commun.* **2007**, 3865-3867.

[18] R. M. Yebeutchou, F. Tancini, N. Demitri, S. Geremia, R. Mendichi, E. Dalcanale, Host-guest driven self-assembly of linear and star supramolecular polymers, *Angew. Chem., Int. Ed.* **2008**, *47*, 4504-4508.

[19] G. G. Condorelli, A. Motta, M. Favazza, I. L. Fragalà, M. Busi, E. Menozzi, E. Dalcanale, Grafting Cavitands on the Si(100) Surface, *Langmuir* **2006**, *22*, 11126-11133.

[20] M. Busi, M. Laurenti, G. G. Condorelli, A. Motta, M. Favazza, I. L. Fragalà, M. Montalti, L. Prodi, E. Dalcanale, Self-assembly of nanosize coordination cages on Si(100) surfaces, *Chem.-Eur. J.* **2007**, *13*, 6891-6898.

[21] For the nomenclature adopted for phosphonate cavitands see reference 11b.

[22] a) J. Terry, M. R. Linford, C. Wigren, R. Cao, P. Pianetta, C. E. D. Chidsey, Determination of the bonding of alkyl monolayers to the Si(111) surface using chemical-shift, scanned-energy photoelectron diffraction, *Appl. Phys. Lett.* **1997**, *71*, 1056-1058.
b) M. M. Sung, G. J. Kluth, O. K. Yauw, R. Maboudian, Thermal Behavior of Alkyl Monolayers on Silicon Surfaces, *Langmuir* **1997**, *13*, 6164-6168.
c) Q.-Y. Sun, L. C. P. M. de Smet, B. van Lagen, M. Giesbers, P. C. Thüne, J. van Engelenburg, F. A. de Wolf, H. Zuilhof, E. J. R. Sudhölter, Covalently Attached

Monolayers on Crystalline Hydrogen-Terminated Silicon: Extremely Mild Attachment by Visible Light, *J. Am. Chem. Soc.* **2005**, *127*, 2514-2523.
d) G. F. Cerofolini, C. Galati, S. Reina, L. Renna, G. G. Condorelli, I. L. Fragalà, G. Giorgi, A. Sgamellotti, N. Re, Functionalization of atomically flat, dihydrogen terminated, 1x1 (100) silicon via reaction with 1-alkyne, *Appl. Surf. Sci.* **2005**, *246*, 52-67.

[23] a) G. F. Cerofolini, C. Galati, S. Reina, L. Renna, O. Viscuso, G. G. Condorelli, I. L. Fragalà, X-ray photoemission spectroscopy study at different takeoff angles of hydrosilylation of 1-alkynes at hydrogen-terminated 1x1-reconstructed (100)-oriented silicon, *Mater. Sci. Eng. C*, **2003**, 23:989-994.
b) G. F. Cerofolini, C. Galati, S. Reina, L. Renna, Functionalization of the (100) surface of hydrogen-terminated silicon via hydrosilation of 1-alkyne, *Mater. Sci. Eng. C* **2003**, *23*, 253-257.
c) G. G. Condorelli, A. Motta, I. L. Fragalà, F. Giannazzo, V. Raineri, A. Caneschi, D. Gatteschi, Single-molecule magnets on silicon: Anchoring molecular magnets on the Si(100) surface, *Angew. Chem., Int. Ed.* **2004**, *43*, 4081-4084.

[24] D. Briggs, In *Practical Surfaces Analysis*, 2nd ed.; D. Briggs, M. P. Seah, Eds.; WILEY-VCH: Weinheim, Germany, **1995**; Vol. 1, p 444.

[25] G. Beamson, D. Briggs, In *High Resolution XPS of Organic Polymers*, The Scienta ESCA300 Database; Wiley & Sons: New York, **1992**.

[26] H. Mansikkamäki, M. Nissinen, K. Rissanen, Encapsulation of diquats by resorcinarenes: a novel staggered anion-solvent mediated hydrogen bonded capsule, *Chem Commun.* **2002**, 1902-1903.

[27] R. M. Yebeutchou, E. Dalcanale, Highly selective monomethylation of primary amines through host-guest product sequestration, *J. Am. Chem. Soc.* **2009**, *131*, 2452-2453.

[28] A. Altomare, M. C. Burla, M. Camalli, G. L. Cascarano, C. Giacovazzo, A. Guagliardi, A. G. G. Moliterni, G. Polidori, R. Spagna, SIR97: a new tool for crystal structure determination and refinement, *J. Appl. Crystallogr.* **1999**, *32*, 115-119.

[29] G. M. Sheldrick, SHELXL97, Program for Crystal Structure Refinement; University of Göttingen: Göttingen, Germany, **1997**.

[30] WinGX: L. J. Farrugia, *J. Appl. Crystallogr.* **1999**, *32*, 837-838.

[31] SAINT, *Software Users Guide*, 6.0; Bruker Analytical X-ray Systems: Madison, WI, **1999**.

[32] G. M. Sheldrick, *SADABS Area-Detector Absorption Correction*, 2.03; University of Göttingen: Göttingen, Germany, **1999**.

[33] SQUEEZE: P. V. D. Sluis, A. L. Spek, BYPASS: an effective method for the refinement of crystal structures containing disordered solvent regions, *Acta Crystallogr. Sect. A* **1990**, *46*, 194-201.

[34] M. Nardelli, Help for checking space-group symmetry, *J. Appl. Crystallogr.* **1996**, *29*, 296-300.

[35] C. D. Wagner, L. E. Davis, M. V. Zeller, J. A. Taylor, R. H. Raymond, L. H. Gale, Empirical atomic sensitivity factors for quantitative analysis by electron spectroscopy for chemical analysis, *Surf. Interface Anal.* **1981**, *3*, 211-225.

[36] a) G. F. Cerofolini, C. Galati, L. Renna, O. Viscuso, M. Camalleri, S. Lorenti, G. G. Condorelli, I. L. Fragalà, X-ray-photoemission-spectroscopy evidence for anomalous oxidation states of silicon after exposure of hydrogen-terminated single-crystalline (100) silicon to a diluted N_2: N_2O atmosphere, *J. Phys. D.: Appl. Phys.* **2002**, *35*, 1032-1038.
b) G. F. Cerofolini, C. Galati, L. Renna, Accounting for anomalous oxidation states of silicon at the Si/SiO_2 interface, *Surf. Interface Anal.* **2002**, *33*, 583-590.

[37] P. Swift, Adventitious carbon - the panacea for energy referencing?, *Surf. Interface Anal.* **1982**, *4*, 47-51.

[38] G. F. Cerofolini, C. Galati, S. Lorenti, L. Renna, O. Viscuso, C. Bongiorno, V. Raineri, C. Spinella, G. G. Condorelli, I. L. Fragalà, A. Terrasi, The early oxynitridation stages of hydrogen-terminated (100) silicon after exposure to N_2:N_2O. III. Initial conditions, *Appl. Phys. A: Mater. Sci. Process.* **2003**, *77*, 403-409.

[39] E. U. Thoden van Velzen, J. F. J. Engbersen, D. N. Reinhoudt, Synthesis of self-assembling resorcin[4]arene tetrasulfide adsorbates, *Synthesis* **1995**, 989-997.

[40] B. Bibal, B. Tinant, J.-P. Declercq, J.-P. Dutasta, Preparation and Structure of [*iiii*] Tetraphosphonatocavitands Bearing Long Chain Functionality at the Lower Rim: Metal Picrates Extraction Studies, *Supramol. Chem.* **2003**, *15*, 25-32.

[41] L. M. Tunstad, J. A. Tucker, E. Dalcanale, J. Weiser, J. A. Bryant, J. C. Sherman, R. C. Helgeson, C. B. Knobler, and D. J. Cram, Host-Guest Complexation. 48. Octol Building Blocks for Cavitands and Carcerands, *J. Org. Chem.* **1989**, *54*, 1305-1312.

[42] C. Naumann, E. Román, C. Peinador, T. Ren, B. O. Patrick, A. E. Kaifer, J. C. Sherman, Expanding Cavitand Chemistry: The Preparation and Characterization of [n]Cavitands with n≥4, *Chem. Eur. J.* **2001**, *7*, 1637-1645.

[43] C. M. Timperley, M. Bird, S. C. Heard, S. Notman, R. W. Read, J. E. H. Tattersall, S. R. Turner, Fluorinated pyridine derivatives, *J. Fluo. Chem.* **2005**, *126*, 1160-1165.

SWCNT functionalized with Cavitands for Biogenic Amines Sensing.

4

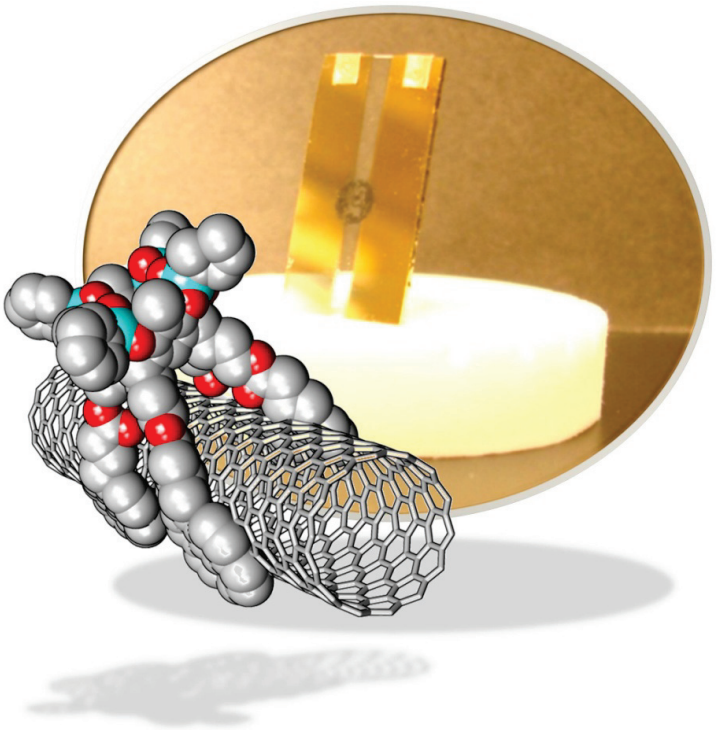

"Chemical Sensors"

4.1 Introduction.

Biogenic amines, e.g. histamine, occur in many different foods. At high concentrations, they are risk factors for food intoxication, whereas moderate levels may lead to food intolerance. Sensitive persons, with insufficient diamine oxidase activity, suffer from numerous undesirable reactions after intake of histamine containing foods. Besides, spoiled foodstuffs, especially fermented foods tend to contain elevated levels of biogenic amines, although their concentrations vary extensively not only between different food varieties but also within the varieties themselves. High histamine content in foods and beverages result from microbial contamination. The evidence of enteral histaminosis represents a challenge for the food industry to produce foods with histamine levels as low as possible.[1]

Herein we report the assembly of cavitand/carbon nanotube (CNT) hybrid for histamine sensing and its detection via amperometry in vapor and water phase.

We propose to detect protonated biogenic amines in vapour phase and water solution exploiting the equilibrium, reported in Scheme 4.1, between the amine and the humidity (vapour phase) or water (solution).

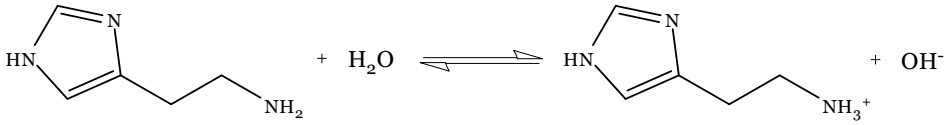

Scheme 4.1. Equilibrium between Histamine and water.

The detection mechanism is the complexation of the ammonium with the tetraphosphonate cavitand that change the CNT conductivity which can be detected via amperometry, measuring the current intensity (I) between two electrodes at a constant potential (V) over the time.

4.2 Results and Discussion.

4.2.1 Sensor Design and Strategy.

Our system is a CNT functionalized with tetraphosphonate cavitands designed to graft onto the CNTs by pyrene π-π stacking. This because grafting through covalent bonds might introduce electron scattering centres that may severely limit the performance of CNT devices.[2] Whereas non-covalent π-π stacking interactions should preserve the CNT conductance and simultaneously assuring the cavitand/CNT interaction.[3]

The device is formed by a glass substrates with two gold strip electrodes where, in between, is deposited the active layer. We measure the electrical current, *I*, through the SWCNT or the functionalized SWCNT device over the time under a constant bias as the sensory response. Upon complexation, a change in the electrical current is expected, so that by measuring this parameter, the guest binding is monitored.

The tetraphosphonate cavitands present remarkable molecular recognition properties toward charged N-methyl derivates in the solid state[4], in solution[5] and in the gas phase.[6] The large K_{ass} values measured for the T_{iiii} *N*-methyl complexes, which exceed 10^7 M^{-1} in dichloromethane, can be attributed to three synergistic interaction modes: (i) N•••O=P cation–dipole interactions; (ii) CH_3-π interactions of the acidic $^+$N-CH_3 group with the π basic cavity; (iii) two simultaneous hydrogen bonds between two adjacent P=O bridges and the two nitrogen protons,[5] in the case of protonated secondary amines.

4.2.2 Receptors Synthesis.

Receptor **31** was prepared according the synthetic pathway shown in Scheme 4.2. At first, an acid catalyzed condensation between 2-methylresorcinol and 2,3-dihydrofuran was exploited to obtain resorcinarene **27** [7], which was subsequently protected at the upper rim with silyl bridges by reacting with dichlorodimethylsilane exploiting a nucleophilic substitution from the resorcinarene OH on the Cl of the bridging agent.

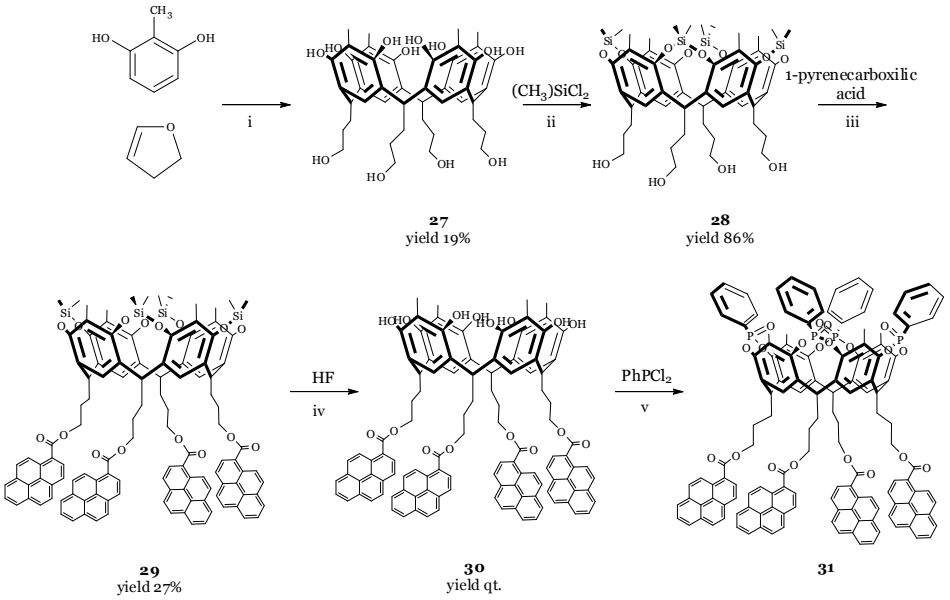

Scheme 4.2. $T_{iiii}[C_3H_6OCOPy; CH_3; Ph]$ synthesis (**31**). i)MeOH/HCl, 7 days, 50°C, ii) dry pyridine, 5 hrs, reflux, iii) dry DCM, DMAP/EDAC, 2 days, r.t., iv) DMF/$CHCl_3$, overnight, 45°C, v) dry pyridine/dry DMA, 3hrs, r.t; H_2O_2/$CHCl_3$, 30 min, r.t.

After isolation of cavitand **28** the insertion of the pyrene at the lower rim was carried out by esterification exploiting the acid activation by N-(3-dimethylaminopropyl)-N'-ethylcarbodiimide hydrochloride (EDAC) and catalyzed by 4-(dimethylamino)pyridine (DMAP). In order to insert phosphonate bridges at the upper rim, silylcavitand **29** was deprotected with hydrofluoric acid 48% to afford resorcinarene **30**. The reaction was carried out using *P,P*-dichlorophenylphosphine to obtain the tetraphosphonite intermediate, subsequently treated *in situ* with hydrogen peroxide in order to oxidized P^{III} to P^{V}. Usually, only the isomer featuring all the P=O groups direct inwards the cavity was formed, because of the stereoselectivity of this bridging method, but in this case the phosphonate insertion failed and also the following attempts performed changing the solvent (pyridine dry), the time reaction (overnight) and the temperature (80°C), did not yield the desired product.

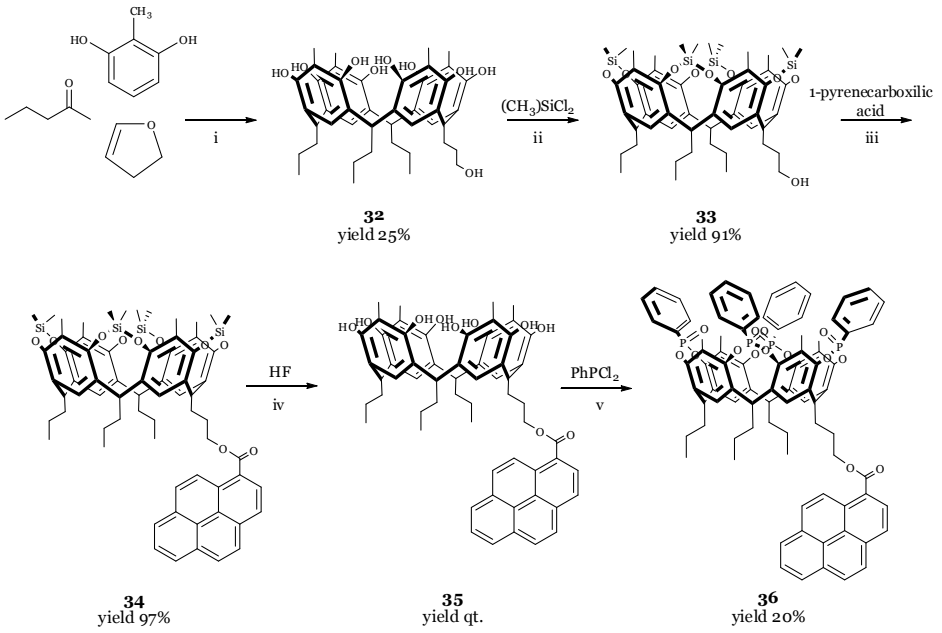

32 yield 25%

33 yield 91%

34 yield 97%

35 yield qt.

36 yield 20%

Scheme 4.3. $T_{iiii}[3(C_3H_7),(C_3H_6OCOPy); CH_3; Ph]$ synthesis (**36**). i) MeOH/HCl, 7 days, 50°C, ii) dry pyridine, 5 hrs, reflux, iii) dry DCM, DMAP/EDAC, 2 days, r.t., iv) DMF/$CHCl_3$, overnight, 45°C, v) dry pyridine, 3hrs, 80°C; H_2O_2/$CHCl_3$, 30 min, r.t.

These unexpected results are due to the presence of four pyrenes at the lower rim which destabilize the cone conformation of the resorcinarene skeleton.

Experimentally this has been demonstrated by the success of the same synthetic strategy when a single pyrene unit is present at the lower rim (Scheme 4.3).

In this case the starting resorcinarene present only one hydroxyl group at the lower rim and it was obtain from an acid catalyzed condensation between 2-methylresorcinol, 2,3-dihydrofuran and butyraldehyde.[8] Tetraphosphonate cavitand **36** was obtained exploiting the reaction with *P,P*-dichlorophenylphosphine in dry pyridine at 80°C, used also for cavitand **31** synthesis, to obtain the tetraphosphonite intermediate, subsequently oxidized *in situ* with hydrogen peroxide.

In order to achieve the initial goal of introducing four pyrenes at the lower rim, we decided to elongate the distance between the cavitand and the

pyrenes using 1-pyrenebutyric acid (Scheme 4.4) to obtain tetraphosphonate cavitand **39**. The latter was prepared following the procedure used for the tetraphosphonate cavitand **29**, moving from the esterification of the silylcavitand **28** with 1-pyrenebutyric acid, followed by the removal of the silyl group and, finally, the functionalization of the upper rim with the phosphonate bridges.

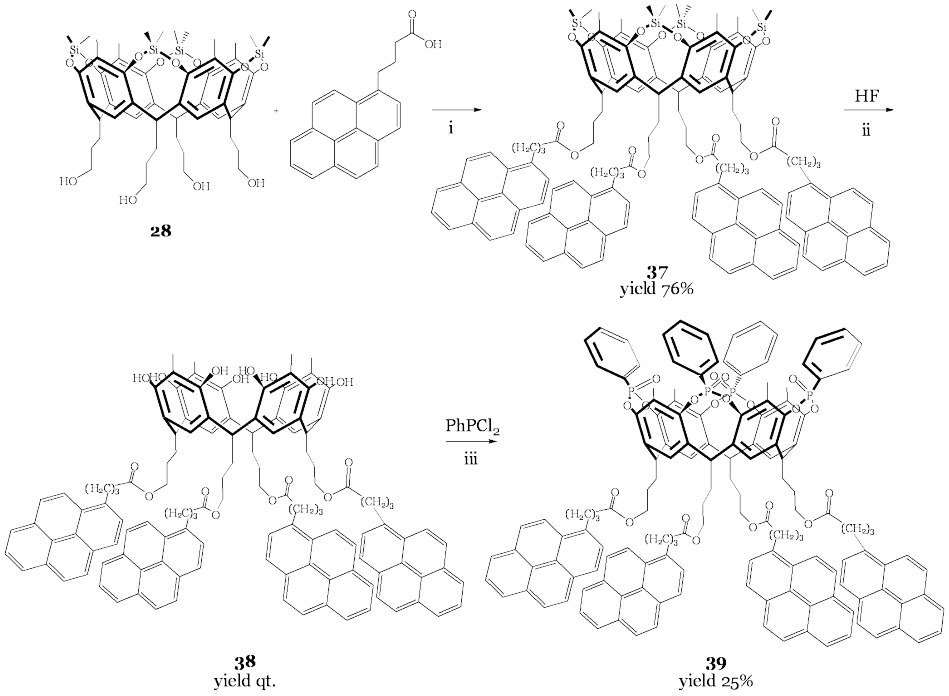

Scheme 4.4. $T_{iiii}[C_3H_6OCOC_3H_6Py; CH_3; Ph]$ synthesis (**39**). i) dry DCM, DMAP/EDAC, 2 days, r.t., ii) DMF/$CHCl_3$, overnight, 45°C, iii) dry pyridine, 3hrs, 80°C; H_2O_2/$CHCl_3$,30 min, r.t.

This same procedure was likewise used to synthesize the tetrathiophosphonate cavitand **40** structurally similar to T_{iiii}**39** except for the presence of four P=S group instead of four P=O introduced via oxidation with S_8 (Scheme 4.5). As already shown in other works,[9] this substitution strongly reduces the guest complexation because the P=S group is less polarized with respect to the P=O analogue and consequently less prone to H-bonding. In addition the cavity of TS_{iiii} is smaller because sulphur is larger (atomic radius=1 Å) than oxygen (atomic radius=0.6 Å).

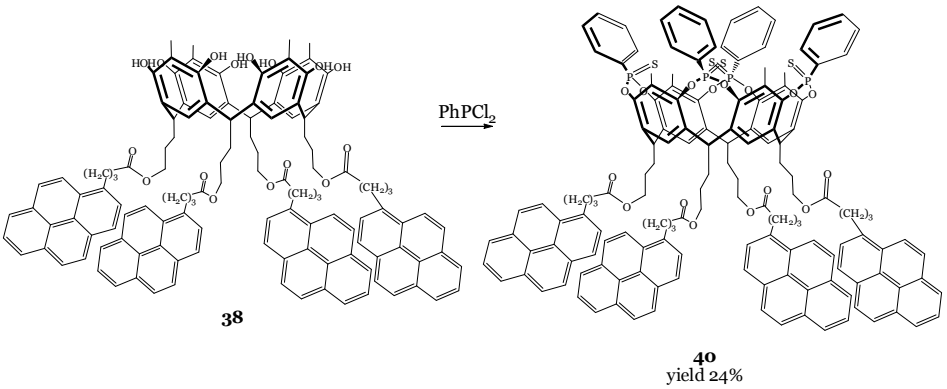

Scheme 4.5. $TS_{iiii}[C_3H_6OCOC_3H_6Py; CH_3; Ph]$ synthesis (**40**) in dry pyridine, 3hrs, 90°C; S_8, 5 hrs, 90°C.

4.2.3 Proof of ammonium complexation.

In order to evaluate if protonated primary amines interact with the receptor, ^1H NMR and ^{31}P NMR titrations of the tetraphosphonate cavitand **39** with ethylamine hydrochloride in DMF-d_6 were carried out.

For the purpose of CNT functionalization, a good dispersion of CNTs in a given solvent is necessary.

DMF was used as solvent, because in it CNTs are very well dispersed. Since the Histamine dihydrochloride guest is insoluble in DMF, ethylamine hydrochloride was used as proxy.

The guest inclusion in the cavity was proved by some chemical shift changes. In particular, in the ^1H NMR titration spectra the usual upfield shift of the cavitand apical methyl group ($\Delta\delta$ = 0.07 ppm, blue oval, figure 4.2) indicative of a cation complexation in the cavity was observed, as well as the downfield shift of the cavitand skeleton ArH_{down} proton ($\Delta\delta$ = 0.48 ppm, red oval, figure 4.1) and the ArCHCH_2 protons ($\Delta\delta$ = 0.27 ppm, green oval, figure 4.2) of the alkyl chain, indicative of their interaction with the anion at the bottom of the cavity. The signals of the guest in the NMR spectra are all broadened, indicating that their exchange timescale is comparable with the NMR acquisition time. Only above 5 eq. of the guest a broad signal start to be seen, which becomes sharp at 25 eq.

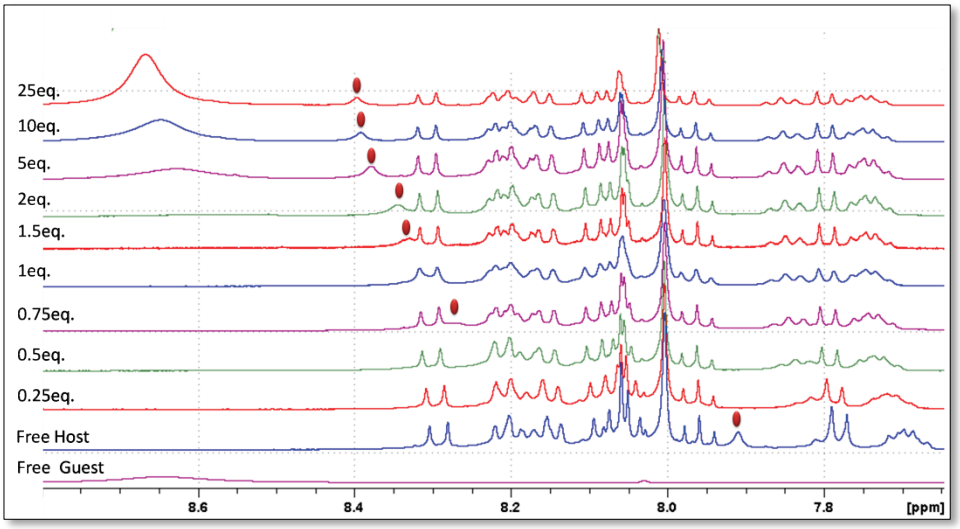

Figure 4.1. Downfield ^{1}H NMR spectra for titration of receptor **39** with ethylamine hydrochloride.

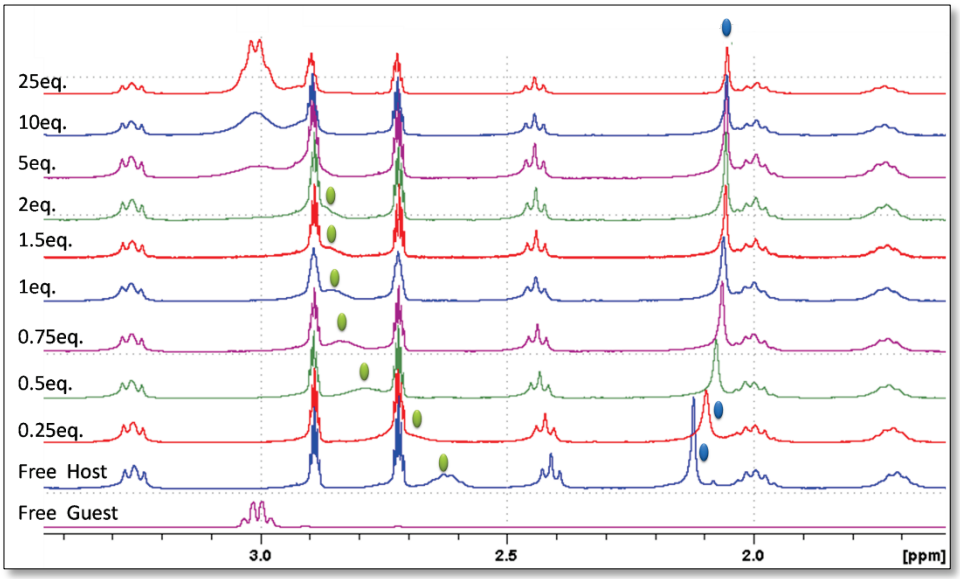

Figure 4.2. Upfield ^{1}H NMR spectra for titration of receptor **39** with ethylamine hydrochloride.

The complexation between the tetraphosphonate cavitand and the ethylamine hydrochloride was confirmed also from the corresponding ^{31}P NMR titrations that showed first a broadening and then a downfield shift of the phosphorous signal ($\Delta\delta$ = 1.31 ppm, figure 4.3).

In conclusion the complexation ability of T$_{iiii}$ **39** toward primary ammonium ions is effective also in DMF.

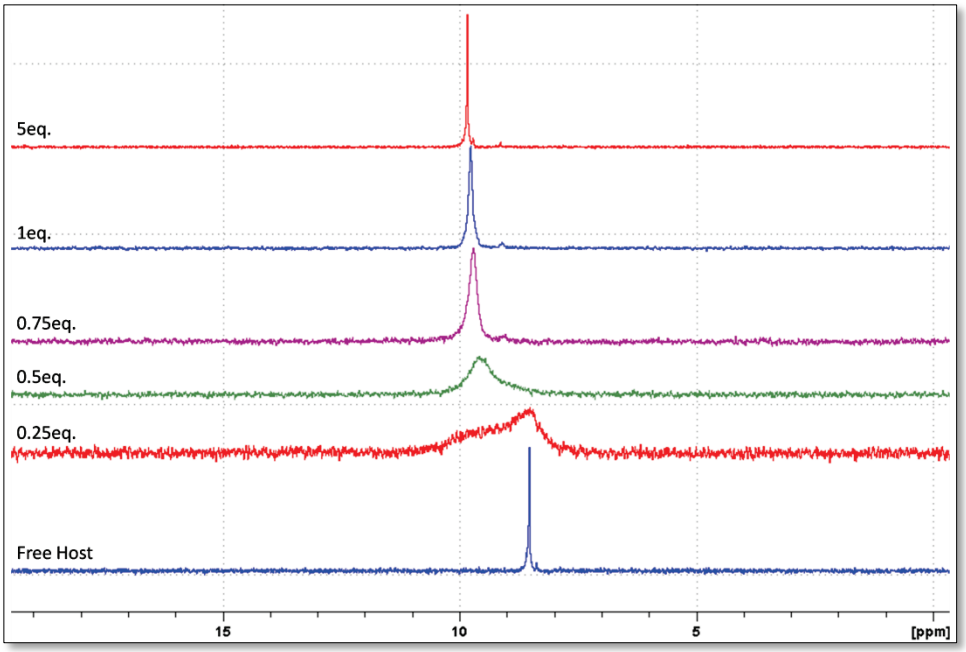

Figure 4.3. ^{31}P NMR spectra for titration of receptor **39** with ethylamine hydrochloride.

4.2.4 SWCNT Hybrids Synthesis.

We focused our attention on the grafting of cavitands **39** and **40**, preferred over **36**, because of the presence of four pyrenes instead of one.

T$_{iiii}$**39**•SWCNT and TS$_{iiii}$**40**•SWCNT hybrids were obtained using a mixture of the SWCNTs, previously cleaned with HNO_3, dispersed in DMF and the corresponding cavitand dissolved in DMF. After the reaction time, the samples were cleaned five times via sonication and centrifugation in dichloromethane. This hybrids were characterized by XPS, TGA and IR.

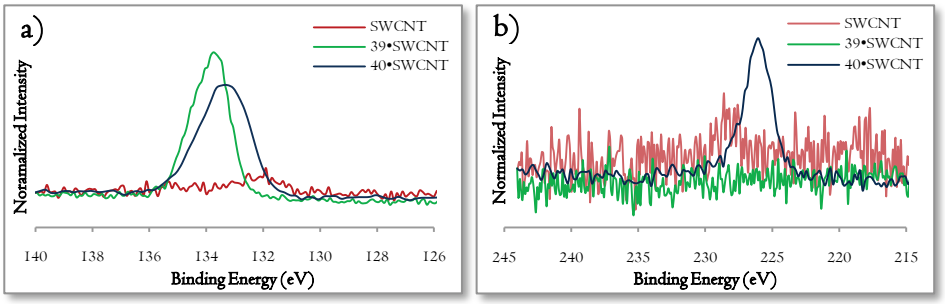

Figure 4.4. High Resolution XPS analysis. a)P 2p region and b) S 2s region.

The presence of the P 2p and S 2s bands in the XPS analysis (Figure 4.4) is indicative of the presence of T$_{iiii}$ and TS$_{iiii}$ cavitands on the SWCNTs. In Table 4.I were reported the atomic fraction of T$_{iiii}$**39**•SWCNT and TS$_{iiii}$**40**•SWCNT.

	T$_{iiii}$**39**•SWCNT	TS$_{iiii}$**40**•SWCNT
C 1s	84.37	83.74
O1s	14.77	15.24
P2p	**0.86**	**0.65**
S2p	**0.00**	**0.35**

Table 4.I. XPS atomic fraction.

The thermal stability of the T$_{iiii}$**39**•SWCNT and TS$_{iiii}$**40**•SWCNT was investigated by TGA under nitrogen atmosphere. Both the ensembles present

a loss of weight of about 32% in the temperature range between 100 and 600 °C (Figure 4.5).

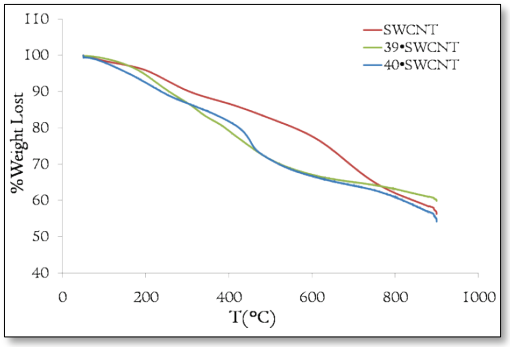

Figure 4.5. Thermogravimetric analysis of SWCNTs cleaned with HNO_3 (red line), T$_{iiii}$**39**•SWCNT (green line) and TS$_{iiii}$**40**•SWCNT (blue line).

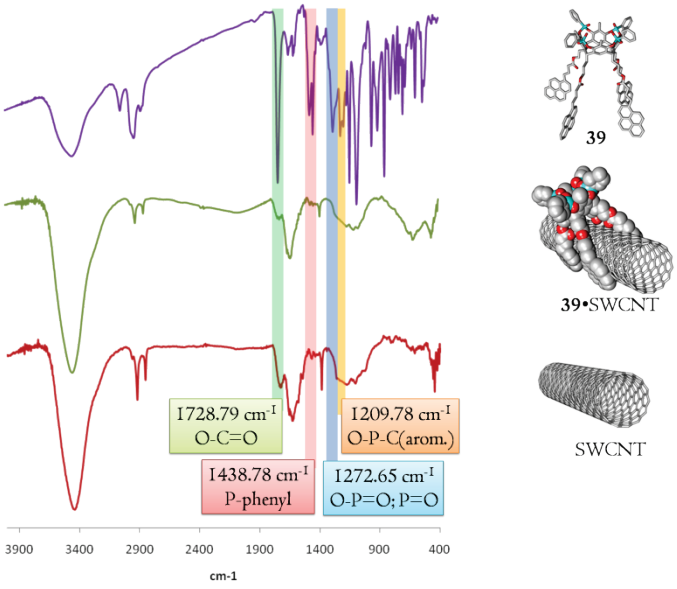

Figure 4.6. IR spectra of pristine SWCNT cleaned with HNO_3 (red line), **39**•SWCNTs (green line) and tetraphosphonate cavitand **39** (violet line).

In the T$_{iiii}$**39**•SWCNT IR spectrum, showed in Figure 4.6, the peaks corresponding to the tetraphosphonate cavitand are absent. The

tetraphosphonate cavitand presents characteristic phosphorous vibration stretching bands at 1438.78 cm^{-1} (P-phenyl), 1272.65 cm^{-1} (O-P=O; P=O)[10] and 1209.78 cm^{-1} (O-P-$C_{aromatic}$).

This result is in contrast with the XPS data. However, due to the higher sensitivity of XPS, we concluded that a limited amount of **39** has been grafted on SWCNT.

Despite the fact that only a tiny amount of **39** has been anchored on the SWCNTs due to the extensive CH_2Cl_2 washing, we decided to test the hybrid material in gas phase towards amines and in particular towards Histamine.

4.2.5 SWCNT Hybrids Vapour Phase Detection.

- *Device Fabrication.*

The glass substrates were cleaned by sonication in acetone/isopropanol/water successively and followed by cleaning with oxygen plasma for 5 min. Two gold strip electrodes (50 nm thick) were sputter-coated, and T**39**•SWCNT, TS**40**•SWCNT and SWCNT dispersion in THF were deposited dropwise on top of the gold electrodes (resistance on the order of megaohms(MΩ)). The devices were then dried for 30 minutes under vacuum.

- *Saturated Vapours Sensing.*

In order to evaluate the response of the device towards unprotonated amines, we performed a preliminary experiment in Histamine saturated vapour. Saturation sensing of Histamine vapour was carried out by monitoring electrical current, *I*, through the SWCNT or the functionalized SWCNT device over the time under a constant bias of 1Volt. The procedure adopted was to detect the current of the devices in air for one minute, followed by the dipping for 30 seconds in the headspace of a vial containing Histamine powder. Saturated vapours were prepared by adding 100 mg of Histamine into a 20 mL vial. A piece of filter paper was put inside the vial to

generate a homogeneous vapour environment. The vial was then sealed, and the system was allowed to equilibrate for 0.5 h before use.

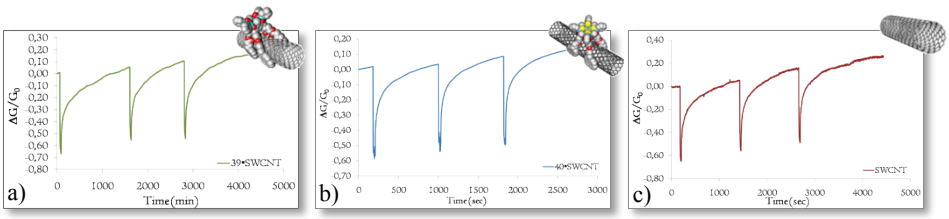

Figure 4.7. Conductance change ($\Delta G/G_0$) of the a) T$_{iiii}$**39**•SWCNT, b) TS$_{iiii}$**40**•SWCNT and c) SWCNT sensors exposed to Histamine saturated vapour.

As shown in Figure 4.7, all three T$_{iiii}$**39**•SWCNT, TS$_{iiii}$**40**•SWCNT and SWCNT sensors exhibit almost the same sensitivity ($\Delta G/G_0$=-0.60) towards Histamine vapours.

This negative result proves the complete insensitivity of T$_{iiii}$ **39** towards unprotonated amines.

Low Concentration Sensing.

The next step was to perform the detection in vapour phase at low concentration and in presence of humidity so as to exploit the equilibrium between the Histamine and the humidity (see Introduction and Scheme 4.1) and the ability of the cavitand to complex cationic species (see subparagraph 4.2.1).

To generate a flow with the analyte desired concentration of 10 ppm, we used a Kin-Tek Permeation System, where as carrier gas was used nitrogen with 30%[11] of relative humidity and the vial containing the Histamine was heated at 50°C. The procedure adopted was the same used in saturation but, in this case, we introduced the devices in the analyte flow of 10 ppm for 30 seconds instead of the saturated vapour.

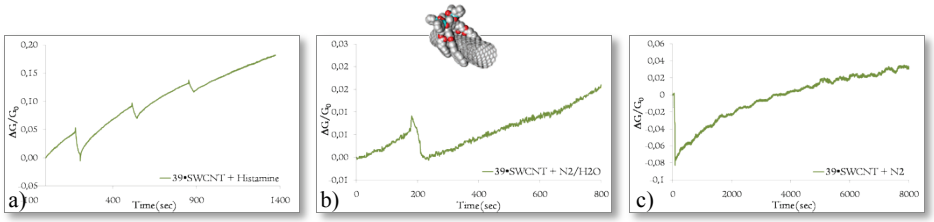

Figure 4.8. Conductance change ($\Delta G/G_0$) of the T$_{iiii}$**39**•SWCNT sensors exposed to a) 10ppm Histamine flow, b) humidified carrier and c) carrier alone.

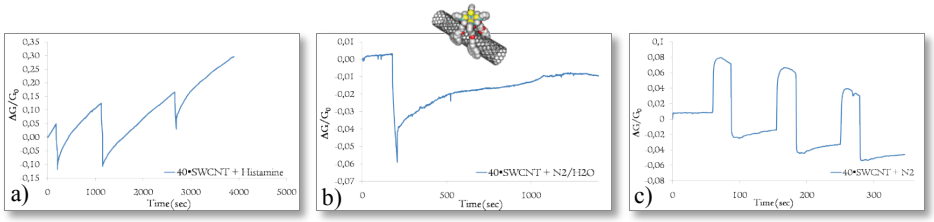

Figure 4.9. Conductance change ($\Delta G/G_0$) of the TS$_{iiii}$**40**•SWCNT sensors exposed to a) 10 ppm Histamine flow, b) humidified carrier and c) carrier alone.

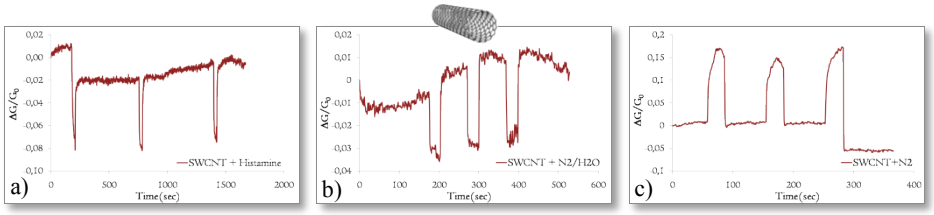

Figure 4.10. Conductance change ($\Delta G/G_0$) of the SWCNT sensors exposed to a) 10 ppm Histamine flow, b) humidified carrier and c) carrier alone.

In these measures, we observed the largest Histamine response from the TS$_{iiii}$**40**•SWCNT sensor ($\Delta\Delta G/G_0$=0.229, figure 4.9a), the smallest from the T$_{iiii}$**39**•SWCNT sensor ($\Delta\Delta G/G_0$=0.025, figure 4.8a) and, in the middle, the SWCNT sensor($\Delta\Delta G/G_0$=0.065, figure 4.10a). The highest answer of the TS$_{iiii}$**40**•SWCNT sensor was unexpacted because of the inability of the tetrathiophosphonate cavitand to complex cations. This means that the presence of the cavitand did not improve the sensor response towards Histamine and/or that the equilibrium with water does not take place. Moreover, we observed response also from the analysis of the humidified carrier with the same trend: the largest response from TS$_{iiii}$**40**•SWCNT

sensor ($\Delta\Delta G/G_0$=0.061, figure 4.9b), followed by the SWCNT sensor ($\Delta\Delta G/G_0$=0.034, figure 4.10b) and, finally, the T$_{iiii}$**39**•SWCNT sensor ($\Delta\Delta G/G_0$=0.009, figure 4.8b). We also found that, the T$_{iiii}$**39**•SWCNT sensor responded to the dry carrier gas ($\Delta\Delta G/G_0$=0.083, figure 4.8c) but, the TS$_{iiii}$**40**•SWCNT ($\Delta\Delta G/G_0$=-0.067, figure 4.9c) and the SWCNT sensors ($\Delta\Delta G/G_0$=-0.160, figure 4.10c) gave opposite response.

There are several problems associated with the responses of such materials. T$_{iiii}$**39**•SWCNT responds very slowly to the humidified and dry carrier gas (Figure 4.8 b and c, a single dipping shown). Moreover, TS$_{iiii}$**40**•SWCNT and pristine SWCNT respond "negatively" to dry N_2.

This means that all the sensors are not only sensitive towards Histamine but also towards water and, in the case of the T$_{iiii}$**39**•SWCNT sensor, also toward nitrogen. Therefore, this system did not show any selectivity between the analyte in humidified nitrogen, humidified nitrogen without analyte and nitrogen alone.

Since the amount of cavitand **39** grafted is minimal, the results obtained can be due either to absence of interactions or to the limited number of receptors grafted on the SWCNTs.

In order to get more reproducible results by increasing the quantity of cavitands in the functionalized SWCNT, we decided to prepare the T$_{iiii}$**39**•SWCNT and TS$_{iiii}$**40**•SWCNT hybrids with the same procedure but without removing the excess of cavitand via CH_2Cl_2 sonication and centrifugation.

4.2.6 SWCNT Mixed Hybrids Synthesis.

T$_{iiii}$**39**•SWCNT$_{mix}$ and TS$_{iiii}$**40**•SWCNT$_{mix}$ hybrids were obtained using a mixture of the SWCNTs, previously cleaned with HCl, dispersed in DMF and the corresponding cavitand dissolved in DMF. After the reaction time, the solvent was removed under vacuum and the samples were used without further purification. These SWCNT:cavitand composites were prepared in I:0.1, I:0.5, I:1, I:1.5 ratio.

The thermal stability of the T$_{iiii}$**39**•SWCNT$_{mix}$ and TS$_{iiii}$**40**•SWCNT$_{mix}$ was investigated by TGA under nitrogen atmosphere.

The percentage of weight lost corresponding to the T$_{iiii}$**39**•SWCNT$_{mix}$ and TS$_{iiii}$**40**•SWCNT$_{mix}$ ensembles at the different ratios between 100°C and 600 °C was reported in Table 4.2.

	0.1	0.5	I	I.5
T$_{iiii}$39•SWCNT$_{mix}$	32%	25%	50%	50%
TS$_{iiii}$40•SWCNT$_{mix}$	26%	42%	59%	7%

Table 4.2. Thermogravimetric analysis: % Weight Lost in the T$_{iiii}$**39**•SWCNT$_{mix}$ and TS$_{iiii}$**40**•SWCNT$_{mix}$ ensembles at different ratio.

The values reported did not increase, as expected, with the quantity of cavitand presents in the samples. This is probably due to the fact that, without cleaning, the excess of cavitand is not homogeneously distributed.

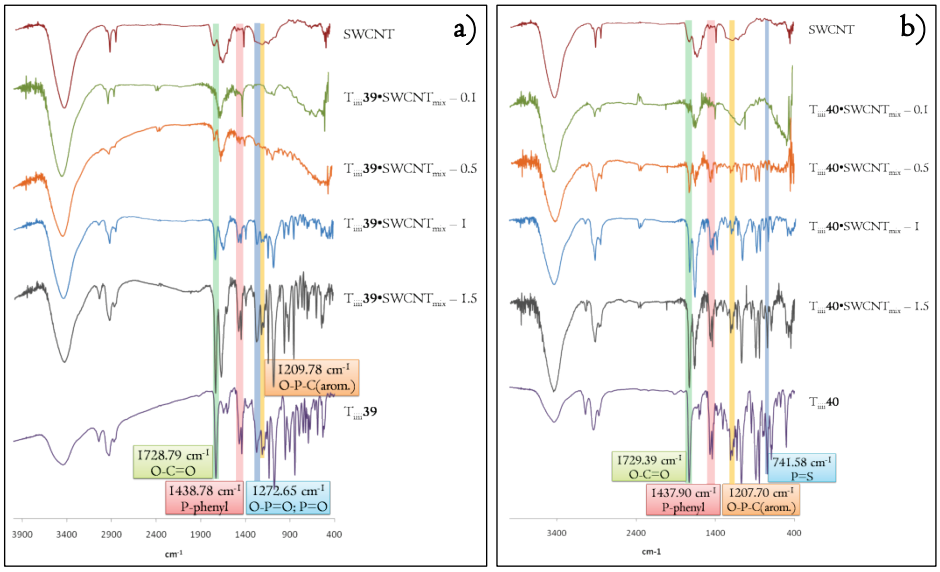

Figure 4.11. IR spectra of a) T$_{iiii}$**39**•SWCNT$_{mix}$ and b) TS$_{iiii}$**40**•SWCNT$_{mix}$ at the different ratios.

In the IR the peaks corresponding to the tetraphosphonate and the tetrathiophosphonate cavitands are now present.

The tetraphosphonate cavitand presents characteristic phosphorous vibration stretching bands at 1438.78 cm^{-1} (P-phenyl), 1272.65 cm^{-1}

(O-P=O; P=O) and 1209.78 cm^{-1} (O-P-$C_{aromatic}$) (Figure 4.11a) while the tetrathiophosphonate cavitand presents the characteristic phosphorous vibration stretching bands at 1437.90 cm^{-1} (P-phenyl), 1207.70 cm^{-1} (O-P-$C_{aromatic}$) and 741.58 cm^{-1} (P=S) (Figure 4.11b).

Since the pyrene acts not only as the grafting group but also as a fluorophore, we studied the fluorescent property of T$_{iiii}$**39**•SWCNT$_{mix}$ (Figure 4.12) and TS$_{iiii}$**40**•SWCNT$_{mix}$ composites. For each ratio the fluorescent spectra at the excitation wavelength of 345 nm and absorbance lower than 0.1 were recorded. The emission spectra present two bands centred around 375 and 395 nm characteristic of the pyrene and a big broad band centres around 478 nm characteristic of the pyrene excimer.

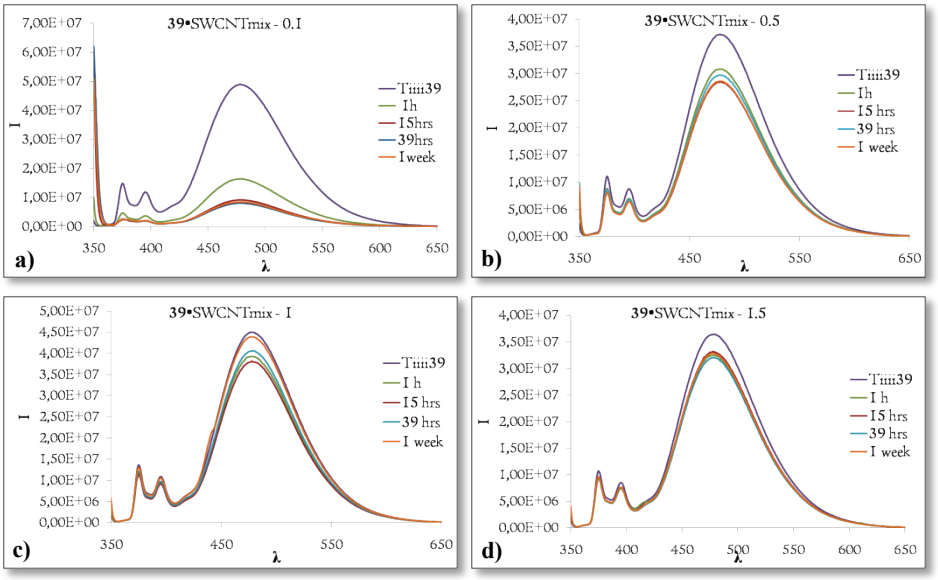

Figure 4.12. Fluorescence emission spectra of a) SWCNT:T$_{iiii}$**39**=I:0.1, b) SWCNT:T$_{iiii}$**39**=I:0.5, c) SWCNT:T$_{iiii}$**39**=I:1, d) SWCNT:T$_{iiii}$**39**=I:1.5 in DMF after different hours of sonication.

The highest quenching of the fluorescence, due to the π-π stacking between the pyrene and the CNTs, was observed in the 0.1 composite (Figure 4.12a), whereas the other ratios presents only a little decrease of the fluorescence. We had never observed a complete quenching, probably due to

the presence on the same molecule of four pyrene that only partly prefer to form the π-π stacking with the CNTs rather than with the other pyrene.

In some case, e.g. for the TS_{iiii}**40**•$SWCNT_{mix}$-I after 1 week of sonication (figure 4.12c), we observed an increase, instead of a decrease, of the fluorescence probably due to the fact that the cavitand in excess could be not homogeneously distributed.

The TS_{iiii}**40**•$SWCNT_{mix}$ composites showed the same trend.

4.2.7 SWCNT Mixed Hybrids Vapour Phase Detection.

- *Device Fabrication.*

With this new hybrid at hand we moved to device fabrication.

The devices were fabricated in the same way already reported for the SWCNT Hybrids in paragraph 4.2.5.

- *Saturated Vapours Sensing.*

In order to evaluate if the devices with the different percentage of tetraphosphonate cavitand are able to detect Histamine vapour with highest sensitivity and selectivity, we carried out saturation sensing with the same procedure adopted for the SWCNT Hybrid showed in Paragraph 4.2.5. We decided to perform the analysis on the SWCNT:cavitand ratios of 1:0.1 because of the highest fluorescent quenching, in comparison with the other composites, and 1:1 to see if the larger quantity of cavitand present increases of the response.

Also in this case the T_{iiii}**39**•$SWCNT_{mix}$-0.1 and T_{iiii}**39**•$SWCNT_{mix}$-I sensors presented almost the same response ($\Delta G/G_0$=-0.09) towards Histamine vapours, whereas SWCNT sensor presented the highest answer of $\Delta G/G_0$=-0.13. Because of the SWCNT behaviour, we decided of not carry out the analysis with the TS_{iiii}**40**•$SWCNT_{mix}$ using SWCNT devices as "blank test".

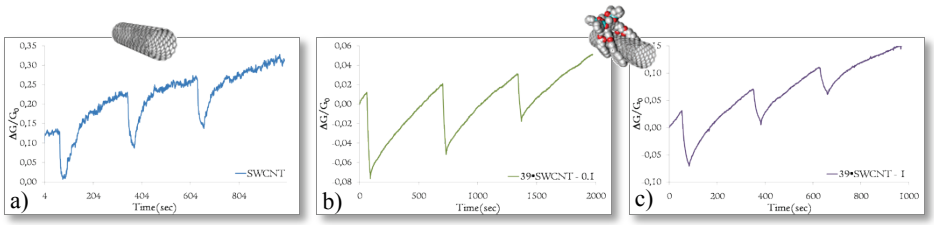

Figure 4.13. Conductance change ($\Delta G/G_0$) of the a) SWCNT, b) T$_{iiii}$**39**•SWCNT$_{mix}$ - 0.1 and c) T$_{iiii}$**39**•SWCNT$_{mix}$ – 1 sensors exposed to Histamine saturated vapour.

The negative results reported, clearly indicate that cavitand grafted on SWCNTs are insensitive to Histamine in the gas phase. In this case the amount of **39** anchored is sizable. This means that the complexation of **39** towards gaseous protonated Histamine is ineffective.

At this point we decided to evaluate the sensing properties of this material in the complexation of protonated amines in water.

4.2.8 SWCNT Mixed Hybrids Detection in Water Solution.

Device Fabrication.

The devices for the water sensing were prepared in the same way of those for vapour sensing. But for water, we deposited 10 nm of Cr and 100 nm of Au to avoid the gold cleavage. The devices used were prepared by deposition of the SWCNT:cavitand composite in the 1:1 and 1:0.1 ratios, and the SWCNT (resistance on the order of MΩ).

Sensing in Water Solution.

Sensing in solution was carried out by monitoring electrical current, *I*, through the SWCNT or the T$_{iiii}$**39**•SWCNT device over the time under a constant bias of 1V of a 1mM solution of the analyte.

The procedure adopted was to detect the current of the devices in air for one minute, followed by the dipping in 19.8 mL of distilled water, under slow stirring, for four minutes to get current stable in water. Then, 200μL of

a 0.1M solution of analyte was added to the measuring vials to obtain a final analyte concentration of 1mM.

As first analyte we choose 2-bromo-N-methylbutyl ammonium bromide (**26**, Scheme 4.6) because it is known that the N^+-CH_3 groups are the strongly bound by T$_{iiii}$ **39**.[12]

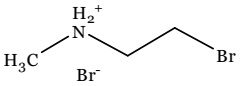

Scheme 4.6. 2-bromo-N-methylbutyl ammonium bromide (**26**).

As already described in the Subparagraph 4.2.1, the tetraphosphonate cavitands are very good receptors for methylammonium salts. To evaluate if functionalized SWCNTs are able to detect **26**, we performed the complexation of pristine SWCNT, T$_{iiii}$**39**•SWCNT and TS$_{iiii}$**40**•SWCNT with **26** in water and we characterized them with XPS. The guest is specifically marked with a bromine atom to allow XPS quantification.

Complexation was performed by adding a 10^{-3} M solution of **26** to a dispersion of pristine and functionalized SWCNT. The mixtures were shaken with a vortex for 30 minutes following by elimination of the physisorbed material via centrifugation and sonication in water (5 times) and acetone (5 times).

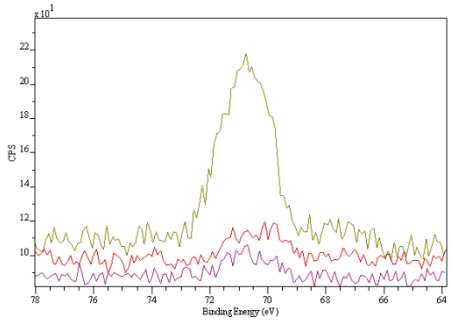

Figure 4.14. Br 3d XPS region of SWCNT (pink curve), T$_{iiii}$**39**•SWCNT (green curve) and T$_{iiii}$**39**•SWCNT (red curve) after treatment with guest **26**.

The XPS Br 3d region, shown in Figure 4.14, demonstrates the presence of guest **26** on T$_{iiii}$**39**•SWCNT, while it is almost absent in the other two materials.

Therefore, guest **26** is complexed by tetraphosphonate cavitand **39** and not by **40** as expected. Moreover, pure physisorption on pristine SWCNT is negligible. It has to be stressed that XPS is a very sensitive technique, therefore the amount of complexed **26** can be very small.

To see if the T$_{iiii}$**39**•SWCNT$_{mix}$-0.1 and the T$_{iiii}$**39**•SWCNT$_{mix}$-1 sensors respond better (*i.e.* they should not return to the baseline) and with higher sensitivity in comparison with the SWCNT device, water sensing with guest **26** was carried out.

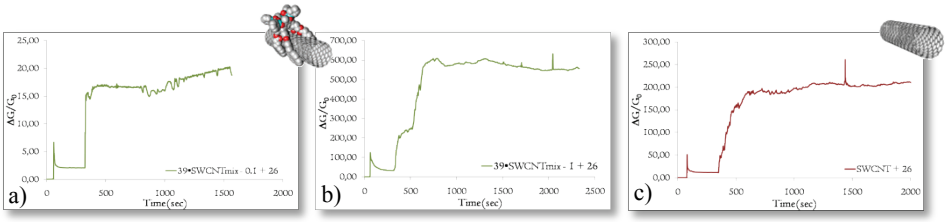

Figure 4.15. Conductance change ($\Delta G/G_0$) of the a) T$_{iiii}$**39**•SWCNT$_{mix}$ - 0.1, b) T$_{iiii}$**39**•SWCNT$_{mix}$ - 1 and c) SWCNT sensors dipped into 1mM of **26** water solution.

In this case we obtain the desired trend of the curve (Figures 4.15a and 4.15b) but, also here, the SWCNT sensors gave a similar response (Figure 4.15c) and this means that there is a strong interaction not only between the cavitand and the analyte but also between the analyte and the CNTs. This implies that a small amount of **39** grafted is not sufficient to trigger a specific response.

Unfortunately we did not get quantitatively reproducible analysis:[13] each device gave different responses, possibly because that the functionalized SWCNTs and the SWCNTs were not well dispersed in THF and so, the amount of composite to be deposited in order to obtain the desired resistance (MΩ) was different each time.

Verified that the 2-bromo-N-methylbutylammonium bromide gives the desire trend, we performed the water solution analysis with Histamine dihydrochloride in the hope that the protonated amine present a better response then the Histamine. No interaction between the Histamine dihydrochloride and the functionalized SWCNT (Figure 4.16) was recorded.

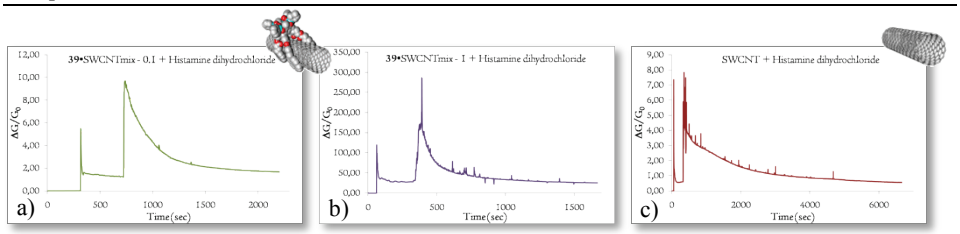

Figure 4.16. Conductance change (ΔG/G0) of the a) T$_{iii}$**39**•SWCNTmix - 0.1, b) T$_{iii}$**39**•SWCNTmix -1 and c) SWCNT sensors dipped into 1mM of Histamine dihydrochloride water solution.

The water solution sensing data highlight two important features: (i) the material deposition is not highly reproducible, and (ii) in water histamine dihydrochloride is not detected.

Sensing in Water Solution using Nafion.

As last hope, we carried out the same analysis preparing the same devices with a Nafion membrane cover in order to increase the sensitivity and the stability of the devices.

Nafion is a sulfonated tetrafluoroethylene based fluoropolymer-copolymer discovered in the late 1960s by Walther Grot of DuPont. It is the first of a class of synthetic polymers with ionic properties which are called ionomers. Nafion's unique ionic properties is a result of incorporating perfluorovinyl ether groups terminated with sulfonate groups onto a tetrafluoroethylene (Teflon) backbone.[14] The most important Nafion property is its high cation conductivity.

This ion-selective membrane has been useful to deliver to the sensor only the desired cationic species. In this way the sensor responses should be only due to interactions with cationic species.

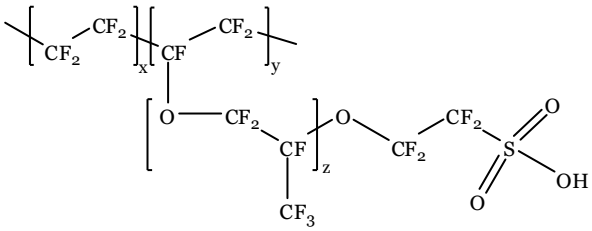

Scheme 4.7. Nafion structure.

After the devices fabrication, the Nafion was deposited placing a drop of a 5% aqueous solution of Nafion and drying. In this way a film of Nafion is present between the active layer on the device and the water solution containing the guest.

As shown in Figure 4.17, the presence of the Nafion membrane did not change the responses of the sensors. This means that the absence of responses is not due to the low selectivity of the system, but to the complete absence of selectivity.

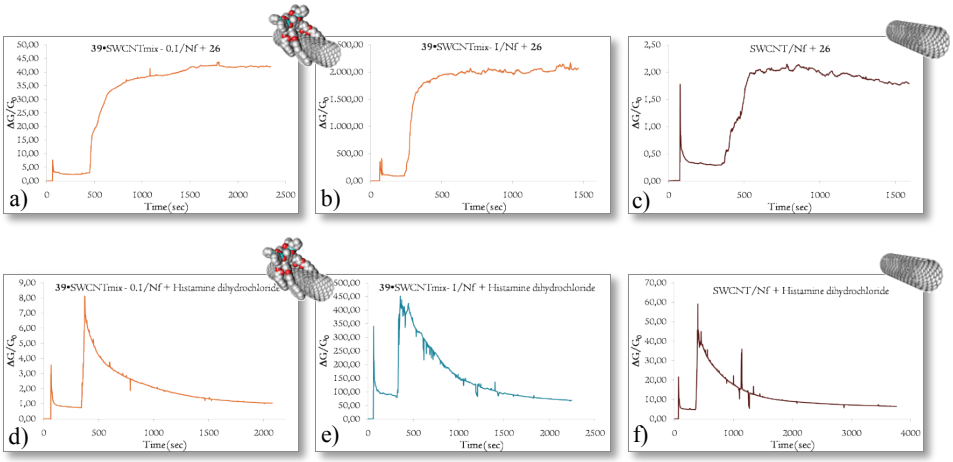

Figure 4.17. Conductance change ($\Delta G/G_0$) of the a) T_{iiii}**39**•$SWCNT_{mix}$ - 0.1/Nf, b) T_{iiii}**39**•$SWCNT_{mix}$ - 1/Nf and c) SWCNT/Nf sensors dipped into 1mM of **26** water solution. d) T_{iiii}**39**•$SWCNT_{mix}$ - 0.1/Nf, e) T_{iiii}**39**•$SWCNT_{mix}$ -1/Nf and f) SWCNT/Nf sensors dipped into 1mM of Histamine dihydrochloride water solution.

4.3 Conclusions.

A large synthetic and sensor study has been performed to fabricate a biogenic amine sensor. A tetraphosphonate cavitand functionalized with four pyrenes at the lower rim has been synthesized and used to develop T$_{iiii}$**39**•SWCNT, T$_{iiii}$**39**•SWCNT$_{mix}$ and T$_{iiii}$**39**•SWCNT$_{mix}$/**Nf** sensors.

A first problem encountered is the amount of cavitand grafted on SWCNT, which turned out to be small and poorly reproducible.

The whole set of sensing experiments performed indicate that only charged guest **26** in water has been clearly complexed. Uncertainty on the amount of **39** anchored and on the effectiveness of the transduction mode, hampers a clear translation of the complexation event of **26** into a readable signal. In all others cases no proofs of complexation were obtained.

Seen in retrospective the choice of cavitand **39** as receptor coated on SWCNTs has not been optimal. The presence of four pyrene units probably reduces the affinity of **39** towards SWCNT by intermolecular π-π stacking among the pyrene units. This will not the case for cavitand **36** having the same 4P=O at the upper rim and only one pyrene at the lower rim.[3]

In any case, independently by the tetraphosphonate cavitand used, the device will have a chance to work only for cationic species in water solution.

4.4 Acknowledgements.

Special thanks to Prof. Timothy M. Swager of the Massachusetts Institute of Technology to give me the opportunity to work and learn in his group.

4.5 Experimental Section.

4.5.1. Reagent, Chemicals and Instruments used.

All commercial reagent were ACS reagent grade and used as received. For the synthesis all solvents were dried and distilled using standard procedures. Single-walled carbon nanotubes were acquired from UNIDYM™ CARBON NANOTUBES (Unidym Grade/lot# P0900) and was purified using either HNO_3 and HCl methods.

- Chromatography was performed using 70-230 mesh silica purchased from Merck and 40-120 μ Sephadex G-10 purchased from Pharmacia Fine Chemicals. Thin layer chromatography was performed on Kieselgel 60 F_{254} and Uniplate™ Silica Gel GF silica-coated glass plates and visualized by UV.

- ^{1}H NMR, ^{13}C NMR and ^{31}P NMR spectra were obtained with a Bruker AVANCE-400 (400 MHz). ^{1}H NMR and ^{13}C NMR chemical shifts (δ) were reported in ppm relative to the proton and carbon resonances resulting from incomplete deuteration of the NMR solvents.

- HR-ESI-MS characterization experiments were performed by the MIT Department of Chemistry Instrumentation Facility (DCIF)

- Ultraviolet-visible absorption spectra were recorded on an Agilent 8453 diode-array spectrophotometer.

- Emission spectra were acquired on a SPEX Fluorolog fluorometer (model FL-321, 450 W xenon lamp) using right-angle detection (solution measurements).

- Conductance was measured with an AUTOLAB PGSTAT 20 potentiostat (Eco Chemie) at constant potential (typically 1 V).

- ♣ Infrared (IR) spectra were recorded as a thin film on KBr plates on a Perkin-Elmer Model 2000 FT-IR System transform spectrophotometer at the DCIF.

- ♣ Elemental and chemical spectroscopic analysis were run with a Kratos AXIS Ultra Imaging X-ray Photoelectron Spectrometer.

- ♣ TGA analysis were performed with a TGA Q50 apparatus (TA Instruments).

- ♣ The Au strip electrodes were sputter coated with a Quorum Technologies SC7620 Sputter Coater and the Cr/Au strip electrodes with a Sputtering System AJA Orion 5.

- ♣ A specific concentration of analyte and relative humidity was generated with a KIN-TEK gas-generating system. Source-drain current change in response.

4.5.2. Synthetic Protocol.

Resorcinarene Res[C_3H_6OH; CH_3]. (27)

To a stirred solution of 2-methylresorcinol (10 g, 80.55 mmol) in methanol (75 mL) cooled to 0 °C, 2,3-dihydrofuran (6.09 mL, 80.55 mmol) was added. HCl (conc) (18 mL) was then added dropwise. After 6 days of stirring at 50 °C, the mixture was allowed to cool to room temperature and poured into distilled water (100 mL). A precipitate formed, which was filtered, and dried under vacuum to give products **I** in 19% yield.

^{1}H NMR (DMSO-d_6, 400 MHz) δ (ppm): 8.63 (s, 8H, ArO*H*), 7.24 (s, 4H, Ar*H*), 4.31 (s, 4H, R-O*H*), 4.14 (t, 4H, J = 7.9 Hz, ArC*H*), 3.39 (t, 8H, J = 6.7 Hz, RCH_2OH), 2.20 (m, 8H, ArCHCH_2), 1.89 (s, 12H, ArCH_3), 1.30 (m, 8H, CH_2CH$_2$OH). **^{13}C NMR** (DMSO-d_6, 100 MHz) δ (ppm): 149.47, 125.21, 121.74, 111.97, 61.08, 34.41, 31.70, 29.71, 10.49. **HR-ESI-MS**: m/z 775.3695 [M-H]$^-$.

Cavitand Silyl[C_3H_6OH; CH_3]. (28)

To a solution of **27** (1 g, 1.29 mmol) in dry pyridine (30 mL), cooled to 0 °C, dichlorodimethylsilane (1.89 mL, 15.45 mmol) was added. The mixture was stirred at 100 °C for 3 hours. The solvent was removed under vacuum and the resulting residue was suspended in methanol (10 mL). The yellow solid obtained after vacuum filtration was purified by column chromatography (silica, CH_2Cl_2), obtaining product **28** in 32% yield.

^{1}H NMR (DMSO-d_6, 400 MHz) δ (ppm) 7.54 (s, 4H, Ar*H*), 4.35 (t, 4H, J = 8.2 Hz, ArC*H*), 4.25 (s, 4H, R-O*H*), 3.39 (t, 8H, J = 6.7 Hz, CH_2OH), 2.27 (m, 8H, ArCHCH_2), 1.79 (s, 12H, ArCH_3), 1.31 (m, 8H, CH_2CH$_2$OH), 0.41 (s, 12H, SiCH_3 out), -0.81 (s, 12H, SiCH_3 in). **^{13}C NMR** (DMSO-d_6, 100 MHz,) δ (ppm): 148.08, 131.43, 122.04, 118.45, 61.05, 35.64, 31.80, 28.89, 10.79, -2.67, -6.27. **ESI-MS**: m/z 1023.38 $[M+Na]^+$.

Cavitand Sylil[$C_3H_6OCOPyrene$; CH_3]. (29)

To a solution of 1-pyrene carboxylic acid (492 mg, 2.0 mmol) dissolved in 8 mL of dry CH_2Cl_2 and 8 mL of Toluene, EDAC (230 mg, 1.20 mmol) and DMAP (293 mg, 2.40 mmol) were added. Then Silylcavitand **28** (200 mg, 0.20 mmol) was added and the resulting mixture was stirred at 70°C for three days. The crude was purified by column chromatography on silica gel by using CH_2Cl_2:AcOEt=99.5:0.5 as eluant to give compound **29** as brown powder in 27% yield.

^{1}H NMR ($CDCl_3$, 400 MHz) δ (ppm): 8.99 (d, 1H, J = 9.44 Hz, Py*H*), 8.34 (d, 1H, J = 8.1 Hz, Py*H*), 7.98-7.64 (m, 7H, Py*H*), 7.37 (s, 4H, Ar*H*), 4.78 (t, 4H, J = 8.1 Hz, ArC*H*), 4.49 (t, 8H, J = 6.9 Hz, RCH_2OCOPy), 2.53 (m, 8H, ArCHCH_2), 1.93 (s, 12H, ArCH_3), 1.91 (m, 8H, CH_2CH$_2$OCOPy), 0.52 (s, 12H, SiCH_3 out), -0.65 (s, 12H, SiCH_3 in). **HR-ESI-MS**: m/z 1935.6314 $[M-H]^-$.

Resorcinarene Res[$C_3H_6OCOPyrene$; CH_3]. (30)

To compound **30** (195 mg, 0.102 mmol) dissolved in 3 mL of DMF and in 3 mL of $CHCl_3$ in a Teflon flask, 400 μL of an aqueous 48% HF solution was added. After 18 hours of stirring at 45 °C the solvent was

removed under vacuum. The crude product was sonicated in distilled water, filtered and dried to give resorcinarene **30** as a brown powder in a 98% yield.

^{1}H NMR (DMSO-d_6, 400 MHz,) δ (ppm): 8.86 (d, 1H, J = 9.44 Hz, Py*H*), 8.83 (s, 8H, ArO*H*), 8.30 (d, 1H, J = 8.2 Hz, Py*H*), 8.30-7.81 (m, 7H, Py*H*), 7.47 (s, 4H, Ar*H*), 4.44 (m, 4H + 8H, ArC*H* + RCH_2OCOPy), 2.54 (m, 8H, ArCHCH_2), 2.0 (s, 12H, ArCH_3), 1.80 (m, 8H, CH_2CH$_2$OCOPy). **ESI-MS**: m/z 1688.51 [M-H]$^-$.

Resorcinarene Res[3C$_3$H$_7$, C$_3$H$_6$OH; CH$_3$]. (32)

To a stirred solution of 2-methylresorcinol (10 g, 80.55 mmol) in methanol (75 mL) cooled to 0 °C, 2,3-dihydrofuran (1.52 mL, 20.14 mmol) and n-butyraldehyde (5.31 mL, 60,42 mmol) were added. Conc. HCl (18 mL) was then added dropwise. After 6 days of stirring at 50 °C, the mixture was allowed to cool to room temperature. A precipitate formed, which was filtered, and dried under vacuum to give a mixture of cavitands with different alkyl chains at the lower rim which was used without further purification.

Cavitand Sylil[3C$_3$H$_7$, C$_3$H$_6$OH; CH$_3$]. (33)

To a solution of crude **32** (8 g, 10.98 mmol) in dry pyridine (250 mL), cooled to 0 °C, dimethyldichlorosilane (16.10 mL, 131.70 mmol) was added. The mixture was stirred at 100 °C for 3 hours. The solvent was removed under vacuum and the resulting residue was suspended in methanol (20 mL). The yellow solid obtained after vacuum filtration was purified by column chromatography (silica, CH$_2$Cl$_2$: MeOH=98:2), giving product **33** in 26% yield.

^{1}H NMR (CDCl$_3$, 400 MHz) δ (ppm): 7.16 (s, 2H, Ar*H*), 7.13 (s, 2H, Ar*H*), 4.57 (t, 4H, J = 7.9 Hz, ArC*H*), 3.69 (t, 8H, J = 6.3 Hz, CH_2OH), 2.29 (m, 2H, ArCHCH_2(CH$_2$)$_2$OH), 2.14 (m, 6H, CH_2 CH$_2$CH$_3$), 1.88 (s, 12H, ArCH_3), 1.54 (m, 2H, CH_2 CH$_2$OH),1.28 (m, 6H, CH$_2$CH_2 CH$_3$), 0.94 (t, 9H, J = 7.2 Hz, CH$_2$CH_3), 0.48 (s, 12H, SiCH_3 out), -0.73 (s, 12H, SiCH_3 in). **^{13}C NMR** (DMSO-d_6, 100 MHz,) δ (ppm): 148.41, 148.30, 148.27, 131.47, 131.24, 131.05, 130.89, 119.95, 119.84, 119.22, 119.11, 62.95, 35.36, 35.18, 31.64, 29.24, 21.25, 14.19,

14.16, 10.59, 1.07, -3.02, -6.29. **ESI-MS**: m/z 953.44 $[M+H]^+$; m/z 953.44 $[M+Na]^+$.

Cavitand Sylil[3C_3H_7, C_3H_6OCOPyrene; CH_3]. (34)

To a solution of 1-pyrene carboxylic acid (387 mg, 1.57 mmol) dissolved in 5 mL of dry CH_2Cl_2, EDAC (302 mg, 1.57 mmol) and DMAP (384 mg, 3.15 mmol) were added. Then silylcavitand **33** (1 g, 1.05 mmol) was added and the resulting mixture was stirred at room temperature overnight. The crude was purified by column chromatography on silica gel by using CH_2Cl_2:Hexane=8:2 as eluant to give compound **34** as brown powder in 95% yield.

^{1}H NMR ($CDCl_3$, 400 MHz) δ (ppm): 9.26 (d, 1H, J = 9.44 Hz, Py*H*), 8.60 (d, 1H, J = 8.1 Hz, Py*H*), 8.17-7.94 (m, 7H, Py*H*), 7.33 (s, 2H, Ar*H*), 7.28 (s, 2H, Ar*H*), 4.83 (t, 1H, J = 8.0 Hz, ArC*H*$(CH_2)_3$OCOPy), 4.72-4.62 (m, 2H + 3H, RC*H*$_2$OCOPy + ArC*H*$(CH_2)_2CH_3$), 2.55 (m, 2H, ArCHC*H*$_2$ $(CH_2)_2$OCOPy), 2.26 (m, 6H, C*H*$_2CH_2CH_3$), 1.98 (m, 12H + 2H, ArC*H*$_3$ + C*H*$_2$ CH_2OCOPy), 1.36 (m, 2H, CH_2C*H*$_2CH_3$), 0.98 (m, 9H, CH_2C*H*$_3$), 0.57 (s, 12H, SiC*H*$_3$ out), -0.63 (s, 12H, SiC*H*$_3$ in). **^{13}C NMR** ($CDCl_3$, 100 MHz) δ (ppm): 168.11, 148.66, 148.48, 148.43, 134.23, 131.58, 131.33, 131.15, 131.13, 130.95, 130.76, 130.33, 129.52, 129.36, 128.39, 127.11, 126.23, 126.12, 124.90, 124.76, 124.13, 124.07, 123.67, 120.05, 119.87, 119.46, 119.22, 65.38, 53.50, 35.43, 35.26, 35.75, 29.86, 27.70, 21.34, 14.29, 14.24, 10.70, -2.94, -6.20. **HR-ESI-MS**: m/z 1181.4875 $[M+H]^+$.

Resorcinarene Res[3C_3H_7, C_3H_6OCOPyrene; CH_3]. (35)

To compound **34** (200 mg, 0.17 mmol) dissolved in 2 mL of DMF and in 2 mL of $CHCl_3$ in a Teflon flask, 400 μL of an aqueous 48% HF solution was added. After 18 hours of stirring at 45 °C the solvent was removed under vacuum. The crude product was sonicated in distilled water, filtered and dried to give resorcinarene **35** as a brown powder in a 98% yield.

^{1}H NMR (Acetone-*d*$_6$, 400 MHz) δ (ppm): 9.24 (d, 1H, J = 9.44 Hz, Py*H*), 8.63 (d, 1H, J = 8.1 Hz, Py*H*), 8.36-8.11 (m, 7H, Py*H*), 7.50 (s, 2H, Ar*H*), 7.41 (s, 2H, Ar*H*), 4.50 (m, 1H + 2H, ArC*H*$(CH_2)_3$OCOPy

+ RC*H*$_2$OCOPy), 4.36 (m, 3H, ArC*H*(CH$_2$)$_2$CH$_3$), 2.54 (m, 2H, ArCHC*H*$_2$(CH$_2$)$_2$OCOPy), 2.24 (m, 6H, C*H*$_2$CH$_2$CH$_3$), 2.01 (s, 12H, ArC*H*$_3$), 1.85 (m, 2H, C*H*$_2$CH$_2$OCOPy), 1.23 (m, 6H, C*H*$_2$ CH$_3$), 0.84 (m, 9H, CH$_2$C*H*$_3$). **^{13}C NMR** (Acetone-*d*$_6$, 100 MHz) δ (ppm): 167.42, 161.94, 149.69, 149.56, 149.50, 134.28, 131.12, 130.79, 130.38, 129.68, 129.34, 128.30, 127.22, 126.66, 126.54, 126.28, 124.95, 124.75, 124.70, 124.59, 124.40, 124.35, 123.98, 121.43, 121.38, 111.3891, 111.1714, 65.1131, 35.76, 35.29, 34.29, 34.05, 30.15, 27.38, 20.98, 20.94, 13.46, 8.99, 8.97. **HR-ESI-MS**: m/z 979.4360 [M+Na]$^+$.

Cavitand T$_{iii}$[3C$_3$H$_7$, C$_3$H$_6$OCOPyrene; CH$_3$, Ph]. (36)

To a solution of **35** (150 mg, 0.33 mmol) in freshly distilled pyridine (20 mL) dichlorophenylphosphine (190 μL, 1.40 mmol) was added slowly, at room temperature. After 3 hours of stirring at 80 °C, the solution was allowed to cool at room temperature and 6 mL of a mixture of aqueous 50% H$_2$O$_2$ and CHCl$_3$ (1:1) was added. The resulting mixture was stirred for 30 minutes at room temperature, then the solvent was removed under reduced pressure and distilled water was added. The precipitate obtained in this way was collected by vacuum filtration, to give the product in 10% yield.

^{1}H NMR (CDCl$_3$, 400 MHz) δ (ppm): 9.23 (d, 1H, J = 9.4, Py*H*), 8.59 (d, 1H, J = 8.1, Py*H*), 8.94-7.96 (m, 7H + 8H, Py*H* + P(O)*H*$_o$), 7.65-7.43 (m, 4H + 8H, P(O)*H*$_p$ + P(O)*H*$_m$), 7.25 (m, 2H, Ar*H*), 7.21 (m, 2H, Ar*H*), 4.91 (t, 1H, J = 7.6 Hz, ArC*H* (CH$_2$)$_3$OCOPy), 4.78 (m, 3H, ArC*H*(CH$_2$)$_3$CH$_3$), 4.64 (t, 2H, RC*H*$_2$OCOPy), 2.60 (m, 2H, ArCHC*H*$_2$(CH$_2$)$_2$OCOPy), 2.31 (m, 6H, C*H*$_2$CH$_2$CH$_3$), 2.12 (s, 12H, ArC*H*$_3$), 2.02 (m, 2H, C*H*$_2$CH$_2$OCOPy), 1.40 (m, 6H, C*H*$_2$ CH$_3$), 1.00 (m, 9H, CH$_2$C*H*$_3$). **^{13}C NMR** (CDCl$_3$, 100 MHz) δ (ppm): 207.23, 168.12, 145.19, 145.08, 134.61, 134.42, 134.21, 133.86, 133.55, 131.59, 131.49, 131.22, 131.01, 130.33, 129.82, 129.57, 128.94, 128.87, 128.78, 128.71, 128.32, 127.15, 126.48, 126.45, 126.28, 125.78, 125.53, 124.88, 124.73, 124.18, 124.07, 123.39, 119.23, 119.04, 64.93, 36.55, 36.40, 33.27, 31.45, 30.98, 29.72, 28.22, 27.32, 21.01, 14.05, 14.01, 11.53. **^{31}P NMR** (CDCl$_3$/D$_2$O, 162 MHz) δ (ppm): 8.87 (s, 4P, *P* = O). **HR-ESI-MS**: m/z 1467.4182 [M+Na]$^+$.

Cavitand Sylil[$(CH_2)_3OCO(CH_2)_3$Pyrene; CH_3]. (37)

To a solution of 1-pyrene butyric acid (507 mg, 1.76 mmol) dissolved in 15 mL of dry CH_2Cl_2, EDAC (459 mg, 2.40 mmol) and DMAP (586 mg, 4.79 mmol) were added. Then silylcavitand **28** (400 mg, 0.40 mmol) was added and the resulting mixture was stirred at room temperature overnight. The crude was purified by column chromatography on silica gel by using CH_2Cl_2:EtOH=99:1 as eluant to give compound **37** as brown powder in 76% yield.

^{1}H NMR ($CDCl_3$, 400 MHz) δ (ppm): 8.15 (d, 4H, J = 9.2 Hz, Py*H*), 8.07-8.04 (m, 8H, Py*H*), 7.95-7.97 (m, 20H, Py*H*), 7.68 (d, 4H, J = 7.6 Hz, Py*H*), 7.13 (s, 4H, Ar*H*), 4.63 (t, 4H, J = 8.4 Hz, ArC*H*), 4.09 (t, 8H, J = 6.6 Hz, RC*H*$_2$OCO$(CH_2)_3$Py), 3.22 (t, 8H, J = 7.8 Hz, RC*H*$_2$Py), 2.30 (t, 8H, J = 7.2 Hz, ROCOC*H*$_2(CH_2)_2$Py), 2.25 (m, 8H, ArCHC*H*$_2(CH_2)_2$OCO), 2.04 (m, 8H, RC*H*$_2CH_2$Py), 1.89 (s, 12H, ArC*H*$_3$), 1.60 (m, 8H, RC*H*$_2CH_2$OCO), 0.50 (s, 12H, SiC*H*$_3$ out), -0.70 (s, 12H, SiC*H*$_3$ in). **^{13}C NMR** ($CDCl_3$, 100 MHz) δ (ppm): 173.48, 148.69, 135.74, 131.38, 130.90, 130.81, 129.91, 128,68, 127.49, 127.35, 127.28, 126.63, 125.76, 125.03, 124.96, 124.80, 123.30, 119.75, 119.43, 64.28, 35.08, 33.80, 32.72, 29.44, 27.31, 26.75, 10.69, -2.94, -6.16. **HR-ESI-MS**: m/z 2103.8198 $[M+Na]^+$.

Resorcinarene Res[$(CH_2)_3OCO(CH_2)_3$Pyrene; CH_3]. (38)

To compound **37** (637 mg, 0.31 mmol) dissolved in 4 mL of DMF and in 4 mL of $CHCl_3$ in a Teflon flask, 640 μL of an aqueous 48% HF solution was added. After 18 hours of stirring at 45 °C the solvent was removed under vacuum. The crude product was sonicated in distilled water, filtered and dried to give resorcinarene 12 as a brown powder in a 98% yield.

^{1}H NMR (Acetone-*d*$_6$, 400 MHz) δ (ppm): 8.27 (d, 4H, J = 9.6, Py*H*), 8.17-8.12 (m, 8H, Py*H*), 8.06-7.93 (m, 20H, Py*H*), 7.74 (d, 4H, J = 7.6, Py*H*), 7.50 (s, 4H, Ar*H*), 4.43 (t, 4H, J = 7.6 Hz, ArC*H*), 4.04 (t, 8H, J = 6.6 Hz, RC*H*$_2$OCO$(CH_2)_3$Py), 3.23 (t, 8H, J = 7.8 Hz, RC*H*$_2$Py), 2.38 (m, 8H, ArCHC*H*$_2(CH_2)_2$OCO), 2.30 (t, 8H, J = 7 Hz, ROCOC*H*$_2$ $(CH_2)_2$Py,), 2.05 (s under Acetone-*d*$_6$ peak, 12H, ArC*H*$_3$), 1.98 (m, 8H, RC*H*$_2CH_2$Py), 1.58 (m, 8H, RC*H*$_2CH_2$OCO).

^{13}C NMR (Acetone-d_6, 100 MHz,) δ (ppm): 172.71, 162.02, 149.81, 136.14, 131.36, 130.88, 129.84, 128.55, 127.43, 127.40, 127.23, 126.55, 126.52, 125.90, 124.86, 124.83, 124.80, 124.77, 124.72, 124.54, 123.33, 121.24, 111.65, 63.87, 50.76, 35.32, 34.25, 33.17, 32.27, 30.22, 29.96, 29.76, 27.34, 26.82. **HR-ESI-MS**: m/z 1874.8259 $[M+NH_4]^+$.

Cavitand T$_{iii}$[$(CH_2)_3OCO(CH_2)_3$Pyrene; CH_3]. (39)

To a solution of **38** (628 mg, 0.34 mmol) in freshly distilled pyridine (5 mL) dichlorophenylphosphine (193 μL, 1.42 mmol) was added slowly, at room temperature. After 3 hours of stirring at 80 °C, the solution was allowed to cool at room temperature and 6 mL of a mixture of aqueous 50% H_2O_2 and $CHCl_3$ (1:1) was added. The resulting mixture was stirred for 30 minutes at room temperature, then the solvent was removed under reduced pressure and distilled water was added. The precipitate obtained in this way was collected by vacuum filtration and purified by preparative TLC on silica gel by using CH_2Cl_2:MeOH=9.5:0.5 as eluant to give compound **39** as yellow powder in 25% yield.

^{1}H NMR ($CDCl_3/D_2O$, 400 MHz) δ (ppm): 8.13 (d, 4H, J = 9.2, Py*H*), 8.08-8.02 (m, 8H + 8H, Py*H* + P(O)H_o), 7.96-7.86 (m, 20H, Py*H*), 7.67 (d, 4H, J = 7.8, Py*H*), 7.62 (m, 4H, P(O)H_p), 7.52 (m, 8H, P(O)H_m), 7.16 (s, 4H, Ar*H*), 4.77 (t, 4H, J = 7.6 Hz, ArC*H*), 4.15 (t, 8H, J = 6.4 Hz, RCH_2OCO$(CH_2)_3$Py), 3.22 (t, 8H, J = 7.7 Hz, RCH_2 Py), 2.33 (m, 8H + 8H, ArCHCH_2 $(CH_2)_2$OCO) + ROCOCH_2 $(CH_2)_2$Py), 2.11 (s, 12H, ArCH_3), 2.06 (m, 8H, RCH_2 CH_2Py), 1.86 (m, 8H, RCH_2 CH_2OCO). **^{13}C NMR** ($CDCl_3/D_2O$, 100 MHz) δ (ppm): 173.50, 145.34, 145.23, 135.50, 133.98, 133.66, 131.59, 131.48, 131.33, 130.77, 129.91, 128.96, 128.80, 128.62, 127.40, 127.32, 127.17, 126.71, 126.39, 125.83, 124.99, 124.92, 124.88, 124.74, 124.38, 123.13, 119.28, 63.85, 53.49, 36.44, 33.79, 32.65, 29.73, 27.75, 27.06, 26.70, 11.54. **^{31}P NMR** ($CDCl_3/D_2O$, 162 MHz) δ (ppm): 9.09 (s, 4P, *P* = O). **ESI-MS**: m/z 2362.8048 $[M+NH_4]^+$.

Cavitand TS$_{iiii}$[$(CH_2)_3OCO(CH_2)_3$Pyrene; CH_3]. (40)

To a solution of **38** (325 mg, 0.18 mmol) in freshly distilled pyridine (3 mL), dichlorophenylphosphine (100 μL, 0.73 mmol) was added slowly, at room temperature. After stirring for 3 hours at 90 °C, S_8 (54 mg, 0.21 mmol) was added and the mixture was stirred again for 5 hours. The solvent was removed under vacuum and distilled water was added. The precipitate obtained in this way was collected by vacuum filtration and purified by preparative TLC on silica gel by using CH_2Cl_2:MeOH=99:1 as eluant to give compound **40** as yellow powder in 24% yield.

^{1}H NMR ($CDCl_3$, 400 MHz) δ (ppm): 8.21-7.87 (m, 32H + 8H, Py*H* + P(O)H_o), 7.66 (d, 4H, J = 7.8, Py*H*), 7.57 (m, 4H, P(O)H_p), 7.51 (m, 8H, P(O)H_m), 7.20 (s, 4H, Ar*H*), 4.74 (t, 4H, J = 7.6 Hz, ArC*H*), 4.15 (t, 8H, J = 6.5 Hz, RCH_2 OCO$(CH_2)_3$Py), 3.22 (t, 8H, J = 7.7 Hz, RCH_2 Py), 2.10 (s, 12H, ArCH_3), 2.06 (m, 8H, RCH_2 CH_2Py), 1.68 (m, 8H, RCH_2 CH_2OCO). **^{13}C NMR** ($CDCl_3$, 100 MHz) δ (ppm): 173.44, 146.01, 145.91, 135.56, 134.13, 133.11, 132.65, 131.51, 131.34, 130.90, 130.80, 129.91, 128.64, 128.60, 128.45, 127.42, 127.32, 127.21, 127.09, 126.68, 125.81, 125.00, 124.89, 124.75, 123.17, 118.53, 63.99, 36.26, 33.77, 32.66, 28.33, 27.13, 26.70, 12.94. **^{31}P NMR** ($CDCl_3$, 162 MHz) δ (ppm): 75.85 (s, 4P, *P*=S). **HR-ESI-MS**: m/z 2426.7134 $[M+NH_4]^+$.

T$_{iiii}$39•SWCNT.

We prepared the SWCNT dispersion in tetraphosphonate cavitand **39** solution by firstly ultrasonicating purified SWCNT (5mg) in 5 mL of DMF for 30 minutes, then adding T$_{iiii}$**39** (15 mg, 6.51 mmol) in 1 mL of DMF and further ultrasonicating for 1 hours followed by stirring overnight. The mixture was, then, purified by high speed centrifugation (14000 rpm, 5 min) adding CH_2Cl_2 to promote the precipitation and sonication (5 min) and to remove the excess of cavitand. The steps of sonication and centrifugation were repeat 5 times. The composite was characterized by XPS, TGA and IR already reported in the Results and Discussion Paragraph.

TS$_{iiii}$40•SWCNT.

We prepared the SWCNT dispersion in tetraphosphonate cavitand **40** solution by firstly ultrasoicating purified SWCNT (5mg) in 5 mL of DMF for 30 minutes, then adding TS$_{iiii}$**40** (15.7 mg, 6.51 mmol) in 1 mL of DMF and further ultrasonicating for 1 hours followed by stirring overnight. The mixture was, then, purified by high speed centrifugation (14000 rpm, 5 min) adding CH_2Cl_2 to promote the precipitation and sonication (5 min) and to remove the excess of cavitand. The steps of sonication and centrifugation were repeat 5 times. The composite was characterized by XPS, TGA and IR already reported in the Results and Discussion Paragraph.

T$_{iiii}$39•SWCNT$_{mix}$.

This composites was prepared with the same procedure reported for the T$_{iiii}$**39**•SWCNT synthesis in 1:0.1, 1:0.5, 1:1 and 1:1.5 (SWCNT:T$_{iiii}$**39**) ratios. In this case the composites were not purified and the DMF was removed in vacuum.

Composite	T$_{iiii}$39	SWCNT
T$_{iiii}$**39**•SWCNT - **0.1**	0.92 mg, 0.39 mmol	3mg
T$_{iiii}$**39**•SWCNT - **0.5**	4.58 mg, 1.95 mmol	3mg
T$_{iiii}$**39**•SWCNT - **1**	9.17 mg, 3.91 mmol	3mg
T$_{iiii}$**39**•SWCNT - **1.5**	13.75 mg, 5.86 mmol	3mg

The composite was characterized by XPS, TGA, IR and Fluorescence already reported and discussed in the Results and Discussion Paragraph.

TS$_{iiii}$40•SWCNT$_{mix}$.

This composites was prepared with the same procedure reported for the T$_{iiii}$**40**•SWCNT synthesis in 1:0.1, 1:0.5, 1:1 and 1:1.5 (SWCNT:T$_{iiii}$**40**) ratios. In this case the composites were not purified and the DMF was removed in vacuum.

Composite	TSiiii**40**	SWCNT
TSiiii**40**•SWCNT - **0.1**	0.94 mg, 0.39 mmol	3mg
TSiiii**40**•SWCNT - **0.5**	4.70 mg, 1.95 mmol	3mg
TSiiii**40**•SWCNT - **1**	9.43 mg, 3.91 mmol	3mg
TSiiii**40**•SWCNT - **1.5**	14.13 mg, 5.86 mmol	3mg

The composite was characterized by XPS, TGA, IR and Fluorescence reported and discussed in the Results and Discussion Paragraph.

4.6 References.

[1] S. Bodmer, C. Imark and M. Kneubühl, Biogenic amines in foods: Histamine and food processing, *Inflamm. Res.* **1999**, *48*, 296-300.

[2] L. Bogani, C. Danieli, E. Biavardi, N. Bendiab, A.-L. Barra, E. Dalcanale, W. Wernsdorfer, A. Cornia, Single-Molecule-Magnet Carbon-Nanotube Hybrids, *Angew. Chem., Int. Ed.* **2009**, 746-750.

[3] Y.-L. Zhao, L. Hu, J. F. Stoddart, G. Grüner, Pyrenecyclodestrin-decorated Single-Walled Carbon Nanotube Field-Effect Transistor as Chemical Sensors, *Adv. Mater.* **2008**, *20*, 1910-1915.

[4] R. De Zorzi, B. Dubessy, J.-C. Mulatier, S. Geremia, L. Randaccio and J.-P. Dutasta, Structure of a 4:1:4 Supramolecular Assembly of Neutral TiiiiPO Cavitands and Tetrakis(N-methylpyridinium)porphyrin Iodide, *J. Org. Chem.* **2007**, *72*, 4528.

[5] J.-P. Dutasta, New Phosphorylated Hosts for the Design of New Supramolecular Assemblies, *Top. Curr. Chem.* **2004**, *232*, 55.

[6] E. Kalenius, D. Moiani, E. Dalcanale and P. Vainiotalo, Measuring H-bonding in supramolecular complexes by gas phase ion–molecule reactions, *Chem. Commun.* **2007**, 3865.

[7] L. Pirondini, D. Bonifazi, E. Menozzi, E. Wegelius, K. Rissanen, C. Massera, E. Dalcanale, Synthesis and Coordination Chemistry of Lower Rim Cavitand Ligands, *Eur. J. Org. Chem.* **2001**, 2311-2320.

[8] a) F. Hauke, A. J. Myles, J. Rebek, *Chem. Commun.* **2005**, 4164-4166
b) R. M. Yebeutchou, F. Tancini, N. Demitri, S. Geremia, R. Mendichi, E. Dalcanale, Host-Guest Driven Self-Assembly of Linear and Star Supramolecular Polymer, *Angew. Chem., Int. Ed.* **2008**, *47*, 4504-4508.

[9] M. Melegari, M. Suman, L. Pirondini, D. Moiani, C. Massera, F. Ugozzoli, E. Kalenius, P. Vainiotalo, J.-C. Mulatier, J.-P. Dutasta, E. Dalcanale; Supramolecular sensing with phosphonate cavitands, *Chem. Eur. J.* **2008**, *14*, 5772-5779.

[10] In the case of the T$_{iii}$**40**•SWCNT the vibration stretching bands of the P=S is at 741.58 cm^{-1}.

[11] I calculated the flows to obtain a final relative humidity (RH) of 30% but I got 60%. I think that the humidity sensor did not work very well.

[12] See Chapter 1, 2 and 3 for the complexation properties of tetraphosphonate cavitands. Synthsis reported in Chapter 3.

[13] For all the sensors both in vapor phase and in solution.

[14] a) C. Heitner-Wirguin, Recent advances in perfluorinated ionomer membranes: structure, properties and applications, J. of Membrane Science **1996**, *120*, 1-33.
b) K. A. Mauritz, R. B. Moore, State of Understanding of Nafion, *Chem. Rev.* **2004**, *104*, 4535-4586.

Molecular Magnetism:
Introduction.

5

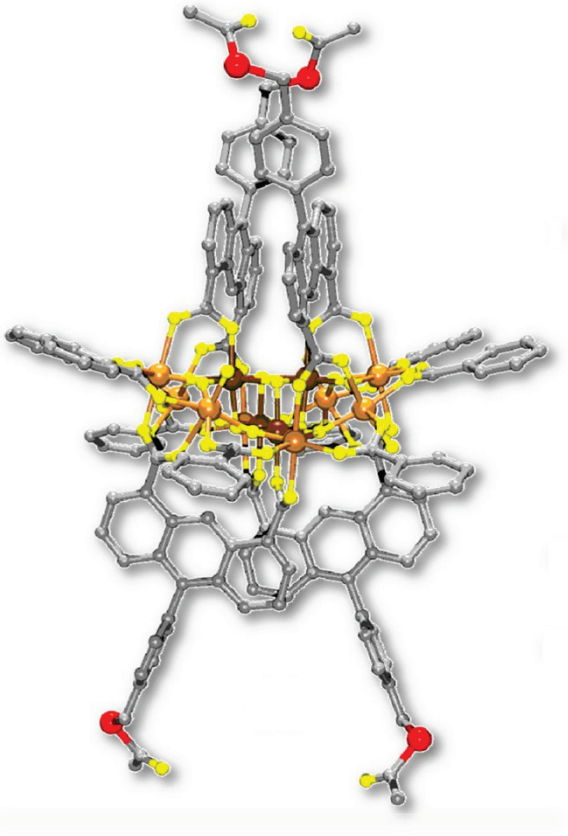

Mn12-Anth[1]

"Single Molecule Magnets open a new door for Information Technology"

5.1 Towards Molecular Magnetism.

Molecular magnetism is a relatively recent scientific field which originated from the transformation of Magnetochemistry in an interdisciplinary area, where chemists and physicists started to collaborate very closely with the stated goal of designing, synthesizing, and characterizing the magnetic properties of molecular based materials. The idea of using molecules, rather than the ionic and metallic lattices of typical magnets, stems from the rapid development of functional molecular materials which started in the second half of the 20th century.

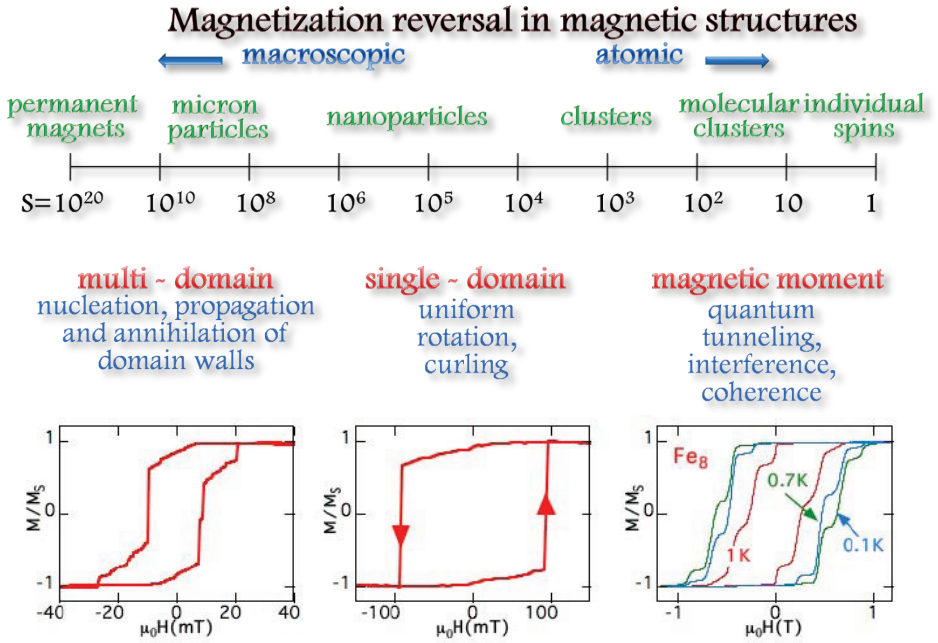

Figure 5.1. Scale of size that goes from macroscopic down to nanoscopic sizes.

A deeper understanding of the magnetic phenomena in the condensed matter and an increasing ability in manipulating molecules were the two essential ingredients for the birth and the development of this new subject.

What is really interesting and fascinating in molecular magnetic materials is that they, on one side, some of them show magnetic hysteresis as ordinary magnets and, on the other side, they are small enough to show quantum

effects. This combination of classical and quantum aspects is very attractive from the theoretical point of view since it provide new challenging questions, but it can have also many technological implications, especially in the fields of data storage and quantum computation.

For this reason, during the years, the attention of the scientists was turned towards the development of magnetic materials of smaller size. In figure 5.1 was reported a scale of size that spans from macroscopic down to nanoscopic sizes in which the scale unit is the number of magnetic moments in a magnetic system (roughly corresponding to the number of magnetic atoms).[2] At macroscopic sizes, a magnetic system is described by magnetic domains that are separated by domain walls. Magnetization reversal occurs via nucleation, propagation, and annihilation of domain walls (Figure 5.1, hysteresis loop on the left). The shape and width of domain walls depend on the magnetic material, on its size, shape and surfaces, and on its temperature.[3] The material dependence on the domain walls led to the definition of two length scales: the domain wall width δ (eq. 5.1) and the exchange length λ (eq. 5.2), where A is the exchange energy, K is the crystalline anisotropy constant and M_s is the spontaneous magnetization.

$$\delta = \sqrt{\frac{A}{K}} \qquad \text{(eq. 5.1)}$$

$$\lambda = \frac{\sqrt{A}}{M_S} \qquad \text{(eq. 5.2)}$$

Qualitatively, the equation 5.1 shows that anisotropy energy favors a thin wall, while the exchange energy favors a thick wall. For very small crystalline anisotropy, the equation 5.1 suggests an infinite domain wall width which has a large total energy. This is due to the magnetostatic energy term that can be reduced by subdividing the ferromagnetic crystal into domains. Therefore, for very small crystalline anisotropy, the domain wall width is of the order of magnitude of the exchange length λ. Both length scales can range from submicrometer scales in alloys to atomic scales in rare earth system.

When the system size is comparable to the domain wall width (δ) or the exchange length (λ), the formation of domain walls requires too much energy. Therefore, the magnetization remains in the so-called single-domain state, and the magnetization reverses by uniform rotation, curling or other nonuniform modes (Figure 5.1, hysteresis loop in the middle).

For system size well below δ and λ, like free clusters made of several atoms or molecular clusters which are structures with a central complex containing magnetic atoms, one must take into account the magnetic moment (spins) and their coupling.[4] By means of simple hysteresis loop measurements, the quantum character of these molecules showed up in well-defined steps which are due to resonant quantum tunneling between the energy level (Figure 5.1, hysteresis loop on the right). Single Molecule Magnets belong to these last systems.

5.2 The different types of magnetic behavior.

The magnetic properties are linked to the orbital and spin motions of the atomic electrons.

On the atomic level there exist two fundamental types of magnetism: diamagnetism and paramagnetism. All the more complex magnetic behavior evolve from these basic magnetic phenomena.[5]

Diamagnetic behavior is characteristic of *"closed shell"* systems. They present a very low magnetic moment in the opposite direction with respect to the applied magnetic field H ($-10^{-5} < \chi_m < -10^{-3}$).

All atomic or molecular materials exhibit diamagnetic behavior, which is completely obscured in the others kind of magnets by the paramagnetic, ferromagnetic, antiferromagnetic and ferrimagnetic contribution. For this reason, the diamagnetic term is usually estimated as a sum of tabulated atomics contributions (called Pascal's constants), characteristic of the atom, and subtracted to the measured susceptibility (χ_m):

$$\chi = \chi_m - \sum Pascal's\ constants.$$

Moreover, the magnetic susceptibility (χ) is independent of temperature (T) and magnetic field (H). This because the diamagnetic response is due to the effect of the applied field on the electron orbital motion and so, aspecific by nature.

The magnetic susceptibility is the quantitative measure of the response of a material to an applied magnetic field.

Paramagnetic behavior, on the other hand, is characteristic of *"open-shell"* materials that include transition metal and rare earths, mostly of which have unpaired *d* or *f* electrons. In the first case, the decrease of the intermolecular interactions is often due to the presence of hindered ligands around the metallic ion. In the second case, the 4*f* electrons responsible of the magnetic properties are shielded by the electrons of the subshells 5*s* and 5*p*, which are completely occupied.

Therefore, paramagnetic materials consist of noninteracting magnetic centers (Figure 5.2) which generate a macroscopic magnetic moment μ_{tot} only in the presence of an applied magnetic field (H) ($10^{-5} < \chi_m < 10^{-3}$).

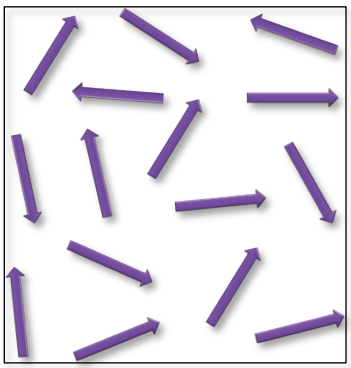

Figure 5.2. Paramagnetic behavior.

The value of $\mu_{tot} = |\mu_{tot}|$ depends first of all on the intensity of the applied field, which is responsible of the partial alignment of the magnetic dipole inside the material. Moreover, it depends strongly on the absolute temperature (T) since the thermal motion favors a random orientation of the

magnetic moments. Finally, if the material is magnetically anisotropic, its properties vary according to the applied direction of *H*.

There are many other types of magnetic behavior most of which can be considered a variation of the four main magnetic behaviors: paramagnetism, ferromagnetism, antiferromagnetism and ferrimagnetism.[4]

Ferromagnetic, antiferromagnetic and ferrimagnetic materials are special types of paramagnetic stuffs because they show paramagnetic behavior above their characteristic critical temperature (T_c or T_N), but beneath it they show a spontaneous alignment of the magnetic spins. In particular, the paramagnetic behavior is due to the fact that the thermal motion breaks the order causing a random orientation of the magnetic spins.

Ferromagnetism is characterized by parallel alignment of adjacent magnetic spins which is due to the interactions between the different centers, called exchange interactions (Figure 5.3).

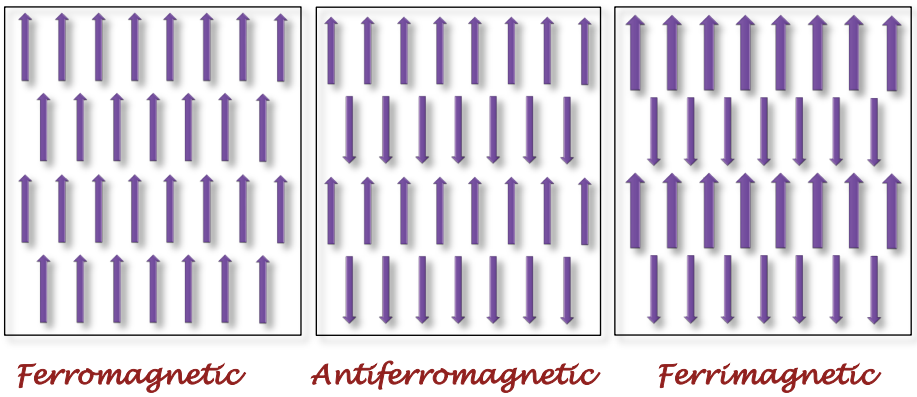

Figure 5.3. Ferromagnetic, antiferromagnetic and ferrimagnetic behavior.

Beneath the Curie's Temperature (T_c), the material "orders" magnetically developing a spontaneous magnetization even without an applied magnetic field ($\chi_m \sim 10^3$-10^4). With the decreases of T beneath T_c the magnetization quickly increases approaching the saturation value. Anyway, at T beneath T_c and in the absence of an applied magnetic field, the macroscopic moment is zero as a result of the presence in ferromagnetic materials of magnetic domains (Figure 5.4). Each of these domains has a net magnetization but, even so, the material results apparently not magnetized

because of the averaging to zero due to random orientation of the magnetic domains within the sample.

These materials show a magnetic *hysteresis loop* in presence of an applied magnetic field and beneath the T_c. In particular, when a ferromagnetic material is magnetized in one direction, it will not relax back to zero magnetization when the imposed magnetizing field is removed. It must be driven back to zero by a field in the opposite direction.

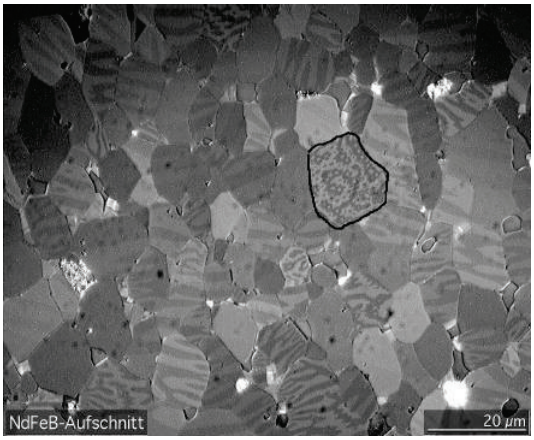

Figure 5.4. Photomicrograph of NdFeB, the magnetic material used to make neodymium rare earth magnets, showing the magnetic domain structure made visible via contrast with a Kerr-microscope.

Therefore, the hysteresis of a sample is determined by looking at magnetization as a function of an applied magnetic field. A typical hysteresis curve for a magnetic material is shown in Figure 5.5.

The lack of retraceability of the magnetization curve is the property called hysteresis and it is related to the existence of magnetic domains in the material. Once the magnetic domains are reoriented, it takes some energy to turn them back again. This property of ferromagnetic materials is useful as a magnetic "memory". Some compositions of ferromagnetic materials will retain an imposed magnetization indefinitely and are useful as "permanent magnets". The magnetic memory aspects of iron and chromium oxides make them useful in audio tape recording and for the magnetic storage of data on computer disks.

A ferromagnetic material that has never been previously magnetized will follow the dashed line as H is increased. As the line demonstrates, the greater is the applied field ($H+$), stronger is the magnetization. At point "a" almost all of the magnetic domains are aligned and an additional increase in the magnetizing force will produce very little increase in magnetization. The material has reached the point of magnetic saturation (M_s).

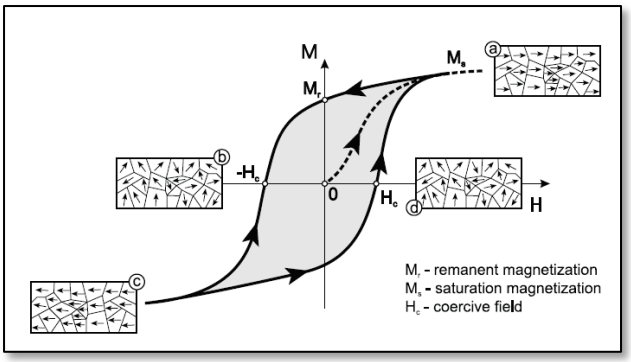

Figure 5.5. A typical Hysteresis loop.

When H is reduced to zero, the curve will move from "a" point to M_r point. At this point, it can be seen that some magnetization remains in the material even though the applied field is zero. This is the retentivity point and indicates the level of residual magnetization (M_r) in the material due to the fact that some of the magnetic domains remain aligned.

As H is reversed, the curve moves to point "b" where the magnetization has been reduced to zero. The applied H required to remove the residual magnetization from the material is called the coercive field ($-H_c$).

As the applied field is increased in the negative direction, the material will again become magnetically saturated but in the opposite direction (point "c", $-M_s$).

Reducing H to zero the material will have a residual magnetization equal in absolute value to that achieved in the other direction ($-M_r$). Increasing H back in the positive direction the magnetization will return to zero. The curve does not return to the origin of the graph because some force is required to remove the residual magnetization.

Using the coercive field value we can do a rough classification of ferromagnetic materials in ***hard*** materials (H_c >100 Oe) and ***soft*** materials (H_c <100 Oe). Hard materials are used to produce permanent magnets, while soft materials for electromagnets, transformer, etc.

Antiferromagnetism is characterized by antiparallel alignment of the magnetic moments beneath the critical temperature, called Néel's Temperature (T_N) (Figure 5.3). As in paramagnetic materials, it is observed a macroscopic magnetic moment only in the presence of an applied magnetic field and there is no spontaneous magnetization.

Antiferromagnetism is the most commonly observed bulk magnetic behavior, and long-range antiferromagnetism is even exhibit by materials that order locally ferromagnetically.

Ferrimagnetism is a special case of antiferromagnetism and therefore characterized by antiparallel alignment of the magnetic moments beneath the T_c (Figure 5.3). However, since the adjacent spins are of different magnitudes, the resulting material exhibits a net magnetic moment in the absence of an applied magnetic field.

For our purposes, it is necessary to describe the ***superparamagnetic*** behavior.[6] It is characteristic of ferromagnetic and ferrimagnetic materials with size comparable or smaller than the domain walls thickness (particle size). The domain walls thickness changes from material to material, since it depends on the balance between the exchange energy, that promotes wide walls, and the magnetocrystalline energy, that promotes thin walls. However, the resulting width is typically on the order of 100nm.

For particles of size lower than 100nm, the gain in magnetostatic energy due to the splitting in domains it is not sufficient to offset the cost in exchange energy associate to the domain wall formation. So, these particles are *monodomain* and they show a very high magnetic moment.

For example, Fe particles of 40-50 Å have magnetic moment on the order of 10^4 μ_B. In these particles, there are often one or more "easy" directions along which the magnetic moment is preferentially aligned.

To rearrange the magnetic moment, it is necessary to overcome a energetic barrier, called anisotropy barrier, with a thermally activated process.

When the thermal energy is enough to overcome the anisotropy barrier, the magnetic moment is free to rearrange and the particle shows a behavior similar to that of a paramagnet but with a very big magnetic moment (superparamagnet). If the thermal energy is not enough, the particle magnetic moment remains confined in one of the easy directions, unless a sufficiently strong field is applied.

The particle shows magnetic hysteresis but, unlike in ferromagnetic materials, it is not due to the domain walls irreversibility but to the anisotropy barrier (see Subparagraph 5.6.2 and 5.6.3).

5.3 Dependence of magnetization on the applied field.

Field dependent behavior of an ideal paramagnet is well described by the *Brillouin function* ($B_s(x)$) which describes the magnetization without regard to the magnitude of H/k_BT.

The magnetic moment has contributions from both the total orbital angular momentum ($\mathbf{L}$) and the total spin angular momentum ($\mathbf{S}$) (eq. 5.3), but the orbital term is usually approximated and, for an isotropic paramagnet with spin $\mathbf{S}$, the macroscopic magnetic moment of each magnetic centers becomes:

$$\mu_{S+L} = g\sqrt{L(L+1) + 4S(S+1)} \qquad \text{(eq. 5.3)}$$

$$\mu = -g\mu_B \boldsymbol{S} \qquad \text{(eq. 5.4)}$$

where μ_B is the Bohr magneton, a physical constant, and g the Landé factor, whose value depend strongly on the spin-orbit coupling.

Such "spin-only formula" is justified by the fact that the orbital angular momentum is usually quenched by crystal field effects.[7] Comparison of theoretical value, determined using both $\mathbf{L}+\mathbf{S}$ and $\mathbf{S}$ expression, with experimental values for compounds of the di- and tri-valent first row transitions-metal ions, showed that the spin-only expression closely approximates the observed behavior[8].

Statistical thermodynamics shows that the molar magnetization, defined as $M_m = MW\mu_{tot}/m$ (with m = weight sample and MW=molecular weight), is:

$$M_m = N_A g \mu_B \boldsymbol{S} B_S(x) \qquad \text{(eq. 5.5)}$$

where N_A is the Avogadro's constant and $B_S(x)$ is the Brillouin function (eq. 5.6).

$$B_s(x) = \frac{2\boldsymbol{S}+1}{2\boldsymbol{S}} \coth\left(\frac{2\boldsymbol{S}+1}{2\boldsymbol{S}} x\right) - \frac{1}{2\boldsymbol{S}} coth\left(\frac{1}{2\boldsymbol{S}} x\right) \qquad \text{(eq. 5.6)}$$

with:

$$x = \frac{g\mu_B \boldsymbol{S} H}{k_B T} \qquad \text{(eq. 5.7)}$$

where k_B is the Boltzmann's constant and $H = |\boldsymbol{H}|$.

From the Brillouin equation we can deduce three "properties" of paramagnets:

1. when $x \rightarrow 0$, $B_s(x) \rightarrow x\frac{\boldsymbol{S}+1}{3\boldsymbol{S}}$ (eq. 5.8)

   and $k_B T >> g\mu_B \boldsymbol{S} H$ (**high temperature limit**)
   the molar magnetization becomes:

$$M_m = N_A g \mu_B \boldsymbol{S} x \frac{\boldsymbol{S}+1}{3\boldsymbol{S}} = \left[N_A \mu_B^2 g^2 \frac{\boldsymbol{S}(\boldsymbol{S}+1)}{3k_B}\right]\frac{H}{T} = C\frac{H}{T} \qquad \text{(eq. 5.9)}$$

   where C is the Curie's constant:

$$C = N_A \mu_B^2 g^2 \frac{S(S+1)}{3k_B} \qquad \text{(eq. 5.10)}$$

Therefore, *in the high temperature regime, the magnetization is proportional to H /T and,* according to the Curie's Law (eq. 5.12), *the magnetic susceptibility* (eq. 5.11) *is field independent and inversely proportional to the temperature* (see Paragraph 5.4).

$$\chi_m = \frac{M_m}{H} \qquad \text{(eq. 5.11)}$$

$$\chi_m = \frac{C}{T} \qquad \text{(eq. 5.12)}$$

2. when $x \to \infty$, $B_s(x) = 1$ (eq. 5.13)
   and $k_B T << g\mu_B SH$ (**low temperature limit**)
   the molar magnetization becomes:

$$M_m = N_A g \mu_B \boldsymbol{S} \qquad \text{(eq. 5.14)}$$

   The *eq. 5.14 expresses the maximum value of the molar magnetization*, called molar magnetization of saturation (M_m(sat)), that is reached when all the magnetic dipoles of the material are aligned with the magnetic field.

3. *The M_m value does not depend separately on H and T but only on their ratio.*

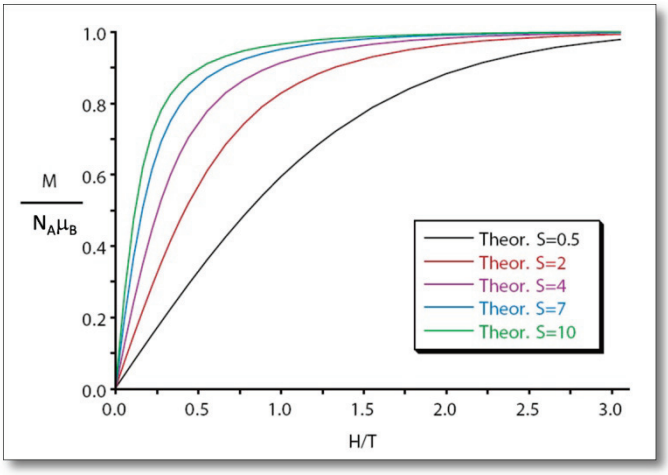

Figure 5.6. Theoretical Brillouin curves for ideal paramagnets with various **S** values are shown. Normalized magnetization is plotted against H / T. Systems with large **S** values saturate more quickly in response to increasing magnetic field than those with low values of **S**.

This means that if normalized magnetization, measured at different fields and temperatures, is plotted as a function of H/T, the experimental curve falls onto a universal curve that depend only on the **S** and g values (Figure 5.6). Any deviation from this behavior is due to the presence of anisotropy, intermolecular interactions or thermally accessible states with different spin.

In practice, this function allows us to determine the spin state of a paramagnet by measuring the field dependence of the magnetization at constant temperature.

5.4 Magnetic Susceptibility and its dependence on temperature.

Before considering the temperature dependence of a paramagnetic material, the concept of magnetic susceptibility (χ) must be defined. Magnetic susceptibility is the quantitative measure of the response of a material to an applied magnetic field. The definition of magnetic susceptibility is given in equation 5.11, while the Curie law (eq. 5.12) describes the temperature dependence of an ideal paramagnet.

All magnetic materials behave as paramagnets at high temperatures, because thermal energy overcomes the alignment and tosses the spins about randomly. The critical temperature of a material is the onset temperature for magnetic order. For a particular material the high and low temperature regimes are defined relative to the critical temperature, with the high temperature region lying above the critical temperature and the low temperature region lying below the critical temperature. A material does not exhibit cooperative magnetism (antiferromagnetism, ferromagnetism and ferrimagnetism) until below its critical point.

Typically, temperature dependant magnetism is observed by examining the susceptibility of a material as a function of temperature. In particular, analysis of the properties of a particular material are carried out by examining the temperature dependence of susceptibility, of the susceptibility-times-temperature product, and of the inverse susceptibility. Each of these analyses provides slightly different information about the cooperative magnetism of the material.

5.4.1 Susceptibility versus Temperature.

Typical plots for magnetic susceptibility as a function of temperature for ferromagnetic, paramagnetic, and antiferromagnetic materials are shown in Figure 5.7. In general, it is difficult to determine the type of magnetic interactions occurring in a sample from this plot.

The most useful information can be obtained for antiferromagnetic materials, which exhibit a maximum at low temperature. The temperature at which the maximum is observed provides information on the strength of the magnetic interactions, with stronger antiferromagnetic interactions occurring at higher temperatures. Magnetic interaction can occur in three dimension and the type and strength of these interactions can be different in each direction. The shape of the maximum suggests the dimensionality of the interactions: with one and two dimensional antiferromagnets marked by a rounded maximum and three dimensional antiferromagnets marked by a sharp peak.

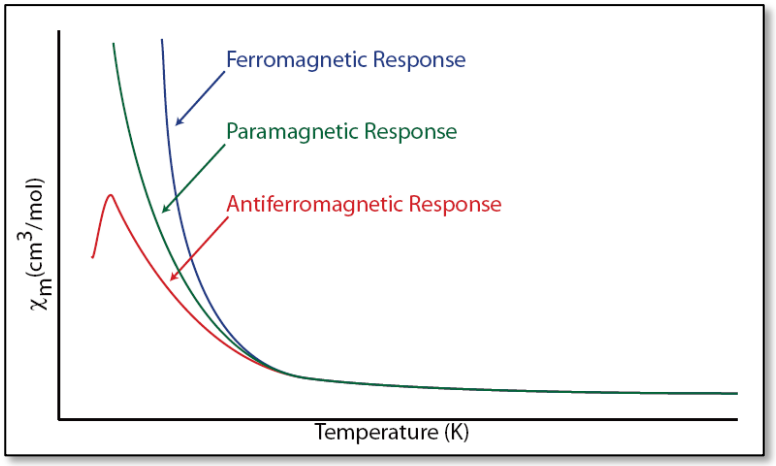

Figure 5.7. Magnetic susceptibility as a function of temperature for paramagnetic, ferromagnetic, and antiferromagnetic materials.

5.4.2 Susceptibility-Times-Temperature Product versus Temperature.

Analysis of the susceptibility-times-temperature product as a function of temperature provides information about the basic interactions occurring in magnetic materials. A typical plot of this product as a function of temperature is shown for an ideal paramagnet, ferromagnet, antiferromagnet, and ferrimagnet in Figure 5.8.

The temperature-times-susceptibility product of a paramagnetic material does not vary with temperature, while variations are observed for other types of magnetism. The invariant portion of $\chi_m T$ at high temperatures for all types of cooperative magnetism is due to the paramagnetic behavior of magnetic materials above their critical temperatures.

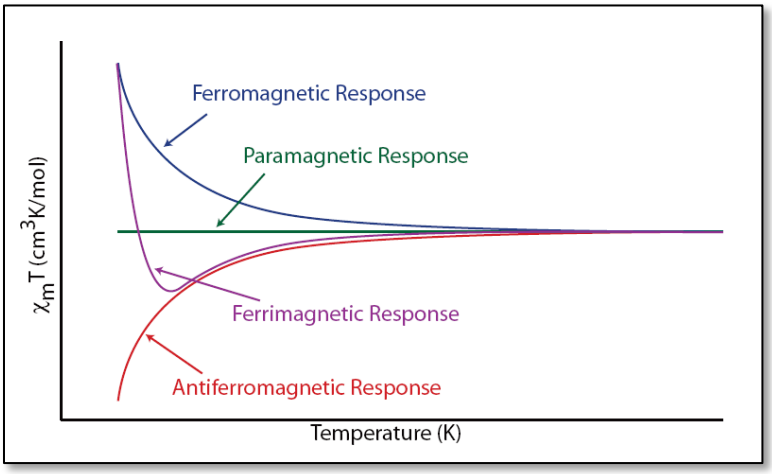

Figure 5.8. A typical plot for the susceptibility temperature product as a function of temperature is shown for paramagnetic, ferromagnetic, antiferromagnetic and ferrimagnetic materials.

Ferromagnetic materials display an upward deviation from the curve for an ideal paramagnet since the ferromagnetic interaction energy overcomes thermal energy. Conversely, antiferromagnetic interactions display downward curvature with the decrease of the temperature since the magnetic moment for the sample goes to zero.

For ferrimagnetic materials a slight downward curvature is first observed, due to interactions between adjacent magnetic moments, followed by an upward curvature due to an increasing spins correlation within the system.

5.4.3 Inverse Susceptibility versus Temperature.

An ideal paramagnet has a linear relationship between inverse susceptibility and temperature that intersects at zero as defined by the Curie law. Deviation from this linear relationship and the Curie law is observed for materials that exhibit cooperative magnetic effects.

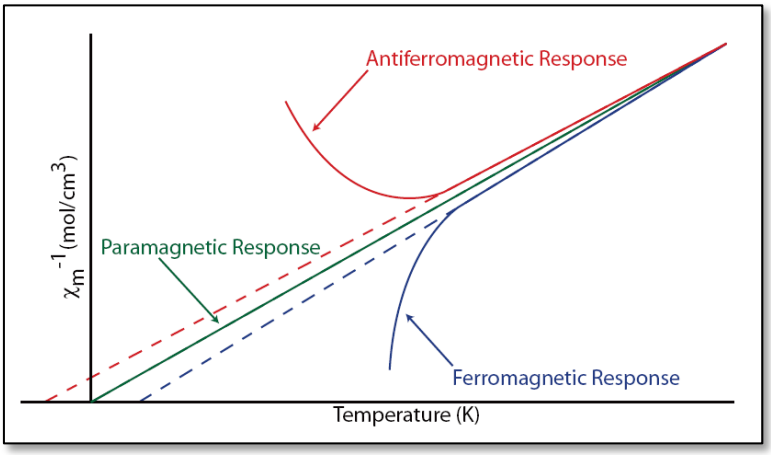

Figure 5.9. A plot of inverse susceptibility as a function of temperature is shown for a paramagnet, a ferromagnet, and an antiferromagent. The dotted lines indicate deviation of the high temperature data from the paramagnetic case.

As seen in Figure 5.9, a ferromagnetic material exhibits a downward deviation, while antiferromagnetic materials exhibits an upward deviations. In all cases the data at high temperature are linear, since thermal energy is greater than the energy of the magnetic interactions (paramagnetic behavior).

$$\chi = \frac{C}{T-\theta} \qquad \text{(eq. 5.15)}$$

A modification of the Curie law (eq. 5.12), known as the Curie-Weiss law (eq. 5.15), describes this deviation. The Weiss constant (θ) is

proportional to the strength of the magnetic interactions observed. Positive Weiss constants indicate ferromagnetic interactions, while negative Weiss constants indicate antiferromagnetic interactions. This framework is useful for looking at the predominant interaction in the material and the strength of that interaction.

5.5 Definition, Importance and Archetype of Single Molecule Magnets.

A single-molecule magnet (SMM) is a molecular material in which each molecule behaves as an individual superparamagnet; the molecules often consist of several transition metal ions linked by bridging ligands and surrounded by capping ligands.

The main feature of the single molecule magnets is the slow relaxation of the magnetization: the molecule can be magnetized in a magnetic field and it will remain magnetized even after switching off the magnetic field. This is a property of the molecule itself and no interaction between the molecules (as in ordinary bulk magnets) is necessary for this phenomenon to occur.

The requirements for observing the SMM behavior are: *a large spin in the ground state* and *a large magnetic anisotropy of the Ising type*, i.e. of the easy axis type.

The first molecule behaving as a SMM, and therefore considered the archetype of the Single Molecule Magnets, was reported in 1993 by the researchers D. Gatteschi , R. Sessoli , A. Caneschi and M. A. Novak who measured the relaxation time of the magnetization in a dodecanuclear manganese cluster[9] (Mn12Ac) of formula $[Mn_{12}O_{12}(CH_3COO)_{16}(H_2O)_4]\cdot 4H_2O\cdot 2CH_3COOH$ having a ground state $S = 10$ and synthesized the first time in 1980 by T. Lis[10]. The experiment gave a relaxation time of the order of a few months at a temperature of 2K and it was estimated of the order of 50 years at 1.5K.[11]

Mn12Ac shows also another characteristic properties of a magnet: the magnetic hysteresis of molecular origin. This behavior is due to the presence of the anisotropy barrier and it is characterized by steps, due to the quantum tunneling.

In the following years other single molecule magnets were discovered. The most famous among them is the cluster Fe8[12] ($\{[(C_6H_{15}N_3)_6Fe_8(\mu_3\text{-}O)_2(\mu_2\text{-}OH)_{12}]Br_7(H_2O)\}Br\cdot 8H_2O$) with $S = 10$, in which for the first time was experimentally observed the oscillation of the tunnel splitting (Figure 5.10). In fact if a field is applied parallel to the hard axis it is expected that the tunnel splitting goes through maxima and minima at regular intervals.[13]

Other clusters have been reported to have SMMs behaviour, these include Fe4, Mn4, V4, CrM6, Ni12 and Mn10. For the purpose of this thesis I will introduce in the next paragraph the Fe4 clusters and their magnetic properties.

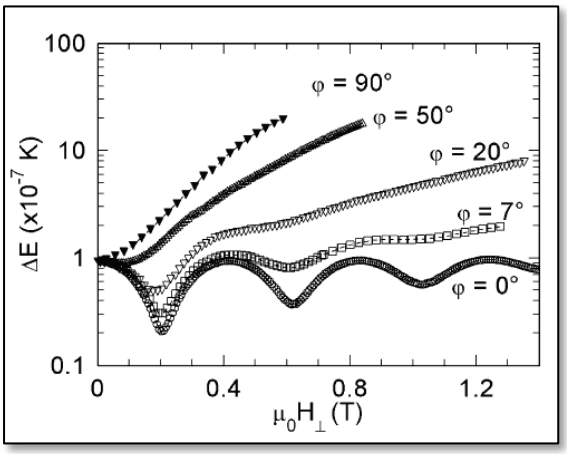

Figure 5.10. Experimental oscillations of the tunnel splitting in Fe8. A variable magnetic field is applied in the xy plane. φ is the angle of the magnetic field with the hard axis.

The interest for molecular nanomagnets is due to the fact that they, on one side, show magnetic hysteresis as a bulk magnet and, on the other side, they are still small enough to show important quantum effect.

These systems are particularly appealing for potential technological applications. The magnetic bistability associated with the hysteresis loop of molecular origin in principle can be used to store information in one single molecule (one molecule can be seen as one bit) leading to unprecedented data densities.

Moreover, the SMMs can be used to investigate the range of sizes in which quantum and classical behavior coexist thanks to the quantum tunneling effects.[14] In principle this features can be exploited for developing new classes of computers in which quantum coherence is used to store and elaborate information.

In order to be considered for real applications, single molecule magnets must have the highest possible blocking temperature, that is the temperature below which the relaxation of the magnetization becomes slow compared to the time scale of a particular investigation technique. Further it is also important that the molecules show clearly observable quantum effects.

5.6 Molecular Magnetic properties: the case of $Fe_4(OMe_3)_6(dpm)_6$.

The smallest iron cluster showing slow relaxation effects in the magnetization at low temperature is $Fe_4(OMe)_6(dpm)_6$, from here called **Fe_4**, considered the archetype of the SMMs family with four iron ions.[15]

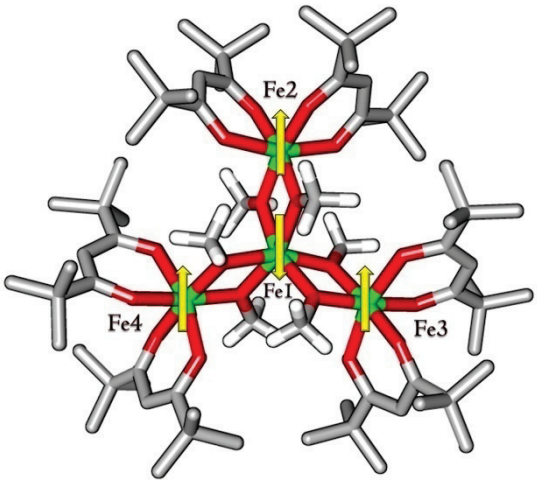

Figure 5.11. Structure of the ferrimagnetic cluster $[Fe_4(OMe)_6(dpm)_6]$ where dpm = 2,2,6,6-tetramethylheptane-3,5-dionate. The iron atoms are in green, oxygen in red and carbon in grey. The arrows correspond to the spin structure in the ground **S** = 5 state.

In the general synthetic procedure, β-diketones with apolar substituents are allowed to react with $FeCl_3$ and an alkali-metal methoxide in an organic solvents. By varying the substituent on the β-diketonate ligands and the combination of the solvents employed, it is possible to modulate the nuclearity and the connectivity of the product. Therefore, use of Hdpm (dipivaloylmethane), NaOMe and an Et_2O:methanol mixture in this procedure, gives $Fe_4(OMe)_6(dpm)_6$ (**Fe4**) in good yield.[16]

The structure of **Fe4** (Figure 5.11) shows a central iron ion connected to three terminal ions by three double μ-alkoxo bridges.

The four iron(III) ions are arranged on the same plane and each of them is coordinated by six oxygen atoms belonging to the dpm^- and the MeO^- ligands, arranged as a distorted octahedron. In particular, three bis(μ-OMe) ligands connect the Fe1 atom to the three peripheral ones, which complete their coordination by binding two dipivaloylmethanide anions.

The crystal symmetry requires a C_2 axis in the cluster passing through Fe1 and Fe2. The three peripheral iron(III) ions define an almost equilateral triangle. The spin topology determines the non-compensation of the spins (ferrimagnetic behavior), since the antiferromagnetic coupling orients the central spin "down" and the external ones "up" giving the total ground state $S = 5$.

5.6.1 The Magnetic behaviour: χT vs T.

The ferrimagnetic nature of the cluster is clearly shown by the χT *vs.* T curve (Figure 5.12). At the temperature of 270 K, the χT value is 11.9 emu K mol^{-1}. With decreasing temperature the curve reaches a broad minimum at ca. 155 K (χT 10.96 emu K mol^{-1}). Further cooling of the system determines a χT increase until a maximum of 14.62 emu K mol^{-1} is reached at at 7K (see Figure 5.8). This latter value is in reasonable agreement with the χT expected value for an $S = 5$ ($\chi T = C = 15$ emu K mol^{-1}, for $g = 2.00$; eq. 5.10), the discrepancy being ascribable to anisotropy effects or intermolecular interactions. The small decrease of χT observed below 7 K might be originated either by intercluster antiferromagnetic interactions or by the

presence of zero field splitting (zfs) of the ground **S** = 5 spin multiplet (see Subparagraph 5.6.2).

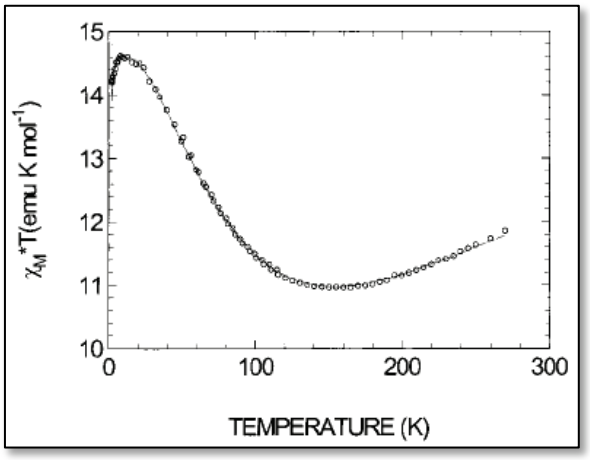

Figure 5.12. Temperature dependence of the χT product for **Fe4**. The solid line is calculated with J = 21.1 cm^{-1}, J' = -1.1 cm^{-1}, and D(S = 5) = -0.20 cm^{-1}.

The spin-spin interactions can occur in two ways: through-space and through-bond. The former are given by the coupling between the magnetic centers through dipolar interactions. In the through-bond interactions we can distinguish the exchange interactions, which occur for direct overlap of magnetic orbitals, and the superexchange interactions, mediated by the ligands bridging the metal ions. In the case of the **Fe4**, superexchange interactions mediated by the μ-OMe ligands are operative between the iron(III) ions, each of which has spin **s**=5/2. These superexchange interactions are defined by the Heisenberg Hamiltonian (eq. 5.16):

$$H = \sum_{ij} J_{ij} \boldsymbol{s}_i \boldsymbol{s}_j \qquad \text{(eq. 5.16)}$$

where $\mathbf{s}_i$ is the spin vector of the i-th ion and J_{ij} is the coupling constant. $J > 0$ is characteristic of antiferromagnetic interaction while $J < 0$ is characteristic of ferromagnetic interactions.

By assuming threefold symmetry the Heisenberg Hamiltonian for **Fe4** can be written as:

$$H = J(\mathbf{S}_1 \bullet \mathbf{S}_2 + \mathbf{S}_1 \bullet \mathbf{S}_3 + \mathbf{S}_1 \bullet \mathbf{S}_4) + J'(\mathbf{S}_2 \bullet \mathbf{S}_3 + \mathbf{S}_3 \bullet \mathbf{S}_4 + \mathbf{S}_2 \bullet \mathbf{S}_4) \quad \text{(eq. 5.17)}$$

where $\mathbf{S}_1$ is the spin of the central iron(III) ion; $\mathbf{S}_2$, $\mathbf{S}_3$, and $\mathbf{S}_4$ are the spins of the peripherals iron(III) ions; J is the coupling constant "to nearest-neighbors" and J′ is the coupling constant "to next-nearest-neighbor". The first term in the Hamiltonian describes the coupling interactions between the central ion and the peripheral ions, while the second contribution describes the coupling interactions between the peripheral ions.

By calculating the energies of the total spin states using equation 5.17, it is possible to reproduce the temperature dependence of χT determining the best-fit parameters J, J' and g ($J = 21.1$ cm^{-1}, $J' = -1.1$ cm^{-1}, $g = 1.97$)[16]. This results confirms the antiferromagnetic nature of the interactions between the central ion and the peripheral ions ($J > 0$), and a weak ferromagnetic interaction between the peripheral ions ($J' < 0$).

5.6.2 The Magnetic Anisotropy.

The anisotropy of a SMM arises from two main sources: single-ion magnetocrystalline anisotropy and dipolar interactions.

The first contribution is due to the spin-orbit coupling which can cause the removal of the spin microstates degeneration. This can affect both the way the magnetic center responds to an external field (Zeeman effect) and its behavior in the absence of an external field (zero-field splitting). The first case is described by using the Zeeman Hamiltonian (eq. 5.18) in which g is the anisotropic term:[17]

$$\mathcal{H} = g\mu_B \boldsymbol{S} H \quad \text{(eq. 5.18)}$$

where $\mathbf{S}$ is the total spin and H is the applied magnetic field.

For the second case, we take into account ions with Russell-Saunders $^6\mathbf{S}$ term (as Fe(III) with $s = 5/2$) in coordination compounds at high spin which can show a significant magnetic anisotropy also in the absence of an applied magnetic field. The spin-orbit coupling, even without acting within the fundamental term (which has $\mathbf{L} = 0$), is able to mix the wave functions of

this latter with the excited terms of suitable spin and symmetry. The mixing in a noncubic chemical environment determines a magnetic anisotropy which is usually described by the Hamiltonian reported in equation 5.19.

$$\mathcal{H}_{zfs} = \boldsymbol{d}\left[\boldsymbol{s}_z^2 - \frac{\boldsymbol{s}(\boldsymbol{s}+1)}{3}\right] + \boldsymbol{e}\left[\boldsymbol{s}_x^2 - \boldsymbol{s}_y^2\right] \qquad \text{(eq. 5.19)}$$

where $\boldsymbol{d}$ is the axial zfs component (z) of the anisotropy and $\boldsymbol{e}$ is the rhombic zfs component (xy) of the anisotropy (or transverse anisotropy).

For the sake of simplicity we consider only the axial anisotropy ($\boldsymbol{e} = 0$) which partially removes the spin degeneration of the fundamental term of the ion. In particular, according to eq. 5.19, the levels energy depends on the absolute value of the z component of the spin.

$$E_{zfs} = \boldsymbol{d}\left[\boldsymbol{m}_s^2 - \frac{\boldsymbol{s}(\boldsymbol{s}+1)}{3}\right] \qquad \text{(eq. 5.20)}$$

Therefore, in a iron(III) ion at high spin with axial coordination geometry, the fundamental term ($\boldsymbol{s} = 5/2$) is splitted in three doublets including the states with quantum number $\mathbf{m}_s = \pm 1/2, \pm 3/2$ e $\pm 5/2$.

The energetic arrangement of the states depend on the $\boldsymbol{d}$ sign. When $\boldsymbol{d} < 0$ the doublet with $\mathbf{m}_s = \pm 5/2$ has the lowest energy. Since in this state the z component of the spin in absolute value is maximum, the anisotropy is of the "easy-axis" type and the spin arranges preferentially along z. While, when $\boldsymbol{d} > 0$ the doublet with $\mathbf{m}_s = \pm 1/2$ has the lowest energy. Since in this state the z component of the spin in absolute value is minimum, the anisotropy is of the "easy-plane" type and the spin arranges preferentially in the xy plane. The presence of the $\boldsymbol{e}$ contribution can induce a further removal of the degeneration of the spin levels in systems with integer spin. In the case of an half-integer spin, the degeneration of the sates with equal $|\mathbf{m}_s|$ is a consequence of the *time reversal symmetry* that all the electronic system follow in the absence of an applied magnetic field (Kramer's Theorem).

The anisotropy of the individuals ions forming the molecule contributes to the molecular magnetic anisotropy, in particular depend on the relative orientation of the local anisotropy tensors. For instance, in the case of the $\mathbf{Fe_4}$ is believed that the central ion has an anisotropy of the "easy-axis" type along

the molecular axis and that the peripheral ions have an anisotropy of the "easy-plane" type in a plane containing the molecular axis. Therefore, the molecular axis is the direction of preferential alignment of the molecular total spin.

The second contribution to the anisotropy is given by the dipolar interactions due to the coupling between the magnetic centers through the space. In a system of two magnetic centers interacting only with a dipolar mechanism, the dipolar interaction tends to align the spins parallel to each other and parallel to the line joining them. If the exchange interactions dominate, as in the majority of the real systems, the effect of dipolar interactions depends on the nature (ferromagnetic or antiferromagnetic) of exchange interactions. In the presence of a ferromagnetic coupling, the dipolar interaction energy is minimum when the dipoles are aligned parallel to the line connecting the centers (as without the exchange interactions). If instead, the coupling is antiferromagnetic, the favored configuration is the one where the dipoles are perpendicular to the line connecting them.

Therefore, we can conclude that in the **Fe4** ground state the spins of the metal centers tends to arrange perpendicular to the lines connecting the iron(III) ions (Fe-Fe), and consequently the perpendicular to the molecular plane represents the easy-axis for the total spin.

The magnitude of the dipolar interactions is inversely proportional to the cube of the distance between the dipoles.

As in the case of an individual ion, also the molecular anisotropy can be described by an Hamiltonian similar to the one reported in eq. 5.19, but related to the total spin $S = 5$:

$$\mathcal{H}_{zfs} = \boldsymbol{D}\left[\boldsymbol{S}_z^2 - \frac{\boldsymbol{S}(\boldsymbol{S}+1)}{3}\right] + \boldsymbol{E}\left[\boldsymbol{S}_x^2 - \boldsymbol{S}_y^2\right] \qquad \text{(eq. 5.21)}$$

The anisotropy of the ground state can be determined using high field EPR spectroscopy. In the case of the **Fe4** it has been confirmed to be quasi axial, and of the Ising type, with $D = -0.20$ cm^{-1}. The rhombic term is very small.

5.6.3 Slow Relaxation of the Magnetization.

The slow relaxation of the magnetization is due to the presence of an energy barrier to be overcome in the reversal of the magnetic moment: the *anisotropy barrier*.[16]

To explain the origin of the barrier, we consider a system with a well defined ground state characterized by a large value of **S** and an easy-axis anisotropy like the **Fe_4** (**S**=5).

The removal of the degeneracy of the **S** multiplet, owing to the zero field splitting and to the presence of an external field parallel to the unique axis of the cluster (z), is described by using the axial Zero-Field Splitting *plus* axial Zeeman Hamiltonian:

$$\mathcal{H}_0 = \boldsymbol{D}\left[\boldsymbol{S}_z^2 - \frac{\boldsymbol{S}(\boldsymbol{S}+1)}{3}\right] + g\,\mu_B H_z S_z \qquad \text{(eq. 5.22)}$$

The energies of the spin levels corresponding to $\mathcal{H}_0$ are in fact easy to calculate as given by equation 5.23, where $-S \leq Ms \leq S$.

$$E(M_s) = D(M_s^2 - 10) + g\mu_B M_s H_z \qquad \text{(eq. 5.23)}$$

The energy levels can be plotted as shown in Figure 5.13a. When no external field is applied all the levels are degenerate in pairs, except Ms=0. Since D is negative the Ms = ±5 levels will lie lowest. In Figure 5.13 the states with positive Ms are plotted in the left potential well, while those with negative Ms in the right one.

When a field is applied parallel to the z axis, the levels characterized by a positive Ms correspond to a projection of the magnetization antiparallel to the field, while those with negative Ms correspond to magnetization parallel to the applied external field (Figure 5.13b).

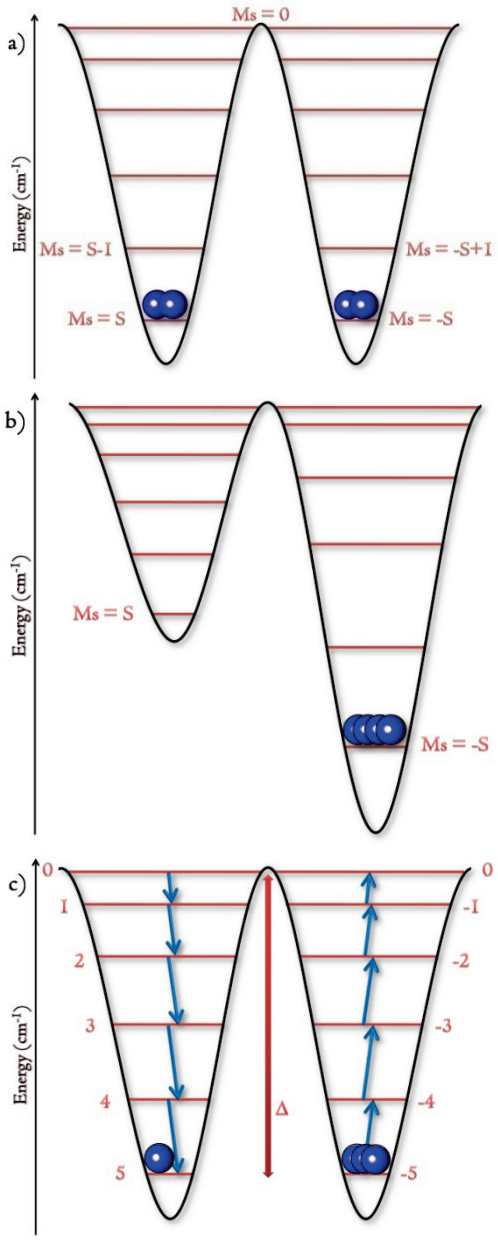

Figure 5.13. Energy levels for a spin state **S** = 5 with easy axis magnetic anisotropy. The +Ms levels are localized in the left well and the -Ms levels in the right well. a) In zero field the two wells are equally populated; b) the application of a magnetic field selectively populates the right well; c) after removing the field the return to equilibrium occurs through thermal relaxation.

If the system is magnetized by applying a magnetic field parallel to the z axis (large H_z) at low temperature, the Ms = -5 state will be the only one populated and the magnetization reaches the saturation value. On switching the field off, the system will revert to thermal equilibrium ("relaxation"), i.e. it will equalize the populations of the Ms = -5 and Ms = +5 states, with no resulting magnetization.

The inversion of the magnetization cannot occur directly, but the system must climb all the levels, one at a time, up to Ms = 0, and then descend (*thermal relaxation*, Figure 5.13c).

The relaxation time for thermally activated behavior follows the Arrhenius law:[18]

$$\tau = \tau_0 \exp\left(\frac{\Delta}{k_B T}\right) \qquad \text{(eq. 5.24)}$$

where Δ is the height of the barrier and τ_0 is the pre-exponential factor proportional to $\mathbf{S}^6/\Delta^3$.

The barrier Δ for the re-orientation of the magnetization is given by the difference in energy between the lowest Ms = $\pm$S states and the highest ones Ms = 0:

$$\Delta = |D|[(\min|Ms|)^2 - (\max|Ms|)^2] = |D|\mathbf{S}^2 \qquad \text{(eq. 5.25)}$$

For a half integer spin the barrier would have been $\Delta = |D|(\mathbf{S}^2 - 1/4)$.

Therefore, the strategy to observe a long relaxation time is that of synthesizing clusters with large spin S and large zero-field splitting.

At low temperature, the relaxation time of magnetization becomes so slow that hysteresis loop of molecular origin can be observed (Figure 5.14).

Usually, the hysteresis loop is characterized by steps: the flat regions correspond to fields at which the relaxation is slow, as a result of the *thermal relaxation* over an anisotropy barrier; the steps correspond to fields at which a rapid increase of the relaxation rate is observed, as a result of *quantum tunneling*.

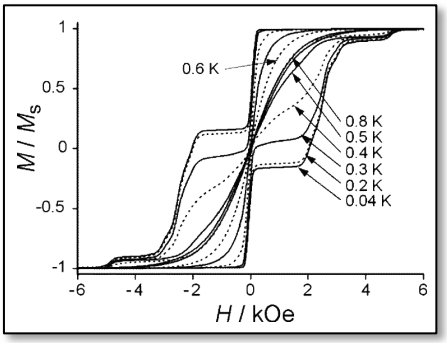

Figure 5.14. Example of magnetic hysteresis loops recorded on a single crystal of $[Fe_4(OEt)_3(L)(dpm)_6]$ with L= $[t\text{-}BuC(CH_2O)_3]^{3-}$ at constant field-sweep rate (170Oe/s) for different temperatures. Ms is the saturation magnetization.[19]

5.6.4 Magnetic Quantum Tunneling.

In the presence of axial anisotropy and without an applied field, the Ms = ±5 levels, for example, are still degenerate. In this situation, if we consider the magnetization in the right well (Ms = -5), the only way it can change its state is to overcoming the barrier Δ, and roll down into the left well until Ms = +5 (thermal relaxation, Figure 5.15a).

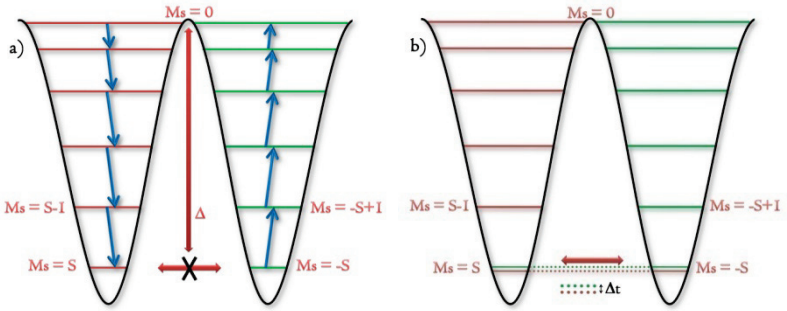

Figure 5.15. Tunneling in a double well system. a) Noninteracting states; b) interacting states giving rise to tunnel splitting ΔT.

If we want to observe tunneling we must introduce a perturbation that allows the mixing of the two states. In a real system the perturbation is due to the presence of transverse anisotropy described, as already reported in subparagraph 5.6.2, by the $\mathcal{H}_1$ Hamiltonian.

$$\mathcal{H}_1 = E(\boldsymbol{S}_x^2 - \boldsymbol{S}_y^2) \qquad \text{(eq. 5.26)}$$

The transverse anisotropy generates a distortion which extends the state wavefunction of the left wall over to the right wall, and vice versa. Therefore, the state must be described by a superposition of the two states and the magnetization could pass from left to right without climbing the barrier but tunneling. The effect is in fact called quantum tunneling.

The actual possibility of observing tunneling depends on the extent of the interaction of the two wavefunctions. In fact, if the two wavefunctions overlap, there must be an interaction between them which splits the two degenerate levels in the left and right well, giving rise to a so-called tunnel splitting, ΔT (Figure 5.15b). One of the two coupled levels is of lower energy than the degenerate levels, while the other is of higher energy. The possibility of tunneling is related to the relative energies of the tunnel splitting and of the barrier. Smaller is the ratio between the two, smaller is the possibility of observing tunneling.

Tunneling may occur not only between the lowest-lying levels Ms = ±5, but also between the higher thermally populated levels offering a shortcut for the relaxation. This mechanism is very important at intermediate temperature because the tunneling frequency is expected to increase on decreasing | Ms | . Therefore, the overall mechanism has been called *thermally assisted quantum tunneling*.

In zero field the lowest lying pairs of Ms levels meet the tunneling condition with the levels on-resonance, and the relaxation is comparatively fast (Figure 5.16, inset a).

Nevertheless, if a magnetic field is applied parallel to the z axis the energies of the Ms levels change rapidly. The energy of the +Ms level increases, while that of the –Ms level decreases, as shown schematically in Figure 5.16, making levels off-resonance and quantum tunneling impossible (Figure 5.16, inset b). Each line of the figure corresponds to the energy of one level.

However, since the energy of the +Ms level increases and that of the –Ms+n level decreases, they will have to meet somewhere (intersection points in figure 5.16), restoring the conditions for resonant tunneling (Figure

5.16a). The field at which the levels are in resonance is given by equation 5.27.

$$H_z = -n\frac{D}{g\mu_B} \qquad \text{(eq. 5.27)}$$

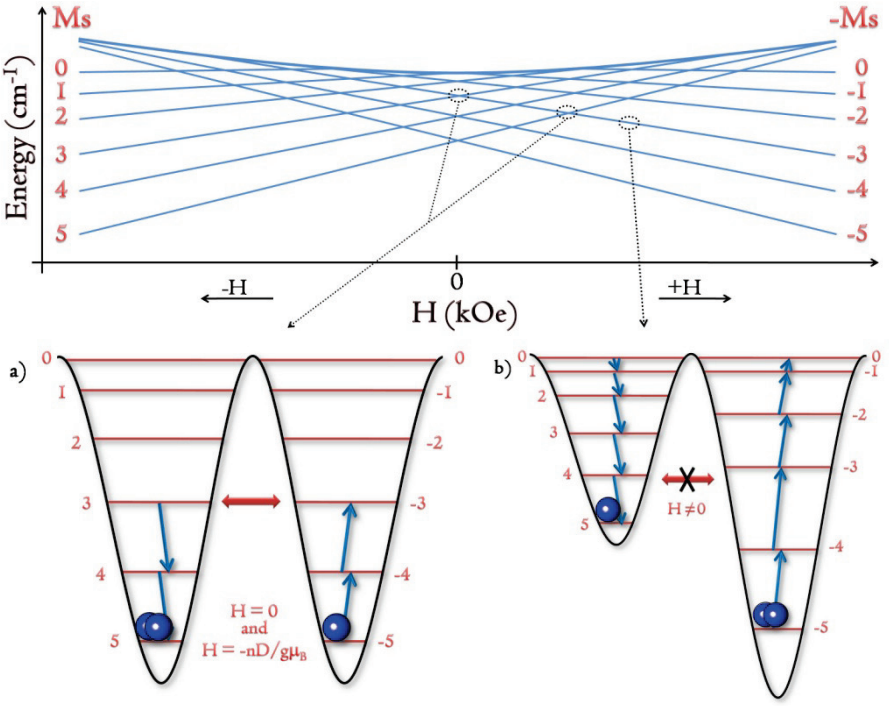

Figure 5.16. Energy levels of a spin state S = 5 in the presence of a magnetic field applied. Inset a) shows the levels on-resonance in zero applied field and for critical value of the field, allowing quantum tunneling; inset b) shows the levels off-resonance as a result of the external magnetic field hampering the tunneling.

5.7 References.

[1] M. Pacchioni, A. Cornia, A. C. Fabretti, L. Zobbi, D. Bonacchi, A. Caneschi, G. Chastanet, D. Gatteschi, R. Sessoli, Site-specific ligation of anthracene-1,8-dicarboxylates to an Mn_{12} core: a route to the controlled functionalization of single-molecule magnets, *Chem. Commun.* **2004**, 2604-2605.

[2] R. S. Skomski, D. J. Sellmyer, D. Li, W. Wernsdorfer, T. Schefl, J. Fidler, D. Suess, V. Tsiantos, X. Zhang, *Handbook of Advanced Magnetic Materials-Nanostructural Effects*, Vol 1, **2006**, Y. Liu, D. J. Seemyer, D. Shindo (Eds.), Springer.

[3] A. Aharoni, *An introduction to the Theory of Ferromagnetism*, Oxford University Press, **1999**, London.

[4] a) S. E. Apsel, J. W. Emmert, J. Deng, L. A. Bloomfield, Surface-enhanced magnetism in nickel clusters, *Phys. Rev. Lett.*, **1996**, 76:1441-1444.
b) I. M. L. Billas, A. Chatelain, W. A. de Heer, Magnetism of Fe, Co and Ni clusters in molecular beams, *J. Magn. Magn. Mat.* **1997**, *168*, 64-84.

[5] a) R. L. Carlin, *Magnetochemistry*, **1986**, Springer-Verlag, Berlin.
b) O. Kahan, *Molecular Magnetism*, **1993**, VCH Publisher Inc., New York.

[6] N. Spaldin, *Magnetic Materials - Fundamentals and Device Applications*, **2003**, Cambridge University Press, Cambridge.

[7] P. W. Selwood, *Magnetochemistry*, 2nd, **1956**, Interscience Publisher Inc., New York.

[8] A. Earnshaw, *Introduction to Magnetochemistry*, **1968**, Academic Press, London and New York.

[9] R. Sessoli, D. Gatteschi, A. Caneschi, M. A. Novak, Magnetic bistability in a metal-ion cluster, *Nature* **1993**, *365*, 141-143.

[10] T. Lis, Preparation, structure, and magnetic properties of a dodecanuclear mixed-valence manganese carboxylate, *Acta Cryst.* **1980**, *B36*, 2042-2046.

[11] D. Gatteschi, R. Sessoli, Molecular nanomagnets: the first 10 years, *J. Magn. Magn. Mat.* **2004**, *272-276*, 1030-1036

[12] a) K. Weighardt, K. Pohl, I. Jibril, G. Huttner, Hydrolysis Products of the Monomeric Amine Complex $(C_6H_{15}N_3)FeCl_3$: The Structure of the Octameric Iron(III) Cation

of $\{[(C_6H_{15}N_3)_6Fe_8(\mu_3\text{-}O)_2(\mu_2\text{-}OH)_{12}]Br_7(H_2O)\}Br\cdot 8H_2O$, *Angew. Chem. Int. Ed.* **1984**, *23*, 77-78.
b) W. Wernsdorfer, T. Ohm, C. Sangregorio, R. Sessoli, D. Mailly, C. Paulsen, Observation of the Distribution of Molecular Spin States by Resonant Quantum Tunneling of the Magnetization, *Phys. Rev. Lett.* **1999**, *82*, 3903-3906.

[13] W. Wernsdorfer, R. Sessoli, Quantum phase interference and parity effects in magnetic molecular clusters, *Science* **1999**, *284*, 133-135.

[14] a) L. Thomas, F. Lionti, R. Ballou, D. Gatteschi, R. Sessoli and B. Barbara, Macroscopic quantum tunneling of magnetization in a single crystal of nanomagnets, *Nature* **1996**, *383*, 145-147.
b) J. R. Friedman, M. P. Sarachik, J. Tejada and R. Ziolo, Macroscopic measurement of resonant magnetization tunneling in high-spin molecules, *Phys. Rev. Lett.* **1996**, *76*, 3830-3833.

[15] D. Gatteschi, R. Sessoli, A. Cornia, Single-molecule magnets based on iron(III) oxo clusters, *Chem. Commun.* **2000**, 725-732.

[16] A. L. Barra, A. Caneschi, A. Cornia, F. Fabrizi de Biani, D. Gatteschi, C. Sangregorio, R. Sessoli, and L. Sorace, Single-Molecule Magnet Behavior of a Tetranuclear Iron(III) Complex. The Origin of Slow Magnetic Relaxation in Iron(III) Clusters, *J. Am. Chem. Soc.* **1999**, *121*, 5302-5310.

[17] A. Cornia, D. Gatteschi, R. Sessoli, New experimental techniques for magnetic anisotropy in molecular materials, *Coord. Chem. Rev.* **2001**, *219-221*, 573-604.

[18] Morrish, A., H. *The Physical Principles of Magnetism*, Wiley & Sons: Inc. New York, **1966**, p 360.

[19] S. Accorsi, A.-L. Barra, A. Caneschi, G. Chastanet, A. Cornia, A. C. Fabretti, D. Gatteschi, C. Mortalò, E. Olivieri, F. Parenti, P. Rosa, R. Sessoli, L. Sorace, W. Wernsdorfer, L. Zobbi, Tuning Anisotropy Barriers in a Family of Tetrairon(III) Single-Molecule Magnets with an S = 5 Ground State, *J. Am. Chem. Soc.* **2006**, *128*, 4742-4755.

The first Carbon Nanotube functionalized with a Tiny Magnet.[†]

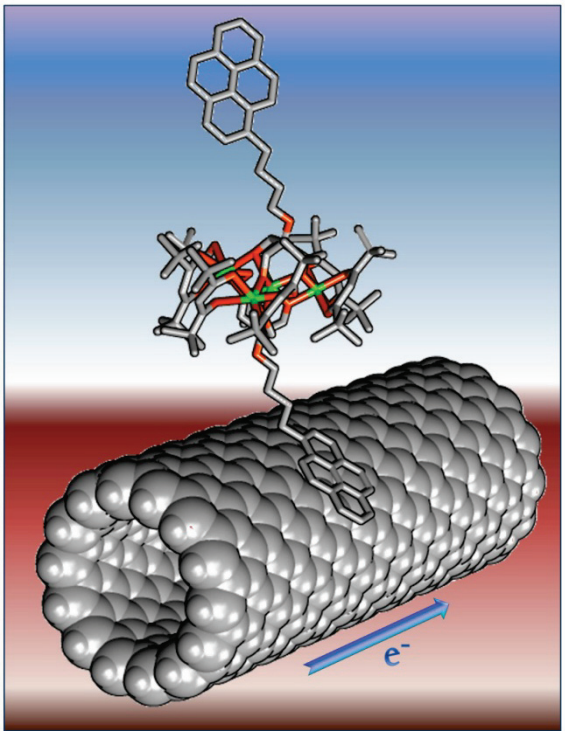

"Organic-Inorganic Hybrids Materials"

[†] This chapter is based on: L. Bogani, C. Danieli, E. Biavardi, N. Bendiab, A.-L. Barra, E. Dalcanale, W. Wernsdorfer, A. Cornia, Single-Molecule-Magnet Carbon-Nanotube Hybrids, *Angew. Chem., Int. Ed.* **2009**, *48*, 746-750.

6.1 Introduction.

Carbon nanotubes (CNTs) hold great promise for sensing[1,2] and nanoelectronics,[3] as core components of chemical and biological[1,2] ultra-sensitive probes and of field-effect transistors (FETs).[3] CNT-SQUID devices[4] in particular could constitute magnetic detectors with single-molecule sensitivity, thus offering a viable route to the long-sought readout of magnetic information stored in individual single-molecule magnets (SMMs).[5]

SMMs are metal-ion clusters with a large easy-axis magnetic anisotropy,[6] exhibiting a magnetic hysteresis loop at low temperature and suggested as components for quantum computing[7] and molecular spintronics.[5] To date, the chemistry needed to bridge the domains of CNTs and SMMs has remained unexplored.

CNT hybrids with gold or magnetic nanoparticles, proteins, enzymes, or luminescent molecules are currently under intense investigation.[1,2,8] The resulting materials usually entail a large number of nanoparticles or molecules per CNT, whereas CNT-SMM detectors and spintronic devices require the sequential addition of a small but very controlled number of nanomagnets. Grafting through covalent bonds might introduce electron scattering centers that may limit the performance of CNT devices. By contrast, noncovalent π-stacking interactions with pristine CNTs should largely preserve the CNT conductance, while guaranteeing SMM-CNT interaction.

Herein we report the assembly of CNT-SMM hybrids using a tailor-made tetrairon(III) SMM, $[Fe_4(L)_2(dpm)_6]$ (**47**; Hdpm = dipivaloylmethane), designed to graft onto the walls of CNTs.

6.2 Results and Discussion.

6.2.1 Tetrairon Clusters Synthesis.

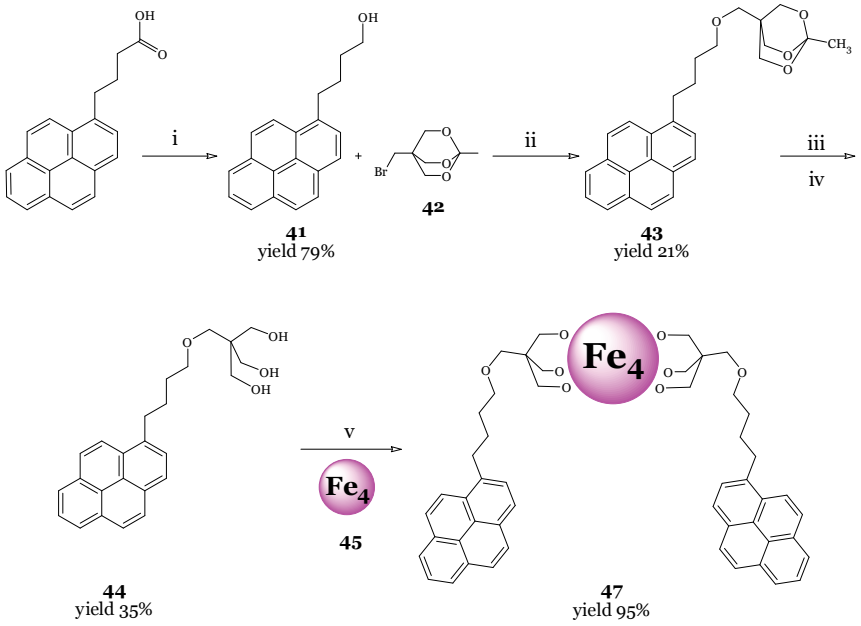

Scheme 6.1. Synthesis of **Fe_4Py_2**: i) BH_3·THF, THF, 0°C, 20 hrs, ii) NaH, DMF, 90°C, 12 hrs, iii) HCl, MeOH, 6 hrs, iv) Na_2CO_3, MeOH, 12 hrs, v) Et_2O, **Fe_4** (**45**).

The ligand L^{3-} (H_3L=2-hydroxymethyl-2-(4-(pyren-1-yl)butoxy)methylpropane-1,3-diol, **44**), featuring an alkyl chain with a terminal pyrenyl group, was synthesized according to the synthetic protocol reported in Scheme 6.1. At first, it was performed the reduction of 4-pyren-1-yl-butyric acid, using BH_3 as reducing agent, affording 4-(1-pyrenil)butanol (**41**) in 79% yield. In order to introduce the triol functionality, compound **41** was coupled with 4-bromomethyl-1-methyl-2,6,7-trioxa-bicyclo[2.2.2]octane (**42**)[9], in the presence of NaH.

Subsequently, a two steps deprotection of the trimethylol function afforded H_3L (**44**), which is finally treated with the preformed[6] complex $[Fe_4(OMe)_6(dpm)_6]$ (**45**) to give **Fe_4Py_2** (**47**) in excellent yield (95%).

Compounds **42**[9], **45**[11] (**Fe4**), **46**[11] ($Fe_4(OMe)_6(dpm\text{-}d_{18})_6$, **Fe4-*d*18**) and **48**[11] ($Fe_4(L')_2(dpm)_6$, **Fe4Ph**) were supplied by Cornia's Group of the Modena University which synthesized them following a published procedures.

Fe4-*d*18 was used for the stability study in solution performed with the ^2H NMR, while **Fe4Ph** is the control cluster for the grafting step.

6.2.2 Fe4Py2 Crystal Structure.

The molecular structure of **Fe4Py2** (Figure 6.1a), determined by single-crystal X-ray diffraction,[10] shows a tetrairon(III) propeller-like core with idealized D_3 symmetry held together by two triply deprotonated **H3L** ligands lying at opposite sides of the molecular plane (see Experimental Section Subparagraph 6.5.2).

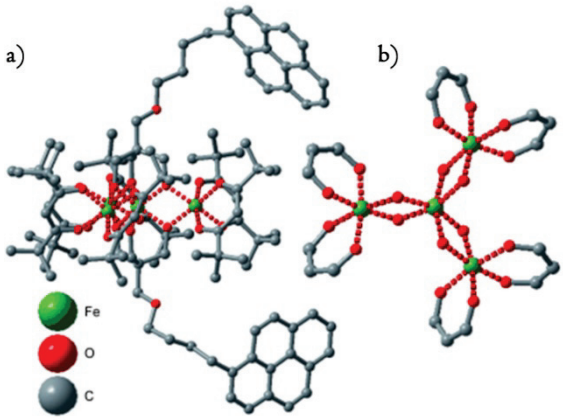

Figure 6.1. a) Crystal structure of **Fe4Py2**, showing the core and the peripheral pyrene-terminated chains (hydrogen atoms omitted). b) View of the tetrairon(III) core along the idealized threefold axis, showing the preserved cluster geometry (ligands H_3L and tert-butyl carbon atoms of dpm omitted).

The structure of **Fe4Py2** shows a central iron ion connected to three terminal ions by three bis(μ-OMe) bridges, which complete their coordination by binding two dipivaloylmethanide anions (Figure 6.1b). The

three peripheral iron(III) ions define an almost equilateral triangle and, with the central iron(III), are arranged on the same plane.

The molecular size of **Fe4Py2** is 1.6-2.3 nm (av.: 1.9 nm).

6.2.3 Magnetic Properties.

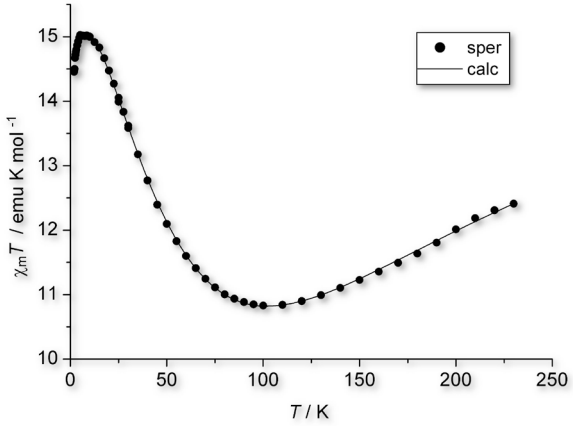

Figure 6.2. DC magnetic properties of a polycrystalline sample of **Fe4Py2**; χ_m is molar magnetic susceptibility. Solid line is a fit to the data.

The temperature dependence of the molar magnetic susceptibility χ_m of compound **Fe4Py2** is shown in Figure 6.2. If the four irons(III) were magnetically non interacting, the material property would be the sum of those of the single ions. Consequently, the $\chi_m T$ value should be independent of temperature, except at very low temperature, and equal to $4C$.

C is the Curie' constant calculated following the eq. 5.10 (Chapter 5) with s = 5/2.

$$4C = 4N_A\mu_B^2 g^2 \frac{s(s+1)}{3k_B} = 17.5\ emu\ K/mol$$

But, the experimental value of $\chi_m T$ at 240 K is lower (12.4 emu K mol^{-1}) than 17.5 emu K mol^{-1} proving that the magnetic centers are interacting. Moreover, $\chi_m T$ depends strongly on temperature. In fact, with decreasing of T, the curve reaches a minimum followed by an increasing until a maximum of 15.06 emu K mol^{-1} at 5K. The curve shows a further decrease below 5 K.

The fitting of $\chi_m T$ vs. T data at T≥ 10 K using a Heisenberg *plus* Zeeman Hamiltonian:

$$\mathcal{H} = J(S_1 \cdot S_2 + S_1 \cdot S_3 + S_1 \cdot S_4) + J'(S_2 \cdot S_3 + S_3 \cdot S_4 + S_2 \cdot S_4) + \mu_B g \mathbf{S} H$$

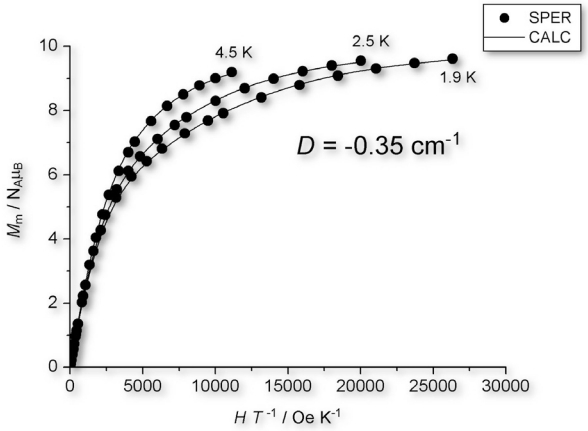

Figure 6.3. Magnetic properties of a polycrystalline sample of **Fe_4Py_2** (Mm is molar magnetization).

gave $J = 14.84(3)$ cm^{-1} and $J' = 0.088(18)$ cm^{-1} with $g = 2.0037(7)$.

The fitting of isothermal magnetization vs. field data (Figure 6.3) afforded the parameters D = -0.350(5) cm^{-1}, g = 2.004(3) in the spin-hamiltonian:

$$\mathcal{H} = D[\mathbf{S}_z^2 - S(S+1)/3] + E[\mathbf{S}_x^2 - \mathbf{S}_y^2] + \mu_B g \mathbf{S} \cdot H$$

These values are typical of tetrairon(III) propellers,[11,12] and indicative of dominant antiferromagnetic exchange interactions between high-spin ($\mathbf{s}_i$ = 5/2) iron(III) ions, affording an $\mathbf{S} = 5$ ground spin state.

The |D| parameter has the lowest value reported for this class of complexes, in nice agreement with the small helical pitch of the propeller-like structure (67.1°) and with a recently-proposed magnetostructural correlation.[11]

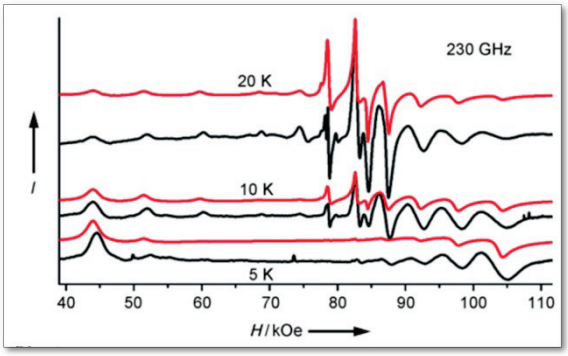

Figure 6.4. Variable-temperature HF-EPR spectra recorded at 230 GHz (black) on a powder sample, along with the best-fit simulations (red).

Moreover, low-temperature high-frequency (HF)-EPR spectra at 190 GHz (Figure 6.23 in Subparagraph 6.5.4) and 230 GHz (Figure 6.4) supports the presence of an **S** = 5 high-spin ground state with an easy-axis magnetic anisotropy (D = -0.409 cm^{-1}). Indeed, single-crystal magnetic measurements reveal a hysteresis loop below 1 K with characteristic quantum-tunneling[6] steps (Figure 6.5), confirming the SMM behavior.

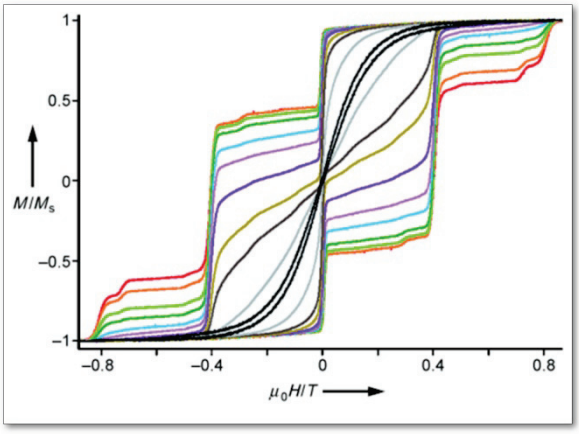

Figure 6.5. Hysteresis cycles recorded on a single crystal of **Fe4Py2** at 11 different temperatures between 1 K (black) and 40 mK (red). The magnetic field is swept at a rate of 170 Oes^{-1} along the magnetic easy axis.

6.2.4 Stability of the cluster in solution.

Following well-established methods, the formation of **Fe_4Py_2** from the precursor $Fe_4(OMe)_6(dpm)_6$ (**Fe_4**) and the ligand H_3L (**44**) was preliminarily studied using NMR methods.

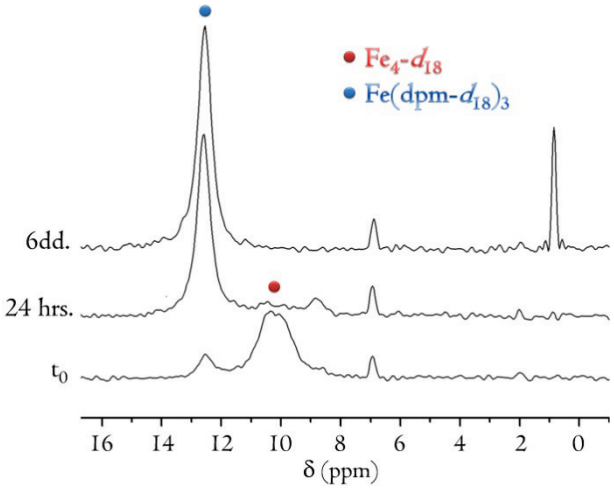

Figure 6.6. ^{2}H NMR time-dependent spectra of a 1.57 mM solution of **Fe_4-d_{18}** in dry toluene. The signals at ca. 7 and 1 ppm are due to the solvent.

The ^{1}H NMR spectra of **Fe_4** clusters at 303 K are dominated by the paramagnetically-shifted and broadened signal of dpm$^-$ *t*-Bu hydrogens at 10.4 ppm.[11,12] This resonance can be used to evaluate cluster stability, as it is very sensitive to molecular magnetism (for instance, it shifts to 12.7-12.9 ppm in monomeric Fe-dpm species).

Using ^{2}H NMR, which affords better-resolved spectra as compared with proton NMR, the deuterated precursor $Fe_4(OMe)_6(dpm\text{-}d_{18})_6$ (**Fe_4-d_{18}**) dissolved in dry Et_2O or toluene was shown to progressively decompose to monomeric $Fe(dpm\text{-}d_{18})_3$ species (Figure 6.6), while the addition of tripodal ligands stabilizes the tetrairon(III) core.[11,12] Thus, we added 2.6 equiv.s of ligand **H_3L** to a 1.58 mM solution of **Fe_4-d_{18}** in anhydrous toluene and we recorded ^{2}H NMR spectra at different times. The ligand synthesized in this work showed a coordinating ability comparable with that of other tripodal

ligands previously investigated,[11,12] as shown by the persistence of the deuteron signal at 10.3 ppm over extended periods (6 days, Figure 6.7).

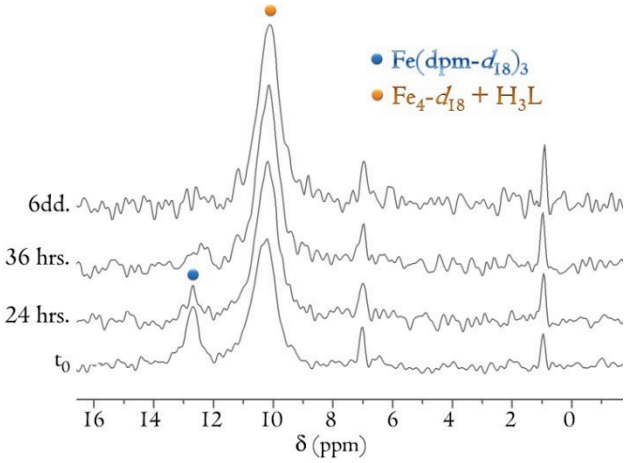

Figure 6.7. ^{2}H NMR time-dependent spectra of a 1.58 mM solution of **Fe$_4$-d_{18}** and **H$_3$L** (2.6 equivs) in dry toluene. The weak signals at ca. 7 and 1 ppm are due to the solvent.

After the isolation of **Fe$_4$Py$_2$** as a pure, crystalline material, its stability in different solvents was studied, using ^{1}H NMR and fluorescence techniques, in order to determine the better condition for the deposition on CNTs.

The ^{1}H NMR spectra of freshly-prepared and aged solutions of **Fe$_4$Py$_2$** in $CDCl_3$, $C_6D_5CD_3$ and CD_2Cl_2 (2.7 mM) are shown in Figures 6.8 a, b and c, respectively. A broad peak due to Fe-dpm species appeared at ca. 12.6 ppm in the spectra of $CDCl_3$ solutions after 24 h, thus indicating a partial decomposition of the cluster presumably due to the known acidity of chloroform solutions.

By contrast, no appreciable changes were detected in the spectra of toluene-d_8 and CD_2Cl_2 solutions after 24 h and 5 days from preparation, confirming the stability of the cluster in these and similar, non-acidic solvents like DCE.

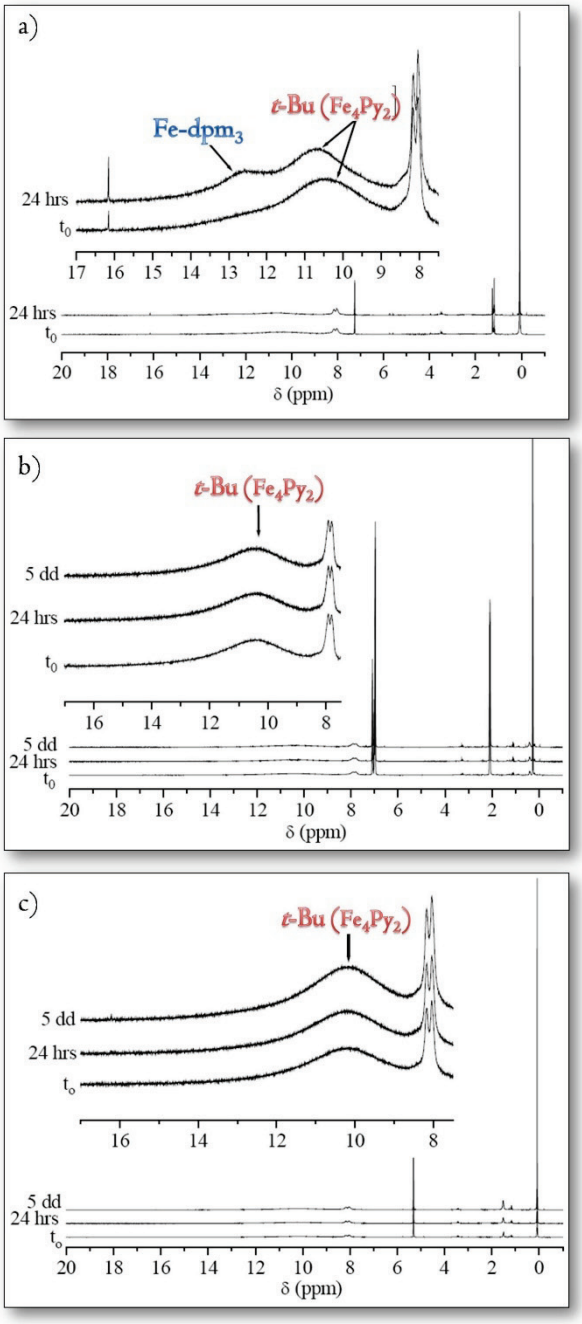

Figure 6.8. ^{1}H NMR spectra of a freshly-prepared and aged solution of **Fe_4Py_2** in a) $CDCl_3$ (2.73 mM), b) in toluene-d_8 (2.77 mM), c) CD_2Cl_2 (2.77 mM).

Fluorescence spectra were registered to demonstrate that the tripodal ligand H_3L remains coordinated to the tetrairon(III) core in solution. Fluorescence quenching of pyrene-functionalized ligands upon metal complexation is a well-studied phenomenon and is widely exploited in the design of fluorimetric sensors.

The fluorescence spectra of 0.5 mM solutions of **Fe_4Py_2** in 1,2-dichloroethane and in toluene were recorded at 48 hours from preparation and compared with the spectra of the free ligand H_3L at similar concentrations (Figure 6.9). Complete fluorescence quenching was observed over 48 hours, thus confirming that the molecular structure is fully retained in solution over such timescales.

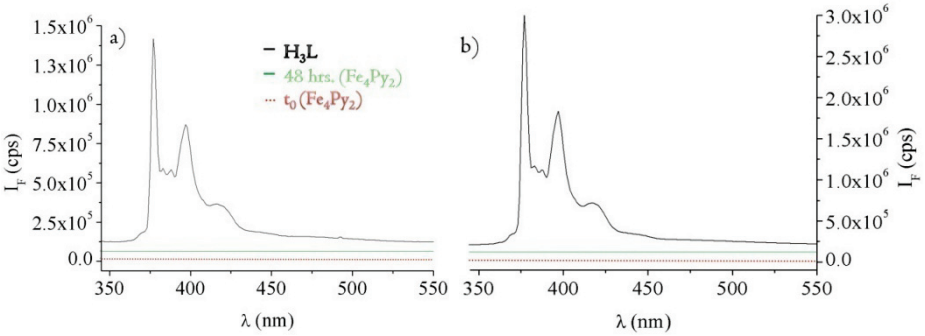

Figure 6.9. Fluorescence spectra of 0.5 mM solutions of **Fe_4Py_2** and H_3L in a) 1,2-dichloroethane and b) toluene with λ_{exc} = 300 nm.

6.2.5 Preparation of the Hybrid CNT-FET.

A scheme of the fabrication process is reported in Figure 6.10.

CNT-FETs were obtained by electron-beam lithography on degenerately *n*-doped silicon wafers covered with a 300 nm thick SiO_2 layer (Siltronix sas).

Gold electrodes were deposited on the surface by deep-UV lithography (Figure 6.10, step a), providing a reference system to locate CNTs. Single-walled CNTs (Rice Univ.) in DCE were spin-coated on the wafers (step b), located by atomic force microscopy (AFM) and connected with Pd leads, separated by 300 nm gaps, by e-beam lithography (step c, 65% of contacts

displayed a resistance lower than 100 kΩ). The sequential grafting of the SMMs (**Fe4Py2**) is then obtained via a self-assembly process (step d).

In particular, the hybrids were produced by immersion of the CNT-FETs in a 3.1 x 10^{-5} M solution of **Fe4Py2** in 1,2-dichloroethane (DCE) for 30 min, followed by extensive washing with pure DCE. ^{1}H NMR, ESI-MS, and fluorescence techniques demonstrate that the complex is completely stable in solution in the conditions used for the deposition. The grafting was reiterated to follow the progressive addition of SMMs.

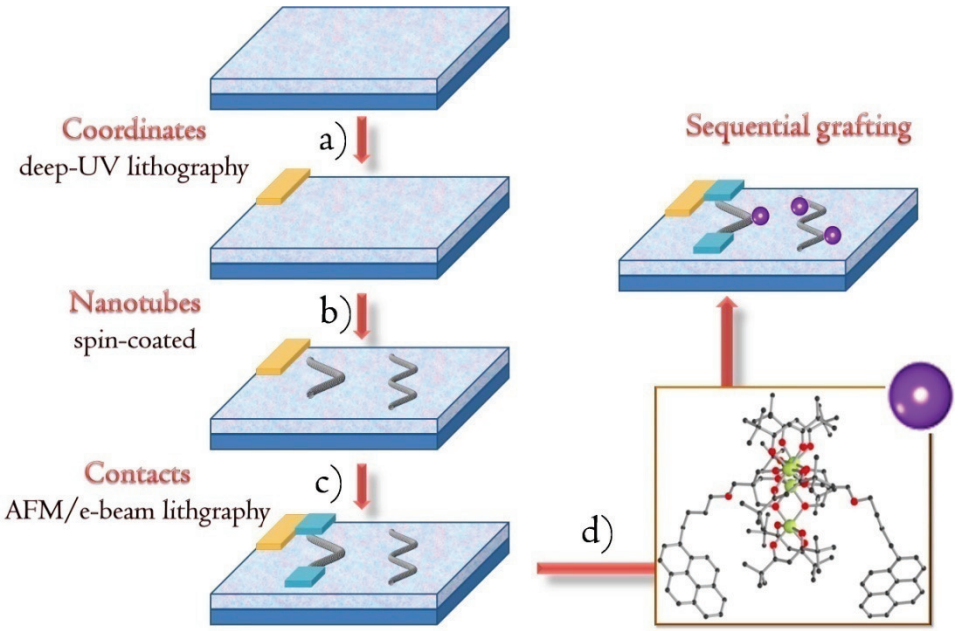

Figure 6.10. Fabrication scheme of the SMM-CNT hybrids.

6.2.6 Atomic Force Microscopy.

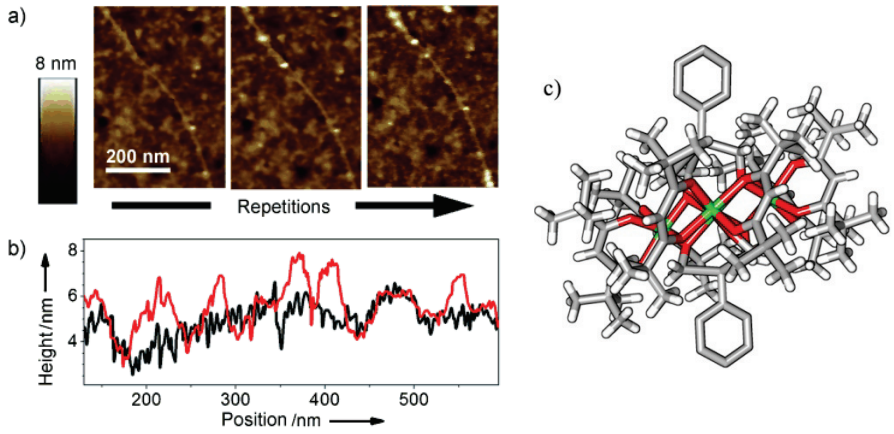

Figure 6.11. AFM topographic analysis of the hybrids. a) Height images of the same CNT acquired on repeating the grafting process: left one time, center four times, right ten times. b) Section profile along the same CNT before (black line) and after (red line) multiple grafting of **Fe_4Py_2**. c) The isostructural cluster $Fe_4(L')_2(dpm)_6$ (**Fe_4Ph**, **48**).

After each treatment a few SMMs were found to stick onto the CNT (Figure 6.11a), while some others were also located on the surrounding surface. The isostructural complex containing H_3L'=2-hydroxymethyl-2-phenylpropane-1,3-diol[11] (**Fe_4Ph**, Figure 6.11c) did not graft onto CNTs in the same experimental conditions. This result is a strong indication that **Fe_4Py_2** has been grafted on the CNT as a result of the pyrenyl functionalities.

The AFM height profile of the same CNT reveals the sequential addition, after each treatment, of objects with size of 1-2 nm (Figure 6.11b).

The height images, reported in Figure 6.12, acquired in tapping mode over a 2 μm-wide square on different samples after repeated treatment with **Fe_4Py_2**, show the selective attachment of the SMMs onto the CNT with respect to the SiO_2 surface.

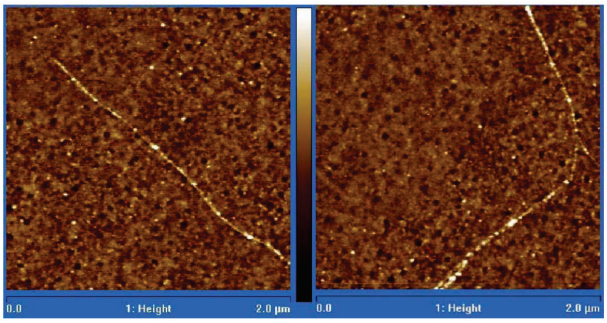

Figure 6.12. Two AFM images showing the selectivity of the grafting. The colorscale in the center represents the height profile, is common for both images, and is 8 nm.

Statistical analysis of small CNTs with diameter of about 1 nm (Figure 6.13a) shows a two-peak distribution that can be fitted ($R^2 = 0.98$) with two Gaussians centered at (1.9 ± 0.3) nm and (1.0 ± 0.3) nm (errors are full-widths-at-half-maxima), with an area ratio of 1:3.

The former peak closely matches the molecular size evaluated from X-ray data and can be assigned to SMMs lying on top of CNTs. The feature of height 1 nm most likely arises from SMMs lying beside a CNT, for which the CNT-SMM height difference is detected (Figure 6.13b), because of the limited lateral resolution of the AFM tip. Thus about 1/4 of the grafted SMMs rest on top of the CNTs, with no direct interaction with the surface.

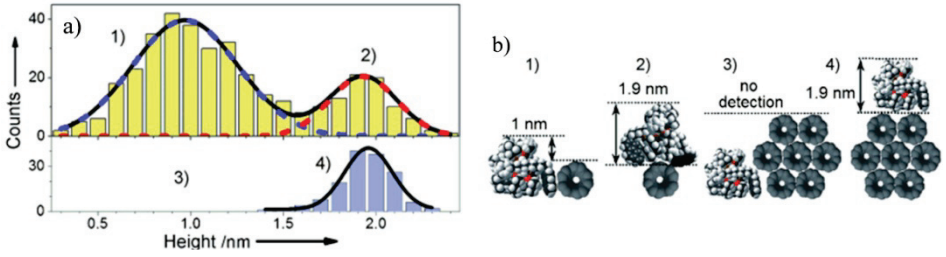

Figure 6.13. a) Heights of the grafted objects. The statistics acquired on single CNTs or small bundles with diameter <1 nm (yellow; 1 & 2 see (b)) differs from that acquired on CNTs or bundles with larger diameter (blue; 3 & 4 see (b)). Lines are fittings with Gaussian distributions. b) Corresponding different dispositions of **Fe4Py2** with respect to CNTs (1 & 2) or bundles (3 & 4).

Inspection of CNTs or bundles with diameter larger than 2 nm shows only one Gaussian peak (R^2 = 0.993) at 2.0 ± 0.2 nm, confirming this interpretation.

6.2.7 Micro-Raman.

Micro-Raman investigation of the CNT-SMM hybrids clearly revealed, superimposed onto CNT and SiO_2 spectra, several peaks associated with intact molecules of **Fe_4Py_2**.

The whole spectrum of the crystalline compound **Fe_4Py_2** is reported in Figure 6.14, and the assignment of a number of relevant peaks is reported in the table. The curved appearance is due to the presence of a small emission background.

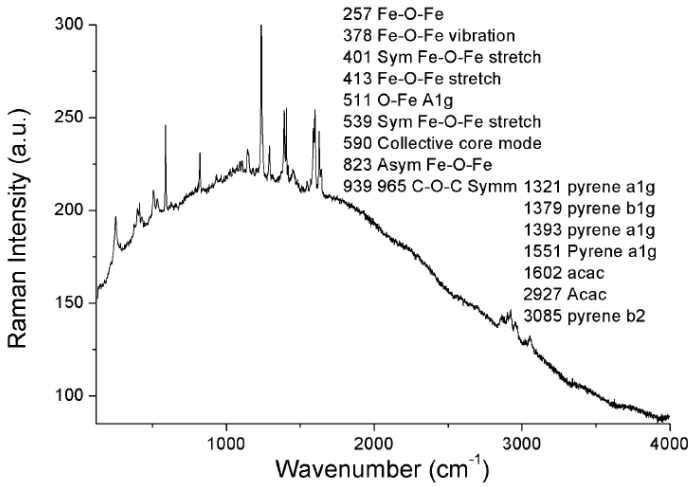

Figure 6.14. Raman spectra of crystalline **Fe_4Py_2** in the 750-4000 cm^{-1} spectral region, together with some assigned peaks.

In Figure 6.15 the same spectrum, after subtraction of the emission background, is compared to that of the CNT-SMM hybrid devices. The spectrum of the hybrids shows several very strong additional peaks, corresponding to the SiO_2 substrate and to the CNT Raman modes. In three regions, displayed in Figure 6.15, the peaks of **Fe_4Py_2** are clearly visible and

no strong CNT or SiO_2 vibrations, which would hide the weaker peaks of **Fe_4Py_2**, are present. As it can be seen the peaks of the ligand are visible at 823, 1146, 1239, 1407, 1419 cm^{-1}, while the low-energy peaks at 378, 401, 413, 590 cm^{-1} are characteristic of the core Fe-O vibrations.

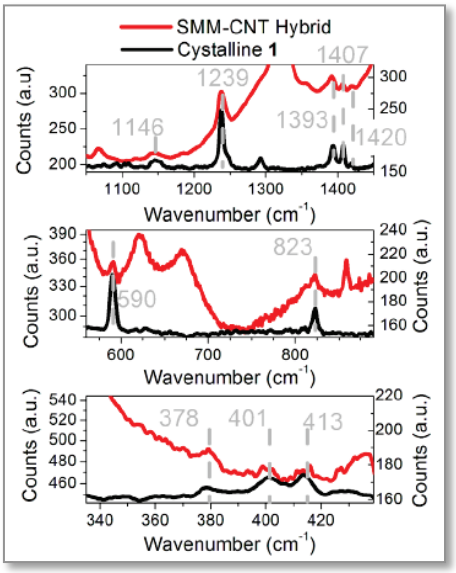

Figure 6.15. Raman spectra in selected, relevant regions of crystalline **Fe_4Py_2** (black line) and of the hybrid devices after multiple treatment (red line), highlighting the presence of the same peaks in both spectra.

To check the correctness of the assignment we intentionally depleted a sample of **Fe_4Py_2** by dissolving it in DCE and letting it rest for 5 weeks. The deposition procedure was then repeated using this sample and Raman spectra were acquired using the same conditions. The results are compared to those of crystalline **Fe_4Py_2** in Figure 6.16. All peaks associated to the core vibrations disappear, and in particular those at 590, 378, 401 and 413 cm^{-1}. Instead only two very weak vibrations are observed at 407 and 613 cm^{-1}.

Furthermore, the fluorescence of pyrene units is quenched in the hybrids, as in solutions of intact **Fe_4Py_2**.

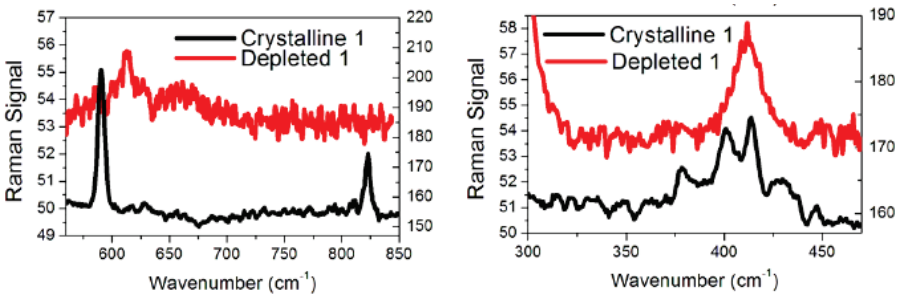

Figure 6.16. Raman spectra of crystalline **Fe4Py2** and the depleted cluster in the selected spectral regions, showing the disappearance of the characteristic core peaks as well as some ligand peaks.

6.2.8 Number of tiny magnets on CNT.

If **Fe4Py2** is randomly distributed along the CNT the probability of having two consecutive molecules at a distance *L* is:

$$P(C,L) = Ce^{-LC} \qquad \text{(eq. 6.1)}$$

where *C* is the linear concentration of **Fe4Py2** on CNTs.[13]

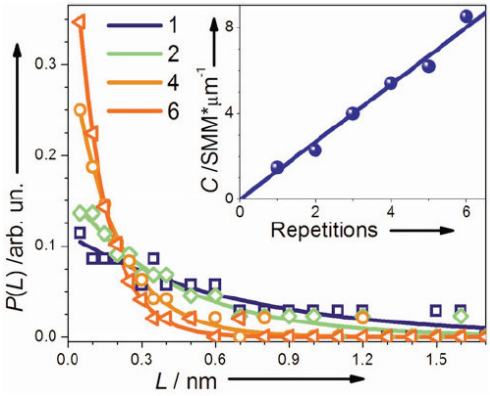

Figure 6.17. Probability of finding a distance *L* between SMMs grafted on CNTs for sequential repetitions of the process. Symbols are experimental data for 1, 2, 4, and 6 repetition and lines are the corresponding fits. Inset: extracted linear concentration (C) as a function of the number of repetitions of the process and linear fit.

Statistical analysis of the distribution of *L*, performed on 40 CNTs, revealed good agreement with the predicted law and allowed *C* to be extracted for each repetition (Figure 6.17). *C* varies linearly (R = 0.998) with the number of repetitions, with 1.5 SMM μm^{-1} deposited at each iteration. Thus, in CNT-FETs with 300 nm gaps, we can graft, on average, one SMM every two treatments, allowing the sequential addition of single SMMs to CNT devices.

6.2.9 Transport Properties.

CNTs are either metallic or semiconducting. Herein we concentrate on the room-temperature transport properties of devices based on semiconducting CNTs, which are better suited for ultra-sensitive detection.[2,3] Current (I_d) versus gate voltage (V_g) curves show *p*-type FET behavior[4] (ON state at $V_g < 0$) with typical I_{ON}/I_{OFF} ratios of three decades (Figure 6.18).

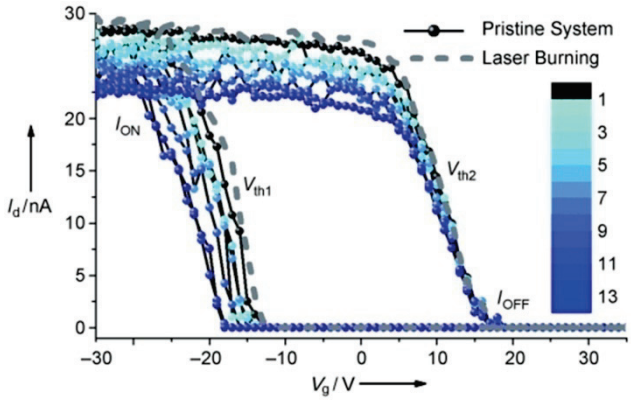

Figure 6.18. Hybrids transport properties. I_d versus V_g curve of a typical CNT-FET shown for the pristine device (black line) and for different numbers (*n*) of grafted SMMs (color scale). The original curve is regained after destruction of **Fe4Py2** by laser burning (gray dashed line) V_{th1} and V_{th2} indicate the ON→OFF and OFF→ON threshold voltages, respectively.

Hysteresis is observed, as a result of charge injection from the CNT to the nearby region.[14] The subthreshold swing (eq. 6.2) remains unchanged upon grafting, indicating that the treatment leaves the gate unaffected.

$$S_W = \frac{dV_g}{dLog(I)} \qquad \text{(eq. 6.2)}$$

While no appreciable variation is observed after repeated treatment of the FETs with DCE alone (Figure 6.19), the I_{ON} current decreases linearly upon SMM grafting, indicating that **Fe_4Py_2** interacts with the electron flow, producing scattering centers.[3] Linear fit of the trend ($R = 0.989$) indicates a contribution of 560 ± 40 pA per SMM (Figure 6.20), which is higher than our instrumental sensitivity of 10 pA and demonstrates single-molecule detection capability.

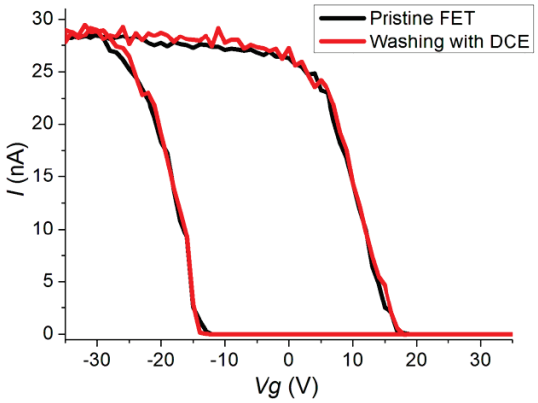

Figure 6.19. Response of a typical CNT-FET before and after repeated washing with DCE.

In the Landauer formulation of incoherent transport regime,[15] such I_{ON} decrease corresponds to an electron reflection coefficient of about 7% per SMM. For comparison, covalent binding of protein molecules on CNTs leads to an electron reflection coefficient of 40% per molecule.[3]

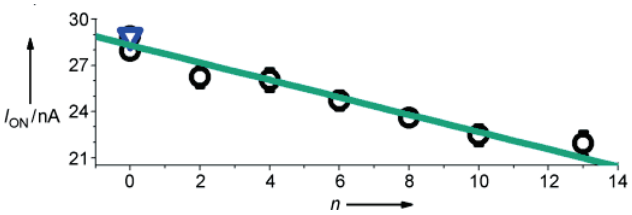

Figure 6.20. Variation of the I_{ON} as a function of the number of grafted molecules (n; circles). The triangle represents the value after laser burning and the line is a fit to the data.

The grafting also produces a gradual decrease in the ON/OFF threshold voltage V_{th1}, along with an increase of the hysteresis width (Figure 6.21). This change is to be attributed to charge-trapping by **Fe4Py2**, as well as a charge transfer between **Fe4Py2** and the CNT.

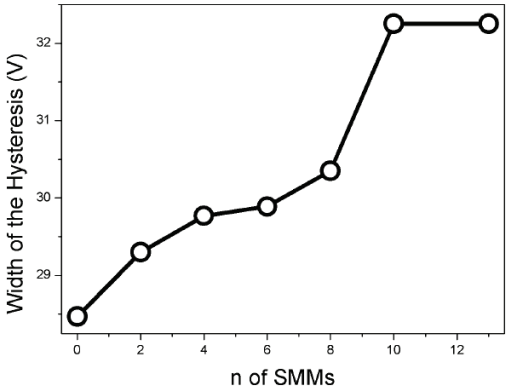

Figure 6.21. Width of the hysteretic response of CNT-FETs as a function of the number of grafted molecules of **Fe4Py2**.

Interestingly **Fe4Py2** can be burnt by laser irradiation (30 mW μm^{-2} at 576.5 nm), causing the disappearance of the Raman fingerprints and the recovery of the original transport curve (Figure 6.18). The grafting-burning procedure can be repeated up to a dozen times, but after this point further iterations fail to recover the original curve, probably because of accumulation of depleted material.

6.3 Conclusions.

In conclusion we bridged the domains of molecular magnetism and CNTs by fabricating the first CNT-SMMs hybrids containing intact pyrene-functionalized SMMs in conditions compatible to the creation of electronic devices. We controlled the grafting of SMMs down to a single-molecule level and we demonstrated the single-SMM sensitivity of CNT-FETs. These results pave the way to the construction of "double-dot" molecular spintronic devices,[5] where a controlled number of nanomagnets is coupled to an electronic nanodevice, and to the observation of the magneto-Coulomb effect. The future use of CNT-SQUIDs may also benefit from the chemical methodology described herein. Finally, the approach may be extended to produce different functional hybrids incorporating charge-transfer complexes, valence tautomers, or photomagnetic materials.[16]

6.4 Acknowledgements.

Special thanks to Cornia's Group of the Modena University for the Fe_4 clusters and Wernsdorfer's Group of the Institut Néel for the CNT study.

6.5 Experimental Section.

6.5.1 Reagent, Chemicals and Instruments used.

All the chemicals were ACS reagent grade and used as received, unless otherwise stated. Anhydrous THF and diethylether, predried over $CaCl_2$, were distilled from Na/benzophenone shortly before use, DMF was distilled over BaO and stored under N_2 in the dark, MeOH was carefully dried by treatment with Mg/I_2 and distilled prior to use. Anhydrous toluene was obtained by distillation over CaH_2 and stored over Na wire. 1,2-dichloroethane was distilled over CaH_2 and stored in the dark over 4 Å molecular sieves.

- Chromatography was performed using 70-230 mesh silica purchased from Merck and 40-120 μ Sephadex G-10 purchased from Pharmacia Fine Chemicals. Thin layer chromatography was performed on Kieselgel 60 F_{254} and Uniplate^{tm} Silica Gel GF silica-coated glass plates and visualized by UV.

- ^{1}H NMR and spectra were recorded on Bruker 300 (300 MHz) and Bruker Avance 300 (300 MHz) spectrometers and all chemical shifts (δ) were reported in parts per million (ppm) relative to proton resonances resulting from incomplete deuteration of NMR solvents. ^{31}P NMR spectra were recorded on AMX-400 (162 MHz) and all chemical shifts were reported to external 85% H_3PO_3 at 0 ppm.

- The NMR experiments were recorded at 303 K with a Bruker FT-DPX200 NMR. The solutions used were prepared with anhydrous solvents and were stored excluding any possible contamination.

- Fluorescence spectra were recorded with a Spex Jobin Yvon FluoroMax 3 fluorimeter equipped with a triangular cell. The solutions used were prepared with anhydrous solvents and were stored excluding any possible contamination.

- ESI-MS characterization experiments were performed on a Waters ACQUILITY SQD Detector equipped with a ESCi® multi mode ionization (APCI/ESI) and a ESI Waters ZQ-4000.
  GC-MS analysis were performed using a HP6890/5973 GC/MS System.

- Elemental analysis on C and H was performed by using a Carlo Erba EA1110 CHNS-O automatic analyzer.

6.5.2 X-Ray Structure Determination.

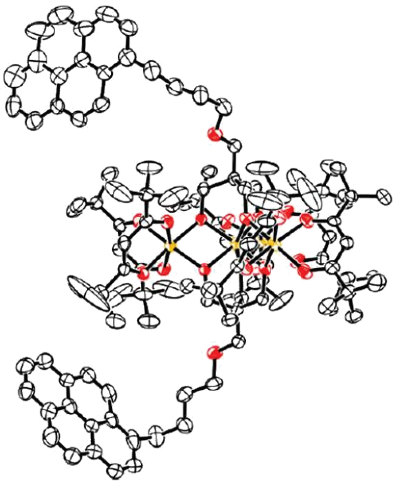

Figure 6.22. Molecular structure of **Fe4-Py2** with displacement ellipsoids drawn at 40-% probability and hydrogen atoms omitted. The disorder on two *t*-Bu groups is not shown for clarity. Color code: black = C, red = O, yellow = Fe.

A single-crystal sample of **Fe4-Py2** with dimensions 0.64 × 0.42 × 0.30 mm, cut from a larger individual using a razor blade, was mounted on a glass fiber with a small amount of vacuum grease and transferred to the cold nitrogen gas stream at 120(2) K of a four-circle Bruxer X8APEX diffractometer (Mo-Kα radiation), equipped with an area detector and a Kryo-Flex cryostat, and controlled by Bruxer-Nonius X8APEX software. Sixty preliminary ω-scan frames were recorded to check the diffracting power

of the sample and to determine the unit cell parameters. Diffraction peaks were systematically found to be structured, pointing to possible pseudo-merohedral twinning effects (see below).

The setting angles of 1036 over 1065 collected diffraction peaks were found consistent with a body-centered monoclinic unit cell with a = 25.10(3) Å, b = 16.26(2) Å, c = 28.27(3) Å, β = 99.06(3)° and V = 11395(9) Å^3 (**cell 1**), corresponding to a conventional monoclinic C cell having a = 34.73(3) Å, b = 16.27(1) Å, c = 28.28(2) Å, β = 134.46(2)° and the same volume (**cell 2**). 42131 intensity data were thus collected from θ = 2.45° to 25.08° and the final unit cell, determined over 9308 reflections, was a = 34.8028(9)Å, b = 16.3092(4) Å, c = 28.3582(7) Å e β = 134.359(1)° and V = 11508.4(8) Å^3 (**cell 2'**). This data set was characterized by a rather high R(int) = 0.0650. Furthermore, a careful analysis of systematic absences showed attenuation but not full extinction of *h*0*l* peaks for odd *l*, thus suggesting the presence of a pseudosymmetry described by a *c*-type glideplane.

Structure solution by direct methods and refinement was then attempted in all *C*-centered monoclinic space groups, using SIR92 [17a] and SHELXL-97[17b] programs implemented in WINGX package.[17c] Structure solution was possible only in space groups *C*2, *Cc* and *C*2/*c*. The tetrairon core was clearly located around a twofold axis and the alkyl chains *plus* the terminal pyrene moieties were found to be disordered over two equally-populated positions. The diffraction pattern was then re-examined in order to check possible deviations from monoclinic symmetry. The setting angles were indeed found consistent with a triclinic cell with a = 16.3398(4) Å, b = 19.1784(5) Å, c = 21.9168(5) Å, α = 87.025(1)°, β = 68.784(1)°, γ = 65.182(1)° and V = 5770.6(4) Å^3 (**cell 3**), with R(int) = 0.0264. Structure solution by direct methods and refinement were successfully carried out in space group *P*-1 affording final indices *wR*2 = 0.2323 (on all data) and *R*1 = 0.0733 [on data with I > 2σ(*I*)] for 19160 unique reflections, 1288 parameters and no restraints. In this space group, no significant disorder effects were found on the alkyl chains and on the terminal pyrene moieties, showing that the correct molecular symmetry is 1 rather than 2. Two *t*-Bu groups were found disordered over two positions with occupancy

factors 0.802(14)/0.198(14) and 0.716(14)/0.284(14), respectively. All non-hydrogen atoms were refined anisotropically, with the exception of the carbon atoms of the disordered *t*-Bu groups in the lower-occupancy position. Hydrogen atoms were treated as fixed contributors in calculated positions and refined isotropically with $U(\mathrm{H}) = kU_{eq}(\mathrm{C})$ where $k = 1.5$ for CH_3 and CH_2 hydrogens, and $k = 1.2$ for CH hydrogens. Final refinement was carried out by introducing the card

TWIN 1.0 0.0 0.0 1.0 -1.0 0.0 1.0 0.0 -1.0 2

in SHELXL-97 program, which accounts for a two-component merohedral or unresolved pseudo-merohedral twinning, with a 80:20 ratio between the two components. The twinning law was deduced from the following considerations. The final triclinic **cell 3** can be transformed into a pseudo-monoclinic body-centered cell similar to **cell I** (a = 25.229Å, b = 16.340 Å, c = 28.364 Å, α = 90.24°, β = 99.20°, γ = 89.19°). The transformation matrix from triclinic cell (t) to pseudo-monoclinic cell (m) is

$$\begin{vmatrix} 1 & -1 & -1 \\ 1 & 0 & 0 \\ 0 & -1 & 1 \end{vmatrix} \begin{vmatrix} a_t \\ b_t \\ c_t \end{vmatrix} = \begin{vmatrix} a_m \\ b_m \\ c_m \end{vmatrix}$$

Because the values of α and γ in the pseudo-monoclinic cell are very close to 90°, a tendency to pseudo-merohedral twinning can be foreseen, based on one of the following two twinning laws:

I) a 180-° rotation around *y*-axis

$$\begin{vmatrix} -1 & 0 & 0 \\ 0 & 1 & 0 \\ 0 & 0 & -1 \end{vmatrix} \begin{vmatrix} a_m \\ b_m \\ c_m \end{vmatrix} = \begin{vmatrix} a_{m'} \\ b_{m'} \\ c_{m'} \end{vmatrix}$$

The same twinning law, in the triclinic cell setting, takes the form

$$\begin{vmatrix} 1 & 0 & 0 \\ 1 & -1 & 0 \\ 1 & 0 & -1 \end{vmatrix} \begin{vmatrix} a_t \\ b_t \\ c_t \end{vmatrix} = \begin{vmatrix} a_{t'} \\ b_{t'} \\ c_{t'} \end{vmatrix}$$

2) a mirror reflection with respect to *xz*-plane

$$\begin{vmatrix} 1 & 0 & 0 \\ 0 & -1 & 0 \\ 0 & 0 & 1 \end{vmatrix} \begin{vmatrix} a_m \\ b_m \\ c_m \end{vmatrix} = \begin{vmatrix} a_{m'} \\ b_{m'} \\ c_{m'} \end{vmatrix}$$

The same twinning law, in the triclinic cell setting, takes the form

$$\begin{vmatrix} -1 & 0 & 0 \\ -1 & 1 & 0 \\ -1 & 0 & 1 \end{vmatrix} \begin{vmatrix} a_t \\ b_t \\ c_t \end{vmatrix} = \begin{vmatrix} a_{t'} \\ b_{t'} \\ c_{t'} \end{vmatrix}$$

Because of the centrosymmetric space group, the two twinning laws are equivalent and can be effectively treated using the above-mentioned TWIN card. It is to be noted that an untwined model affords abnormally-elongated displacement ellipsoids on the carbon atoms of alkyl chains and pyrene groups, and converges to higher *R*-indices [*wR*2(all) = 0.3020, *R*1 ($I > 2\sigma(I)$) = 0.0973].

6.5.3 Magnetic Measurements.

Magnetic data on a polycrystalline 14.37 mg sample of **Fe4-Py2** were recorded using a Cryogenic S600 SQUID magnetometer. Magnetic susceptibility, assumed to correspond to the M/H ratio, was measured as a function of temperature from 1.9 to 230 K with applied fields of 10 kOe (for T > 30 K) and 1 kOe (for ≤ 30 K) in order to reduce saturation effects. Magnetization was also measured at 4.5, 2.5 and 1.9 K in fields up to 50 kOe. Data were reduced assuming a molecular mass of 2101.87 and a diamagnetic correction of $-1283 \cdot 10^{-6}$ emu/mol, estimated from Pascal's constants. Spin Hamiltonian calculations required for data fitting were carried out as previously reported using in-house developed software.[12]

6.5.4 HF-EPR.

High-frequency EPR (HF-EPR) spectra were recorded at the Grenoble High Magnetic Field Laboratory on a homebuilt spectrometer working in

single-pass mode, at temperatures ranging from 5 to 20 K. Gunn diodes operating at 95 GHz or 115 GHz, equipped with a frequency doubler were used as source excitation. The polycrystalline sample used for the experiments was pressed in a pellet in order to avoid orientation effects. Simulation of the spectra was carried out as described elsewhere.[18]

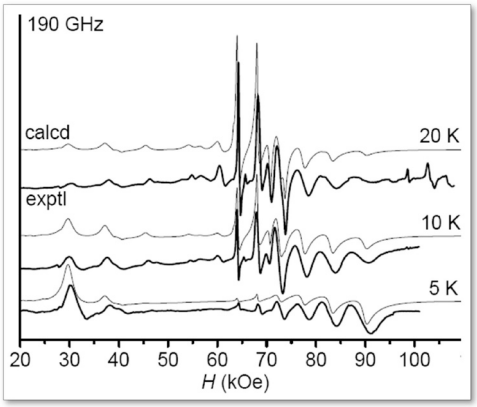

Figure 6.23. HF-EPR spectra of a polycrystalline sample of **Fe4-Py2** (bold lines) along with best-fit simulated spectra (thin lines) with D=-0.409 cm^{-1}, E=0.008 cm^{-1}, B_4^0=2.4·10^{-5} cm^{-1} and g = 2.000±5 in the spin hamiltonian.

6.5.5 Atomic Force Microscopy.

AFM images were acquired using a Veeco D3100 instrument in tapping mode.

6.5.6 Raman.

Raman data were recorded using a LabRam Infinity spectrometer focusing on an area of **Fe4-Py2** μm^2 for Raman spectra at 632.8 nm. Acquisitions were performed on connected, isolated CNTs, typically with 60 accumulations with a 30 seconds acquisition time.

6.5.7 Synthetic Protocol.

4-Pyren-1-yl-butan-1-ol. (41)

A solution of complex BH_3-THF in THF (1 M, 2.08 mL, 2.08 mmol) was added dropwise to an ice-cooled solution of 4-pyren-1-yl-butyric acid (300 mg, 1.04 mmol) in anhydrous THF (10 mL). The reaction was allowed to reach room temperature and stirred overnight, excess borane was quenched with anhydrous methanol and the mixture was stirred for further 8 hours. Volatile organic solvents were removed under reduced pressure and the residue was purified by column chromatography (dichloromethane:EtOH 99:1) to give 4-pyren-1-yl-butan-1-ol (**1**) as a white solid (225 mg., 0.82 mmol, 79%).

^{1}H NMR ($CDCl_3$, 300 MHz) δ(ppm): 8.23-7.97 (m, 8H, Pyrene*H*), 7.81 (d, 1H, J =7.8 Hz, Pyrene*H*), 3.60 (t, 2H, J = 6.6 Hz, C*H*$_2$ OH), 3.26 (t, 2H, J = 7.5 Hz, Pyrene-C*H*$_2$), 1.85 (m, 2H, C*H*$_2$ CH_2OH), 1.67 (m, 2H, C*H*$_2$ CH_2-Pyrene). **GC-MS (EI):** m/z 274 $[M]^+$.

4-bromomethyl-1-methyl-2,6,7-trioxabicyclo[2.2.2]octane. (42)

Compound **42** was prepared following a published procedure.[9]

1-Methyl-4(4-pyren-1-yl-butoxymethyl)-2,6,7-trioxabicyclo[2.2.2] octane. (43)

To a stirred solution of **41** (755 mg, 2.75 mmol) in anhydrous DMF (15 mL) under N_2, solid NaH (264 mg, 11 mmol) was added in one portion. The resulting suspension was stirred for 1 hour at room temperature, then 4-bromomethyl-1-methyl-2,6,7-trioxa-bicyclo[2.2.2]octane (613 mg, 2.75 mmol, **42**) was added in one portion. The temperature was raised to 90°C and the reaction was stirred at that temperature overnight under N_2. After cooling to room temperature, excess NaH was quenched with dilute HCl and the reaction mixture was extracted with dichloromethane, the organic phase was then dried over MgSO4, filtered and concentrated. The residue was purified by column chromatography (dichloromethane:EtOH 95:5) to yield 1-methyl-4-(4-pyren-1-yl-butoxymethyl)-2,6,7-trioxa-bicyclo[2.2.2]octane (**43**) as a brown oil (239 mg., 0.575 mmol, 21%).

^{1}H NMR ($CDCl_3$, 300 MHz) δ(ppm): 8.25 (d, 1H, J = 9.3 Hz, Pyrene*H*), 8.17-8.09 (m, 4H, Pyrene*H*), 8.02 (s, 2H, Pyrene*H*), 7.98 (t, 1H, J = 7.6 Hz, Pyrene*H*), 7.85 (d, 1H, J = 7.8 Hz, Pyrene*H*), 4.17 (s, 2H, C^{IV}-(CH_2 O)($CH_2O)_2$), 3.60 (m, 4H, C^{IV}-(CH_2O)(CH_2 O)$_2$), 3.46 (t, 2H, J = 6.4 Hz, CH_2CH_2 O), 3.41 (s, 2H, O-CH_2-C^{IV}), 3.34 (t, 2H, J = 7.6 Hz, PyreneCH_2), 2.05 (s, 3H, CH_3), 1.90 (m, 2H, CH_2 CH_2O), 1.74 (m, 2H, CH_2 CH_2 Pyrene). **GC-MS (EI):** m/z 416 $[M]^+$.

2-Hydroxymethyl-2-(4-pyren-1-yl-butoxymethyl)-propane-1,3-diol. (H_3L, 44)

To a stirred suspension of **43** (239 mg, 0.574 mmol) in methanol (10 mL), dilute HCl (2 M, 5 mL, 10 mmol) was added. The resulting mixture was stirred at room temperature for 6 hours, then solid Na_2CO_3 (73 mg, 0.689 mmol) was added. The reaction mixture was stirred overnight at room temperature and the solvent was carefully removed under reduced pressure. The residue was extracted in anhydrous methanol and purified by column chromatography (dichloromethane:MeOH 95:5) to yield 2-hydroxymethyl-2-(4-pyren-1-yl-butoxymethyl)-propane-1,3-diol (H_3L, **44**) as a dark yellow solid (80 mg., 0.20 mmol, 35%).

^{1}H NMR: (acetone-d_6, 300 MHz) δ(ppm): 8.33 (d, 1H, J = 9.3 Hz, Pyrene*H*), 8.22-8.09 (m, 4H, Pyrene*H*), 8.06 (s, 2H, Pyrene*H*), 8.00 (t, 1H, J = 7.6 Hz, Pyrene*H*), 7.89 (d, 1H, J = 7.8 Hz, Pyrene*H*), 3.70 (s, 6H, CH_2OH), 3.51 (s, 2H, OCH_2C^{IV}), 3.48 (t, J = 6.0 Hz, 2H, CH_2CH_2O), 3.34 (t, 2H, J = 6.0 Hz, Pyrene-CH_2), 1.88 (m, 2H, CH_2 CH_2O), 1.70 (m, 2H, CH_2 CH_2Pyrene). **ESI-MS:** m/z 427.2 $[M+Cl]^-$.

$Fe_4(OMe)_6(dpm)_6$. (Fe_4, 45)

Fe_4 was prepared in Cornia's Group following a published procedure.[11]

$Fe_4(OMe)_6(dpm\text{-}d_{18})_6$. ($Fe_4$-$d_{18}$, 46)

Fe_4-d_{18} was prepared in Cornia's Group following a published procedure.[11]

$Fe_4(L)_2(dpm)_6$. (Fe_4Py_2, 47)

To a stirred solution of $[Fe_4(OMe)_6(dpm)_6]$ (60 mg, 0.040 mmol) in anhydrous diethylether (25 mL), H_3L (**44**, 42 mg, 0.107 mmol) was added. The reaction was stirred until complete dissolution of the ligand. Slow vapour diffusion of dry methanol (40 mL) into the clear solution at room temperature afforded dark orange crystals, which were collected by filtration, washed with the external solvent mixture and dried under vacuum (79 mg, 0.038 mmol, 95%).

ESI-MS: m/z 2102.7 $[M+H]^+$. **Anal. calcd.** (%) for $Fe_4O_{20}C_{116}H_{164}$: C, 66.29; H 7.87. Found: C, 66.30; H, 8.24.

$Fe_4(L')_2(dpm)_6$. (Fe_4Ph, 48)

Fe_4Ph was prepared in Cornia's Group following a published procedure.[11] H_3L'=2-hydroxymethyl-2-phenylpropane-1,3-diol.

6.6 References.

[1] a) J. Kong, N. R. Franklin, C. Zhou, M. G. Chapline, S. Peng, K. Cho, H. Dai, Nanotube molecular wires as chemical sensors, *Science* **2000**, *287*, 622-625.
b) P. G. Collins, K. Bradley, M. Ishigami, A. Zettl, Extreme oxygen sensitivity of electronic properties of carbon nanotubes, *Science* **2000**, *287*, 1801-1804.
c) K. Besteman, J.-O. Lee, F. G. M. Wiertz, H. A. Heering, C. Dekker, Enzyme-coated carbon nanotubes as single-molecule biosensore, *Nano Lett.* **2003**, *3*, 727-730;
d) A. Star, J. C. P. Gabriel, K. Bradley, G. Gruener, Electronic detection of specific protein binding using nanotube FET devices, *Nano Lett.* **2003**, *3*, 459-463.
e) R. J. Chen, S. Bangsaruntip, K. A. Drouvalakis, N.Wong Shi Kam, M. Shim, Y. Li, W. Kim, P. J. Utz, H. Dai, Noncovalent functionalization of carbon nanotubes for highly specific electronic biosensore, *Proc. Natl. Acad. Sci. USA* **2003**, *100*, 4984-4989.

[2] Y. B. Zhang, M. Kanungo, A. J. Ho, P. Freimuth, D. van der Lelie, M. Chen, S. M. Khamis, S. S. Datta, A. T. C. Johnson, J. A. Misewich, S. S. Wong, Functionalized Carbon Nanotubes for Detecting Viral Proteins, *Nano Lett.* **2007**, *7*, 3086-3091.

[3] a) M. Ouyang, J.-L. Huang, C. L. Cheung, C. M. Lieber, Energy gaps in "metallic" single-walled carbon nanotubes, *Science* **2001**, *292*, 702-705.
b) P. Avouris, Z. Chen, V. Perebeinos, Carbon-based electron ics, *Nat. Nanotechnol.* **2007**, *2*, 605-615.
c) S. J. Tans, A. R. M. Verscheuren, C. Dekker, Room-temperature transistor based on a single carbon nanotube, *Nature* **1998**, *393*, 49-52.
d) D. N. Futaba, K. Hata, T. Yamada, T. Hiraoka, Y. Hayamizu, Y. Kakudate, O. Tanaike, H. Hatori, M. Yumura, S. Iijima, Shape-engineerable and highly densely packed single-walled carbon nanotubes and their application as super-capacitor electrodes, *Nat. Mater.* **2006**, *5*, 987-994.

[4] a) J.-P. Cleuziou, W. Wernsdorfer, V. Bouchiat, T. Ondarçuhu, M. Monthioux, Carbon nanotube superconducting quantum interference device, *Nat. Nanotechnol.* **2006**, *1*, 53-59.
b) P. Jarillo-Herrero, J. A. van Dam, L. P. Kouwenhoven, Quantum supercurrent transistors in carbon nanotubes, *Nature* **2006**, *439*, 953-956.

[5] a) L. Bogani, W. Wernsdorfer, Molecular spintronics using single-molecule magnets, *Nat. Mater.* **2008**, *7*, 179-186.
b) L. Bogani, W. Wernsdorfer, A perspective on combining molecular nanomagnets and carbon nanotube electron ics, *Inorg. Chim. Acta* **2008**, *361*, 3807-3819.

[6] a) D. Gatteschi, R. Sessoli, J. Villain, *Molecular Nanomagnets*, Oxford University Press, Oxford, UK, **2006**.
b) D. Gatteschi, R. Sessoli, Quantum tunneling of magnetization and related phenomena in molecular materials, *Angew. Chem., Int. Ed.* **2003**, *42*, 268-297.
c) A. L. Barra, A. Caneschi, A. Cornia, F. F. De Biani, D. Gatteschi, C. Sangregorio, R. Sessoli, L. Sorace, Single-Molecule Magnet Behavior of a Tetranuclear Iron(III) Complex. The Origin of Slow Magnetic Relaxation in Iron(III) Clusters, *J. Am. Chem. Soc.* **1999**, *121*, 5302-5310.

[7] a) M. N. Leuenberger, D. Loss, Quantum computing in molecular magnets, *Nature* **2001**, *410*, 789-793.
b) F. Troiani, A. Ghirri, M. Affronte, S. Carretta, P. Santini, G. Amoretti, S. Piligkos, G. Timco, R. E. P. Winpenny, Molecular Engineering of Antiferromagnetic Rings for Quantum Computation, *Phys. Rev. Lett.* **2005**, *94*, 207208.
c) F. Troiani, M. Affronte, S. Carretta, P. Santini, G. Amoretti, Proposal for Quantum Gates in Permanently Coupled Antiferromagnetic Spin Rings without Need of Local Fields, *Phys. Rev. Lett.* **2005**, *94*, 190501.
d) J. Lehmann, A. Gaita-Ariño, E. Coronado, D. Loss, Spin qubits with electrically gated polyoxometalate molecole, *Nat. Nanotechnol.* **2007**, *2*, 312-317.

[8] a) S. Banerjee, T. Hemraj-Benny, S. S. Wong, Covalent surface chemistry of single-walled carbon nanotubes, *Adv. Mater.* **2005**, *17*, 17-29.
b) D. M. Guldi, G. M. A. Rahman, F. Zerbetto, M. Prato, Carbon Nanotubes in Electron Donor-Acceptor Nanocomposites, *Acc. Chem. Res.* **2005**, *38*, 871-878
c) V. Georgakilas, D. Gournis, V. Tzitzios, L. Pasquato, D. Guldi, M. Prato, Decorating carbon nanotubes with metal or semiconductor nanoparticles, *J. Mater. Chem.* **2007**, *17*, 2679-2694.
d) K. Kurppa, H. Jiang, G. R. Szilvay, A. G. Nasibulin, E. I. Kauppinen, M. B. Linder, Controlled hybrid nanostructures through protein-mediated noncovalent functionalization of carbon nanotubes, *Angew. Chem., Int. Ed.* **2007**, *46*, 6446-6449.
e) K. Jiang, A. Eitan, L. S. Schadler, P. M. Ajayan, R.W. Siegel, N. Grobert, M. Mayne, M. Reyes-Reyes, H. Terrones, M. Terrones, Selective Attachment of Gold Nanoparticles to Nitrogen-Doped Carbon Nanotubes, *Nano Lett.* **2003**, *3*, 275-277.

[9] A. B. Padias, H. K. Hall, Synthesis and polymerization of pentaerythritol monoacrylate and methacrylate and their bicyclic ortho esters, *Macromolecules* **1982**, *15*, 217-223.

[10] Crystal structure data for **Fe_4Py_2**: $C_{116}H_{164}Fe_4O_{20}$, M_r=2101.87, crystal dimensions 0.64x0.42x0.30 mm, triclinic, space group *P*-1, a = 16.3398(4), b = 19.1784(5), c = 21.9168(5) Å, α = 87.025(1)°, β = 68.784(1)°, γ = 65.182(1)°, V = 5770.6(2) Å^3, Z = 2, ρ_{calcd}= 1.210 gcm^{-3}, μ = 0.556 mm^{-1}, Mo$^{K\alpha}$ radiation, λ = 0.71073 Å, T = 120(2) K, $2\theta_{max}$ = 50.16°, 42131/19160 reflections collected/unique (R_{int} = 0.0264), $R1$=0.0733, $wR2$=0.2323, largest diff. peak and hole 0.985/-0.558 eÅ^{-3}.

CCDC-704776 (**Fe4Py2**) contains the supplementary crystallographic data for this paper. These data can be obtained free of charge from The Cambridge Crystallographic Data Centre via www.ccdc.cam.ac.uk/data_request/cif.

[11] S. Accorsi, A.-L. Barra, A. Caneschi, G. Chastanet, A. Cornia, A. C. Fabretti, D. Gatteschi, C. Mortalò, E. Olivieri, F. Parenti, P. Rosa, R. Sessoli, L. Sorace, W. Wernsdorfer, L. Zobbi, Tuning Anisotropy Barriers in a Family of Tetrairon(III) Single-Molecule Magnets with an S = 5 Ground State, *J. Am. Chem. Soc.* **2006**, *128*, 4742-4755.

[12] A.-L. Barra, F. Bianchi, A. Caneschi, A. Cornia, D. Gatteschi, L. Gorini, L. Gregoli, M. Maffini, F. Parenti, R. Sessoli, L. Sorace, A. M. Talarico, New single-molecule magnets by site-specific substitution: incorporation of "alligator clips" into Fe4 complexes, *Eur. J. Inorg. Chem.* **2007**, 4145-4152.

[13] a) N. L. Johnson, S. Kotz, *Distributions in Statistics*, Wiley, New York, **1972**.
b) For the conceptually identical problem of randomly placed diamagnetic sites in a magnetic chain, see: L. Bogani , A. Caneschi, M. Fedi, D. Gatteschi, M. Massi, M. A. Novak, M. G. Pini, A. Rettori, R. Sessoli, A. Vindigni, Finite-size effects in single chain magnets: an experimental and theoretical study, *Phys. Rev. Lett.* **2004**, *92*, 207204.
c) L. Bogani , R. Sessoli, M. G. Pini, A. Rettori, M. A. Novak, M. Massi, M. Fedi, L. Giuntini, A. Caneschi, D. Gatteschi, Finite-size effects on the static properties of a single-chain magnet, *Phys. Rev. B* **2005**, *72*, 064406.

[14] a) K. Bradley, J. Cumings, A. Star, J.-C. P. Gabriel, G. Gruener, Influence of mobile ions on nanotube based FET devices, *Nano Lett.* **2003**, *3*, 639-641.
b)W. Kim, A. Javey, O. Vermesh, Q. Wang, Y. Li, H. Dai, Hysteresis Caused by Water Molecules in Carbon Nanotube Field-Effect Transistors. *Nano Lett.* **2003**, *3*, 193-198.

[15] a) M. Blockrath, W. Liang, D. Bozovic, J. H. Hafner, C. M. Lieber, M. Tinkham, H. Park, Resonant electron scattering by defects in single-walled carbon nanotubes, *Science* **2001**, *291*, 283-285.
b) A. Bachtold, M. S. Fuhrer, S. Plyasunov, M. Forero, E. H. Anderson, E. Zettl, P. L. McEuen, Scanned probe microscopy of electron transport in carbon nanotubes, *Phys. Rev. Lett.* **2000**, *84*, 6082-6085.

[16] a) J. S. Miller, J. C. Calabrese, R. S. McLean, A. J. Epstein, meso-(Tetraphenylporphinato)manganese(III) tetracyanoethenide, $[MnIIITPP]^{+}[TCNE]^{\cdot}$. A new structure-type linear-chain magnet with a Tc of 18 K, *Adv. Mater.* **1992**, *4*, 498-501.

b) A. Dei, Photomagnetic effects in polycyanometallate compounds: An intriguing future chemically based technology?, *Angew. Chem., Int. Ed.* **2005**, *44*, 1160-1163.
c) C. Carbonera, A. Dei, J.-F. Ltard, C. Sangregorio, L. Sorace, Thermally and light-induced valence tautomeric transition in a dinuclear cobalt-tetraoxolene complex, *Angew. Chem., Int. Ed.* **2004**, *43*, 3136-3138.
d) K. Matsuda, M. Irie, . Photoswitching of intramolecular magnetic interaction using a photochromic spin coupler. An ESR study, *J. Am. Chem. Soc.* **2000**, *122*, 8309-8310.

[17] a) A. Altomare, G. Cascarano, C. Giacovazzo, A. Guagliardi, Completion and refinement of crystal structures with SIR92, *J. Appl. Crystallogr.*, **1993**, 26:343-350;
b) G. M. Sheldrick, SHELX97, *Programs for Crystal Structure Analysis (Release 97-2)*, University of Göttingen, Göttingen, **1997**.
c) L. J. Farrugia, WinGX suite for small-molecule single-crystal crystallography, *J. Appl. Crystallogr.* **1999**, *32*, 837-838.

[18] C. J. H. Jacobsen, E. Pedersen, J. Villadsen, H. Weihe, ESR characterization of trans-diacidatotetrakis(pyridine)vanadium and -manganese trans-VII(py)4x2 and trans-MnII(py)4x2 (X = NCS, Cl, Br, I; py = pyridine), *Inorg. Chem.* **1993**, *32*, 1216-1221.

Tiny Magnet Functionalized with Charged Ligand.

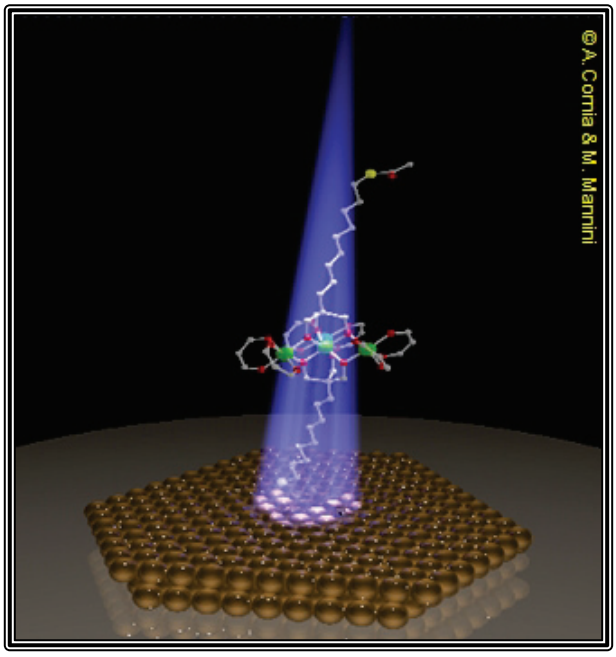

"Magnetic Molecule tethered on Surface"

Image refers to: M. Mannini, F. Pineider, P. Sainctavit, C. Danieli, E. Otero, C. Sciancalepore, A. M. Talarico, M.-A. Arrio, A. Cornia, D. Gatteschi, R. Sessoli, Magnetic memory of a single-molecule quantum magnet wired to a gold surface, *Nature Materials* **2009**, *8*, 194-197.

7.1 Introduction.

The synthesis of molecular magnets has undergone rapid progress in recent years. In particular, the bottom-up technologies in which molecules are used as single data-processing devices are enormously promising in terms of storage and data-handling density. The most promising architecture in molecular electronics is a hybrid system in which a dense array of molecular devices is hosted on a silicon-based microelectronic circuit.

One of the key factor in the development of those devices is the establishment of a dense array on the surface ordered in a suitable and accessible way so that their state can be probed.

Unlikely, until now the attempts to organized **Mn12**-based clusters, the archetype of SMM[1], on Au(111) surface keeping intact its magnetic properties were unsuccessful.[2] In particular, it was clearly observed a partial reduction of metal ions to Mn^{II} upon deposition on Au(111) leading to a partial or entire loss of the magnetic behaviour.

A recent paper showed the possibility of anchoring **Mn12** cluster on a surface of technological importance such as Si(100).[3] The present work is focused on the anchorage of **Fe4** cluster which, like **Mn12**, is not intrinsically suited for direct anchoring on silicon. Therefore, two different strategies can be adopted, based either on modification of the cluster with suitable functionalities capable of surface binding, or on modification of the surface with a layer capable of cluster coordination. The first approach, which entails the silicon grafting, presents severe drawbacks due to the thermal instability of the Fe_4 core.[4] On the contrary, the previous functionalization of the silicon surface allows the cluster anchorage under mild conditions and thus precludes degradation of the core.

In particular, SMMs functionalization must meet three basic requirements:

i) magnetic properties of SMMs must not be negatively affected by the presence of the introduced functional groups.

ii) the anchored group should allow an effective interaction with the surface.

iii) the molecule must be able to interact with the surface with a small number of different orientation; for this purpose, it is

essential that the anchored groups are in limited number and spatially arranged in a controlled manner (site-specific functionalization).

In this Chapter the attempt to graft the **Fe4** on silicon surfaces via complexation with tetraphosphonate cavitands, previously grafted on the wafer, is reported.

7.2 Results and Discussion.

One of the key issue in the anchorage of SMMs on surface is to keep intact the magnetic properties of the cluster. To this purpose, we decided to graft it through noncovalent interaction exploiting the molecular recognition properties of the tetraphosphonate cavitands towards *N*-methyl pyridinium. In fact, grafting through covalent bonds not only modified the cluster structure but also connect it directly with the surface leading to magnetic properties alteration.

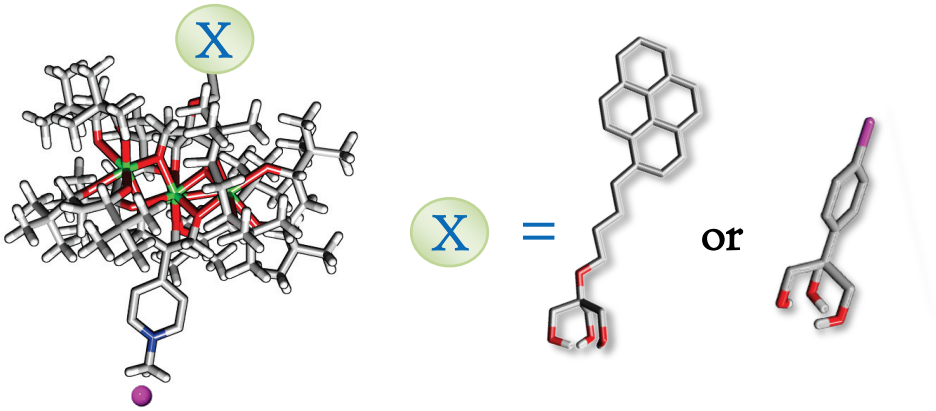

Figure 7.1. Di-substitued **Fe4** cluster.

Therefore, our idea was to functionalized the **Fe4** cluster with two different tripodal ligand: on the one hand a methyl pyridinium ligand, in order to introduce the recognition moiety for the cavitand, on the other hand a fluorophore or an halogens moiety (Figure 7.1), in order to characterize the surface via Fluorescence and X-Ray Photoelectron Spectroscopy respectively.

Unfortunately, functionalized **Fe4** clusters are synthesized exclusively via crystallization. This means that is favoured the omo-substituted while the di-substituted is almost impossible to obtain. Separation method like column chromatography are unsuitable for this kind of molecules, since they decompose.

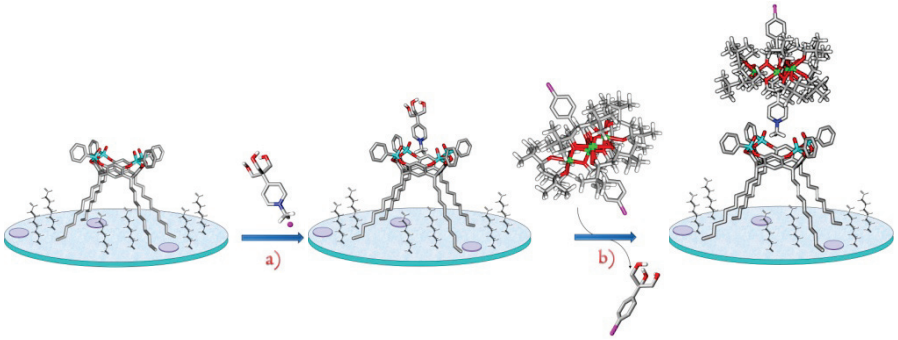

Figure 7.2. SMM Grafting protocol on Silicon.

To solve this problem we decided to perform at first the complexation on surface of the *N*-methyl pyridinium tripodal ligand with the cavitand (Figure 7.2, step a), followed by the anchorage of the **Fe4(PhCl)2** cluster (**52**) via ligand exchange directly on surface (Figure 7.2, step b).

7.2.1 Synthetic Protocol.

The synthesis of **Fe4Py2** (**47**) cluster was already reported in Chapter 6.

The reaction protocol for T^{iiii}[$C_{11}H_{23}$, H, Ph] cavitand (**2**), used for the titration, and T^{iiii}[C_3H_7, CH_3, Ph] cavitand (**4**), employed for crystal structure, were described in Chapter 2.

Moreover, the synthesis of T^{iiii}[$C_{10}H_{19}$, H, Ph] (**16**) and the preparation of the Si-T^{iiii} (χ = 1) wafer were previously described in Chapter 3.

Tripodal ligand **51** and **Fe4(PhCl)2** (**52**) were supplied by Cornia's Group of the Modena University. In particular, compound **52** was synthesized following a published procedures[5], while ligand **51** (called PhMe in the tetrairon cluster), featuring a methyl pyridinium as recognition moiety towards the cavitand and a triol as interacting group with the tetrairon, was synthesized according to the pathway reported in Scheme 7.1.

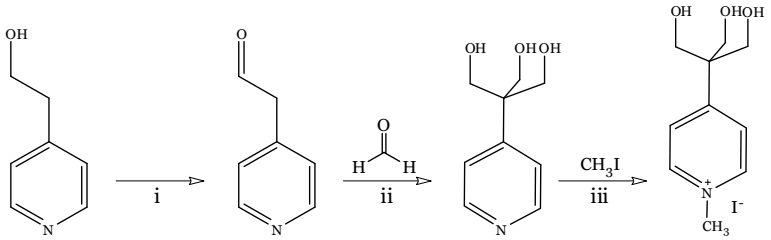

Scheme 7.1. Synthesis of tripodal ligand **51**. i) trichlorocyanuric acid, TEMPO, 15min, r.t, ii) $Ca(OH)_2$, 4 days, 65°, iii) CH_2Cl_2, 12hrs, reflux.

At first, it was performed the oxidation of 4-(2-hydroxyethyl)pyridine, using trichlorocyanuric acid and TEMPO, affording 4-pyridineacetaldehyde (**49**). In order to introduce the triol functionality, compound **49** was reacted with paraformaldehyde in the presence of $Ca(OH)_2$ obtaining compound **50** which was finally methylated with iodomethane giving the desired product **51**.

7.2.2 Ligand-Cavitand complexation and Ligand-SMM exchange in solution.

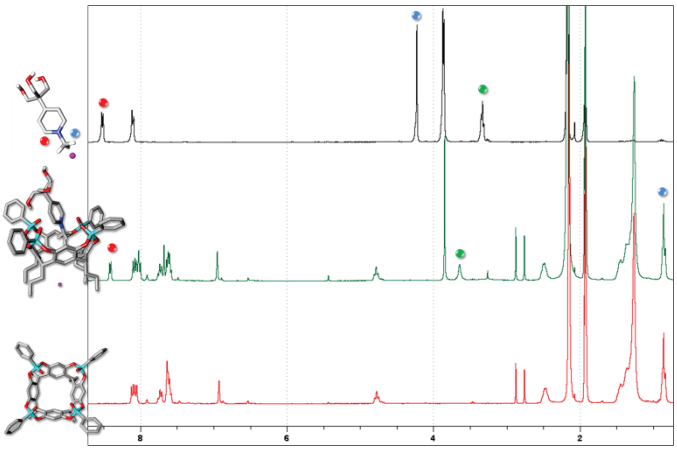

Figure 7.3. ^1H NMR (300 MHz, CD_3CN) spectra of a 1.9 mM solution of receptor **2** (bottom); of an equimolar solution of cavitand **2** and ligand **51** (middle) and of a 1.9 mM solution of ligand **51** (top). In the modeling hydrogen atoms and part of the cavitand chains are omitted for clarity.

In order to evaluate if tripodal ligand **5I** complexes the cavitand, a ^{1}H NMR titration of the T$_{iiii}$[$C_{11}H_{23}$, H, Ph] cavitand (**2**) with compound **5I** in CD_3CN was carried out. The guest inclusion in the cavity is proved by the usual upfield shift of the orto hydrogen of the ligand pyridinium (Py*H*$_o$, $\Delta\delta$ = 0.1 ppm, red ball, Figure 7.3), and by the upfield shift of the ligand methyl ($\Delta\delta$ = 3.37 ppm, blue ball, Figure 7.3) under the methyl of the alkyl chains of the cavitand. Moreover, we also observed a downfield shift of the O*H* hydrogen ($\Delta\delta$ = 0.31 ppm, green ball, Figure 7.3) probably due to hydrogen bonding with the P=O (see crystal structure).

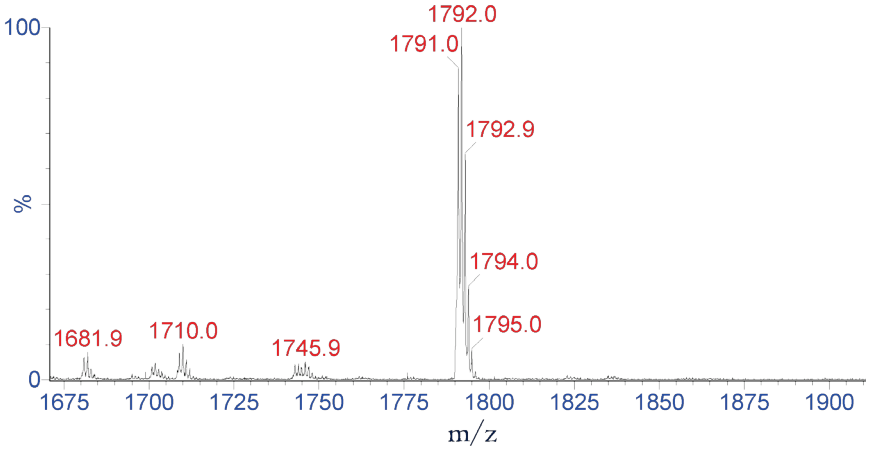

Figure 7.4. ESI MS spectrum of complex **2@5I** in CD_3CN showing [(**2@5I**)-I]$^+$ signal at m/z 1792.0.

The formation of the complex is confirmed by ESI mass spectrometry, which showed the diagnostic [(**2@5I**)-I]$^+$ signal at 1792.0 m/z (Figure 7.4), and by the crystal structure of cavitand **4** complexed with **5I** grown in a solution of acetonitrile and trifluoroetanol (Figure 7.5 and Experimental Section).

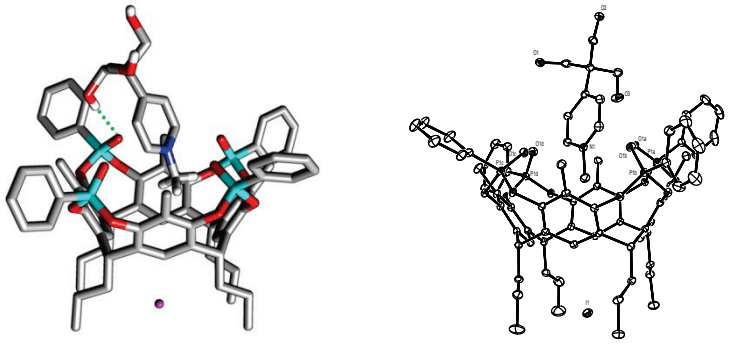

Figure 7.5. Crystal structure of **4@51**@5CH_3CN complex in stick style (left) and ortep view (right, 20% ellipsoid probability). Hydrogen atoms and acetonitrile solvent molecules are omitted for clarity.

The ligand exchange was assessed via ESI MS experiment. The mass spectrum (Figure 7.6) recorded on **$Fe_4(PhCl)_2$** cluster dissolved together with ligand **51** in $CHCl_3/CH_3CN$, shows the diagnostic signals at 856.44 m/z, 1730.70 m/z and 1840.14 m/z corresponding to the disubstituted dicharged [**$Fe_4(PyMe)_2$**-2I]$^{2+}$, the monosubstituted monocharged [**$Fe_4(PyCl)(PyMe)$**-I]$^{+}$ and the disubstituted monocharged [**$Fe_4(PyMe)_2$**-I]$^{+}$ (very low abundance) respectively. Therefore, it was demonstrated that the ligand exchange takes place and that it is fast.

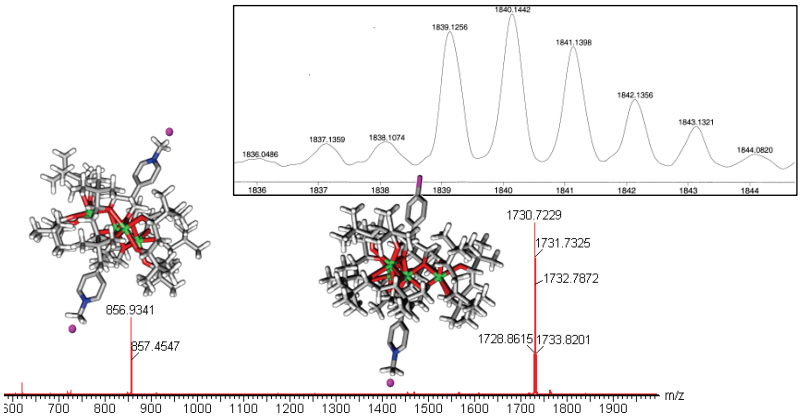

Figure 7.6. ESI MS spectrum showing the exchange diagnostic signal corresponding to [**$Fe_4(PyMe)_2$**-2I]$^{2+}$, [**$Fe_4(PyCl)(PyMe)$**-I]$^{+}$ and [**$Fe_4(PyMe)_2$**-I]$^{+}$.

7.2.3 Complexation and Exchange on Surface.

The *N*-methyl pyridinium-cavitand complexation on surface was already described and demonstrated in Chapter 3. In particular, the complexation was performed by dipping Si-T_{iiii} (χ = 1) substrate for 30 minutes in a 10^{-3} M solution of ligand **51** in acetonitrile (Figure 7.2, step a). After the time reaction the wafer was removed from the solution and rinsed in acetonitrile.

Subsequently, in order to anchorage **$Fe_4(PhCl)_2$** on surface, Si-T_{iiii}@**51** wafer was dipped in a 10^{-6} M solution of the tetrairon cluster in diethyl ether for 6 hours to exchange the PhCl tripodal ligand of the cluster with ligand **51** already complexed on surface (Figure 7.2, step b). The wafer was rinsed with diethyl ether, sonicated in the same solvent and analyzed.

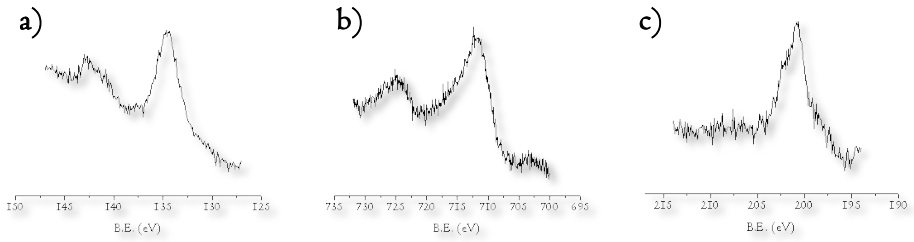

Figure 7.7. High resolution XPS of the Si-T_{iiii}@**51** (χ = 1) treated with **$Fe_4(PhCl)_2$** showing: a) P 2p band of the cavitand **16** grafted on surface, b) Fe 2p bands of **Fe_4** cluster anchored on surface and c) Cl 2p band of **Fe_4** cluster anchored on surface.

The XPS analyses show the presence of the P 2p band (BE P 2p = 134.4 eV), supporting the presence of T_{iiii} cavitand on the surface, while the anchoring of the nanomagnet is supported by the presence of a doublet in the Fe 2p region (BE Fe $2p_{3/2}$ = 711.0 eV) and by the presence of the Cl 2p band (BE Cl 2p = 200.7 eV) (Figure 7.7).

The control experiment was carried out by dipping a Si-T_{iiii} (χ = 1) wafer in the solution of the cluster in diethyl ether (10^{-6} M) for 6 hours. The wafer was rinsed with diethyl ether, sonicated in the same solvent and analyzed. In this case, the surface is not complexed with ligand **51**, so that we expected no ligand exchange and therefore no nanomagnet anchorage.

Unfortunalely, also in the control we observe the presence of the Fe 2p band and the Cl 2p band (Figure 7.8). This means that we have direct interaction between the nanomagnet and the tetraphosphonate cavitands, probably due to the interference of the P=O in the coordination sphere of the cluster. In particular, could be that some C=O•••Fe bonds was substituted by P=O•••Fe bonds.

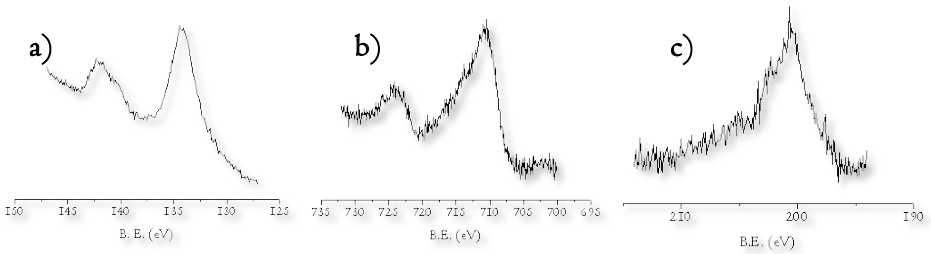

Figure 7.8. High resolution XPS of the Si-T$_{iiii}$ (χ = 1) treated with **Fe$_4$(PhCl)$_2$** showing: a) P 2p band of the cavitand **16** grafted on surface, b) Fe 2p bands of **Fe$_4$** cluster anchored on surface and c) Cl 2p band of **Fe$_4$** cluster anchored on surface.

Further problem could be that tripodal ligand **51** is too short and, as can see in the crystal structure (Figure 7.5 and 7.9), methyl pyridinium **51** does not protrude significantly from the cavity.

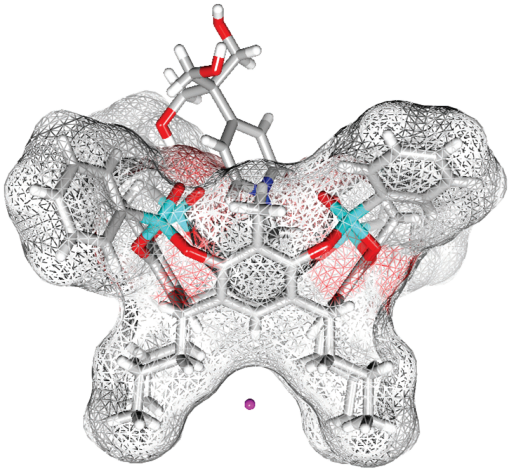

Figure 7.9. Crystal structure of **4@51** complex.

Therefore, there is the possibility that the exchange becomes hard as a result of the steric hindrance between the phenyl, linked to the cavitand phosphonate group, and the dipivaloylmethane ligands of the tetrairon cluster. As a consequence, we decided to synthesized a longer and rigid tripodal ligand hoping that the exchange reaction is much faster than the interaction with the cavitand.

7.2.4 Elongated Tripodal Ligand Synthesis.

The new target molecule features a rigid phenylacetylene spacer between the pyridine unit and the triol moiety. The multistep synthesis is reported in Scheme 7.2 and 7.3.

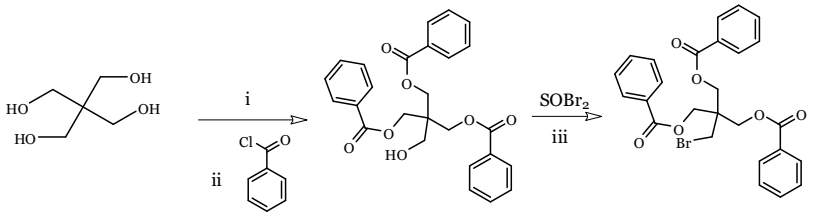

Scheme 7.2. Synthesis of protected pentaerythritol **54**. i) toluene/pyridine, 30 min., r.t; ii) 30 hrs, 50°C; iii) DMF, 2hrs, 50°C.

First of all, we synthesized the protected triol moiety (**53**) by reaction of pentaerythritol with benzoyl chloride. The subsequent bromination with thionyl bromide, afforded the desired product **54** in 98% yield.

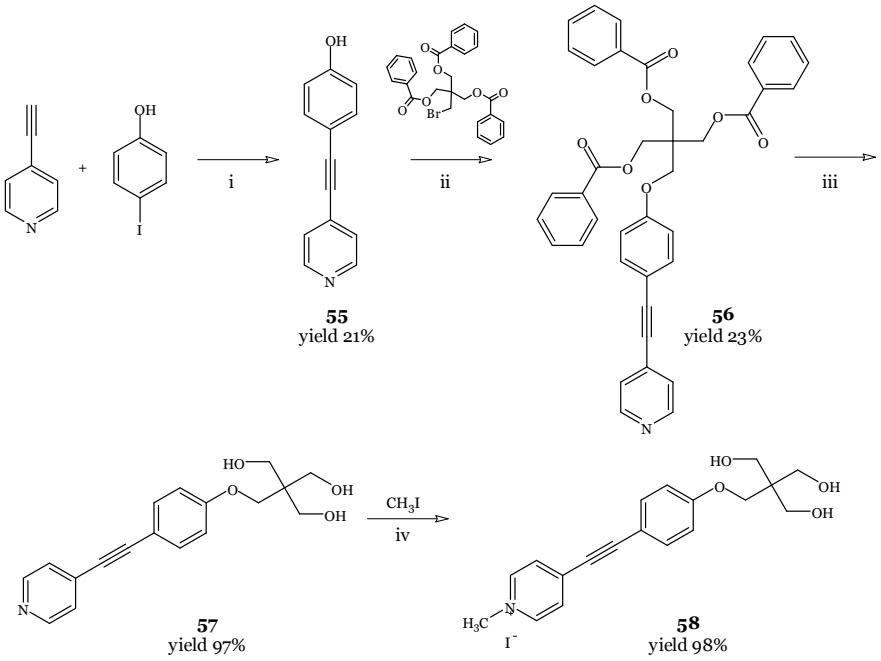

Scheme 7.3. Synthesis of ligand **58**. i) Et_3N degassed, $Pd(PPh_3)_2Cl_2$, CuI, PPh_3, 2 hrs, 60°C; ii) DMA dry, NaH, o.n. 90°C; iii) MeOH, K_2CO_3, 1h, r.t.; iv) DMF, CH_3I, o.n., 50°C.

The four-step synthesis of tripodal ligand **58** was then made. The first step was a Sonogashira coupling executed between 4-iodophenol and ethynylpyridine affording derivative **55**, which was then subjected to a nuclueophilic aromatic substitution to give the protected triol **56**. The subsequent treatment of **56** with K_2CO_3 caused the deprotection of the triol moiety leading to compound **57**, which was finally methylated with iodomethane affording the desired product **58** in quantitative yield.

7.2.5 Elongated Ligand-SMM Exchange in solution.

As for the shorter ligand, we studied if the exchange can take place by ESI MS. In this case, we met some problem to find a solvent for the ligand compatible with the tetrairon stability. At the end, we decided to use DMF in which both ligand **58** and $Fe_4(PhCl)_2$ are soluble.

The mass spectrum recorded on **$Fe_4(PhCl)_2$** cluster dissolved together with ligand **58** in DMF/CH_3NO_2, shows an high signal at 1563.7 m/z corresponding to the exchange of all the dipivaloylmethane of the cluster with DMF **$[Fe_4(DMF)_6(PhCl)_2+K]^+$** (Figure 7.10). Moreover, it is also possible to see the diagnostic signal at 987.0 m/z and 1863.6 m/z corresponding to the disubstituted dicharged **$[Fe_4(PhPyMe)_2\text{-}2I]^{2+}$** and the monosubstituted monocharged **$[Fe_4(PyCl)(PhPyMe)\text{-}I]^+$** respectively. Therefore, we observed the ligand exchange, also if at a slower rate in comparison with ligand **51**.

Unfortunately, when we studied the stability of the cluster with ligand **58** by ^2H NMR in toluene-*d*$_6$, by using the same procedure reported in Chapter 6, we observed a complete decomposition of the cluster after only 20 minutes from the dissolution.

The instability is probably due to the reduction of the iron from the iodide.

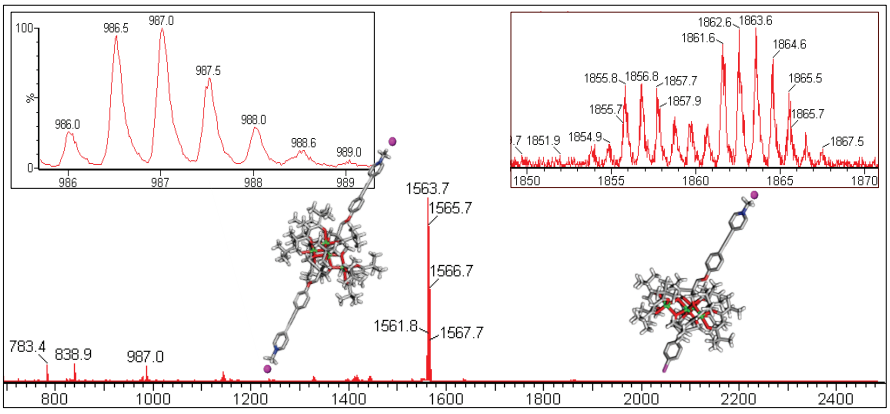

Figure 7.10. ESI MS spectrum showing the exchange diagnostic signal corresponding to **$[Fe_4(PhPyMe)_2\text{-}2I]^{2+}$**, **$[Fe_4(PyCl)(PhPyMe)\text{-}I]^+$** and **$[Fe_4(DMF)_6(PhCl)_2+K]^+$**.

7.3 Conclusions.

In this Chapter we have reported the attempts to graft **Fe4** on silicon surface exploiting host-guest interaction and a ligand exchange on surface. In particular we demonstrated via ESI MS, both with ligand **51** and **58**, that the ligand exchange takes place. Unfortunately, when we performed the grafting on silicon with ligand **51** we observed direct interaction between the cavitand and the tetrairon cluster. Moreover, we noticed in the crystal structure of the tetraphosphonate cavitand with **51** that the ligand is almost completely nested inside the cavity making the ligand exchange difficult because of the steric hindrance between the cavitand phenyl and the dipivaloylmethane of the cluster.

In order to favour the exchange on the surface, we synthesized a rigid elongated tripodal ligand (**58**). Also in this case we observed fast ligand exchange in solution, but a very low stability of the cluster which already after twenty minutes is completely destroyed.

Therefore, we can conclude that the idea to anchorage **Fe4** on silicon surface exploiting host-guest interaction followed by ligand exchange is not possible because of the interaction between the free cavitand and the cluster, and the instability of the cluster substituted with methyl pyridinium ligands. The instability is probably due to the reduction of the iron from the iodide.

This work in more general terms is part of our ongoing effort to integrate **Fe4** SMM into supramolecular structures. To this purpose the synthesis of the compound depicted in Figure 7.11 will be attempted in the future.

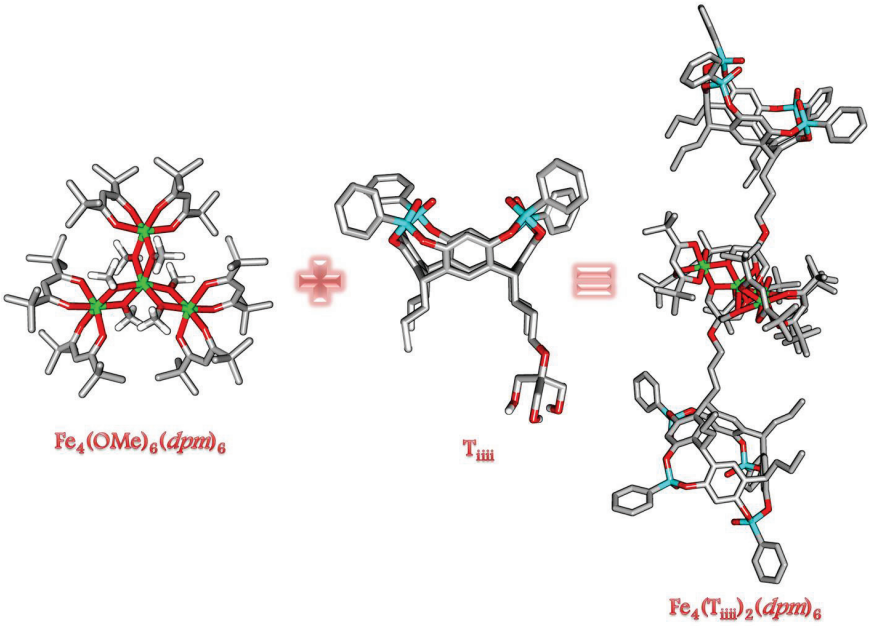

Figure 7.11. Future activity.

7.4 Acknowledgements.

Special thanks to Cornia's Group of the Modena University for the **Fe4(PhCl)2** and triol **51**, Dr. Chiara Massera of the Parma University for the X-Ray Crystal Structure and Dr. Federica Bianchi for the ESI-MS analyses.

7.5 Experimental Section.

7.5.1 Reagent, Chemicals and Instruments used.

All commercial reagent were ACS reagent grade and used as received. For the synthesis all solvents were dried and distilled using standard procedures.

- ♣ Chromatography was performed using 70-230 mesh silica purchased from Merck and 40-120 μ Sephadex G-10 purchased from Pharmacia Fine Chemicals. Thin layer chromatography was performed on Kieselgel 60 F_{254} and Uniplate^{tm} Silica Gel GF silica-coated glass plates and visualized by UV.

- ♣ ^{1}H NMR and spectra were recorded on Bruker 300 (300 MHz) and Bruker Avance 300 (300 MHz) spectrometers and all chemical shifts (δ) were reported in parts per million (ppm) relative to proton resonances resulting from incomplete deuteration of NMR solvents.

- ♣ ESI-MS characterization experiments were performed on a Waters ACQUILITY SQD Detector equipped with a ESCi® multi mode ionization (APCI/ESI).

- ♣ Ligand exchange experiments were performed on a ESI Waters ZQ-4000.

7.5.2 X-ray Crystallographic Studies.

Crystal data and experimental details for data collection and structure refinement are reported in Table 7.1.

The crystal structure of compound **4@51**@5CH_3CN was determined by X-ray diffraction methods. Intensity data and cell parameters were recorded at 173 K on a Bruker AXS Smart 1000 single-crystal diffractometer (employing a MoK_α radiation and a CCD area detector). The raw frame data were processed using SAINT and SADABS to yield the reflection data file.[6] The

structures were solved by Direct Methods using the SIR97 program[7] and refined on F_o^2 by full-matrix least-squares procedures, using the SHELXL-97 program.[8]

The PLATON SQUEEZE procedure[9] was used to treat regions of diffuse solvent which could not be sensibly modeled in terms of atomic sites. Their contribution to the diffraction pattern was removed and modified F_o^2 written to a new HKL file. The 275 electrons per unit cell thus located are included in the formula, formula weight, calculated density, μ and F(000). This residual electron density was assigned to twelve molecules of acetonitrile per unit cell.

	4@51@5CH_3CN
Formula	$C_{88}H_{99}IN_6O_{15}P_4$
Molecular weight	1731.51
Crystal system	Monoclinic
Space group	*P*21/c
a / Å	15.479(3)
b / Å	37.943(6)
c / Å	16.352(3)
β / °	113.988(2)
V / Å^3	8775(2)
Z	4
T / K	173(2)
ρ / g cm^{-3}	1.311
μ / mm^{-1}	0.504
F(000)	3608
Data / parameters	19711 / 950
Total reflections	71985
Unique reflections (R_{int})	19711 (0.0384)
Observed reflections [$I>2\sigma(I)$]	13715
Goodness–of–fit on F^{2a}	1.002
R indices [$I>2\sigma(I)$][b] R1, wR2	0.0484, 0.1296
Largest diff. peak and hole / eÅ^{-3}	0.827, -0.1.097
[a]Goodness-of-fit S = $[\Sigma w(F_o^2-F_c^2)^2/(n-p)]^{1/2}$, where n is the number of reflections and p the number of parameters. [b]R1 = $\Sigma \| F_o \| - \| F_c \| / \Sigma \| F_o \|$, wR2 = $[\Sigma[w(F_o^2-F_c^2)^2]/\Sigma[w(F_o^2)^2]]^{1/2}$	

Table 7.1. Crystal data and structure refinement information for **4@51**@5CH_3CN.

All non-hydrogen atoms were refined with anisotropic atomic displacements with the exclusion of one acetonitrile molecule; the hydrogen atoms were included in the refinement at idealized geometry (C-H 0.95 Å) and refined "riding" on the corresponding parent atoms.

The weighting scheme used in the last cycle of refinement was $w = 1/[\sigma^2 F_o^2 + (0.0848P)^2 + 1.4464P]$, where $P = (F_o^2 + 2F_c^2)/3$.

Molecular geometry calculations were carried out using the PARST97 program.[10] Drawings were obtained by ORTEP3 in the WinGX suite.[11]

7.5.3 Synthetic Protocol.

$Fe_4(L'')_2(dpm)_6$. ($Fe_4(PhCl)_2$, 52)

$Fe_4(PhCl)_2$ was prepared in Cornia's Group following a published procedure.[5] H_3L'' = 2-(4-chloro-phenyl)-2-hydroxymethyl-propane-1,3-diol.

2-(benzoyloxymethyl)-2-(hydroxymethyl)propane-1,3-diyl dibenzoate. (53)

To a stirred solution of pentaerythritol (500 mg, 3.672 mmol) in toluene (3 mL), pyridine (177 μL) was added. The mixture was stirred for 30 minutes at room temperature, then 1.28 mL of benzoyl chloride were dropped into the flask at 0°C. The reaction mixture was stirred at 50°C for 30 hours. After cooling to room temperature, the solvent was removed under vacuum and the resulting residue was extracted in CH_2Cl_2/H_2O. The organic phase was purified by column chromatography (dichloromethane:MeOH 95:5) affording the desired product as a clear oil (659 mg, 1.469 mmol, 40%).

^{1}H NMR ($CDCl_3$, 300 MHz) δ(ppm): 8.01 (d, 6H, J = 7.1 Hz, ArH_o), 7.56 (m, 3H, ArH_p), 7.41 (m, 6H, ArH_m), 4.59 (s, 6H, $C^{IV}(CH_2OCOPh)_3$, 3.78 (s, 2H, $C^{IV}CH_2OH$). **ESI-MS:** m/z 471.02 $[M+Na]^+$.

2-(benzoyloxymethyl)-2-(bromomethyl)propane-1,3-diyl dibenzoate. (54)

A solution of compound **53** (291 mg, 0.649 mmol) in thionyl bromide (5 mL) and DMF (3 drops), was stirred at 50°C for two hours. After cooling to room temperature, the residue was purified by column chromatography

(dichloromethane:MeOH 95:5) to yield the desired product as a clear oil (326 mg, 0.639 mmol, 98%).

^{1}H NMR (DMSO-d_6, 300 MHz) δ(ppm): 7.99 (d, 6H, J = 7.8 Hz, ArH_o), 7.65 (m, 3H, ArH_p), 7.48 (m, 6H, ArH_m), 4.59 (s, 6H, C^{IV}(CH_2OCOPh)$_3$), 4.02 (s, 2H, $C^{IV}CH_2$Br). **ESI-MS:** m/z 533.1 $[M+Na]^+$.

4-(pyridyl-4-ylethynyl)phenol. (55)

100 mL of dry Et_3N were degassed in a dry flask for 30 minutes. Then, 4-iodophenol (500 mg, 2.273 mmol), ethynylpyridine hydrochloride (508 mg, 3.636 mmol), $Pd(PPh_3)_2Cl_2$ (33 mg, 0.047 mmol), CuI (17 mg, 0.089 mmol) and PPh_3 (47 mg, 0.178 mmol) were added and the mixture was stirred for 24 hours at 60°C. After cooling to room temperature, the solvent was removed under vacuum, the residue sonicated in dichloromethane and filtered. The crude was purified by column chromatography (AcOEt:Hexane 6:4) affording the desired product in 21% yield.

^{1}H NMR (DMSO-d_6, 300 MHz) δ(ppm): 10.09 (s, 1H, ArOH), 8.58 (bd, 2H, PyH_o), 7.44 (m, 2H + 2H, PyH_m + ArH_m), 6.82 (d, 2H, J = 8.6 Hz, ArH_o). **ESI-MS:** m/z 196.1 $[M+H]^+$.

2-(benzoyloxymethyl)-2-((4-(pyridin-4-ylethynyl)phenoxy)methyl)propane-1,3-diyl dibenzoate. (56)

To a stirred solution of **55** (148 mg, 0.759 mmol) in anhydrous DMA (10 mL) under N_2, solid NaH (264 mg, 11 mmol) was added in one portion. The resulting suspension was stirred for 30 minutes at room temperature, then compound **54** (464 mg, 0.910 mmol) was added in one portion. The temperature was raised to 90°C and the reaction was stirred at that temperature overnight under N_2. After cooling to room temperature, excess NaH was quenched with dilute HCl and the reaction mixture was extracted with dichloromethane. The residue, obtained from the organic phase dried, was purified by column chromatography (dichloromethane:MeOH 99:1) affording the desired product (**55**) as a brown oil (112 mg, 0.179 mmol, 23%).

^{1}H NMR ($CDCl_3$, 300 MHz) δ(ppm): 8.56 (d, 2H, J = 5.8 Hz, PyH_o), 8.00 (d, 6H, J = 7.2 Hz, OCOArH_o), 7.58 (m, 3H, OCOArH_p),

7.47 (d, 2H, J = 8.8 Hz, $C^{IV}OAr\mathit{H}_m$), 7.40 (m, 6H, $OCOAr\mathit{H}_m$), 7.34 (d, 2H, J = 5.8 Hz, $Py\mathit{H}_m$), 6.91 (d, 2H, J = 8.8 Hz, $C^{IV}OAr\mathit{H}_o$), 4.75 (s, 6H, $C^{IV}(C\mathit{H}_2\ OCOPh)_3$), 4.31 (s, 2H, $OC\mathit{H}_2\ C^{IV}$). **ESI-MS:** m/z 626.3 $[M+H]^+$.

2-(hydroxymethyl)-2-((4-(pyridyl-4-ylethynyl)phenoxy)methyl)propane-1,3-diol. (57)

To a stirred suspension of compound **56** (100 mg, 0.160 mmol) in methanol (5 mL), K_2CO_3 (73 mg, 0.528 mmol) was added. The resulting mixture was stirred at room temperature for one hour. Then, the solvent was removed and the residue extracted in dichloromethane and water. The removal of the solvent afforded the desired product as a brown solid (49 mg, 0.156 mmol, 97%).

^{1}H NMR (Acetone-d_6, 300 MHz) δ(ppm): 8.60 (bd, 2H, $Py\mathit{H}_o$), 7.52 (d, 2H, J = 8.9 Hz, $C^{IV}OAr\mathit{H}_m$), 7.45 (d, 2H, J = 5.9 Hz, $Py\mathit{H}_m$), 7.01 (d, 2H, J = 8.9 Hz, $C^{IV}OAr\mathit{H}_o$), 4.06 (s, 2H, $OC\mathit{H}_2\ C^{IV}$),3.79 (m, 3H, $CH_2O\mathit{H}$), 3.72 (d, 6H, J = 5.0 Hz, $C^{IV}(C\mathit{H}_2OH)_3$). **ESI-MS:** m/z 336.8 $[M+Na]^+$.

4-((4-(3-hydroxy-2,2-bis(hydroxymethyl)propoxy)phenyl)ethynyl)-1-methylpyridinium iodide. (58)

To a solution of compound **57** (40 mg, 0.128 mmol) dissolved in 5 mL of DMF, iodomethane (24 μL, 0.384 mmol) was added. The reaction was stirred overnight at 50 °C. The solvent was removed and the crude was sonicated in acetone and filtered bearing the desired product (57 mg, 0.125 mmol, 98%).

^{1}H NMR (MeOD, 300 MHz) δ(ppm): 8.80 (d, 2H, J = 6.8 Hz, $Py\mathit{H}_o$), 8.05 (d, 2H, J = 6.8 Hz, $Py\mathit{H}_m$), 7.63 (d, 2H, J = 8.8 Hz, $C^{IV}OAr\mathit{H}_m$), 7.06 (d, 2H, J = 8.8 Hz, $C^{IV}OAr\mathit{H}_o$), 4.35 (s, 3H, $NC\mathit{H}_3$), 4.04 (s, 2H, $OC\mathit{H}_2C^{IV}$), 3.69 (s, 6H, $C^{IV}(C\mathit{H}_2OH)_3$). **ESI-MS:** m/z 328.1 $[M-I]^+$.

7.6 References.

[1] a) T. Lis, Preparation, structure, and magnetic properties of a dodecanuclear mixed-valence manganese carboxylate, *Acta Crystallogr. Sect. B.* **1980**, *36*, 2042-2046.
b) R. Sessoli, D. Gatteschi, A. Caneschi, M. A. Novak, Magnetic bistability in a metal-ion cluster, *Nature* **1993**, *365*, 141-143.
c) G. Christou, D. Gatteschi, D. N. Hendrickson, R. Sessoli, Single Molecule Magnets, *MRS Bull.* **2000**, *25*, 66-71.

[2] G. Rogez, B. Donnio, E. Terazzi, J.-L. Gallani, J.-P. Kappler, J.-P. Bucher, M. Drillon, The Quest for Nanoscale Magnets: The example of [Mn12] Single Molecule Magnets, *Adv. Mater.* **2009**, *21*, 4323-4333.

[3] G. G. Condorelli, A. Motta, I. L. Fragalà, F. Giannazzo, V. Raineri, A. Caneschi, D. Gatteschi, Anchoring Molecular Magnets on the Si(100) Surface, *Angew. Chem., Int. Ed.* **2004**, *43*, 4081-4084.

[4] a) A. B. Sieval, A. L. Demirel, J. M. Nissink, M. R. Linford, J. H. van der Maas, W. H. de Jeu, H. Zuilhof, E. J. R. SudhKlter, Highly Stable Si-C Linked Functionalized Monolayers on the Silicon (100) Surface, *Langmuir* **1998**, *14*, 1759-1768.
b) G. F. Cerofolini, C. Galati, S. Reina, L. Renna, Functionalization of the (100) surface of hydrogen-terminated silicon via hydrosilation of 1-alkyne, *Mater. Sci. Eng. C.* **2003**, *23*, 253-257.

[5] G. G. Condorelli, A. Motta, G. Pellegrino, A. Cornia, L. Gorini, I. L. Fragalà, C. Sangregorio, L. Sorace, Site-Specific Anchoring of Tetrairon(III) Single Molecule Magnets on Functionalized Si(100) Surfaces, *Chem. Mater.* **2008**, *20*, 2405-2411.

[6] a) SADABS Bruker AXS; Madison, Wisconsin, USA, **2004**; SAINT, Software Users Guide, Version 6.0; Bruker Analytical X-ray Systems. In *Software Users Guide, Version 6.0; Bruker Analytical X-ray Systems*, Madison, WI, **1999**.
b) G. M. Sheldrick, SADABS v2.03: *Area-Detector Absorption Correction.* University of Göttingen, Germany, **1999**.

[7] A. Altomare, M.C. Burla, M. Camalli, G. L. Cascarano, C. Giacovazzo, A. Guagliardi, A. G. G. Moliterni, G. Polidori, R. Spagna, SIR97: a new tool for crystal structure determination and refinement, *J. Appl. Crystallogr.* **1999**, *32*, 115-119.

[8] a) G. M. Sheldrick, SHELXL-97. Program for Crystal Structure Refinement. University of Göttingen, Germany, **1997**.

b) G. M. Sheldrick, A short history of SHELX, *Acta Crystallogr.* **2008**, *A64*, 112-122.

[9] SQUEEZE - P. V.d Sluis and A. L. Spek, BYPASS: an effective method for the refinement of crystal structures containing disordered solvent regions, *Acta Crystallogr., Sect A.* **1990**, *46*, 194-201.

[10] a) M. Nardelli, PARST: a system of FORTRAN routines for calculating molecular structure parameters from results of crystal structure analyses, *Comput. Chem.* **1983**, *7*, 95-98.
b) M. Nardelli, PARST95 - an update to PARST: a system of Fortran routines for calculating molecular structure parameters from the results of crystal structure analyses, *J. Appl. Crystallogr.* **1995**, *28*, 659.

[11] L. J. Farrugia, ORTEP-3 for windows - a version of ORTEP-III with a graphical user interface (GUI), *J. Appl. Crystallogr.* **1997**, *30*, 565.